Alma Mater Studiorum - Università di Bologna

DOTTORATO DI RICERCA IN

AUTOMOTIVE PER UNA MOBILITÀ INTELLIGENTE

Ciclo 34

Settore Concorsuale: 09/E2 - INGEGNERIA DELL'ENERGIA ELETTRICA

Settore Scientifico Disciplinare: ING-IND/32 - CONVERTITORI, MACCHINE E AZIONAMENTI ELETTRICI

PCM-BASED BATTERY THERMAL MANAGEMENT SYSTEMS, ENERGY SAVING MATERIALS AND LCA STRATEGY FOR AUTOMOTIVE

Presentata da: Morena Falcone

Coordinatore Dottorato

Nicolò Cavina

Supervisore

Beatrice Pulvirenti

Co-supervisore

Dario Croccolo

Esame finale anno 2022

LONG ABSTRACT

This PhD work arises from the necessity to give a contribution to the energy saving field, considering automotive applications. The research program have taken steps in several directions: from innovative materials to cutting-edge battery thermal management systems (BTMSs) and also dealing with the life cycle assessment (LCA) of the battery packs (BPs). The aim was to produce a multidisciplinary work to show how much important is taking into account different aspects of an electric car realization as they all contribute to the overall energy consumption.

Regarding the materials, it has been chosen to focus on carbon fiber composites as their use allows realizing light products with great mechanical properties. Processes and methods to produce carbon fiber goods have been analysed with a special attention on the *Emilia 4* case study: the solar car made by the sport team *Onda Solare* represents an example of how carbon fibers can be an effective solution to the weight reduction and, consequently, the and energy saving in automotive.

The lightening of a car is just one of the effective moves to lower the energy consumption: in an electric car lot of attention has to be put on the battery pack and and its cooling systems which allows it working properly. This is why the work presents several BTMSs which are the most common on the market and, then, it deepens some of the most innovative ones. Among the ordinary ones the attention has been focused on air-cooled systems, cooling plates and heat pipes. Then, some innovative cooling strategies have been discussed such as the immersive and the thermoelectric ones and the BTMSs based on phase change materials (PCMs).

It has been decided to meticulously study this last avant-garde cooling strategy as it was not available a clear and detailed literature about the PCM-based BTMSs. A previous experimental campaign has been necessary to characterize the PCMs and interesting results have come out: in particular, the investigations have dealt with initial qualitative tests regarding the melting time of a PCM, an aluminum-foam-loaded PCM and a copper-foam-loaded PCM, then quantitative tests have been carried on. The temperature homogeneity on the planes (x,y) during the melting cycle of the PCM has been studied and a comparison between the melting cycles of a pure PCM and a copper-foam-loaded PCM has been done, focusing on the thermal conductivity and thermal homogeneity enhancements.

After the PCM characterization it has been possible to proceed with a complex experimental campaign regarding PCM-based BTMSs, considering both uninsulated and insulated systems. About the first category, the tested systems have been pure PCM-based and copper-foam-loaded-PCM-based BTMSs; the insulated tested systems have been pure PCM-based and copper-foam-loaded-PCM-based BTMSs and both of these systems equipped with a liquid cooling circuit. Results have shown

that with an uninsulated system the copper-foam-loaded-PCM-based BTMS represents a valid choice both in terms of proper working temperatures for the Li-ion batteries (LIBs) and considering the negative convective motions which develop with pure PCM but are hindered by the metal foam. With an insulated BTMS the use of a PCM-based (passive) cooling method is not enough to satisfy the LIB thermal requirements and a liquid (active) cooling circuit is necessary: the coupled use of active and passive systems allows achieving the desired temperatures and the proper temperature distribution inside the BP.

The choice of lighter building materials and the optimization of the BTMS are strategies which helps in reducing the energy consumption considering both the energy required by the car to move and the BP state of health (SOH). Focusing on this last factor, a clear explanation regarding the importance of taking care about the SOH (reducing the aging phenomena and allowing a longer BP duration) is given by the analysis of a BP production energy consumption. This is why a final dissertation about the life cycle assessment (LCA) of a BP unit has been presented in this thesis.

Three main research macro-topics have been considered: the cells support, the Li-ion cells and the BTMS. For each of these components the extraction, processing and transporting impacts have been estimated and the partial and total values of the energy demand (ED) and the global warming potential (GWP) have been shown and discussed. A final interpretation of the data allows understanding the possible ways to reduce these values.

CONTENTS

INTRODUCTION

The research topics on which this PhD thesis has been based come out from the awareness that the global energy demand is constantly increasing as well as the world population and, consequently, the greenhouse gas emissions. The balance between the energy demand and consumption and the strategies to lower the CO_2 emissions are two of the hardest challenges of our time and many efforts are daily spent by researchers all over the world trying to face and solve these issues.

This PhD thesis arises from this necessity and aims to give its contribution to the cause, proposing several energy-saving solutions concerning the electric vehicles field. From the cutting-edge building materials to the comparison between ordinary and innovative battery thermal management systems (BTMSs) and also analysing the life cycles of the battery packs, several discussions and multidisciplinary investigations are presented in this work.

The starting research questions concerned the possibility of facing the energy-saving topic both in terms of energy needed by the car to move its own weight while on motion and analyzing existing and innovative solutions to preserve the vehicle BP. In particular, this last aspect finds its basis in the consideration that the lower are the aging issues, the longer is the life of the car parts considered and, consequently, the lower is the production energy consumption. A strong push to proceed in this research direction, studying cutting-edge building materials and ordinary and novel BP cooling systems with an experimental approach, was given by the analysis of the current state of the art. The existing literature is plenty of analytical works dealing with the research questions mentioned above, but there is a scarcity of experimental studies which would be useful to validate the analytical ones. For this reason, the approach chosen to carry on the investigations presented in this thesis has been strongly experimental but always supported by the analytical studies present in the literature.

The first part of this thesis concerns the composite materials, their structure, how they are classified. It focuses on the carbon fiber composites as one of the best solutions to lower the car weight and, consequently, reducing the energy (or fossil fuel in heat engine cars) consumption. Several methods to realize carbon fiber products are presented such as the hand layup, the under-vacuum process and autoclave cure, the compressing molding, the resin transfer molding and the vacuum-assisted resin transfer molding. An optimization strategy regarding the production process of carbon fiber objects is proposed and carried on with the product lifecycle management software *Fibersim*. Finally, experimental evidences of the lightening brought by the carbon fiber use are shown thanks to the *Onda Solare* project, the university solar car team which designs and realizes competitive cars fully made of carbon fibers.

The second part of the thesis deals with the battery thermal management systems, presenting a deep study about the most common BTMSs on the market such as the forced-air-based ones, the cooling plates and the heat pipes, highlighting their pros and cons and also showing some of the most innovative battery pack cooling technologies. Among these systems it has been chosen to deepen the phase-change-material-based BTMS.

To do this, a previous overview about the phase change materials (PCMs) is reported, presenting qualitative and quantitative experimental tests regarding the physical behaviour of these materials during the phase change process. In particular, the temperature distribution and the thermal conductivity have been investigated. After this preparatory phase, all the experiments concerning the PCM-based BTMS are shown. The tests have been divided into two main experimental campaigns: the uninsulated BTMS tests and the insulated BTMS ones. During the experimental campaign about the uninsulated BTMSs three cooling systems have been tested: the forced-air, the pure PCM and the copper-foam-loaded-based one. During the experimental campaign about the insulated BTMSs four cooling systems have been tested: the pure PCM-based BTMS, the copper-foam-loaded-based one and these two systems coupled with a further liquid-cooling circuit.

The last part of this thesis presents the life cycle assessment (LCA) of a BP unit, not only as analytical research method to estimate the energy demand and the CO_2 emissions but also as the proper mindset with which every industry stakeholder should work. A LCA study regarding a *LiBER* (Lithium Battery for Emilia-Romagna) battery pack unit is shown with investigations about the energy demand (ED) and the Global Warming Potential (GWP) related to the raw materials extraction, their processing and the components transportation impact. A final interpretation of the results proposes several energy-saving solutions.

1

COMPOSITE MATERIALS

1.1 INTRODUCTION

The importance of composite materials derives from their very nature: it is possible to combine two materials with different physical and chemical properties, creating a new material which is the appropriate one considering a precise application. It is since the Mesopotamian society that the composites are used: in 3400 B. C. people who lived those lands started to produce plywood gluing together different wooden stripes, in 2181 B. C. the Egyptians soaked linen or papyrus with plaster to make death masks and in 1200 A. D. the Mongols exploited the composites in the war field, making bows with wooden, bamboo, bones and horns, animal tendons and silk, everything bonded with pine resin [1]. An important step froward was done at the end of the XIX century when, thanks to polymerization processes, new synthetic resins (useful as matrices in the future composite materials) were prepared for the first time. During World War II, as hedge against the rationing of metals which had become precious materials, many car companies started to carry on several experiments to produce composites for their vehicles. One of the most famous result was the Ford "hemp" car, a vehicle with the body and the fenders made of a plastic composite material obtained with soy, corn, hemp and wheat beans [2] and whose final weight was about 450 *kg* lighter than the average of the common cars at that time.

Figure 1.1. *Henry Ford during the famous resistance to impact test carried out with an axe on his personal hemp car [3].*

Another famous example of composite cars is the Stout 46, a car with a fully composite frame realized by the *Owens Corning* company in collaboration with William Stout [4] in the '40s: from that moment on, there was a composites use escalation in the automotive field.

Composites are a very attractive solution, in particular in those fields where the strength to weight ratio needs to be as lower as possible and also thanks to their high strength to stiffness ratio. On the today market there is a huge variety of composite materials like fiber reinforced composites [5], particle reinforced composites [6], sandwich panels [7], metal matrix composites [8] and ceramics matrix composites [9] which differ from each other in the build-up, the matrix and the reinforcement type. Nowadays composite materials are used in several fields such as electronics [10], aeronautics [11], aerospace [12], sports [13], automotive [14].

The automotive field of the last forty years has been interested by a huge increase in the use of light materials with high mechanical properties. Considering the constant rise of the energy demand, the choice of the carbon fibers as automotive building material seems to be one of best the solutions in terms of energy saving. The leitmotiv is that the lighter is a car the lower are the consumption, whatever is their nature (fossil fuel, electricity or solar energy): this is why in the extreme automotive applications as supercars [15] or competition cars (for instance the Formula 1 vehicles), the weight always plays a key role. Studies demonstrated that the substitution of metal parts with carbon fiber ones brings to a significant weight reduction which can even reach the 80% [16]. Further, the success of the carbon fibers also derives from the environmental aspect: many recent studies are involved into the carbon fiber second life to obtain recycled short fibers [17] useful both in the design field and in the building one [18] so that it is possible to reduce the costs and the wastes [19].

1.2 COMPOSITES STRUCTURE AND CLASSIFICATION

A composite material is a heterogeneous material with final characteristics designed to be superior to those of its constituents. Composites are usually made of two principal components such as a reinforcement and a matrix. The reinforcement is the discontinuous and more resistant phase; the matrix is the continuous and less resistant phase whose work is to incorporate and bind the reinforcement.

There are several ways to classify the composite materials. One of the most common and used criteria is that which takes into account the shape and the orientation of the reinforcement. The following main composite classes (Figure 1.2) are presented in order of increasing strength, stiffness and cost:

- Particle reinforced composites;
- Short fiber composites;
- Long fiber composites;

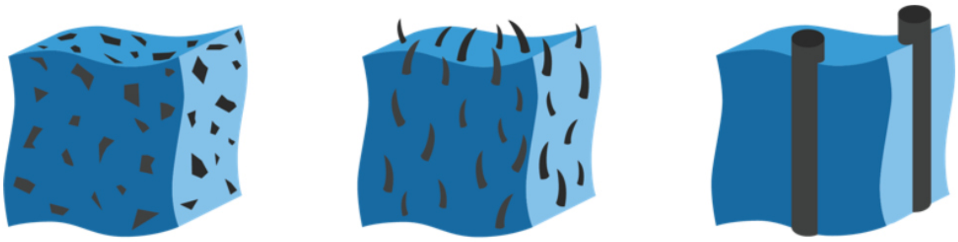

Figure 1.2. *The most common classification of the composite materials [20].*

Particle reinforced composites can be loaded with lamellar or spherical (solid or hollow) particles. The lamellae are usually made of talc or mica and their presence slightly increases the stiffness and the strength of the composites. The spheres can be made of glass, silica, rubber, carbon black, giving the final structure the same benefits of the lamellae in terms of mechanical properties. In addition, based on what material they are made of, the reinforced composites can also be tougher (with rubber) or more resistant to photo-aging (black carbon). In particle reinforced composites the improvement of the mechanical properties is not so significant as the load is equally distributed between the matrix and the reinforcement and the stiffness and strength improvements involve all the directions (isotropic behaviour). This kind of materials is mainly used where high levels of wear-resistance are required such as for road surfaces. These composites are easy to produce and have a low cost [21].

Short fiber composites are materials whose reinforcement is made of fibres with a diameter which ranges from $d_{\text{min}} = 10\ \mu m$ to $d_{\text{max}} = 30\ \mu m$, a length from $l_{\text{min}} = 1\ cm$ to $l_{\text{max}} = 10\ cm$ and a random orientation (they are rarely oriented in one single precise direction). The matrix can be a vinyl one or it can be made of polyester, the reinforcement can be realized with glass or carbon fibers. The improvement of the mechanical properties is greater than that obtainable with particle reinforced composites but not comparable with that achievable with long fiber composites. When the fibers are randomly distributed, the stiffness and strength increase involves all the direction (isotropic behaviour). Further, these materials are more resistant to corrosion compared to metals. Typical applications are in the nautical, sport and building fields and their cost is intermediate between the particle reinforced and the long fiber composites.

Long fiber composites have a length which is comparable to that of the final object. It is reasonable to assume that with this kind of composites a load with a direction parallel to the fibers is applied on the fibers themselves, not on the matrix. This last element works for the load distribution, keeps the fibers together and protects them against corrosion phenomena. Long fiber composites find their application in several fields, from sport to building, until the automotive.

From a structural point of view there is a sort of hierarchy in the composite world (Figure 1.3): aligned fibers incorporated into a matrix create a ply (or lamina); the stacking of two or more plies with several fiber directions gives a composite laminate as a result. The ply is an orthotropic element (anisotropic with three mutually orthogonal planes of symmetry), it is very resistant in the direction parallel to the fibers but, at the same time, its strength is low in the direction transverse to the fibers: in that case the load is completely applied to the matrix. The laminate is an isotropic element and its stiffness and strength can vary depending on how the fibers are oriented in every ply it is composed of. A composite structure is made of two or more laminates, properly put together on the basis of what is the final result desired. Further, from the dimensional scale on which the attention is focused derives a different way to analyze the mechanical behaviour of the studied object.

Looking at Figure 1.4 and Figure 1.5 the pros in the use of composites are clear: these materials allow obtaining extremely high specific strength and specific stiffness values on the plane. Additionally, composites do not show important thermal expansion effects as in the metals, they are corrosion resistant and the starting investment to build a composite production pole is affordable.

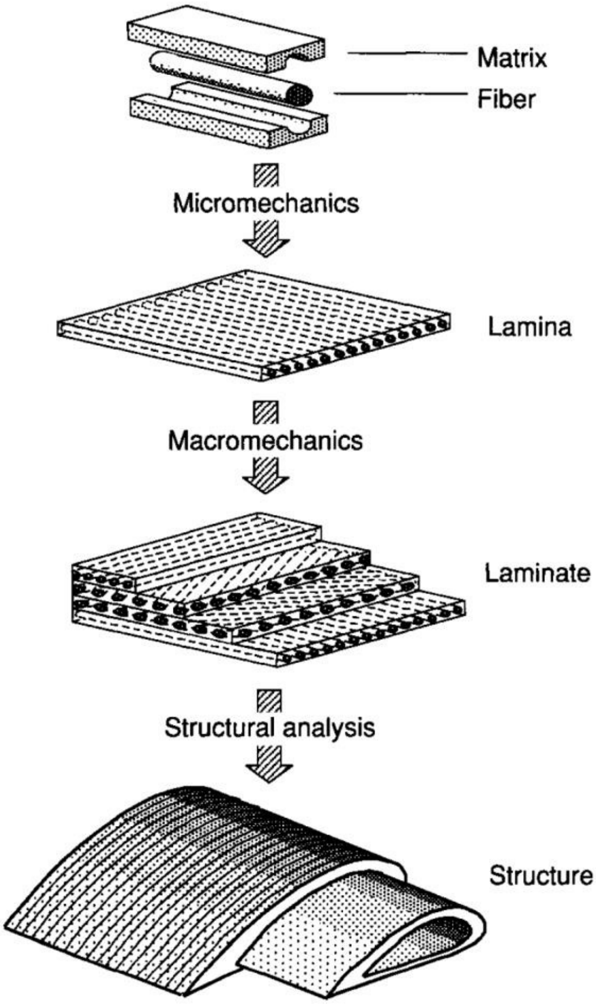

Figure 1.3. *Dimensional scale: from the fiber to the composite structure [22].*

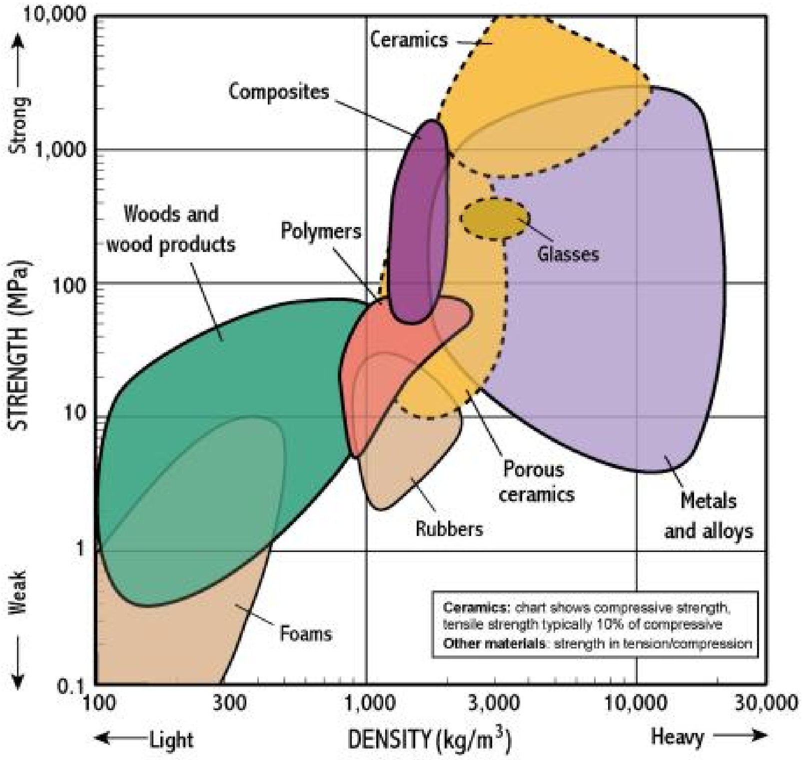

Figure 1.4. *Strength over density for different classes of materials [23].*

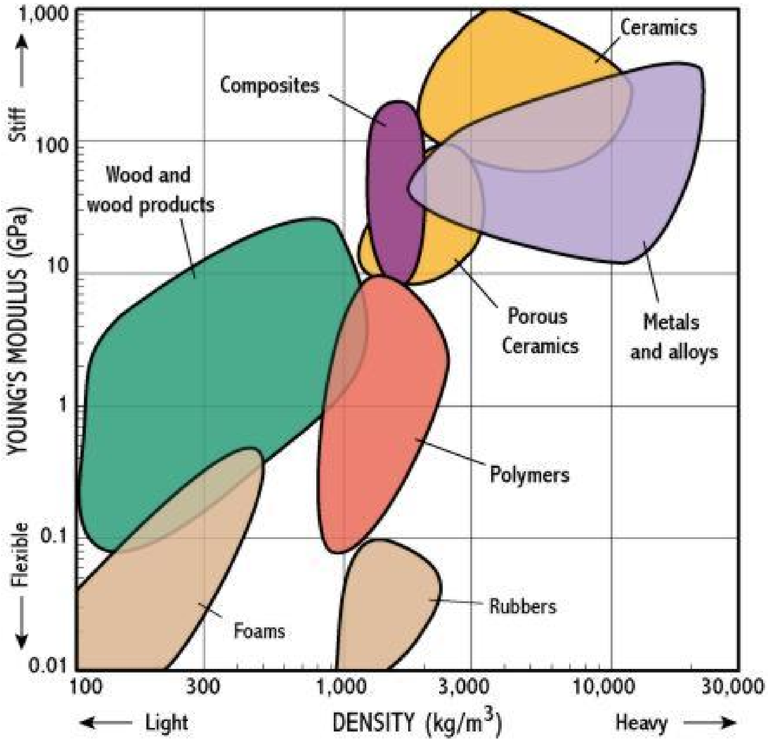

Figure 1.5. *Young's modulus over density for different classes of materials [23].*

Unfortunately composite materials have also a low specific fracture toughness and, once the composite structure is compromised, the propagation of the damage usually follows a precise pattern. Firstly it occurs the matrix cracking but in this phase nothing is visible with the naked eye as all the plies seem to be still stacked together. Secondly the delamination begins and the damage is clear as the plies start to detach one from each other. It all ends with a catastrophic failure. The difficulty in evaluating a damage during the matrix cracking phase often brings to catastrophic failures: it is necessary to pay a lot of attention in the choice of the proper composites and in the analysis of the loads that will be applied on the final composite structure. Other cons of the composite materials are the low strength outside the plane, the anisotropic behaviour of the laminate for which it is necessary a complex design phase, important stresses on the free edges due to the different stiffness of the plies which compose the laminate and which are often responsible for delamination phenomena.

Further, depending on the material, the maximum working temperature for the common composites is around $T = 250$ °C [22] (higher temperature can be tolerated by high performance carbon fiber composites which can reach $T = 450$ °C [24] or by innovative HfB_2-powder-based composites, useful for a very few niche applications, which can reach $T = 3000$ °C [25]). Hence, an appropriate evaluation needs to be done before choosing a composite material, considering all the pros and the cons and not forgetting that the mechanical properties of the composites have a high variability degree due to the poor repeatability of the lamination process.

1.2.1 *Carbon fiber composites*

Among the long fiber composites there are the fiber reinforced plastics (FRPs) which present a polymeric matrix that keeps together high strength fibers. In this kind of composites the reinforcement can be made of several materials such as glass, carbon or Kevlar® fibers and the matrix can be a thermosetting (e.g. epoxy, polyester, vinyl) or a thermoplastic one (e.g. PEEK, nylon). Although the high specific strength and stiffness of the fibers, the overall values related to the final composites are always much lower due to the low strength and stiffness of the polymeric matrices (Figure 1.6).

Carbon fibers are reinforcements characterized by high strength and stiffness, properties which can even be 10 times higher than the glass fiber ones. There are two main classes of carbon fibers:

- **HS** (high-strength) fibers;
- **HM** (high-modulus) fibers.

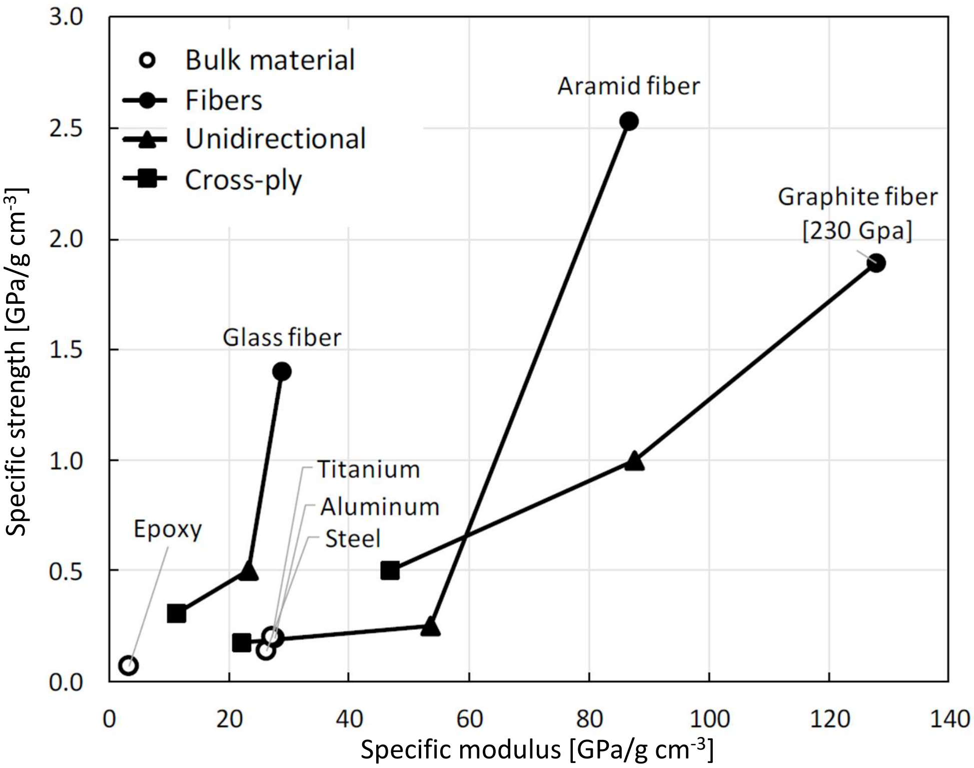

Figure 1.6. *Specific strength related to the specific modulus for different kind of composite materials and their components [22].*

The first category presents high strength values which can range from $\sigma_{\min} = 4\ GPa$ to $\sigma_{\max} = 7\ GPa$ but a medium stiffness which can vary from $k_{\min} = 240\ GPa$ to $k_{\max} = 300\ GPa$. The second class shows high values of stiffness which can cover the interval from $k_{\min} = 400\ GPa$ to $k_{\max} = 900\ GPa$ but a low strength which can go from $\sigma_{\min} = 2\ GPa$ to $\sigma_{\max} = 3\ GPa$ [22].

Considering how the fibers are oriented, the carbon plies are called unidirectional (1D or UD) if they are made of parallel carbon fibers, fabrics (2D) if they are made of woven fibers (Figure 1.7). A unidirectional ply has better mechanical properties (strength and stiffness) and it is cheaper with respect to a woven one but it is not always possible to use it. As the fibers are not woven, it is hard to manipulate the ply without damaging them: to laminate pieces with a complex shape avoiding to shred the fibers, the use of fabrics is the best choice.

Fibers need to be immersed into a matrix as them alone are not able to support compression stresses, transverse or shear loads. Matrices avoid the so called buckling issues which are problems derived from a loss of fiber elastic stability [26] and they also provide a protection from environmental factors (UV rays, humidity) and corrosive agents.

A thermosetting matrix is made of a resin and a hardener: it is by mixing these two components in a precise stoichiometric ratio chemical that reactions occurs. At the beginning the viscosity of the mixture decreases (this helps the fiber impregnation) and during this phase the temperature has a key role: the higher is the temperature, the faster drops the viscosity. Then a reticulation phase begins, ionic and covalent bonds are formed among the functional groups of the two reagents and there is the formation of small branched molecules (gelation phase). Finally, the viscosity sharply increases until the reticulation is completed and a 3D cross-linked structure is formed.

Figure 1.7. *A unidirectional carbon fiber roll (left) and a fabric carbon fiber roll (right).*

For thermosetting-matrix-based composites the glass transition temperature T_g has to be taken into account: this is a characteristic of the amorphous materials and represents a limit value above which the carbon chains start to move (the gap between the molecular chains increases by 2.5 times [27]). Once the transition from a hard and relatively fragile state to a gummy one is reached, the resulting state is irreversible.

A thermoplastic matrix is made of thermoplastic polymers whose chains have a bad cross-linking degree: there are both amorphous and crystalline regions which result in a semicrystalline structure [22]. As for amorphous materials there is the temperature limit T_g, for the crystalline ones there is the melting temperature T_m above which they are able to flow. This means that in thermoplastic-matrix-based composites, as they have semicrystalline matrices, the temperature limit T_l depends on the structure and $T_g < T_l < T_m$. T_l will be closer to T_g or to T_l if its structure has more amorphous or crystalline regions, respectively [27].

1.3 PRODUCTION METHODS

The processes by which carbon fiber objects are produced differ from each other considering how the plies are manipulated, how the resin impregnates the fibers, the time the process takes and its cost. Although all these factors it is possible to divide the production method into two main phases:

- Lamination process;
- Cure cycle.

The lamination is the phase during which the carbon fiber plies are positioned on the moulds and modeled on them. This process is carried on following the instructions written in the so called plybook: here all the fundamental layering data are collected. The plybook information deal with the type of the carbon plies (HS or HM), where they have to be put on the mould, their orientation, dimensions, if and how many cuts and overlaps are admitted.

At the end of the lamination process it may follow a phase during which the laminated piece is put under vacuum coupled with a manual or automated resin injection if dry fibers (not pre-impregnated) are used for the lamination. The production process ends with the cure, an operation during which the laminated piece is subjected to a heating cycle under precise values of temperature and pressure.

1.3.1 *Hand layup*

The hand layup technique is the easiest and most common composite lamination method. If the composite ply used is made of dry fibers, after putting it on the mould the manufacturer has to manually apply the resin (matrix), wetting the fibers and equally distributing this component everywhere on the composite surface. This has to be repeated for every ply stacked on the other ones to compose the final laminate, until the desired thickness value (written on the plybook) is reached. In this case the laminate can also be cured at the environmental temperature (although a heating cycle would help in accelerating the matrix catalyzing process) and the under-vacuum phase is not strictly necessary (but it would be positive in terms of final quality).

The advantages in using dry fibers are the cheap and minimal equipment needed (autoclave or vacuum pumps are not required) so that it is also possible to use this method in emergency situations (as during competitive challenges, when there is a lack of all the workshop facilities, Figure 1.8) and the possibility to laminate huge and complex components. On the other hand, there are several cons such as the volatile compound emissions, the difficulty to obtain uniform pieces, long cure cycles at the environmental temperature, a low production rate and the dependency of the laminate piece from the manufacturer ability.

A solution to some of these problems is represented by pre-impregnated (pre-preg) carbon fibers. This kind of fibers are industrially impregnated with a controlled quantity of resin so that the laminated piece has a more uniform distribution of fibers (70%) and matrix (30%) everywhere in the laminate [22]. With pre-preg plies the lamination process (Figure 1.9) is easier, the volatile compound emissions are lower and the final strength among the plies is higher thanks to the lower presence of air inclusions (a common issue with the manual fiber impregnation). As with dry fibers, the autoclave cure and the under-vacuum processes are not strictly necessary but the overall cost is higher due to the use of the more expensive pre-preg material.

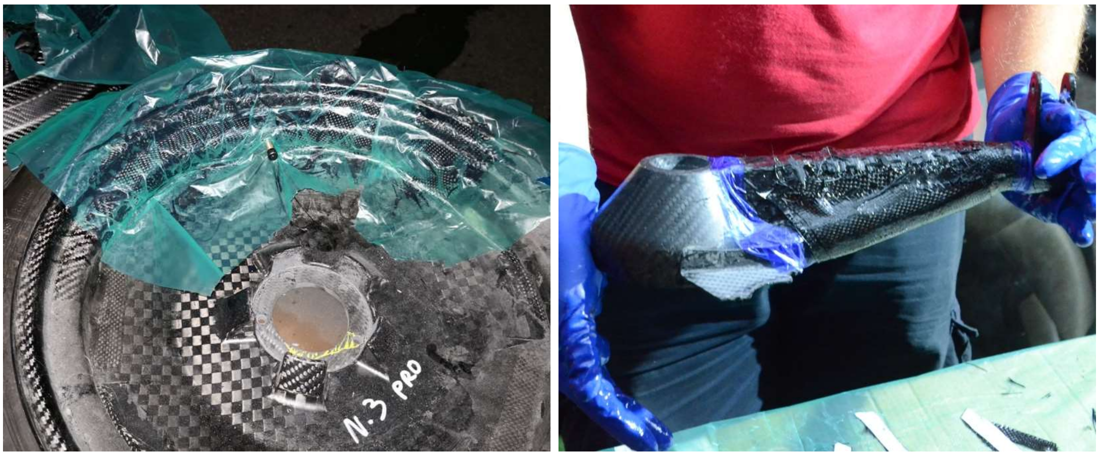

Figure 1.8. *Hand layup technique applied during a crack repair of a carbon fiber rim (left) and a carbon fiber bracket link in the course of the American Solar Challenge 2018.*

Figure 1.9. *Lamination process of a solar car rim with pre-preg carbon fiber plies.*

1.3.2 *Under-vacuum process and autoclave cure*

Independently from the kind of fibers used (dry or wet), the adoption of under-vacuum processes allows obtaining higher quality results. Once the lamination phase ends the laminate can be vacuum-packed: it is possible to cover the whole laminate with a flexible plastic bag which has to perfectly seal the mould or both the laminate and the mould can be put inside the vacuum bag. As it is possible to see in Figure 1.10, a release film has to be put on the laminate to prevent the plastic bag from sticking to the composite fibers. Then, a fabric called breather (or bleeder) is placed between the release film and the plastic bag to better distribute the vacuum and to absorb the exceeding resin. Finally, the vacuum pumps can be turned on. With the under-vacuum bag, the atmospheric pressure uniformly works on the composite laminate: this procedure is the best solution against air inclusions among the plies and it is also useful to squeeze the exceeding resin out from the carbon fiber plies, allowing the breather to absorb it.

Figure 1.10. *A carbon fiber rim laminated on a carbon fiber mould (left); a release film put in contact with the last carbon fiber ply and then covered by a breather (right).*

Figure 1.11. *A flexible sealed plastic bag, not under vacuum yet (left); the bag put under vacuum and placed into the autoclave (right).*

When the cure cycle has to be done in an autoclave the under-vacuum process is mandatory. Once the vacuum-bag is ready, it is put inside the autoclave (Figure 1.11): at that point the laminate is subjected both to the vacuum inside the bag and to the pressure inside the autoclave which acts on the composite piece. The value of the autoclave pressure is higher compared to the atmospheric one, ranging from $P_{\min} = 4\ bar$ to even $P_{\max} = 12\ bar$ [28]. The temperature increases until the set-up value (common cure temperatures for automotive or aeronautical applications vary from around $T_{\text{min}} = 120$ °C to $T_{\text{max}} = 180$ °C [29]) and the catalyzing process of the resin (matrix reticulation, see Section 1.2.1) starts. A typical autoclave cure cycle is shown in Figure 1.12. This method allows achieving final laminates with a very low air inclusion degree but the necessity of an autoclave often represents an obstacle in terms of cost.

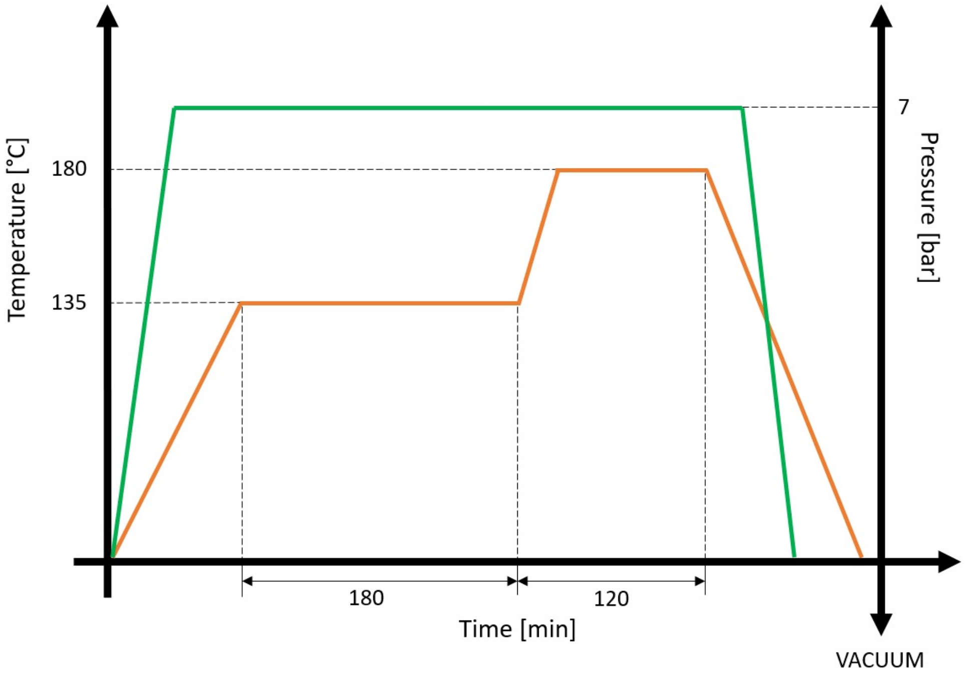

Figure 1.12. *Example of autoclave cure cycle for pre-preg carbon fiber composites.*

1.3.3 *Compression molding*

The compression molding is a completely automated process. A calculated quantity of material (fibers and resin) is loaded on a bottom mould during the charging phase; a hydraulic press pushes a top mould (countermould) on the bottom one with a defined pressure (even until $P = 100$ bar), releasing heat at the same time. The more the press pushes, the more the load occupies the empty spaces and acquires the shape of the mould. With the compression molding method the lamination time is drastically reduced as well as the waste of material. The obstacle in the spread of this technology is the initial cost (the press is an expensive machine) and the fact that the compression molding allows using only short fibers.

Lamborghini used this technology for its *Sesto Elemento* model (the name reminds to the sixth element of the periodic table that is carbon) [30] a supercar designed to drive in the circuits which is almost entirely made of carbon fibers: its total weight is equal to 999 kg. The underside of the monocoque and the suspension arms (Figure 1.13) are produced with the so called Forged Composite process that is exactly a compression molding used by *Lamborghini* for the *Sesto Elemento* [31].

Figure 1.13. *The underside of the monocoque (left) and one bracket (right) of the Lamborghini Sesto Elemento produced with a compression molding process.*

1.3.4 *Resin transfer molding (RTM)*

For the resin transfer molding technique it is necessary to use dry fibers: first they have to be positioned on a bottom mould and then a top mould is put on the bottom one. This top part of the mould is equipped with some orifices through which the matrix flows in and the air is drawn (Figure 1.14). When the resin is pumped it soaks the fibers and this is helped by the pushing action of the press. As the mould is filled with resin, the orifices are sealed and the cure begins inside the molding machine itself. It is a fast completely automates process (it can even take just 15 minutes) and the great advantage with respect to the compression molding is that it is also possible to work with long fiber composites. The cons are that the initial cost is high, the design of the mould is not so easy and sometimes there can occur impregnation problems when the resin is not able to completely fill the space between the top and the bottom moulds.

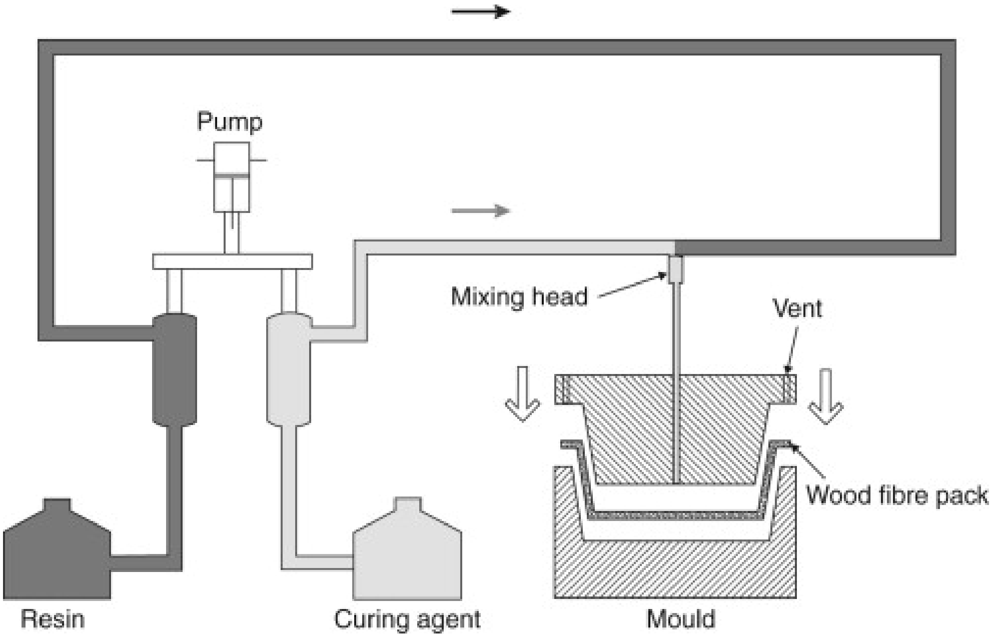

Figure 1.14. *Scheme showing the RTM of a wood fiber laminate [32].*

1.3.5 *Vacuum-assisted resin transfer molding (VARTM)*

A method similar to the RTM is the vacuum-assisted resin transfer molding which exploits the vacuum instead of the pressure applied by the press. As the press work is not required, it is also possible to build a VARTM machine with just the bottom half of the mould, substituting the top half with a vacuum bag. In general, the steel moulds used for the RTM are not necessary here as there are not high operating pressures and lighter moulds made of wood, epoxy resin or sheet metal are enough. The VARTM is a low volatile emission process and finds application in the realization of huge composite parts with a high fiber ratio. A risk not to underestimate is the possible formation of areas not completely impregnated: this can cause a bad adherence among the plies of the laminate and can bring to later delamination issues.

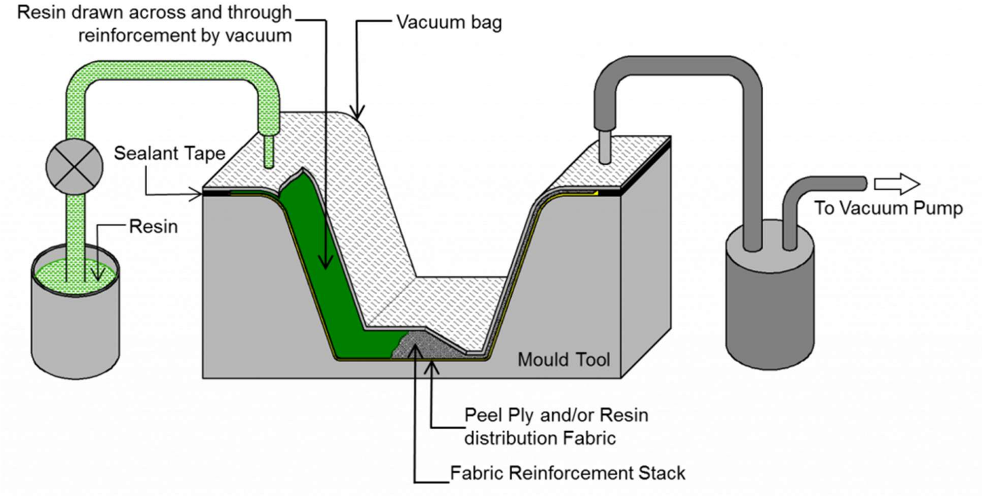

Figure 1.15. *Scheme showing a VARTM system [33].*

1.4 LAMINATION PROCESS OPTIMIZATION: FIBERSIM

The industrial processes have to be carried on both paying attention to the final quality of the results and not wasting time and materials. The adoption of process optimization plans lead a company to save time and energy, both important topics from the economic and environmental-friendly points of view.

During my PhD program I spent a period working in the *Mind Composites* [34], a company involved into the automotive field and where the entire composite production chain is handled, from the CAD design to the manufacturing processes. As member of the technical division I worked at two main projects (NDA covered) which dealt with the carbon fiber lamination process design. The first project was about the sides and the air intakes of a *Bugatti Divo*: the goal was to obtain carbon look vehicle parts considering a carbon fiber deviation tolerance $\alpha = 0.3°$. The second work concerned the pillars of a *Lamborghini Aventador* and the aim was to design a manufacturing process with as few cuts and overlaps as possible.

To optimize these two carbon fiber lamination processes I used *Fibersim*. *Fibersim* is a product lifecycle management (PLM) software developed by *Siemens* which works as an expansion of some of the most used CAD programs such as *CATIA*, *Creo*, *NX* and allows companies to simulate the lamination processes evaluating their feasibility or highlighting how to improve them. Using *Fibersim* coupled with *CATIA* (the CAD software I used in *Mind Composites*) the main steps to simulate a lamination process are the following:

- Drawing the mould on which the lamination will be done;
- Choosing the mould reference system;
- Defining the all the laminates (systems of plies) that will be realized (Figure 1.16);
- Choosing the rosettes (reference systems) for the laminates, one for all their different orientations;
- Defining all the plies that will be used for the lamination (UD or fabric, dry or wet, etc.) linking each of them to the proper laminate (Figure 1.17).

At this point the simulation can be run and the results will be something like those shown in Figure 1.18. A mesh allows understanding if the lamination process is well designed and if all the composite fibers are oriented with the desired angle (blue mesh), if there is a borderline situation with a slight fiber deviation angle (yellow mesh) or if the deviation exceeds the limits set (red mesh). A blue meshed simulation is always approved. The approval of a yellow meshed simulation depends on the application because different fields have different tolerance degrees: aerospace, automotive and sport are the fields with the most stringent limits both for safety and for aesthetics reasons. A red meshed simulation means that the piece cannot be laminated in the designed way and some changes need to be done: cuts, overlaps, different starting points or laying directions for the ply placement and the choice of another kind of ply can be some valid options.

After several iterations, once a satisfying simulation is obtained, it is possible to collect all the lamination information in a plybook which will be useful by the manufacturers. In this way they will have a clearer list of instructions to follow so that they can work not wasting material and with a higher certainty degree about the quality of the final result. Another useful advantage is that *Fibersim* simulations allow calculating the dimensions of the plies needed to exactly cover the moulds: starting from the 3D mesh, it is possible to obtain the flat patterns of the plies (DXF format files) which, in turn, will be directly read by the plotter that will cut the carbon fiber rolls.

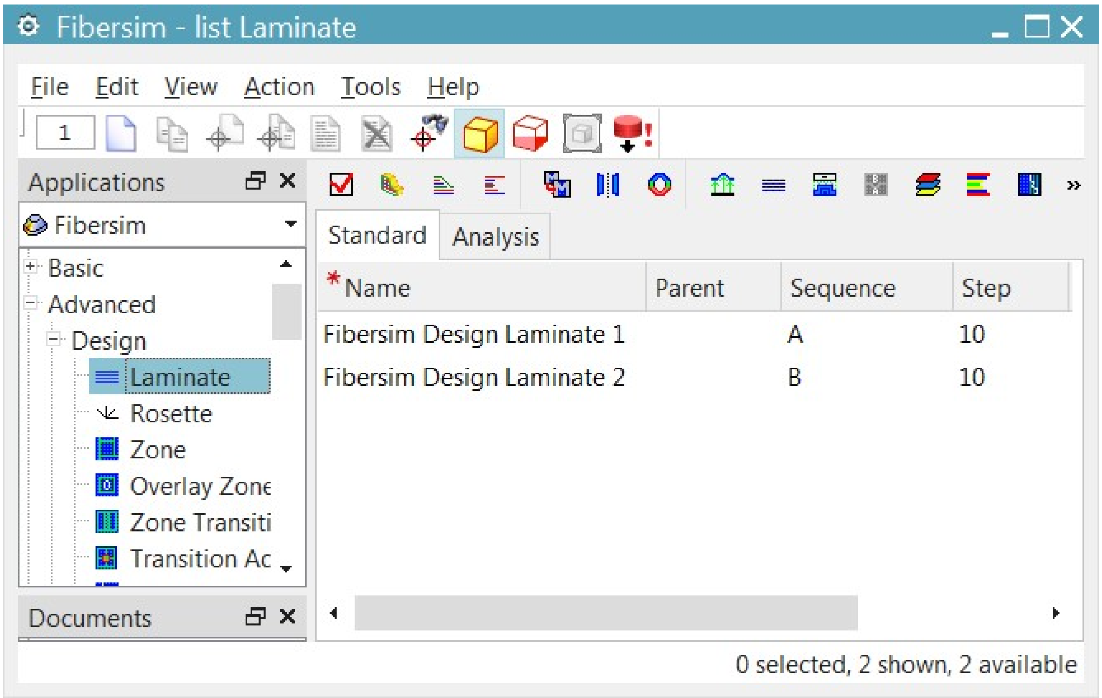

*Name	Parent	Sequence	Step
Fibersim Design Laminate 1		A	10
Fibersim Design Laminate 2		B	10

0 selected, 2 shown, 2 available

Figure 1.16. *Definition of the composite laminates to run a Fibersim simulation [35]: in this example two different laminates are designed.*

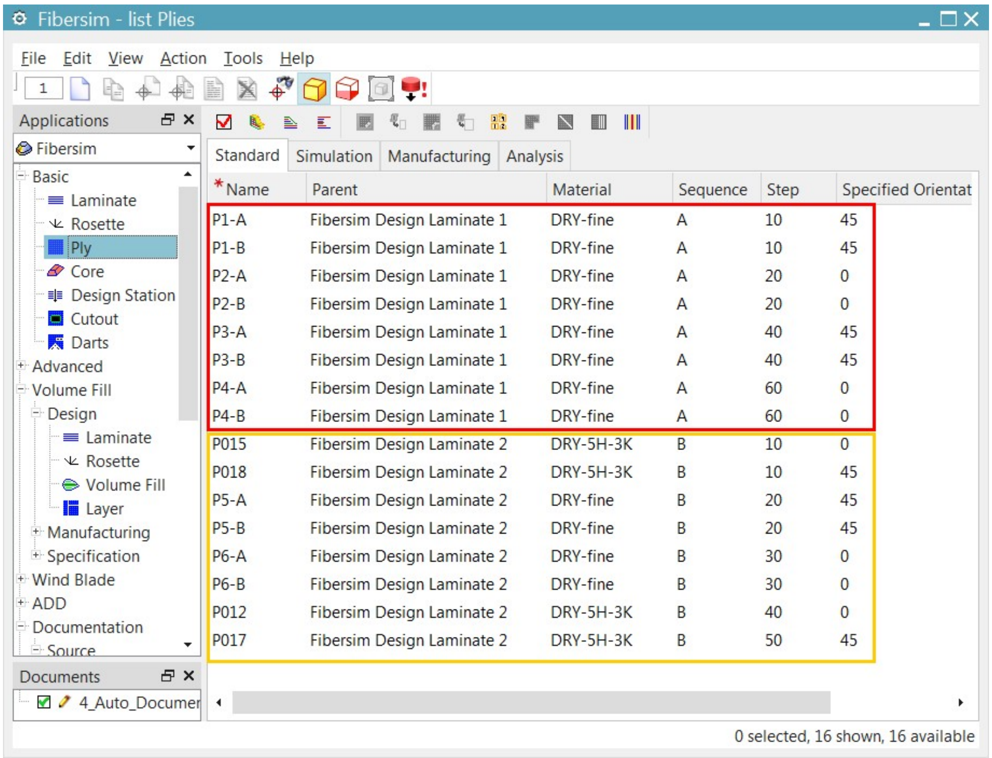

*Name	Parent	Material	Sequence	Step	Specified Orientat
P1-A	Fibersim Design Laminate 1	DRY-fine	A	10	45
P1-B	Fibersim Design Laminate 1	DRY-fine	A	10	45
P2-A	Fibersim Design Laminate 1	DRY-fine	A	20	0
P2-B	Fibersim Design Laminate 1	DRY-fine	A	20	0
P3-A	Fibersim Design Laminate 1	DRY-fine	A	40	45
P3-B	Fibersim Design Laminate 1	DRY-fine	A	40	45
P4-A	Fibersim Design Laminate 1	DRY-fine	A	60	0
P4-B	Fibersim Design Laminate 1	DRY-fine	A	60	0
P015	Fibersim Design Laminate 2	DRY-5H-3K	B	10	0
P018	Fibersim Design Laminate 2	DRY-5H-3K	B	10	45
P5-A	Fibersim Design Laminate 2	DRY-fine	B	20	45
P5-B	Fibersim Design Laminate 2	DRY-fine	B	20	45
P6-A	Fibersim Design Laminate 2	DRY-fine	B	30	0
P6-B	Fibersim Design Laminate 2	DRY-fine	B	30	0
P012	Fibersim Design Laminate 2	DRY-5H-3K	B	40	0
P017	Fibersim Design Laminate 2	DRY-5H-3K	B	50	45

0 selected, 16 shown, 16 available

Figure 1.17. *Definition of the carbon fiber plies to run a Fibersim simulation [35]: in this example two groups of plies are designed and linked to the two laminates previously created (Figure 1.16).*

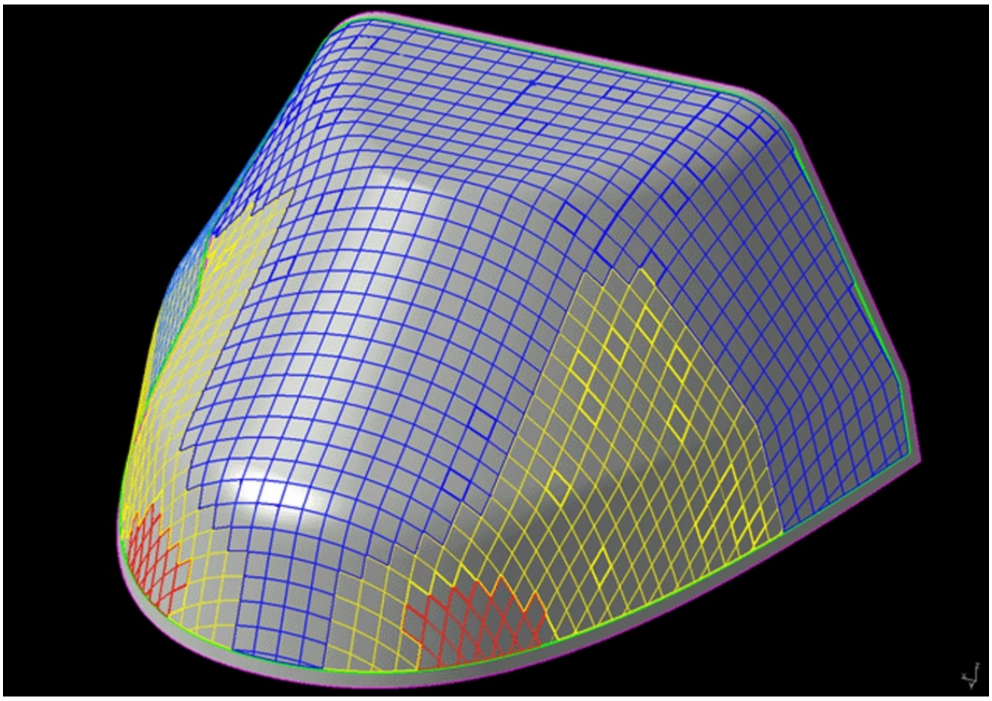

Figure 1.18. *A lamination process simulated by Fibersim [36].*

To resume, a proper optimization of the lamination process is achievable using *Fibersim* so that it is possible to:

- analyze the fibers deformations and deviations;
- evaluate the fibers alignment between the plies (carbon look requirement);
- minimize the number of cuts and choose the best position for them;
- minimize the number of overlaps;
- simulate any kind of composite material;
- create flat patterns and DXF files to cut the plies with a plotter;
- obtain a clear summary plybook about the whole process.

1.5 ONDA SOLARE PROJECT

The knowledge acquired during the PhD program about carbon fiber composites improved my work as member of *Onda Solare*, the sport association which, in collaboration with the University of Bologna, builds carbon fiber solar cars to attend competitive challenges around the world [37].

Onda Solare realizes solar vehicles since 2005, when a solar-powered carbon fiber bicycle called *Emilia 1* was realized and the team won the *World Solar Cycle Challenge 2005*, taking the third place. From 2011 to 2017 *Onda Solare* competed first with *Emilia 2* and then with *Emilia 3*, both challenger class (single-seat) solar cars with one rear in-wheel electric motor. With *Emilia 3* the team got the second place at the *Carrera Solar Atacama 2016* and the first place at *Moroccan Solar Race 2016* and at the *Albi Solar Challenge 2017*. In 2018 *Onda Solare* presented to the public *Emilia 4* (Figure 1.19), its first cruiser class (multi-seats) solar car.

Designed to bring four passengers on board (pilot included), the main characteristics of *Emilia 4* were two rear in-wheel electric motors, 5 m^2 of monocrystalline silicon solar panels on the roof and a Li-ion battery pack (1344 cells) whose total weight was 64 kg. Considering that the weight is one of the key-points in the solar car design, the use of carbon fibers is essential to compensate the weight of the electrical heavy components such as the in-wheel motors, the battery pack and the inverter. Before starting to build *Emilia 4*, several studies were carried on about the aerodynamics [38], the monococque chassis and the springs [39], the wheels (it is proven that a lighter unsprung mass lead to increased performances [16]). With the aim of realizing the lightest car possible and always taking into account the limits imposed by the regulations of the solar car challenges, the result was a car with a final weight equal to 333 kg (battery pack included).

Figure 1.19. *Emilia 4 is presented at the Ferrari Museum in Maranello on 11th June 2018.*

With *Emilia 4* the team won the *American Solar Challenge 2018* (*ASC18*), a solar car competition 2760 km long, from Omaha, Nebraska, to Bend, Oregon (Figure 1.20). *Onda Solare* participated in the cruiser category getting the first place cup and the two coveted special prizes: the Mechanical Design and Use of Composites Award and the Battery Design Award.

Figure 1.20. *Bend (OR), July 2018: the Onda Solare team crosses the finish line and won the ASC18 with Emilia 4.*

After the ASC18 the team went back to work with the aim of modifying *Emilia 4*, preparing it for the *Bridgestone World Solar Challenge 2019* (*BWSC19*): this is the oldest solar car competition where the participants have to drive for 3000 km, crossing the Australian desert from Darwin (Northern Territory) to Adelaide (South Australia). The *BWSC19* regulation imposed an average speed $\tilde{v} \geq 75\ km/h$ which was much higher compared to the average speed kept during the *ASC18* ($\tilde{v} = 55\ km/h$) so that the energy capacity of the battery had to be increased: a new battery pack was designed and this time its weight reached about 120 kg. Consequently, many works to lighten all the other parts became necessary. To face this increase in weight new aerodynamics studies were also carried on and lead to the realization of a novel long tail [40] which gave the name to the new solar car model: *Emilia 4 LT* (long tail).

One of the hardest challenges was the lamination of the upper rear and front brackets: these components were the only metal parts of the car (made of Ergal) so, although their shape was not easy in terms of lamination, it was worthy trying to realize them with composite materials. The experience acquired with *Fibersim* was fundamental for this activity as the shape of the moulds (Figure 1.21) required many cuts and overlaps on the carbon fiber plies: thanks to the previous practice done with the software, it has been possible to minimize them.

Looking at the results in Table 1.1 it clearly appears that the lamination was successful in terms of weight reduction: with the carbon fiber composite the total weight for the car brackets (two rear and two front) was 1810 g instead of 6360 g obtained with Ergal, with a resulting weight reduction by 71.54%.

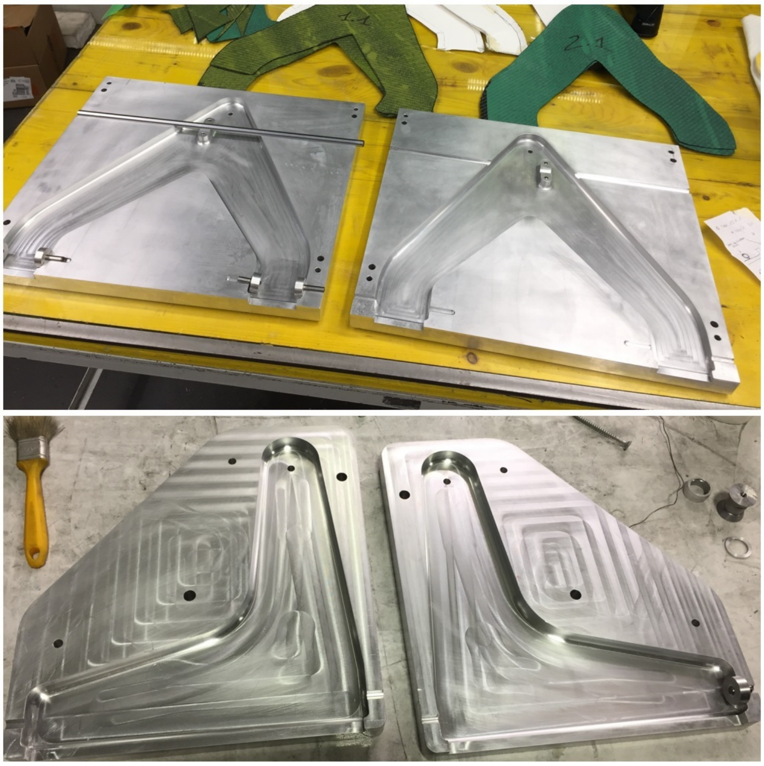

Figure 1.21. *Moulds for the lamination of the upper front (top) and rear (bottom) brackets.*

Figure 1.22. *Comparison between the upper front (top) and rear (bottom) brackets made of Ergal (left) and carbon fibers (right).*

Table 1.1. *Comparison between the weights of the upper front and rear brackets made of Ergal and carbon fibers.*

	Ergal	Carbon fiber
Front brackets	2200 g	558 g
Rear brackets	980 g	347 g

Other main lightening works involved the windscreen, the bracket links, the rims, the roof, the roll-bar: in particular, these last two parts were significantly modified. About the roof, the aim was to obtain an innovative lighter object made of ultra-light composite sandwich panels [41] which was able to support 5 m^2 of solar panels, leaving them a wider free surface for the natural convection cooling of the silicon monocrystalline cells [42] (Figure 1.23). At the same time there was the necessity to modify the *Emilia 4* roll-bar due to different competition safety criteria (*ASC18* and *BWSC19* regulations were different): as the previous titanium roll-bar had to be dismounted, the idea was to substitute it with a carbon fiber one, realizing a structural roll-cage thanks to which it was possible to light the roof even more (Figure 1.24). Results [43] showed that, although the carbon fiber roll-bar (14 kg) was heavier than the titanium one (7 kg), the installation of this composite structure allowed obtaining a roof with an alternation of structural and non-structural (lighter) parts, with an overall roof weight reduction of around 15 kg (Figure 1.23).

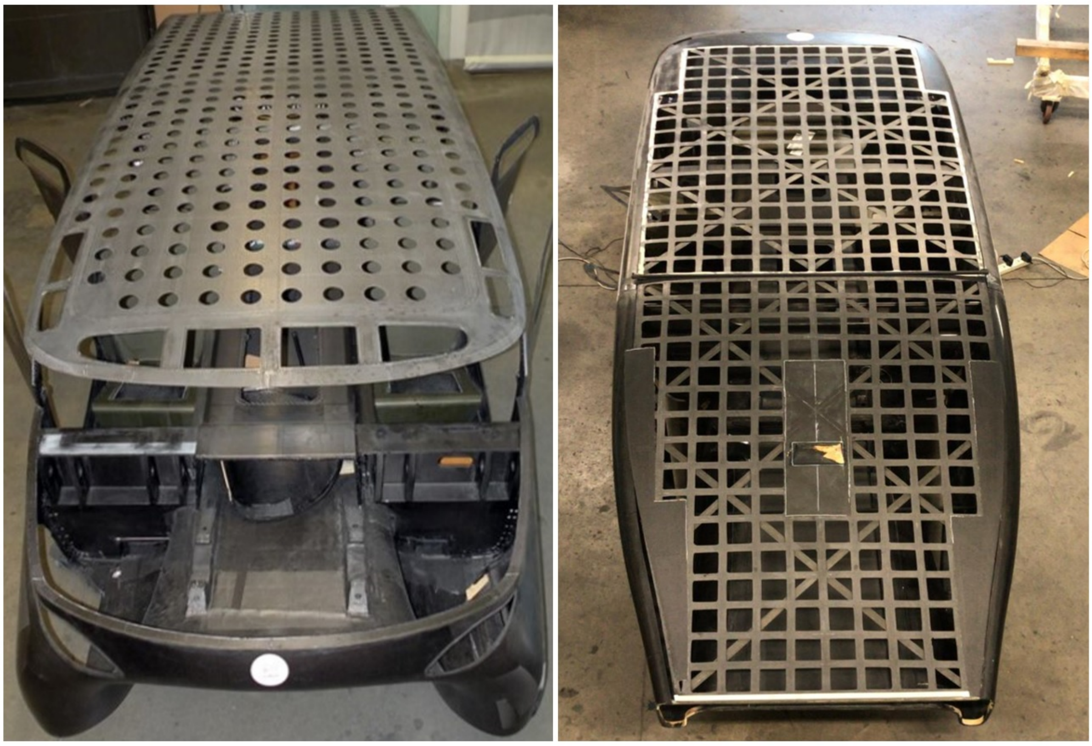

Figure 1.23. *The Emilia 4 heavier roof (left) and the Emilia 4 LT lighter one (right).*

In Figure 1.24 it is evident how the roll-cage of the solar car has been deeply modified: the central titanium bar placed in the middle of the windscreen was removed as well as the bars between the two front seats. This left space to a single carbon fiber structural beam (coupled, as said, with the structural parts of the roof). Further, the lighter roll-cage solution of *Emilia 4 LT* resulted in a vehicle easier to drive, with a better visibility degree from the pilot point of view.

Emilia 4 LT was presented to the public on 31st July 2019 at the *Ferrari Museum* in Maranello (Figure 1.25). *Onda Solare* attended the *BWSC19* only taking the 10th place (Figure 1.26) but in 2021 the team was able to capitalize all the improvements previously made to the car, competing and winning the *iLumen European Solar Challenge 2021* (*ESC21*), a 24 hours challenge in the circuit of Zolder, Belgium (Figure 1.27).

Figure 1.24. *Comparison between the Emilia 4 roll-cage (top) and the Emilia 4 LT one (bottom).*

Figure 1.25. *Emilia 4 LT is presented at the Ferrari Museum in Maranello on 31st July 2019.*

Figure 1.26. *October 2019, Adelaide (SA): the Onda Solare team gets the 10th place at the BWSC19 with Emilia 4 LT.*

Figure 1.27. *September 2021, Zolder (Belgium): Onda Solare wins the ESC21 with Emilia 4 LT.*

As initially said and as showed above, the lightening of a car (solar, electric or fossil fuel powered) plays a key-role from the energy consumption point of view but it is not the only possible move. The research work regarding the lightest materials and the best production processes to realize lighter pieces has to be coupled with a studies about the more energy-intensive components. Talking about electric cars it appears clear that a lot of attention has to be payed on the battery pack and its cooling systems which will be deepened in Chapter 2 and Chapter 3.

2

BATTERY THERMAL MANAGEMENT SYSTEMS

2.1 ENERGY STORAGE DEVICES

Driven by the growing improvements in technology levels and by the necessity of moving frequently and fast all around the world, the global demand for energy resources, especially for fossil fuels, is rising more and more [44]. Intending to reduce fossil emissions, the interest in electric vehicles (EVs) is greatly increasing. EV technologies represent striking options to reach climate goals in the transport sector with policy makers, manufacturers and research institutions, renewing their commitment toward the reduction of transport-related greenhouse gas emissions by 2050 [45, 46]. One of the most challenging issues about EVs is related to the limited amount of the energy stored in the on-board lithium-ion battery pack (BP). EV performances can significantly vary in extreme weather conditions, with range reductions up to 30% in summer and 60% in winter [47]. In addition to performance issues, the safety [48] and the lifetime [49] of lithium-ion batteries (LIBs) are proven to be in close relation with the cell temperature and the C-rate [50].

Lithium-ion cells are commonly used in battery electric vehicles (BEVs) for their high energy density whose common maximum value is around 180 Wh/kg (Figure 2.1), with peaks until 255 Wh/kg for high-performance applications [51] (competitive supercars) and an expected increase until 270 Wh/kg [51] which will follow the ascending LIB demand predicted for the next few years [52] (compound annual growth rate $CAGR = 25.45\%$ [53], Figure 2.2). Other advantages which make the LIBs one of the most used kinds of batteries are the lower self-discharge rate, the increasing recyclability degree, the lower weight and the compact size. In particular, this last factor is very helpful in those applications where there is a lack of space such as automotive or aerospace. LIBs have also a longer life cycle with respect to the other rechargeable batteries such as the lead-acid, the nickel-cadmium (Ni-Cd) or the nickel-metal hydride (Ni-MH) ones [54, 55].

Today the most used LIB packs in the automotive field are those made of 18650 cells (with a diameter $d = 18\ mm$ and a length $l = 65\ mm$) or 21700 ones ($d = 21\ mm$, $l = 70\ mm$). This choice is mainly due to their small size: as the cells contain a limited amount of energy, if a failure event occurs the effect is much more restrained compared to that expected from larger cells [56]. 18650 cylindrical cells were introduced by *Tesla* more than 10 years ago on the pioneer *Roadster* model and then massively substituted by the 21700 ones used for the other cars of the Silicon Valley company such as the *Tesla Model X* and *Model 3*. As a matter of facts, this type of cells is increasingly used in the automotive field thanks to the evolution of their capacity [57] and, consequently, the reduction of the costs (less cells are necessary to have the same amount of energy) [58]. Recently, the Elon Musk's company presented the innovative

4860 cells (Figure 2.3) but, although *Panasonic* declared its commitment in working together with *Tesla* to produce this new product [59], these kind of batteries is still far from a worldwide spread.

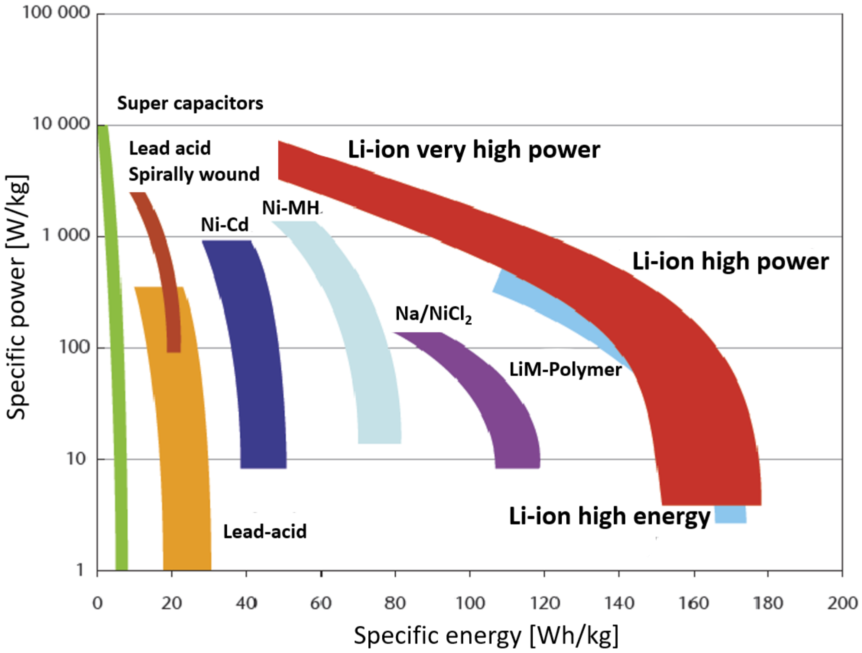

Figure 2.1. *Comparison among energy storage devices present on the market considering their power density [W/kg] and energy density [Wh/kg] values [60].*

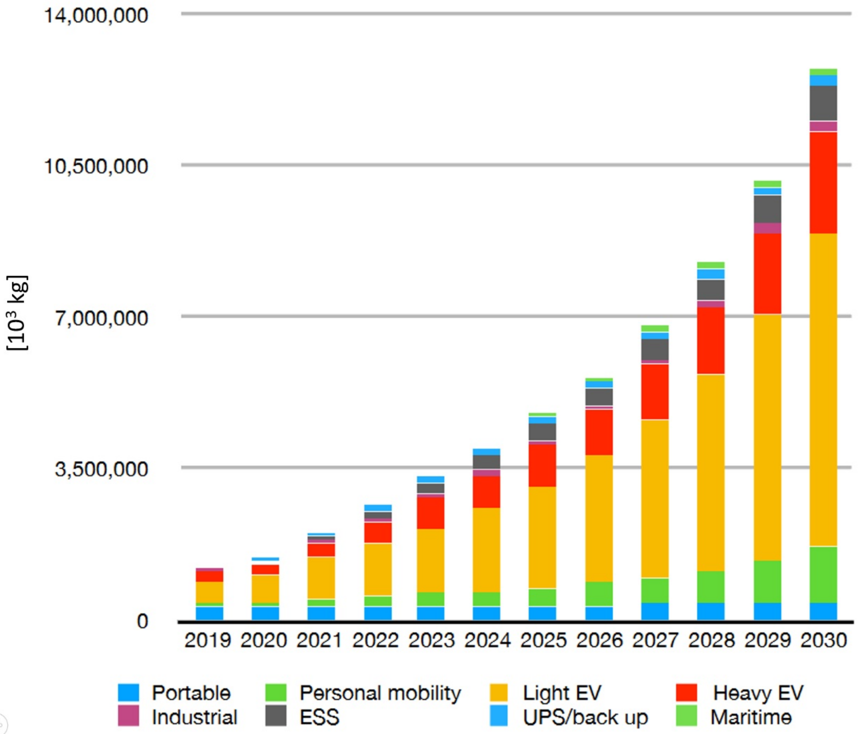

Figure 2.2. *LIBs placed on the market: prevision from 2019 to 2030 [53].*

Nowadays many efforts are made to understand what are the factors which positively influence the efficiency of the LIBs. Researches investigate about why LIBs represent one of the best choices for EVs [61] and present a considerable amount of simulation studies. For instance, Huang et al. use 3D simulations to study the convection in the cell spacing and analyze what is their best arrangement [62]. Experimental works are also fundamental and represent the final step to validate the theoretical researches: a lot of experiments are carried on about the effects of the different arrangements and shapes of the cells [63, 64, 65].

Figure 2.3. *Different cell formats (from the left to the right): AAA, AA, 18650, 21700 (or 2170), 4860.*

Scientific researches are essential to study the high anisotropic thermal properties of the Li-ion cells caused by the different layers of the electrodes [66]. This can represent a serious problem in application fields such as the automotive one: here the necessity of compact BPs leads not to have much space among the cells and, consequently, this brings to high temperature and non-uniform thermal distribution conditions. These situations can worse the efficiency of the cells and can degenerate in a dangerous and uncontrolled thermal runaway.

A thermal runaway is caused by a cascade process, with reactions that feed each other and, in the worst scenario, lead to fire and combustion [67]. To avoid an uncontrolled situation like this and, in general, to monitor the thermal health of the battery pack, a properly designed battery thermal management system (BTMS) has to be installed.

2.2 BATTERY THERMAL MANAGEMENT SYSTEMS: AN OVERVIEW

Talking about thermal management there are several methods and systems to control the temperature of a BP, maintaining it in the right thermal range.

A thermal management method is considered:

- **active** if it works adding or removing energy using a substance which increases heat transfer processes;
- **passive** if it relies upon the thermodynamics of the heat transfer (conduction, convection and radiation) [68].

The first category includes air or liquid-based management methods, whereas technologies which involve substances such as phase change materials (PCMs) belong to the second BTMS class.

Many researchers are involved into several aspects of the BTMSs aiming to reduce the energy wasting and trying to understand what are the thermal management key-factors to achieve the best battery performances. Each BTMS has its own pros and cons and it is more suitable for a precise application rather than another: this is why it is important to carefully select the thermal management system on the base of the boundary conditions imposed by the surrounding environment.

In literature there are several values about the best operating temperature for LIBs: on average it ranges from $T_{\text{min}} = 15$ °C and $T_{\text{max}} = 40$ °C [69]. If the temperature rises above $T = 50$ °C the charging efficiency and the longevity of the batteries decreases [70]. As the purpose of a thermal management system is to maintain the battery temperature within the optimum range and improve its uniformity inside all the single battery modules [71], when the battery temperature is under the acceptable lower limit, heating is essential as much as cooling [72]. At low temperatures, charged LIB discharging processes are easier than discharged LIB charging processes [73]: Figure 2.4 shows that the capacity of Li-ion batteries can decrease even until 95% when the energy storage system (ESS) is operating at $T = -10$ °C comparing the capacity drop to that recorded at $T = 20$ °C [74].

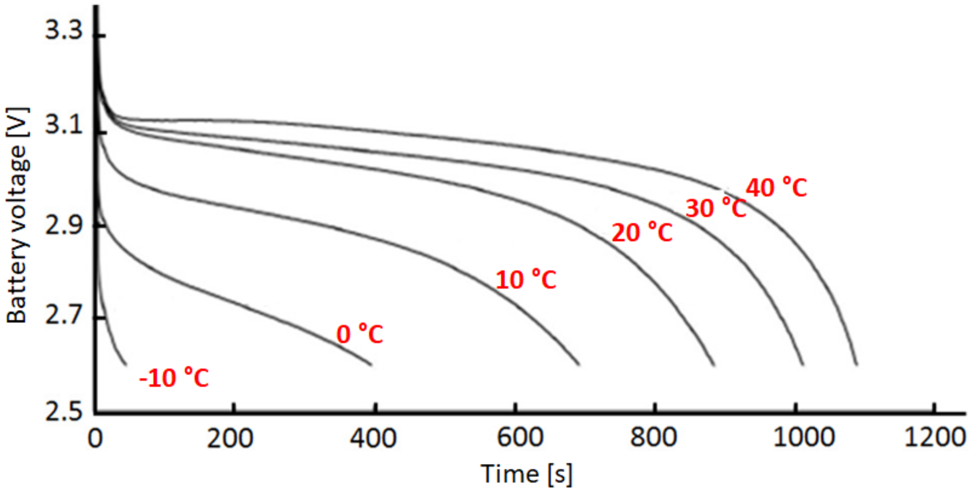

Figure 2.4. *LIB capacity drops at different temperature values, for a fixed 3C discharge rate [74].*

It is probably due to the exothermic nature of the chemical reactions inside the batteries that not many studies deal with the LIB heating management [75], considering that as a rarer issue. However, there are some promising researches about internal self-heating strategies to overcome the poor battery performances at too low temperatures [76] and contrast the battery life reduction [77].

While studying the BP heat dissipation, two main indexes are usually taken into account: the maximum temperature rising ($T_{\text{ris, max}}$) and the maximum temperature difference ($T_{\text{dif, max}}$). $T_{\text{ris, max}}$ is the maximum difference between the battery pack temperature and the environmental temperature. $T_{\text{dif, max}}$ is the maximum difference recorded inside the battery pack. Desirable values for these indexes are $T_{\text{ris, max}} < 10\ K$ and $T_{\text{dif, max}} < 5\ K$ [78]. If T_{ris} increases more and more it means that the environmental conditions are not good enough to properly cool the battery and the heat generated from the BP will not be taken away without the installation of an external BTMS [79]. If T_{dif} has a too much high value it means that there is not a good temperature distribution inside the battery pack [71] and possible heat peaks can degenerate in a thermal runaway situation. An appropriate cooling system design is necessary to reduce both $T_{\text{ris, max}}$ and $T_{\text{dif, max}}$.

As seen before, BTMSs can be grouped in active or passive systems but it is not the only way to classify them. Considering the work the system does to bring the BP back to the proper LIB working temperature it is possible to distinguish:

- Preheating BTMSs
- Cooling BTMSs

The first ones help the BP in case of cold weather, increasing its temperature: they can be divided into external or internal (faster and more efficient) heating systems [80]. The conventional BTMSs are usually active cooling ones and exploit air or liquid refrigerants as working fluids. The second kind of BTMSs are designed to lower the temperatures so that the BP can properly work within the optimal temperature range.

What follows comes out from a meticulous literature research and aims to show the reader the most common BTMSs such as the air-based and the liquid-based ones. Then a brief overview about the uncommon and most innovative thermal management technologies is presented to be later deepened in Chapter 3. Finally, important strategies against dangerous BP fire situations have been discussed.

2.3 AIR COOLING

One of the easiest ways to manage the BP temperature is represented by the air cooling. This can be realized with natural or forced ventilation: the first method is not so efficient and it is often unable to ensure the battery health even in case of $T_{\text{ris}} \simeq T_{\text{ris, max}}$. For this reason this section focuses on forced ventilation cooling systems.

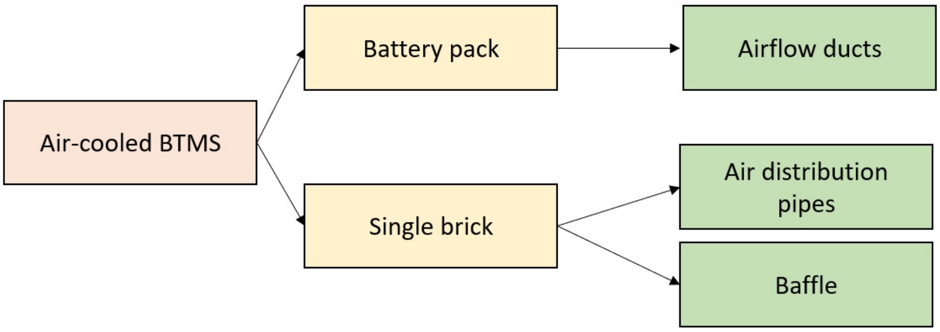

Figure 2.5. *Classification of the most used air-cooled BTMSs.*

About forced-air cooling methods [81], Zhou et al. [71] show the advantages of an air distribution pipe thermal manage system, Xu et al. [78] study the optimization of the forced-air cooling, testing the effects of different airflow duct modes, whereas Xie et al. [82] go forward towards the same goal but modifying factors such as the air-inlet and outlet angles. There are also researches which propose a multi-parameter control strategy for air-based BTMSs [83]: the aim is to monitor the state of health (SOH) of the battery and the energy consumption as functions of the temperature fluctuations and the air flow rate.

Many experiments have been carried on not only to optimize the whole BTMS, but also to analyze the thermal conditions inside the single battery modules, improving the temperature uniformity and investigating on the $T_{\text{dif, max}}$ values inside the bricks [84]. Several methods have been explored, with analytical and experimental tests such as the installation of a baffle plate [85], different cell arrangements [64], the spacing optimization among the battery cells [86], the installation of a secondary vent [87] in an air-cooled BTMS. Other examples are the addition of an inlet plenum [88], special axial-flow air-cooling systems [89], nanofluid-based cooling techniques with forced-air flows to remove the heat from the battery pack [90].

2.3.1 *Forced ventilation: prismatic cell BP*

Several researches deal with the temperature distribution and analyze the streamlines obtained with different air-flow arrangements in the case of batteries made of densely packed prismatic cells.

Focusing on the research of Xu et al. [78] it is possible to extrapolate interesting results. In a parallel flow arrangement (Figure 2.6 (a)) the air flows parallel to the battery cells and it is expelled by the fans from the air-outlets. The highest temperature areas inside the battery are close to the air-outlets. With this configuration the heat dissipation performance is not satisfying and with any of the environmental temperatures considered ($T_{\text{env, 1}} = 20$ °C, $T_{\text{env, 2}} = 27$ °C, $T_{\text{env, 3}} = 40$ °C) the battery temperature is outside the proper working range.

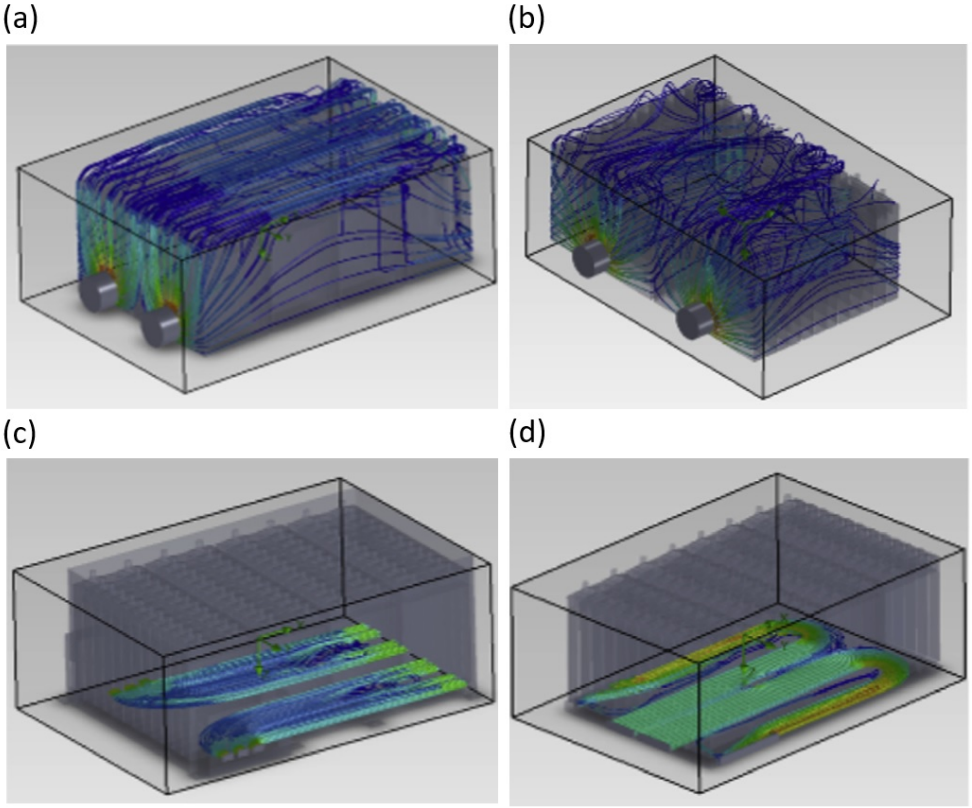

Figure 2.6. *Streamlines in case of parallel flow (a), cross-flow (b), with a bottom passage (c) and a 2U-passage (d) [78].*

Table 2.1. *Temperature decrease obtained moving from a parallel flow cooling method to a 2U-passage technology at different environmental temperatures [78].*

		$T_{\text{env}} = 20$ °C		$T_{\text{env}} = 27$ °C		$T_{\text{env}} = 40$ °C	
		$T_{\text{ris, max}}$[°C]	$T_{\text{dif, max}}$[°C]	$T_{\text{ris, max}}$[°C]	$T_{\text{dif, max}}$[°C]	$T_{\text{ris, max}}$[°C]	$T_{\text{dif, max}}$[°C]
Layout	Parallel flow	A_{20}	B_{20}	A_{27}	B_{27}	A_{40}	B_{40}
	Cross-flow	−2.25%	−7.91%	−1.98%	−7.27%	−1.50%	−5.75%
	Bottom passage	−36.80%	−63.83%	−37.04%	−63.84%	−37.55%	−63.87%
	2U-passage	−38.38%	−72.58%	−39.03%	−73.03%	−38.97%	−72.15%

In a cross-flow arrangement (Figure 2.6 (b)) the air flows perpendicularly to the battery cells and the shorter air-flow paths improve the heat dissipation. The temperature peaks are lower, showing that this configuration is better than the parallel-flow one in terms of heat dissipation. Other approaches such as the addition of air passages on the bottom of the BP can increase the heat transfer performances. With the bottom passage (Figure 2.6 (c)) the temperature values are lower compared to the previous tests but not enough to satisfy the heat dissipation requirements for all the T_{env} considered (only for $T_{\text{env},\,2}$ and $T_{\text{env},\,3}$). In the case of a double U-passage (2U-passage in Figure 2.6 (d)) it clearly appears that the temperature field distribution is more uniform with respect to the bottom passage. Temperatures are lower compared to all the previous cases and satisfy the heat dissipation requirements for all the T_{env} considered. In Table 2.1 $T_{\text{ris, max}}$ (A) and $T_{\text{dif, max}}$ (B) related to the parallel flow test have been taken as reference values and then compared with those recorded during the other tests: the table shows the temperature drops.

Other evaluations take into account several factors such as the battery SOC and the charge/discharge rate. About the SOC, with the double U-passage the heat dissipation requirements are satisfied for $SOC = 70\%$ and $SOC = 100\%$ but results are better for the lower SOC percentage: this means that with insufficient heat dissipation conditions, it could be helpful to work with lower SOC values [78]. The heat dissipation requirements are satisfying both for the charge and for discharge rates $0.6C$, $0.8C$ and $1C$ with the best result for the lowest of these values: considering this, if the heat dissipation is not satisfying it could be helpful to work with lower charge and discharge rates [78]. The angle between the air-inlet and the cells, the one between the air-outlet and the cells and the air-flow channel width are all crucial elements in terms of battery thermal benefit as well as the cell spacing. Properly tuning all these parameters, $T_{\text{ris, max}}$ and $T_{\text{dif, max}}$ can respectively drop even by 12.82% and 29.72% [82].

2.3.2 *Forced ventilation: cylindrical cell BP*

The BTMS state of the art does not only consider whole BPs but also deal with what happens inside them. Here some air-cooling techniques adopted for the thermal management of cylindrical cell bricks are proposed.

Zhou et al. [71] take into account 18650 LIB bricks, monitoring the temperature of every single cell with K-type thermocouples (TCs) in three different points: the top, the middle and the bottom where they record the related temperatures T_{TOP}, T_{MID}, T_{BOT}. Air distribution pipes inserted among the cells present orifices arranged along their entire length. Three kinds of pipes have been tested: the first presents three orifices with a diameter $d_1 = 1\ mm$, the second has four orifices with $d_2 = 15\ mm$ and the third pipe has five orifices with $d_3 = 2\ mm$. As it is possible to see in Figure 2.7 the air flows into the pipes from the upper inlets and gets out from the orifices. Before starting the cooling test, considering a constant discharge rate process, researchers [71] have noticed that the temperature increases from the negative pole to the positive one and this is explainable with a higher internal resistance related to the battery caps (high heating due to the Joule's effect). Four main factors have been considered in the test to optimize the air distribution pipe system: the number and the diameter of the orifices, the air-inlet pressure and the discharge rate.

For all the diameters of the orifices $T_{\text{MID}} < T_{\text{TOP}}$, $T_{\text{MID}} < T_{\text{BOT}}$ and, in particular, T_{MID} decreases as the orifice diameter increases. This is the effect of an enhanced heat transfer area between the battery surface and the airflow. Choosing pipes with bigger orifices lead to an increase of the forced air inlet area. At the same time, the power consumption increases but it has not significant effects. Regarding the inlet pressure, the higher is its value, the higher is the inlet airflow rate. As a consequence T_{dif} decreases (while the power consumption increases [71]).

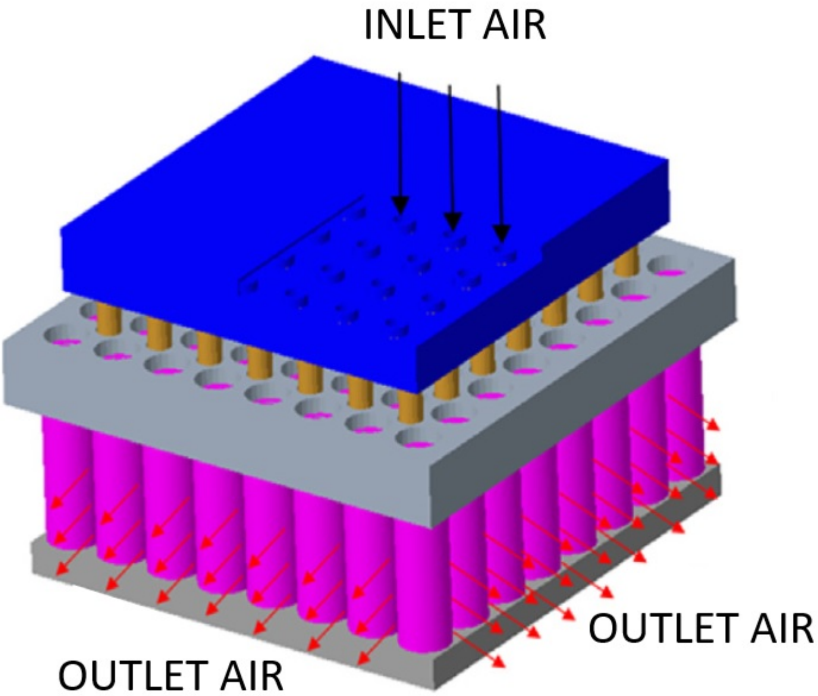

Figure 2.7. *Battery brick and air distribution pipes used in the experiment [71].*

As shown by the experiments of Xu et al. [78] on prismatic cells, the discharge rate affects the temperature, too. This is because as the heat dissipation rate remains the same the heat generation rate changes: if it is too much high, the dissipation is not sufficient to keep the thermal balance, so the temperature starts to increase. For each discharge rate there is a degree of discharge (DOD) value from which the temperature starts to drop but, at the same time, the higher is the discharge rate, the higher is the T_{max} of the battery: the cooling rate declines with the increase of the discharge rate. $T_{\text{dif, max}}$ increases with the discharge rate, too.

In the forced-air cooling field, promising results at a brick level have also been achieved equipping the bricks with baffles. Jiaqiang et al. [85] study the influence of different air-inlet and air-outlet positions, comparing a more ordinary forced-air cooling strategy with that involving the use of a baffle: the discussion deals with the benefits in terms of heat dissipation. The tested brick is made of 18650 Li-ion batteries. Figure 2.8 shows the temperature distribution obtained within the brick under different forced ventilation conditions: lateral inlet and outlet on the same side, lateral inlet and outlet on opposite sides and with the presence of a baffle.

In the first condition (Figure 2.8 (a)) the cells near the air-inlet have the lowest temperatures and the highest peaks are concentrated where the air hardly flows through the cells. The recorded $T_{\text{dif, max}}$ is unacceptable. With the second setup (Figure 2.8

(b)) the temperature distribution remains almost the same, the highest temperature values decrease but not enough to have an acceptable $T_{\text{dif, max}}$. Thanks to the baffle installation, with the third layout (Figure 2.8 (c)) it is possible to narrow and concentrate the airflow: this simple and cheap solution results in an improvement of the airflow cooling ability. The temperature distribution is close to the previous cases but this time the T_{max} inside the battery is in the proper LIB working range ($15\,°C < T < 40\,°C$ [69]). However, problems of temperature uniformity still have to be fixed to satisfy the requirement of $T_{\text{dif, max}} < 5\ K$.

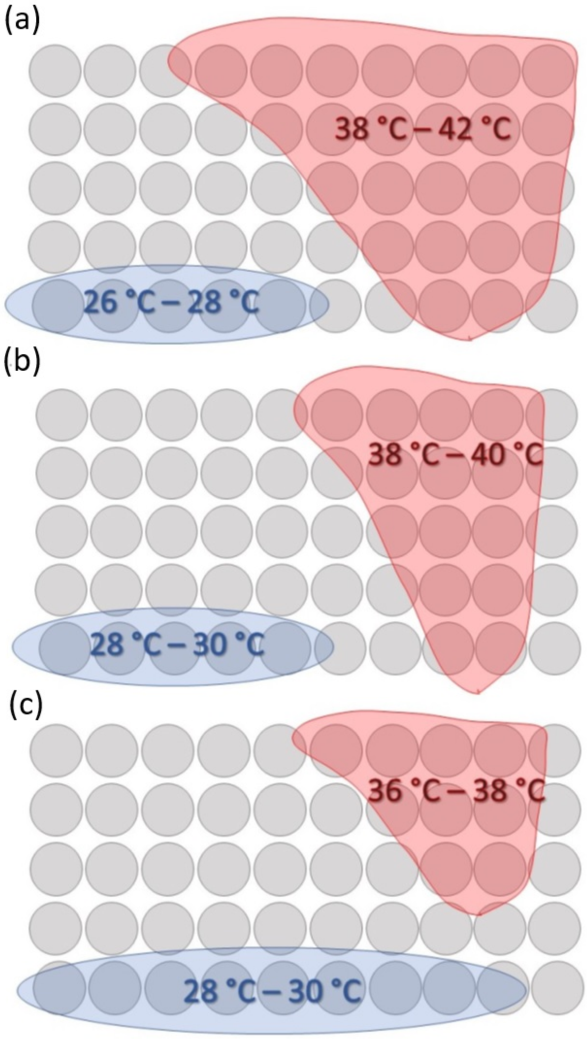

Figure 2.8. *Temperature distribution obtained under different air-forced conditions: lateral inlet and outlet on the same side (a); lateral inlet and outlet on opposite sides (b); baffle installation (c) [91].*

To resume, there are lots of possibilities to improve the air-cooled BTMS efficiency: it is possible to go from a natural convection system to a forced ventilation one, placing air-inlets and air-outlets in the right places, equipping the system with properly designed air distribution pipes and installing simple baffles. But all these solutions could be not enough to reach an acceptable T_{dif}. In this case, it becomes necessary to move on to higher effectiveness technologies such as the liquid-based BTMSs.

2.4 LIQUID COOLING

Liquid-based BTMSs provide very effective LIB cooling methods, showing promising performances thanks to the high thermal conductivity of the refrigerants: current researches focus their attention on the peak temperature reduction [92].

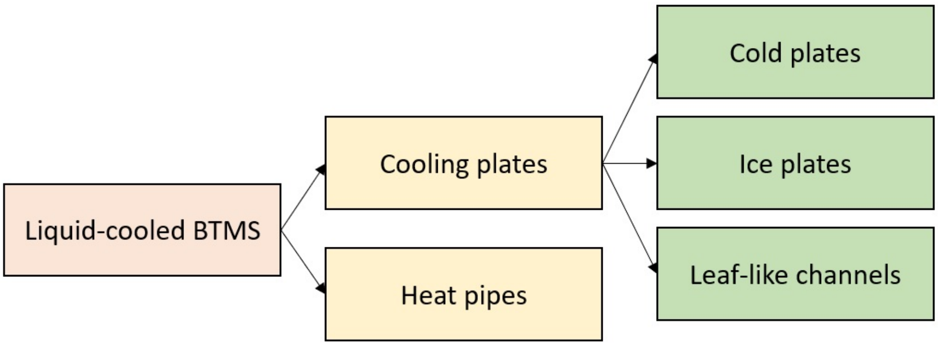

Figure 2.9. *Classification of the most used liquid-cooled BTMSs.*

Chang et al. [93] study the effect of reciprocating liquid flows in a liquid-based BTMS and show that reciprocation leads to consistent reductions of T_{dif}, flow rates and heating power. Liu et al. [94] carry on experimental investigations about the role of the heat capacity and the charge/discharge ratio: they put in evidence how the thermal management of a single BP surface can be not effective enough in terms of temperature uniformity and, under specific conditions, the immersive cooling (discussed in Section 2.5.1) represents a better choice. In a recent work by Tang et al. [95] the performances of liquid BTMSs are analysed considering experimental data and with the help of a BTMS automated calibration model: thanks to this model it is possible to fit the non-linear relationship between the coefficient of performance (COP) related to the system, the cooling capacity and the thermal characteristics of the battery.

One of the liquid BTMS downsides is their relative heavy weight (including the coolant and the sealing elements necessary to avoid fluid leakages) and the high manufacturing cost for the fluid circulation system [71]. These penalties have to be accepted anyway when high cooling performances are required and an air cooling system is not sufficient. Here below, the leading liquid cooling technologies such as cooling plates and heat pipes are presented.

2.4.1 *Cooling plates*

A typical cooling plate is made of a metal plate on which several flow paths are machined (Figure 2.10). The cooling liquid flows along the paths, absorbing the heat of the cells and dissipating it through the plates by means of conduction and convection heat transfer processes. The factors which more influence the efficiency of this technology are the shape and the size of the flow paths, the contact surface between the coolant and the walls of the paths, the type of coolant, the flow rate and the material of the plates. Cooling plates can be divided into two main categories:

- Cold plates
- Ice plates

Ice plates show the best performances and are positioned among the battery cells (Figure 2.10); cold plates perform worse but, as they are placed under the cells like a cell-floor, they are easier to install. Ice plates are often preferred in BEVs for their high efficiency, but the tight spaces represent a hard challenge.

Darcovich et al. [96] compare the ice and cold plate technologies showing what happens to the cell T_{max} if changing the cell case material and the coolant. They also take into account two different driving cycles: the US06, an urban-like driving-cycle, and the HWY, thought for cars which drive along the highways. Further, they obtain the cell T_{max} and the battery lifetime as functions of SOH values.

Results show a better temperature uniformity with ice plates than with cold plates. The higher is the value of the heat transfer coefficient, the lower is the T_{max} of the battery for any kinds of case materials and driving-cycles. One consequence is a longer battery lifetime which, in this case study, is about 2 years for US06 driving-cycles and 1 year for the HWY ones.

Figure 2.10. *Cooling plates used to cool cylindrical cell BPs.*

Studies about novel technologies suitable to improve cooling plate systems deal with new kinds of channels such as leaf-like channels. The design project of Deng et al. [97] (Figure 2.11) provides four collection channels arranged along the diagonal lines where the temperature decrease is more necessary. Several simulations put in evidence the key-factors which more influence the effectiveness of this system: the width to length ratio of the channels, their thickness and the inlet flow rate. Further, leaf-like channels can be helpful in the study of fractal networks for cold plates [97].

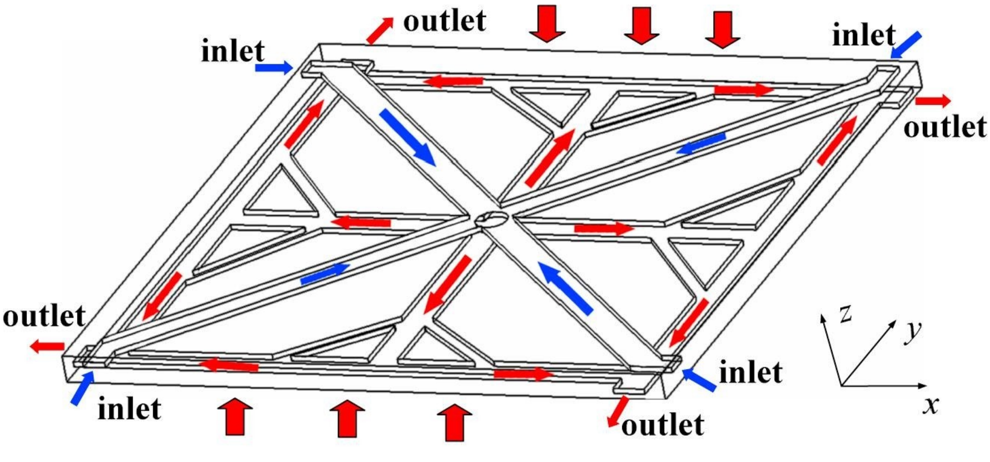

Figure 2.11. *An example of leaf-like channels [97].*

The choice of the right cooling plates has to be done considering the case material, the battery $T_{\max}$ but also taking into account the space availability. If the BP geometry does not allow the installation of the plates, heat pipes (discussed in Section 2.4.2) could be the right solution thanks to their flexibility which makes this BTMS suitable for any size and shape of BPs. In this case, to choose the proper heat pipes it has to be payed attention to the several factors which influence the cooling efficiency such as the coolant and the heat-flux load [98]. Another good practice is proceeding with an orthogonal test, evaluating the right geometric pipe parameters [99].

2.4.2 *Heat pipes*

Heat pipes (HP) are passive capillary-driven two-phases systems that represent another solution to manage the temperature of EV battery packs. They are two-phase systems as the heat transfer occurs thanks to a phase change and, in this case, thanks to the liquid-vapor one.

A HP-based cooling system is made of three main parts: the evaporator (heat source), the adiabatic section (which links the first part to the the third one and along which the heat transport happens) and the condenser (heat sink). The evaporation and the condensation rule the thermodynamic cycle: the coolant within the pipes (usually made of copper) absorbs the heat of the BP cells causing the evaporation of the cooling liquid itself; then the fluid moves along the pipes towards the condenser. The heat transfer is a high efficiency process thanks to the vaporization latent heat.

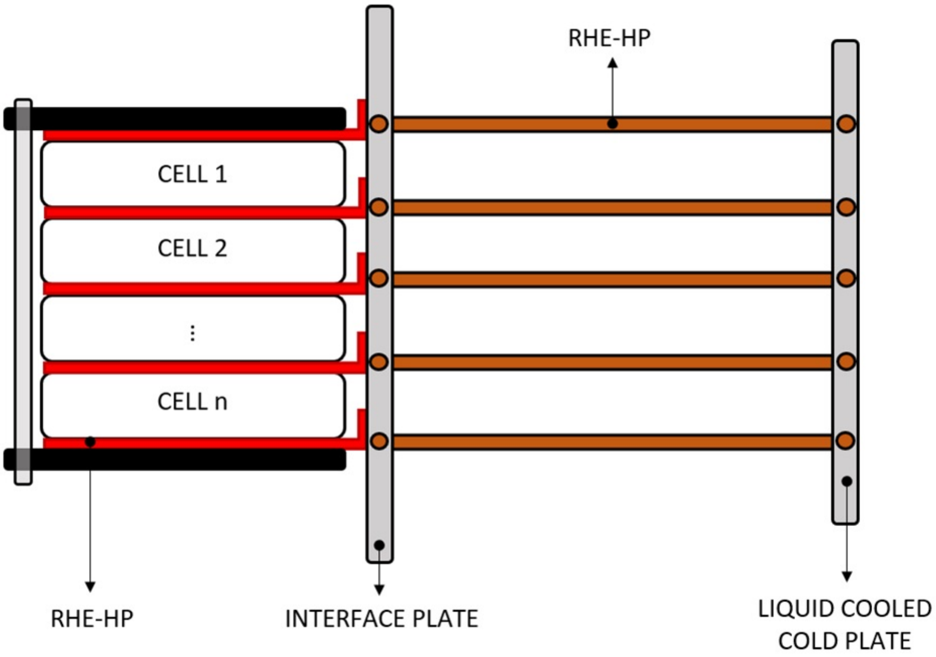

Figure 2.12. *Top view of a HP-based BTMS assembly equipped with a RHE-HP system.*

Once the vapor reaches the condenser another phase change happens and it turns to liquid again: the heat is so dissipated. Simulations [100] have shown that a BTMS based on HPs allows saving EV energy, keeping the battery at $T_{\text{max}} < 50$ °C and $T_{\text{dif, max}} < 5\ K$ so that a good temperature distribution inside the BP is achievable.

The possibility to easily bend the pipes makes them suitable in almost any battery design, creating unique cooling systems specially realized for the considered application. In Figure 2.12 it is shown a scheme of a particular kind of HP-based BTMS: a remote heat transfer heat pipe system (RHE-HP) that is a HP technology equipped with a further U-pipe system which helps in the heat transport. The interface plate connects the heat pipe cooling plate system (HPCP) and the RHE-HP one.

Several researches deal with the influence of many factors on the efficiency of HP systems. For their experiments, Putra et al. [98] use different coolants (distilled water, alcohol 96% and acetone 95% with a filling ratio of 60%) and modify the heat flux load, studying the final T_{max} of the battery and the best system performance. Firstly, during the transient the evaporator temperature increases fast and then it follows a drop: this is due to super-heating which occurs when the boiling point is reached. Considering that if the heat flux load increases the duration of the transient decreases, the shortest transients have been obtained with acetone and alcohol as coolants, for any evaporator and condenser temperature values.

During the steady-state the same temperature trends for distilled water and alcohol have been recorded, except when the highest heat flux load is reached: in that case alcohol and acetone have an equal temperature trend. It has been found that for the highest heat flux loads, the acetone condenser temperature is very different from the other coolant ones. This is due to both the super-heating which occurs in the evaporator and the vapor infiltration which causes a consequent increase of the liquid temperature with much more heat transported towards the condenser. However, the lowest ΔT between the evaporator and the condenser has been obtained with acetone for the most moderate heat flux load. Final results show that the best performance is achievable using acetone as a coolant and with the highest heat flux load.

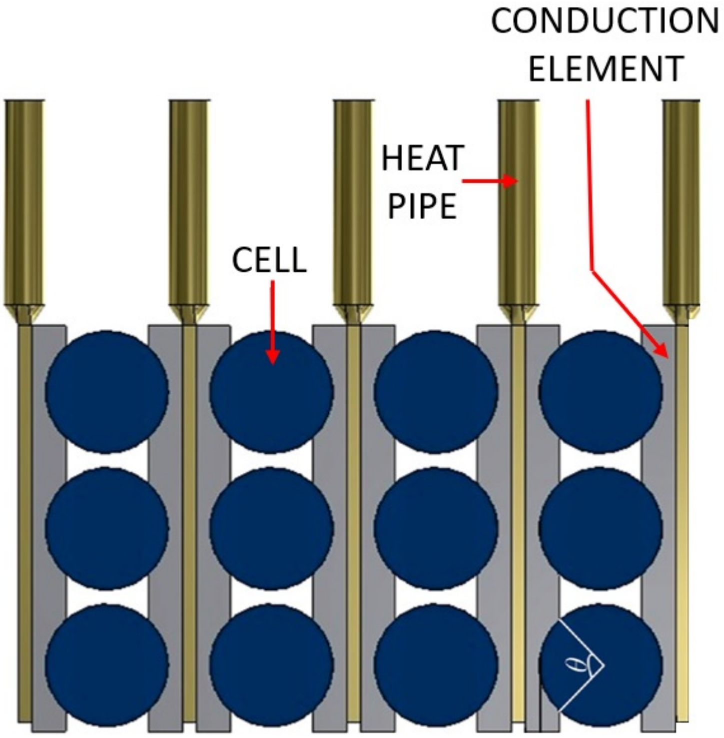

Figure 2.13. *Top view of the HP-based BTMS considered in the tests of Wang et al. [99].*

Wang et al. [99] study the cylindrical cell HP-based BTMS performances focusing on the effects of several structural parameters such as the cell spacing, the angle between the battery and the conductive elements and their thickness. Simulations show that the height of the conductive elements is the parameter which most influences the temperature distribution. The angle is a second influencing factor, while the thickness of the conductive elements and the cell spacing have a minimum effect.

2.5 INNOVATIVE COOLING STRATEGIES

Among all the different battery cooling systems some of them have begun to be more considered just in the last few years: in the past they were only used for heat-exchange laboratory experiments and nobody thought about them as possible cooling strategies to be exploited in the automotive field. These BTMSs (Figure 2.14) combine the ordinary cooling technologies such as the air or liquid-based ones with innovative methods, resulting in hybrid versatile cooling systems.

Several recent researches about BTMSs propose immersive solutions, thermoelectric cooling (TEC) systems [101] or PCM-based BTMSs [91, 102] which provide immersive methods or not (PCMs and the cooling methods related to these materials will be discussed in Chapter 3). These cooling options show great results but they are not widespread yet due to the high costs.

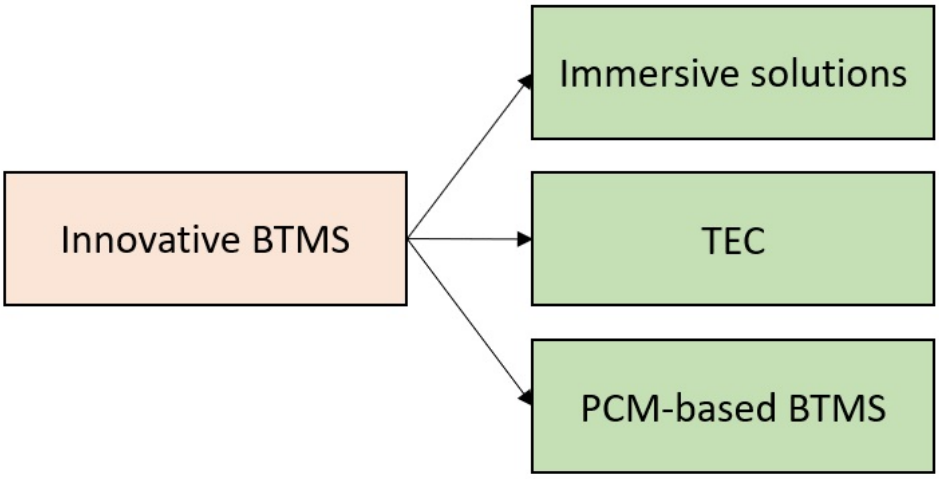

Figure 2.14. *Classification of the most innovative BTMSs.*

2.5.1 *Immersive solution*

Immersive methods are innovative strategies adopted to improve the performances of several kinds of BTMSs. This solution is often used coupled with cold plates, HP-based BTMSs or more simple liquid-based cooling systems. In this kind of cooling BTMSs the cells are literally immersed into a more or less dense fluid so that the heat transfer surface of the cells is completely exploited. There are several options to choose the battery filling material: thermal greases [103], silicon-based gels [104], intumescent pastes [51], dielectric oils [105].

Talking about dielectric-oil-based immersive applications, a great example is the *XING Mobility* patent. In collaboration with *Castrol*, *XING Mobility* realized a modular BP cooled thanks to the immersive method: the coolant is a very low viscosity fluid with a high flash point and a strong electrical insulation [105]. Further, this innovative BP is made of stackable micro-modules so that it is possible to configure the system for all the sizes and shapes required by the precise application. In Figure 2.15 the 1969 *Chevrolet Camaro* electrified by *XING Mobility* is shown: inside the car hood it is possible to see the so called *Immersion Cooled Modular Battery Pack System*.

Figure 2.15. *The 1969 Chevrolet Camaro electrified by XING Mobility [106].*

2.5.2 *Thermoelectric cooling (TEC)*

With a thermoelectric cooler all the processes concern about transformations from electricity to heat and vice-versa. These systems can work like coolers as well as like heaters (useful for applications in extremely low temperature environments). The TEC technology is also used in combination with more common air or liquid-based cooling systems resulting in hybrid BTMSs.

Lyu et al. [101] compare the temperatures reached by a cylindrical lithium-ion cell first cooled with the ordinary BTMSs and then with a hybrid BTMS which combines air and liquid cooling methods with a TEC system. Results show that during the test performed just with the air cooling system the cell temperature increases with the voltage: the higher is this value, the faster is the temperature rising. With the liquid cooling system the cell and the water temperatures rise almost together, with a more moderate trend compared to the air cooling case. Lower cell temperatures have been obtained equipping the BTMS with a TEC system.

2.6 LIB FIREFIGHTING METHODS

The incredible spread of LIBs seen in these years is easily understandable thinking about their specific capacity and energy density. All these characteristics are higher in LIBs rather than in the outdated batteries but this new technology is not completely issue-free: one of the hardest challenges is to find valid methods to prevent or face the so-called thermal runaway. As said, it is a dangerous phenomenon during which the temperature rises, exothermic cascade reactions are triggered and this could lead to fire or explosions [107]. There may be several causes that generate the thermal runaway: short circuits, battery overcharging, design and manufacturing defects [108].

There are several ways to act against the thermal runaway and it is possible to divide these methods into three categories considering their effects. The first category regards preventive measures such as the addiction of flame retardants. The second class includes fail-safe measures which stop or decrease the damage caused by the thermal runaway and involves the addition of separators or the adoption of cell venting techniques. Finally, the third category is a multiple-level strategy concerning actions to extinguish fires when the thermal runaway has already occurred [108].

2.6.1 *Multiple-level thermal runaway strategies*

There is another way to classify the firefighting strategies which deals with the techniques to prevent the thermal runaway or how to reduce its damages. Three main ways of acting correspond to the following three levels of protection:

- Cell-to-cell
- Module-to-module
- Battery pack

The so called cell-to-cell technique is the highest level of protection using engineered materials among all the cells. Considering the space constraints typical of certain application fields this represents a hard challenge, but the advantages are relevant. As a matter of fact, if a thermal runaway occurs the material surrounding the cells absorbs the exceeding heat and minimizes the propagation of the thermal effects to the adjacent cells [68]. PCMs are a good solution at a cell-to-cell level protection thanks to their nature of heat storage materials. The module-to-module protection level follows the same philosophy of the cell-to-cell one but it separates the modules from each other. It has a lower protection effectiveness with respect to the previous level one but it is a lighter solution, easier to adopt for several kinds of BPs. Finally, the battery pack firefighting strategy represents the lowest level of protection: it does not work against the heat propagation between the cells or the modules, it just provides a BP insulation from the outside. For instance, in an automotive application the car occupants would have more time to escape from the car cockpit, saving themselves.

2.6.2 *Emergency spray cooling*

If emergency situations occur there might be necessary rapid cooling actions. It is usually hard to face these events with a common BTMS, having the right timing: an efficient solution for these issues is the installation of a supplementary refrigerant spray cooling system [109]. This technology is not only useful to lower the temperature fast but also to suppress oxygen which is one of the possible causes of exothermic reactions. When the thermal sensors detect an incoming thermal runaway, the refrigerant is sprayed inside the battery box and gasifies due to the high temperature, strengthening the heat convection. In this way, a rapid temperature decrease occurs and the generated refrigerant gasses push the oxygen out of the box. Vents positioned in the right places can contribute to the oxygen flow out, too. Several tests have been carried on about different spray modes. The most common ones can be divided into the following mode categories:

- Continuous;
- Fixed-interval intermittent;
- Non-fixed-interval intermittent.

The continuous spray mode results in the most efficient cooling method, obtaining the lowest T_{dif} value (the highest temperature uniformity degree). On the other hand, the oxygen suppression is not better than that achievable with the intermittent modes. With these techniques the higher is the frequency of the spray, the better is the efficiency of the cooling. About the temperature uniformity, the non-fixed-interval intermittent mode is less influenced by the spray frequency than the fixed-interval intermittent one. Another advantage of the intermittent modes is that adopting them it is easier to keep a low oxygen concentration.

2.7 CONCLUSIONS

The study of the cooling technologies available on the market is fundamental for a further approach to the novel systems not greatly widespread yet and about which less researches are available. Knowing the most common BTMSs means to understand the benefits they can bring to a BP but also their limits and what is still necessary to satisfy the heat dissipation requirements.

In this chapter several air and liquid-based BTMSs have been analyzed and a lot of attention has been payed on the influence which many factors have on the cooling efficiency of the systems. For instance, considering an air-based BTMS it has been showed what happens in terms of temperature and temperature distribution modifying the position of the air-inlets and outlets, cooling the bottom of the BP or installing a baffle. Further, the influence of the geometrical factors has been investigated in a cooling system equipped with air distribution pipes. Regarding the liquid-based BTMSs, evaluations have been done regarding cooling plates (cold or ice plates, leaf-like channels) and heat pipes equipped or not with a remote heat transfer system. Discussions concerning the typical factors which influence the liquid-based BTMSs efficiency have mainly taken into account the position of the cooling plates, the geometry of the channels where the coolant flows, the kind of refrigerant and its flow rate, the driving-cycle. Literature investigations like these have been useful to put the basis for a CFD study about a liquid-cooled BP brick with cylindrical cells staggered into a solid plastic matrix and wavy liquid cooling channels put among the cells [91]. To conclude this chapter, an overview regarding some of the novel cooling technologies (some of them deepened in Chapter 3) has been presented and a conclusive dissertation dealing with firefighting strategies has been proposed.

3

PHASE CHANGE MATERIALS FOR BATTERY COOLING

3.1 PHASE CHANGE MATERIALS

Phase change materials (PCMs) are substances which change their physical state from solid to liquid and vice-versa to store and release heat. This is a superior way of storing thermal energy both for the PCM high storage capacity and for the isothermic nature of the storage processes [110].

During a melting process a solid PCM initially behaves like a sensible heat storage (SHS) material (Figure 3.1): the more the time passes the more it absorbs heat and its temperature increases. Then, when it reaches a certain temperature value (it depends on the specific PCM), the melting begins and the PCM starts storing a large amount of heat at an almost constant temperature: this is the latent contribution. This isothermic process proceeds until all the PCM is melted and, at that point, a further energy supply is stored as sensible heat and the temperature starts rising again.

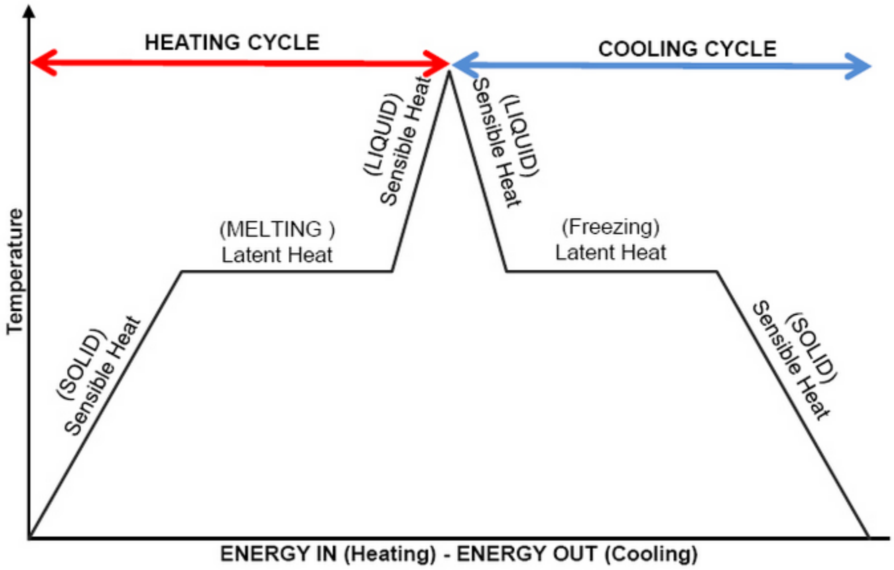

Figure 3.1. *Theoretical energy trend during PCM heating and cooling cycles [111].*

There is a huge number of parameters which contribute to the PCM characterization. This represents a potential advantage because it is possible to choose the material which better meets the thermal, physical, chemical and economical requirements for the precise application [112]. On the other hand, this variety of factors makes the choice hard.

Considering their chemical composition, PCMs are broadly classified into:

- **Inorganic** (hydrted salts, metals);
- **Organic** (paraffins, fatty acids);
- **Eutectics** (two or more organic or inorganic PCMs mixed) [113].

About the properties, Abhat et al. [114] identify four classes of criteria that should be taken into account while characterizing the PCMs. These categories deal with:

- Thermodynamics
- Kinetics
- Chemistry
- Economics

Following this classification it comes out that the PCMs comprehended in each of these groups can be distinguished considering factors such as their stabilization shape [115], the phase-change temperature range, the latent heat of fusion, the thermal conductivity (which influences slower or faster charging/discharging cycles), the volume change during the phase transition, the cost [113]. Further, PCMs show a high chemical stability, non-toxicity, non-corrosive and non-flammable properties, they are relatively cheap and there are no availability issues [116].

For all these reasons PCMs have spread in several application fields. In particular, their most appreciated property is the very high latent heat storage (LHS) capability considering a relatively small volume [117].

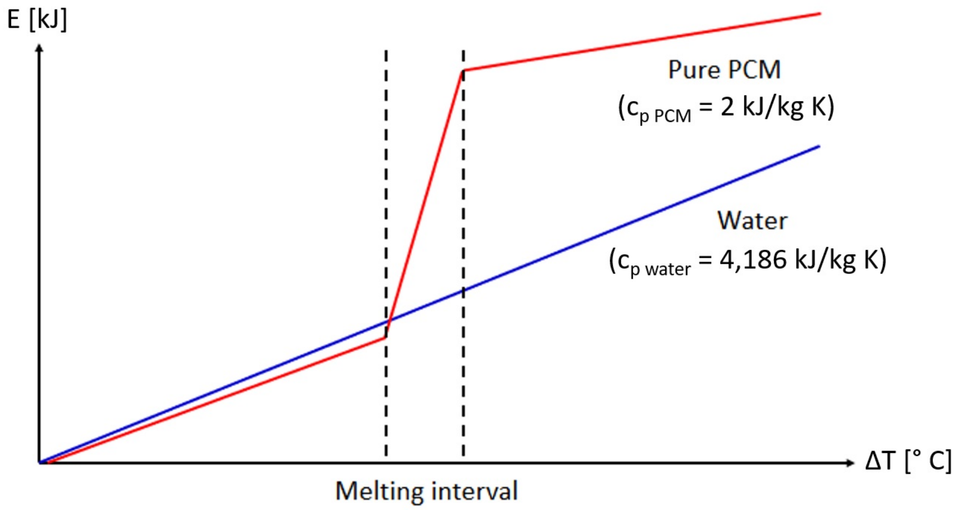

Figure 3.2. *Stored energy over time during water and PCM heating cycles.*

This characteristic behaviour is exploited in many different fields where the energy storage is required or when thermal comfort is needed. As shown in the graph of Figure 3.2, the benefit brought by a PCM in terms of thermal storage capability is evident. Before reaching its characteristic melting temperature (T_{melt}), the PCM energy storage capability is slightly lower than the water one but, as soon as the PCM reaches T_{melt} it starts the storage of a huge quantity of energy which is much higher than that absorbed by water.

3.2 PCM RESEARCH AND APPLICATIONS

Renewable energies are usually non-programmable sources which need storage systems to balance the energy demand with the energy production. Talking about thermal applications, if the heat generation is obtained using discontinuous energy sources like solar or wind energy [118], the introduction of thermal energy storage systems (TESSs) is mandatory. Among the TESSs, the PCM-based ones are acquiring more and more importance thanks to the high latent heat storage capability of these materials which can allow a significant reduction of the storage volume for a fixed quantity of energy stored [119].

Many papers have been devoted to the characterization of the latent thermal energy storage systems (LTESSs) and nowadays PCM-based LTESSs find application in several fields: civil [120, 118], textile [121, 122], food transport [123, 124], agriculture [125], air conditioning [126], electronics [127, 128, 129], solar systems [130, 131], automotive [132, 133, 134, 135]. Among the PCMs, the paraffin-based ones are very popular thanks to their small temperature drop during the heat recovery, a low vapour pressure and, in addition, their high chemical inertia, stability and non-toxicity [136].

Figure 3.3. *A PCM textile application: a jacket and a pair of motorbike gloves made by BMW with internal PCM pouches.*

Conversely, a common negative property of many PCMs is their low thermal conductivity ($\lambda < 1\ W/m\ K$) which represents one of the biggest challenge in this research field. As a matter of fact, the low PCM thermal conductivity limits the potential of these materials leading to low heat storage/release rates and a low utilization efficiency of the stored energy [137]. Different methods have been proposed to increase the PCM thermal conductivity: the addition of fins [138, 139, 140], nanoparticles [141, 116, 142, 143], both fins and nanoparticles together [144], the use of PCM loads such as graphite [145], carbon-fibers [146], metal wools [147], 3D metallic periodic structures [148, 149] or high-porosity metal foams [150, 151, 125, 137, 136, 152, 153, 154, 102]. This last solution is found to be very effective thanks to the high thermal conductivity of the metal foams [155, 156], their significant surface area to volume ratio, the highly interconnected structure and the natural fluid mixing effect [137].

Righetti et al. [148, 149] studied how to enhance the heat conductivity of paraffin PCMs with different phase change temperatures, using various 3D metallic periodic structures immersed into the paraffin materials and supplying different heat fluxes to the system. They found that the 3D structures greatly improves the heat transfer performance, significantly reducing the charging/discharging time. About 3D metallic non-periodic structures, Alhusseny et al. [151] studied the effects of a copper foam inside a LTESS made of staggered bundled tubes already filled with pure paraffin PCM and around which the water flows as heating/cooling fluid: they obtained good results in terms of PCM charging/discharging rate (accelerated by more than 50% with respect to the corresponding system with pure PCM) and efficiency.

Esapour et al. [136] enriched this research field studying a multi-tube heat exchanger (MTHX), analyzing the effects of the metal foam porosity, the number of tubes and their arrangement on the LTES thermal characteristics. Results showed that a greater number of inner tubes filled with metal-foam-loaded PCMs has more influence on phase change rates with respect to the case with tubes filled with pure PCMs. Further, in agreement with Righetti et al. [157] and Rehman et al. [154], the charging/discharging time decreases with the porosity. On the contrary, the arrangement of the inner tubes has no effect on the melting rate of the composite PCMs.

Playing with the porosity parameter to achieve a more uniform temperature in the whole system, Mahdi et al. [153] suggested a multiple-segment metal foam characterized by a cascade porosity in the heat flow direction, put in a shell-and-tube storage containment heat exchanger. Dinesh et al. [158] focused their attention on the size of the metal foam pores demonstrating that, even for the same porosity, the pore size distribution strongly affects the PCM melting rate with smaller pores resulting in faster melting processes and higher heat transfer rates. Ghahremannezhad et al. [152] analysed the effects of non-homogeneous porous metal foams (structures presenting positive and negative porous gradients in several spatial directions) on the melting behaviour of PCMs. Their simulations highlighted that the heat transfer is remarkably influenced by the porous characteristics of the metal foams and there are also changes considering the heat source location due to the gravity effect. The analysis of the open literature puts in evidence that many numerical studies have been published on this topic but there is still a lack of experimental data.

3.3 PCM CHARACTERIZATION

The following work arises from the necessity to enrich the experimental branch of the PCMs state of the art, aiming to demonstrate the positive impact of the metal foams in enhancing the PCMs thermal conductivity, lowering their melting time and, at the same time, improving the temperature distribution of the PCM-based systems. Further, as projecting and testing new innovative systems presupposes a deep knowledge of the physics behind, before studying a cutting-edge PCM-based BTMS it has been fundamental to proceed with the following PCM characterization tests.

3.3.1 *Qualitative tests*

The first tests were qualitative evaluations regarding the PCM conductivity increase using metal foams. The experiments were conducted using a polymeric case (Figure 3.4) filled first with pure PCM and then with metal-foam-loaded PCMs. The selected PCM was a commercial paraffin (the RT35 made by *Rubitherm* [159]) fully compatible with both plastic and metallic containers, highly stable, with a low toxicity and flammability degree. A case was built with 5 *mm* thick polycarbonate (softening temperature $T_{\text{soft}} \simeq 115$ °C) sheets and used as PCM container. An electric heater was put on the top of the PCM volume and linked to an analogical variac which supplied a voltage $V = 40\ V$ for all the tests: the amount of released heat was always the same. All the properties of the materials are shown in Table 3.1.

Figure 3.4. *Poycarbonate case used for the qualitative tests and filled with pure PCM.*

Two couples of tests were carried on comparing the heating cycles of pure and foam-loaded PCMs. The first comparison was that between a pure PCM heating cycle and an aluminum-foam-loaded PCM one. The second comparison dealt with a pure PCM heating cycle and a copper-foam-loaded PCM one.

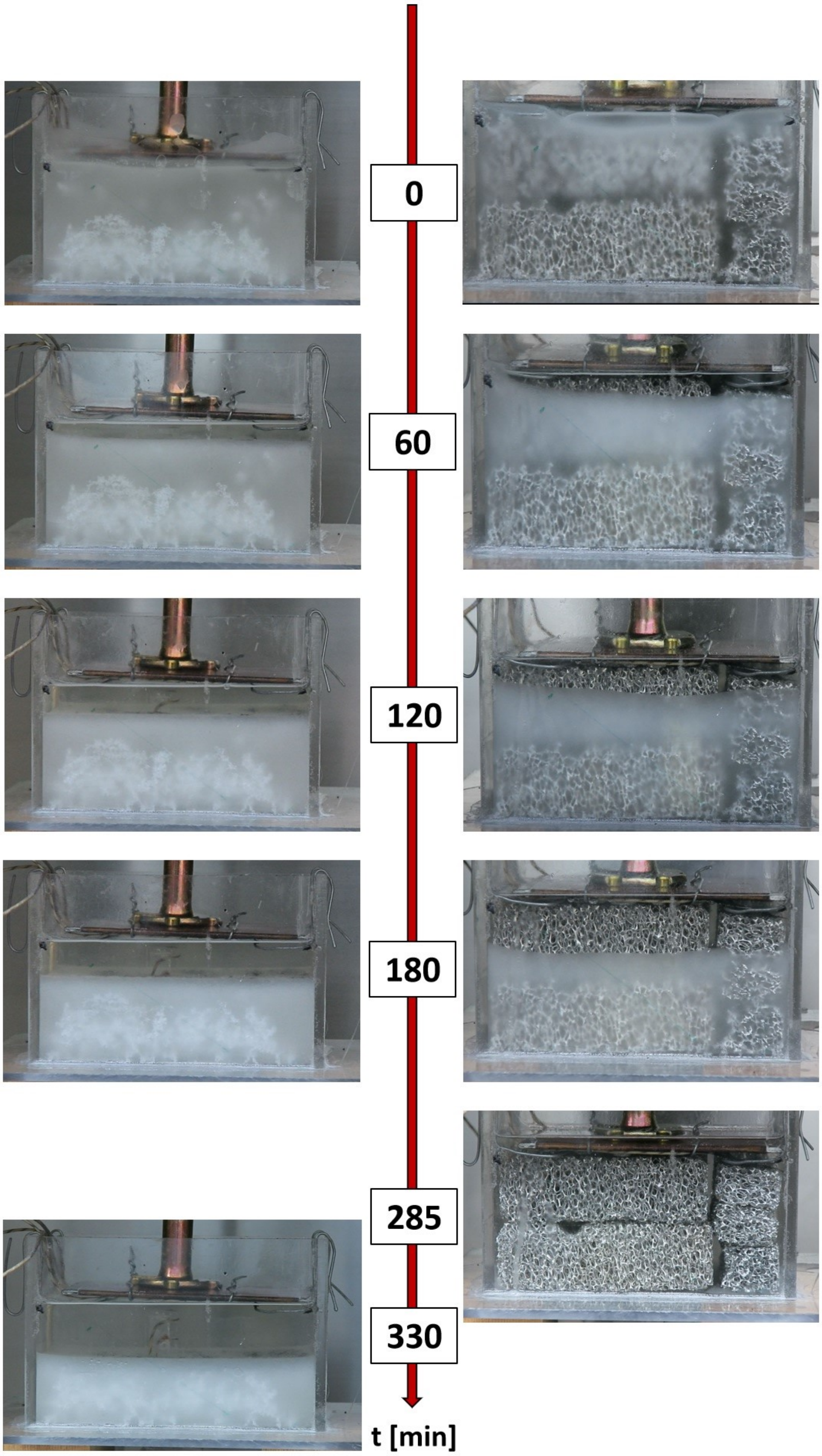

Figure 3.5. *Comparison between a pure PCM heating cycle (left) and an aluminum-foam-loaded PCM one (right).*

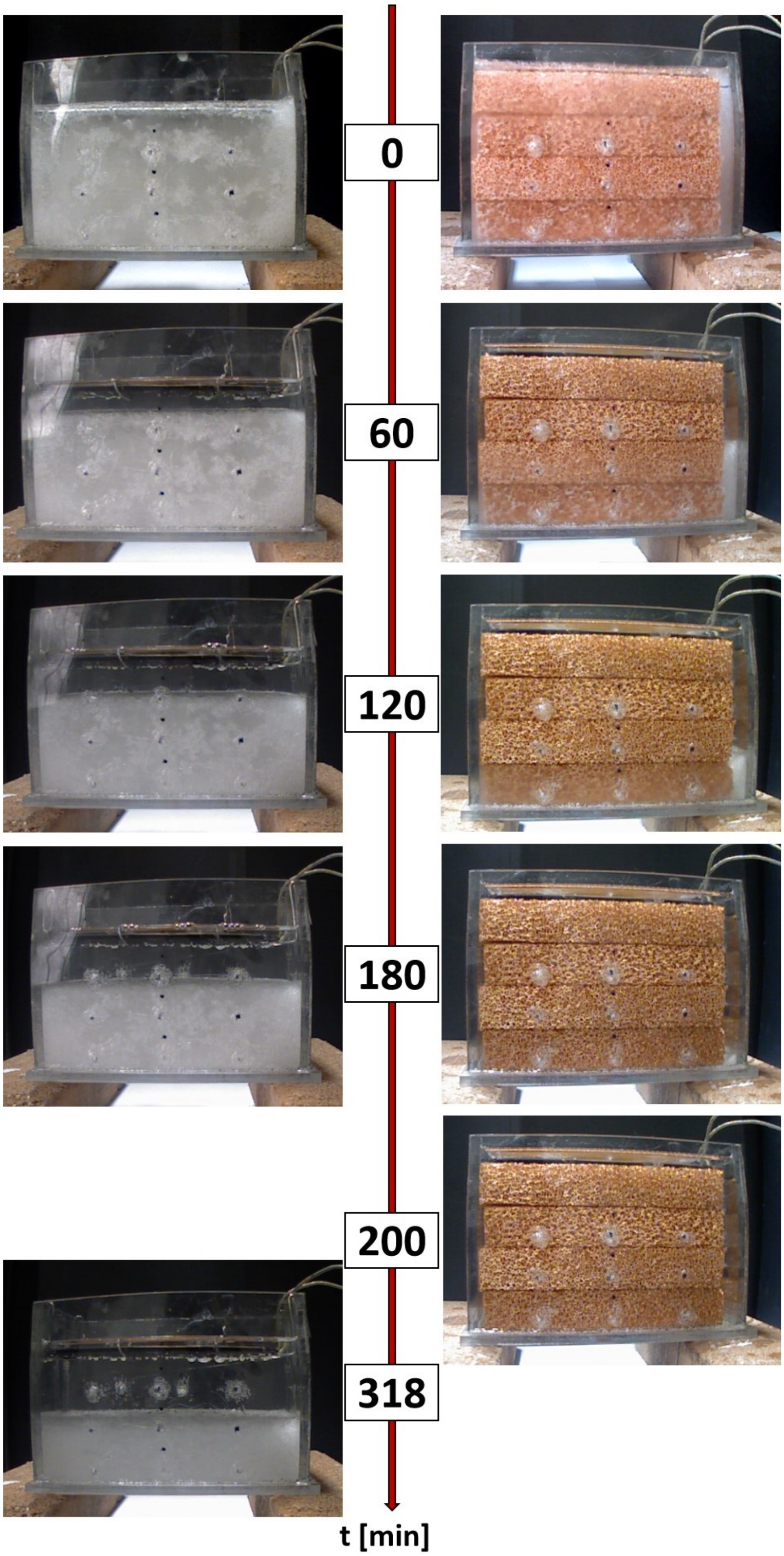

Figure 3.6. *Comparison between a pure PCM heating cycle (left) and an copper-foam-loaded PCM one (right).*

Table 3.1. *Materials properties provided by the manufacturers.*

PCM	Symbol	Unit	Value
Phase change temperature (solid → liquid)	$T_{\text{S-L}}$	[°C]	$29 \div 36$
Phase change temperature (liquid → solid)	$T_{\text{L-S}}$	[°C]	$36 \div 31$
Heat storage capacity	H	[kJ/kg]	160
Specific heat capacity (solid)	$c_{\text{p, S}}$	[kJ/kg K]	3
Specific heat capacity (liquid)	$c_{\text{p, L}}$	[kJ/kg K]	2
Density (solid)	ρ_{S}	[kg/l]	0.86
Density (liquid)	ρ_{L}	[kg/l]	0.77
Heat conductivity (solid, liquid)	λ_{SL}	[W/m K]	0.2
Volume expansion (solid → liquid)	V_{exp}	[%]	12.5
Flash temperature	T_{flash}	[°C]	167
Maximum working temperature	$T_{\text{w, max}}$	[°C]	65
Aluminum foam			
Heat conductivity	λ_{Al}	[W/m K]	239
Porosity	ϕ	[%]	96
Pores per inch	PPI		10
Copper foam			
Heat conductivity	λ_{Cu}	[W/m K]	385
Porosity	ϕ	[%]	95
Pores per inch	PPI		20
Polycarbonate			
Heat conductivity	λ_{pc}	[W/m K]	0.21
Density	ρ_{pc}	$[\text{g/cm}^3]$	1.2
Softening temperature	$T_{\text{soft, pc}}$	[°C]	115
Polystyrene			
Heat conductivity	λ_{ps}	[W/m K]	0.035
Density	ρ_{ps}	$[\text{g/cm}^3]$	1.05
Softening temperature	$T_{\text{soft, ps}}$	[°C]	90
EUROBATEX®			
Heat conductivity	λ_{ps}	[W/m K]	$0.033 \div 0.039$
Working temperature	$T_{\text{w, opt}}$	[°C]	$-45 \div 110$

Figure 3.5 shows the first couple of tests: during the pure PCM test a half of the PCM volume melted in $t_{1,\,\text{pure}} = 330\ min$, while the aluminum-foam-loaded PCM completely melted in $t_{1,\,\text{Al}} = 285\ min$. In Figure 3.6 it is possible to see the second couple of tests: during the pure PCM test a half of the PCM volume melted in $t_{2,\,\text{pure}} = 318\ min$, while the copper-foam-loaded PCM completely melted in $t_{2,\,\text{Cu}} = 200\ min$.

The results of these qualitative experiments confirmed the benefits brought by the metal foams to the PCM in terms of heat conductivity enhancement and, consequently, melting time reduction. From the impossibility to melt the entire PCM volume during both of the tests with pure PCM, the idea to insulate the whole experimental setup came out. The aim was to get as close as possible to an ideal adiabatic system where there were no heat losses so that it was possible to proceed with more accurate quantitative tests to characterize the PCM.

3.3.2 *Temperature homogeneity on the plane*

The goal of the tests was to check if the heat transfer could be considered as monodimensional (1D) into the PCM, under precise heating conditions. Having a 1D heat transfer process means that it is possible to proceed with a temperature evaluation just considering the temperatures in the direction of the heat gradient, avoiding usefulness recordings and facilitating the measurements.

3.3.2.1 *Experimental setup*

For this series of tests a new polycarbonate case was designed and drawn with the *CATIA* CAD software. Then it was realized using a *Roland MDX-40A* milling machine, thanks to the coupled use of *SRP Player* (a CAM software) and *Vpanel* (a controlling machine program) [160]. The resulting case had a final volume $V_{\text{case}} = 1.08 \cdot 10^6\ mm^3$ and it was equipped with 12 T-type thermocouples (TCs) previously calibrated (see Appendix 1). As it is possible to see in Figure 3.7 the TCs were placed inside the case at two fixed heights: 6 TCs were fixed at a distance of $5\ mm$ from the bottom of the case, 6 TCs were placed at a distance of $45\ mm$ from the bottom of the case. Finally, the case was filled with RT35 PCM [159].

In Figure 3.9 the whole experimental setup is shown. An electric resistance (heater) was put on the top of the PCM, at $67\ mm$ from the bottom of the case, so that it was completely immersed and in direct contact with the PCM. Two TCs were placed in contact with the heater to monitor its temperature and one additional TC was used to record the temperature of the room (T_{AIR}) during the experimental tests. A power supplier was connected to the heater in order to impose the heat flux generated by Joule effect and the values of voltage and current were monitored thanks to an ammeter and a voltmeter: these data are shown in Table 3.2 together with the full scales (FS) considered and the full scale uncertainties ($\%FS$) related to the instruments. With these values of voltage and current, the resulting power supplied was $P = V \cdot i = 3.5\ W/m^2$ and its related uncertainty value was

$U(P) = \sqrt{U^2(i) + U^2(V)} = 11.77\%$. The temperature values were acquired thanks to a series of NI-9213 modules for TCs and the use of a *LabVIEW* project specifically realized for this purpose. The typical uncertainty value of the T-type thermocouples (estimated by means of a series of comparison with a RTD reference sensor) was $U(T) = 0.4 \div 0.7\ K$.

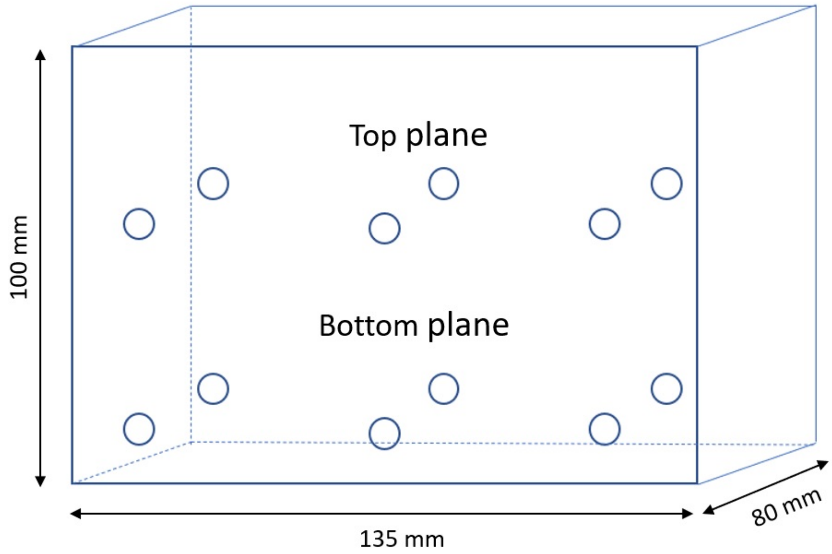

Figure 3.7. *Scheme of the polycarbonate case used to test the temperature homogeneity along the (x,y) plane.*

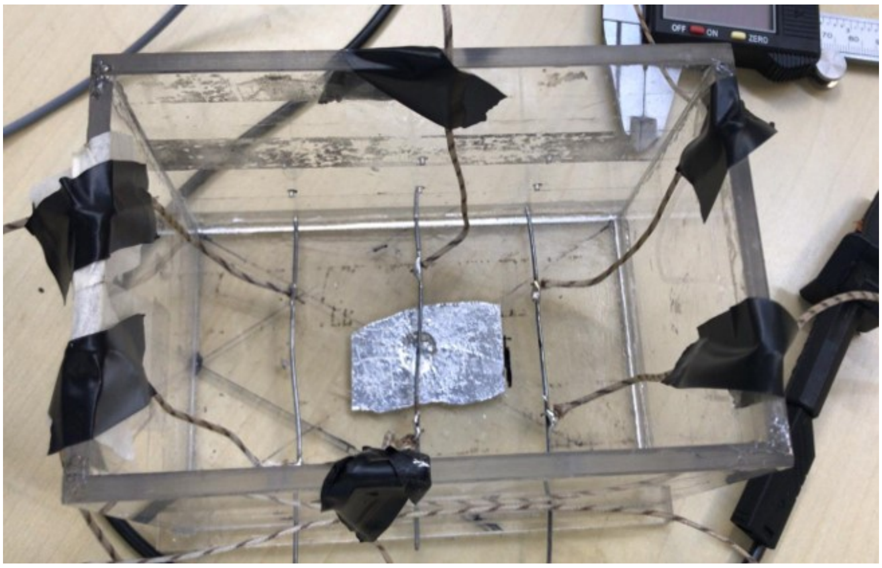

Figure 3.8. *A building phase of the case: welding of the TCs on the supporting iron wires at the bottom level.*

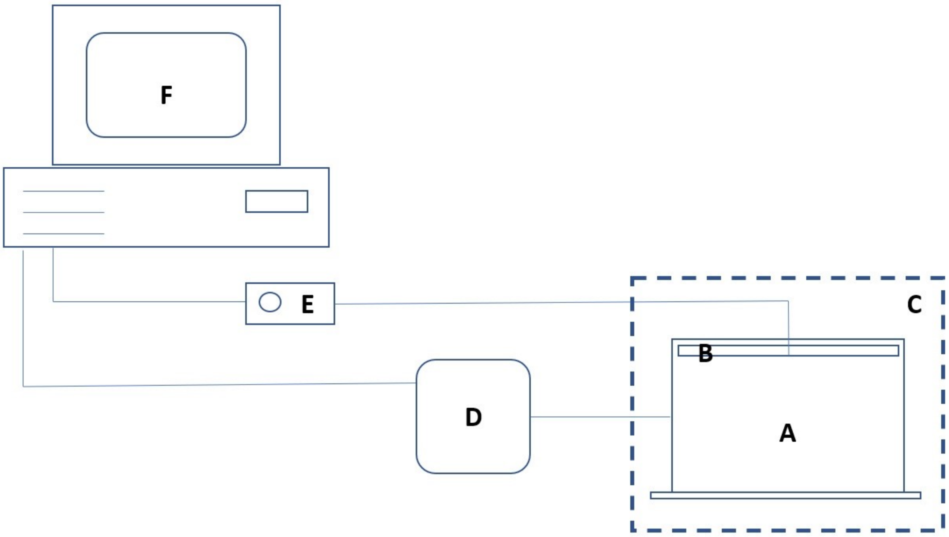

Figure 3.9. *Experimental setup composed of the polycarbonate case (A) the heater on the top of the case (B), the polystyrene box which insulates the case (C), the NI-9213 module for TCs (D), the power supply (E) and the computer (F).*

Table 3.2. *Instruments used to monitor the electrical current and voltage values and the related full scale (FS) and full scale uncertainty ($U(\%FS)$) values.*

Instrument	Quantity	Unit	Measured value	FS	U(%FS)
Ammeter	i	[A]	0.2	1	2
Voltmeter	V	[V]	17.5	30	3.6

To obtain the complete melting of the whole PCM volume (result not achieved with the pure PCM tests discussed in Section 3.3.1), the case was enclosed into a polystyrene box with 100 mm thick walls and a global heat transfer coefficient $U = 0.132\ W/m^2K$ (calculation in Appendix 2): the aim was to minimize the heat losses.

3.3.2.2 *Results*

In order to check if the heat transfer within the case could be considered as monodimensional, the PCM was heated from the top of the case, ensuring that the heat was transferred within the PCM only by pure conduction. Due to the symmetry of the geometry it was expected that the temperature was homogeneous on the horizontal planes (x,y), which means that the only heat flux component different from zero was the vertical (z) one. As it is possible to see in Figure 3.10, the temperature trends recorded by all the 6 top plane TCs, as well as by the other 6 bottom plane ones, were very similar during the whole charging/discharging cycle. In addition, in Figure 3.10 the room temperature T_{AIR} is reported during the complete cycle.

It is evident how T_{AIR} was almost constant during the cycle which lasted 35 h (the graph shows just the first 30 h) with an average value of $\widetilde{T}_{\mathrm{air}} = 27.2$ °C: this is the reason why the initial temperature of the PCM in the case was very close to the phase change interval of RT35. For a heat flux $P = 3.5\ W/m^2$ applied on the top for 18.2 h (charging phase), the maximum temperature recorded on the top plane was $T_{\mathrm{TP}} \simeq 90$ °C, the maximum temperature recorded on the bottom plane was $T_{\mathrm{BP}} \simeq 60$ °C. The discharging phase, during which the PCM volume was cooled down to the initial temperature value (33.3 °C), lasted about 34.8 h.

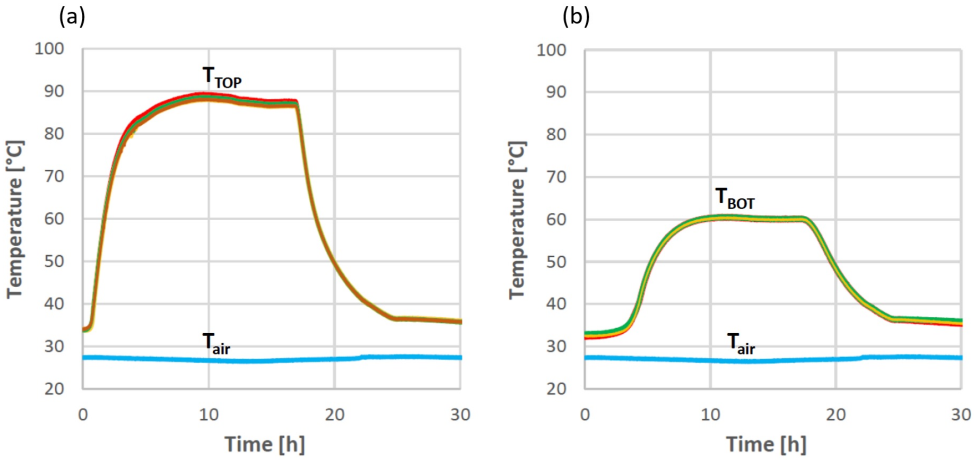

Figure 3.10. *Temperature trends recorded by the 6 TCs on the top plane (a) and by the 6 TCs on the bottom plane (b) [161].*

It is clear how, independently from the position of the TCs on the same horizontal plane (top or bottom), all the temperature trends recorded by the TCs and showed in Figure 3.10 (a) and Figure 3.10 (b) are overlapped. The maximum temperature differences recorded during the whole charging phase by the TCs on the same plane were $\Delta T_{\mathrm{TP}} = 0.4\ K$ for the top plane and $\Delta T_{\mathrm{BP}} = 0.5\ K$ for the bottom plane, within the uncertainty range of TCs. This result confirms that the temperature field can be considered as variable only along the vertical direction z, especially in the central region of the case. The time needed to reach a quasi-steady state temperature on the top plane, closer to the heater, was about 8 h. This time was longer for the bottom plane (far from the heater) where about 10 h were necessary to obtain a stable temperature value. The discharging phase lasted about 6 h for both the top and the bottom plane.

3.3.3 *PCM thermal conductivity enhancement*

A series of experimental tests were conducted using a polycarbonate case filled first with pure PCM and then with copper-foam-loaded PCM. The aim of these experimental tests was to show that loading a PCM with a metal foam is a useful technique to enhance its thermal conductivity and improve the temperature distribution in the whole system.

3.3.3.1 *Experimental setup*

Once verified the temperature homogeneity along the x and y directions, the experimental setup was changed to better monitor the evolution in time of the melting front from the top to the bottom of the case. The polycarbonate case used for the previous tests (see Section 3.3.2.1) was modified and properly adapted to proceed with the new experiments. In Figure 3.11 the scheme of the new case is showed: 7 T-type thermocouples were inserted in the case, 2 TCs were placed below the electric heater, in contact with its bottom surface, and 5 TCs were fixed along the central axis of the case, at different heights from the case bottom. More in detail, TC_{H1} and TC_{H2} were at 67 mm from the case bottom, TC_1 was at 55 mm, TC_2 at 42 mm, TC_3 at 29 mm, TC_4 at 16 mm, TC_5 at 3 mm.

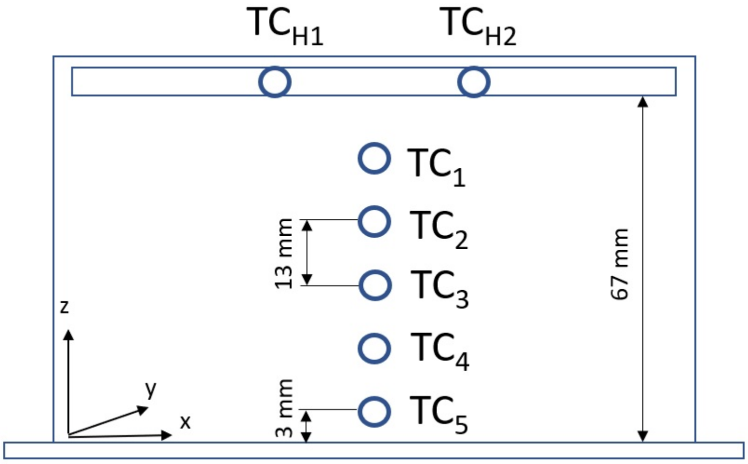

Figure 3.11. *Scheme of the polycarbonate case used to monitor the melting front progress.*

Figure 3.12. *Experimental rig with 5 TCs placed along the z-axis.*

Another setup improvement concerned the insulation box: the thin air cavities between its polystyrene walls and the polycarbonate case (Figure 3.13 (a)) were filled with *EUROBATEX*® [162], a dense insulating elastomeric foam (FEF) with a low thermal conductivity coefficient ($\lambda = 0.033 \div 0.039\ W/mK$) which helped in lowering the heat losses. This material is often used for the thermal insulation both in civil and in the industrial field. A *EUROBATEX*® layer was also used to cover the inner surface of the polystyrene top (Figure 3.13 (b) and Figure 3.13 (c)) and to insulate the thermal bridges among all the parts of the polystyrene box (Figure 3.13 (d)). With these changes the insulation was greatly enhanced as showed by the global heat transfer coefficient $U = 0.044\ W/m^2K$ (calculation in Appendix 2) which decreased by 66.6%.

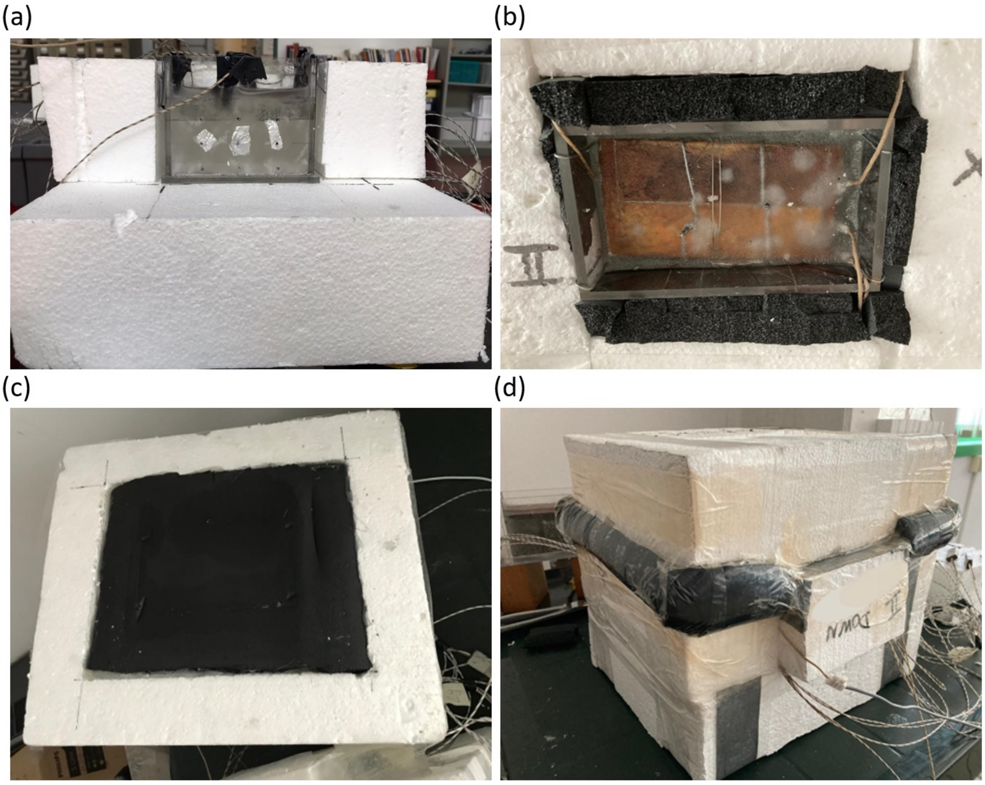

Figure 3.13. *Assembling of the polystyrene box: front view (a), detail of the air cavities filled with EUROBATEX® [162] (b), inner surface of the polystyrene top wrapped with a EUROBATEX® layer (c), final assembly of the insulation box.*

This experimental setup was useful to analyze the temperature distribution within the case, along the vertical direction (z) at the center of the case, and to verify the effect of the metallic foam on the temperature distribution during the PCM charging phase. Besides the case changing, the rest of the experimental setup remained the same as in Figure 3.9.

3.3.3.2 *Results*

Two series of tests were conducted: the first was carried on filling the polycarbonate case with pure PCM, for the second one the PCM was loaded with copper foam. The electric heater was put on the top of the case, supplying power for 23.7 h (charging phase). The heat flux imposed on the top by Joule effect was $P = 3.5\ W/m^2$.

In Figure 3.14 (a) and Figure 3.14 (b) the evolution in time of the temperature within the case is presented for both pure PCM and copper-foam-loaded PCM. In addition, in these graphs the temperature of the lower surface of the electric heater (red curve) is shown: this temperature has been obtained as the average of the temperatures measured by the two TCs placed below the heater (see Figure 3.11).

In Figure 3.14 (a) the trends of the temperatures recorded in presence of pure PCM are reported. After 15 h the temperature difference between the closest TC to the heater and the furthest one (i.e. TC_1 and TC_5) was $\Delta T_{1\text{-}5,\,\mathrm{PURE}} = 20\ K$. This large temperature difference within the case highlights how much strong is the thermal resistance offered by the pure PCM due to the low thermal conductivity typical of the paraffin. Starting from an initial temperature $T_{0,\,\mathrm{PURE}} = 23\ °C$, the whole volume of pure PCM melted in 23.7 h, when the PCM temperature close to the heater (average between TC_{H1} and TC_{H2}) reached a value of 66 $°C$.

In presence of the copper foam, the charging test was repeated and monitored thanks to the 7 TCs, supplying to the heater the same power used for the test with pure PCM. This was guaranteed by imposing the same electrical voltage and current to the heater. In Figure 3.14 (b) it is possible to see the trends of the temperatures recorded in presence of copper foam. The graph shows that after 15 h the temperature difference between TC_1 and TC_5 was $\Delta T_{1\text{-}5,\,\mathrm{FOAM}} = 3\ K$: this means that loading the PCM with the copper foam allows reducing the thermal resistance of about one order of magnitude.

This result confirmed the beneficial effect of copper metal foam if the goal of the designer is to reduce the melting time and accelerate the heat transfer rate. The presence of the high porosity metal foam significantly increased the effective thermal conductivity of the system and reduced the temperature gradient along the vertical direction z.

The graphs in Figure 3.15 (a) and Figure 3.15 (b) show the evolution in time of the vertical temperature profile recorded by the 5 TCs placed along the central axis of the case, during the charging phase with pure (Figure 3.15 (a)) and metal-foam-loaded (Figure 3.15 (b)) PCMs. Further, in these graphs it is also shown the temperature of the electric heater lower surface (red curve). Two dashed vertical lines indicate the temperature melting range for the RT35 PCM.

As it is possible to see in Figure 3.15 (a), with pure PCM the melting process began just after 1 h the charging process started, close to the heater (at 55 mm from the bottom); on the contrary, in presence of the copper foam (Figure 3.15 (b)) the melting range was not reached, yet. As a matter of fact, in presence of the copper foam, when the charging process started the heat was transferred faster by conduction from the top to the bottom layers and a larger thickness of PCM started to be charged.

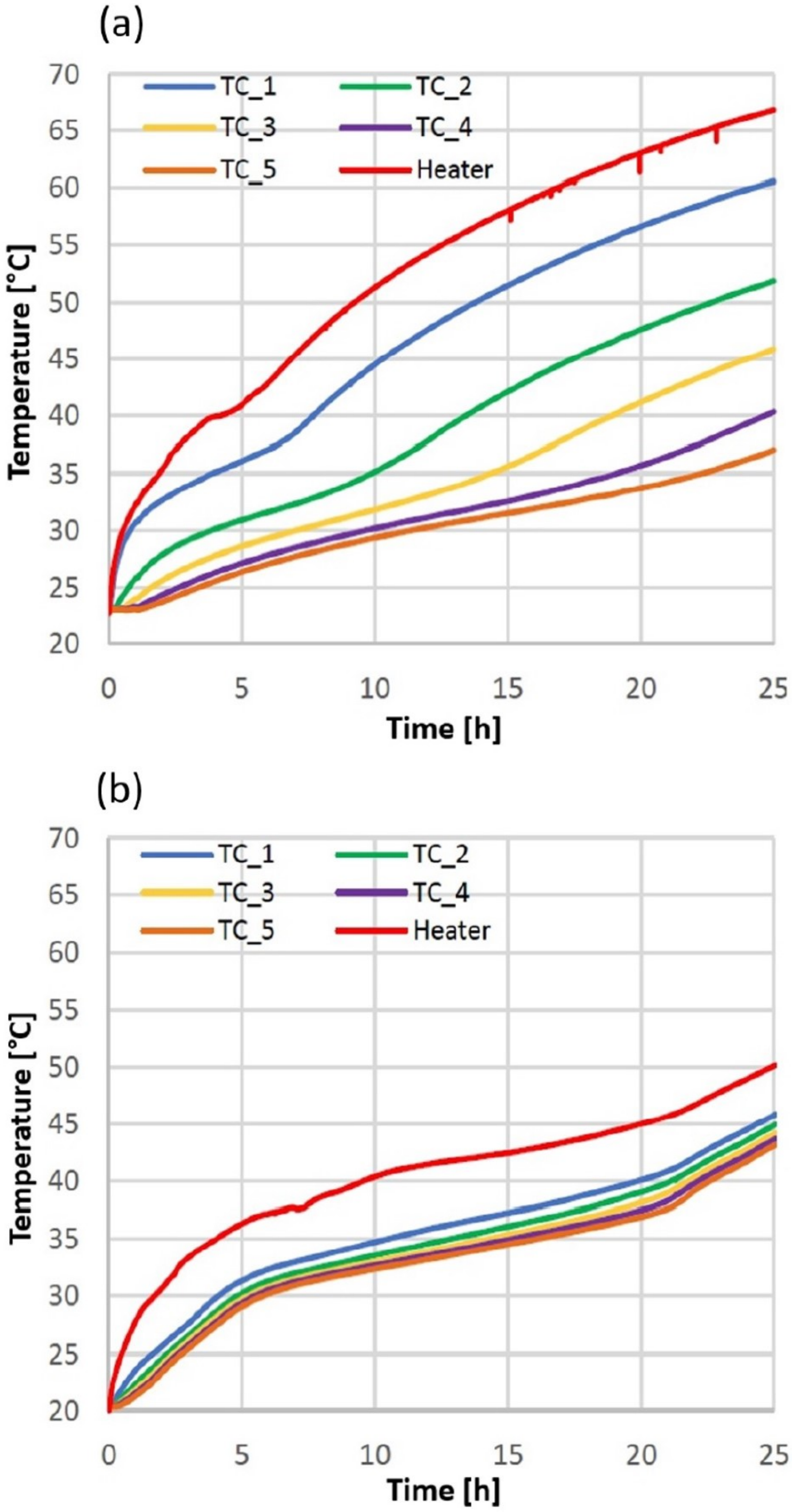

Figure 3.14. *Temperature trends recorded by the TCs during the tests with pure PCM (a) and with copper-foam-loaded PCM (b).*

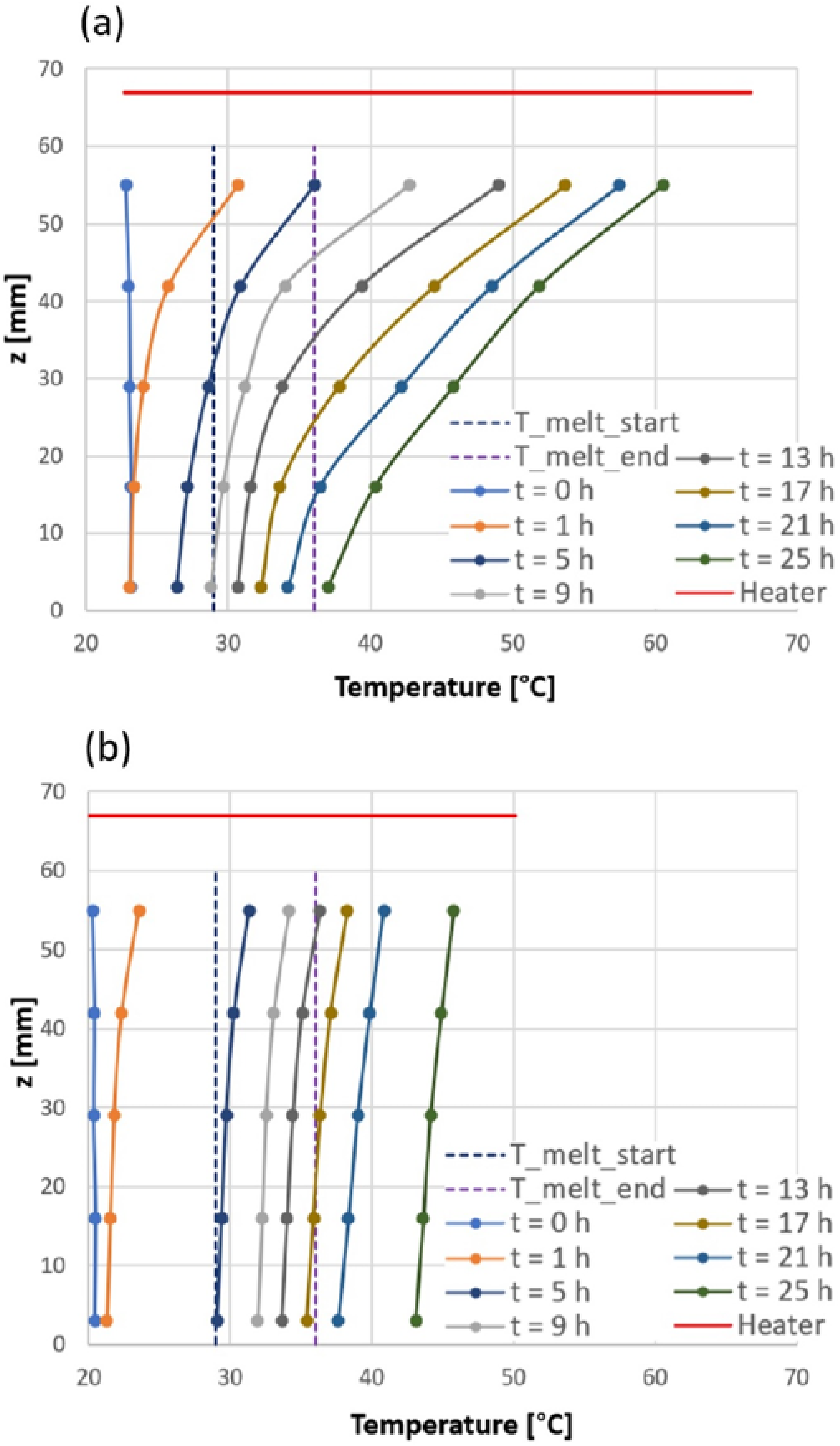

Figure 3.15. *Vertical temperature profiles recorded by the TCs during the tests with pure PCM (a) and with copper-foam-loaded PCM (b).*

In presence of pure PCM (Figure 3.15 (a)) the temperature difference between the closest TC to the heater and the furthest one ($\Delta T_{\text{1-5, PURE}}$) strongly increased over time: the heat was slowed down as it passed through the paraffin due to its low thermal conductivity. The last thermocouple reached the melting temperature after 9 h. In presence of copper-foam-loaded PCM (Figure 3.15(b)) the 5 TCs worked with very similar temperature values during the whole charging phase, with a maximum temperature difference between the closest TC to the heater and the furthest one equal to $\Delta T_{\text{1-5, FOAM}} = 2.7\ K$ after 25 h. Although the test with copper-foam-loaded PCM started with an initial temperature ($T_{\text{0, FOAM}}$) within the case equal to 21 °C (lower than $T_{\text{0, PURE}}$), the whole PCM volume completely melted in 16 h (7.7 h earlier than in presence of pure PCM), when TC_5 reached 35 °C.

Figure 3.15 (a) and Figure 3.15 (b) demonstrate how, in presence of copper foam, the vertical temperature distribution within the case was always more uniform than in presence of pure PCM during the whole charging process. After $t = 5\ h$, with copper foam the entire volume of the PCM was in the melting range; on the contrary, with pure PCM only 59.4% of the case volume was in that range. From $t = 9\ h$ to $t = 13\ h$, the copper-foam-loaded PCM was completely involved into the melting process and after $t = 13\ h$ about the 7.8% of the PCM volume was already into superheated liquid state. On the contrary, in presence of pure PCM, the more the time passed, the higher the thermal difference between the top and bottom layers became: after $t = 9\ h$ the solid phase was still present on the case bottom; after $t = 13\ h$ there was no more solid PCM but the thermal distribution indicates that the PCM layers close to the heater were in a liquid state, while the bottom layers were still involved into the melting process.

As clearly evidenced by Figure 3.15 (a) and Figure 3.15 (b), the complete melting was reached in 23.7 h with pure PCM and in 16 h with the copper-foam-loaded PCM. This result confirmed the positive effect of the metal foam on the acceleration of the melting phase. In addition, comparing Figure 3.15 (a) and Figure 3.15 (b) it is possible to see that after $t = 25\ h$ the temperature difference between the extreme TCs (TC_1 and TC_5) was $\Delta T_{\text{1-5, PURE}} \simeq 23.6\ K$ with pure PCM but only $\Delta T_{\text{1-5, FOAM}} \simeq 2.7\ K$ in presence of the copper foam: this highlights the strong increase of the temperature uniformity along the vertical direction obtained with the introduction of the foam.

Another important point is the difference between the heater temperature with and without the copper foam: after $t = 25\ h$ (see Figure 3.15 (a) and Figure 3.15 (b)), the heater reached $T_{\text{H, PURE}} = 67°\ C$ with pure PCM and $T_{\text{H, FOAM}} = 50.1°\ C$ in presence of the copper foam. In order to melt the whole PCM volume, the heater had to reach a temperature $T_{\text{H, PURE}} = 66°\ C$ with pure PCM and $T_{\text{H, FOAM}} = 44°\ C$ in presence of the copper foam.

With pure PCM the higher heater temperature is a clear consequence of the low thermal conductivity of the paraffin which acts as a shield against the heat transfer. This point is fundamental because it demonstrates that, with an enhanced thermal conductivity, the PCM can be completely (and more rapidly) melted, even using lower temperatures, finally obtaining faster and energy saving charging processes.

3.3.4 *Conclusions*

The experimental campaign has been conducted with the aim to investigate how much the presence of a copper metal foam with high porosity (95%) and 20 PPI influences the thermal performances of a commercial paraffin PCM during a solid-liquid phase change process. The presence of the metal foam guarantees an enhancement of the heat conduction within the medium, compensating the low thermal conductivity of the pure RT35 PCM ($\lambda_{\text{SL}} = 0.2\ W/m\ K$ both for liquid and solid phase).

First of all, it has been demonstrated that during the charging/discharging phase the melting front remains planar and horizontal due to a uniform temperature field along both the directions x and y. Monitoring the temperature evolution over time and along the central axis of the case, results show how a faster complete melting can be reached with a metal-foam-loaded PCM with respect to a pure one. In particular, in the experiments discussed in Section 3.3.3 the copper-foam-loaded PCM melted in 16 h instead of 23.6 h, with a time reduction by 32.5%. The copper foam is responsible for a more uniform temperature along the vertical direction z which testifies a reduced thermal resistance of the metal-foam-loaded PCM layers. A strong reduction of the maximum temperature needed to melt the whole PCM volume is evidenced with the presence of the metal foam (44 $°C$ instead of 66 $°C$), maintaining the imposed heat flux at the top of the case as a constant ($P = 3.5\ W/m^2$).

The experimental results presented in this chapter highlight that, using metal foams to load PCM-based LTESSs, it is possible to obtain a more uniform heating of the PCM volume, faster charging and discharging processes with lower working temperatures and the consequent possibility to save energy. Last but not least, the reported experimental results can be exploited as a benchmark for the numerical models used to analyze the thermal behaviour of metal-foam-loaded PCMs. The absence of convective motions linked to the position of the heater makes the case study easy to be numerically modeled [163]: for this reason, these tests represent a useful starting point for a critical analysis about the effective properties of the metal foams and, in general, to achieve a deeper knowledge regarding these materials.

3.4 PCM-BASED BTMS

Among the technologies under investigation, one of the most promising solutions to obtain an optimised BTMS is the one which relies on the use of PCMs, exploiting their ability to act as a thermal storage systems [161, 164]. Besides the widely used air-based and liquid-based cooling strategies, which take advantage of being designed on well-known technologies, PCM-based strategies have a great potential for improvements if exploited both alone or in combination with other BTMSs like heat pipes and TEC systems [165]. In this context, immersive solutions provide a considerably higher thermal capacity if compared with other more ordinary solutions [110].

Many recent studies focus their attention on the PCM-based thermal management for LIBs: several researches investigate about the role of fillers like metal foams, fibers or graphite immersed into the so called loaded PCMs [166, 167]. For instance, considering the field of BTMSs, Samimi et al. studied innovative carbon-fiber-loaded PCMs [146] to increase their thermal conductivity and, consequently, to improve the temperature distribution inside the battery pack. For their experiments the researchers compared different cooling media (air, pure PCM, carbon-fibre-loaded PCM) during the discharge of a LIB: it resulted that air was the worst media with which the highest cell temperatures were reached; the situation improved using pure PCM and the best temperature results were obtained with carbon-fibre-loaded PCMs. Further, it turned out that the higher the percentage of carbon fibre loading was, the lower the resulting cell temperature became.

In general, after loading the PCMs with the proper materials, consistent performance developments can be observed both on the maximum temperature of the cells (T_{max}) and on a better temperature uniformity among them [168]. Accurate decisions in terms of thickness and melting temperature of the PCMs need the proper consideration as these two parameters have a significant impact on the thermal behaviour of the system [169, 170, 132, 171]. Despite the simplicity of mixing two components obtaining a more thermally conductive PCM filled with metal foams, the confirmation of their benefits needs the proper experimental validation [172, 173, 156] as showed in Section 3.3. Metal-foam-loaded PCMs are expected to merge the benefits of the high latent thermal capacity of the PCMs with the good thermal conductivity of the metal foams, improving the performances of the BTMSs.

In the following sections several laboratory experiments are presented, all involving LIB cooling methods. After showing the performances of a forced-air-based BTMS, the work goes ahead dealing with a comparison between two different kinds of BTMSs: a pure PCM-based system and a metal-foam-loaded-based one, both without insulation. Then, the whole experimental BTMS has been insulated to get closer to a more realistic case where the BP is usually enclosed into a safety boxe. Several other tests have been carried on with this new experimental setup and discussed in this thesis. These tests deal with different kinds of BP thermal management such as the use of pure PCM, metal-foam-loaded PCM, pure PCM or metal-foam-loaded PCM coupled with a liquid cooling system.

The PCM chosen for the experimental campaign has been the same used for all the experiments discussed in the previous sections: the commercial paraffin RT35, made by *Rubitherm* [159]. Besides its compatibility with both plastic and metallic containers, the high stability and the low toxicity and flammability degree [161], the melting of this precise PCM is exactly in the optimal working temperature interval of the LIBs. The main characteristics of the RT35 PCM as well as of the metal foam and all the other materials used in these tests have been summarized in Table 3.1.

3.4.1 *4-cells element: experimental setup*

All the experiments were conducted testing a module which simulates a LIB brick made of four 21700 cylindrical cells which, in turn, formed the 4-cells element (Figure 3.16). This element represents a battery unit that can be combined with other similar ones, resulting in a modular BP arrangement. From a thermodynamic point of view, this module represents a heating source composed of 4 elementary units each of which simulates one Li-ion cell. A single unit was realized with a 40 mm long cylindrical cartridge heater [174], with a diameter $d_{\text{cart}} = 6.5\ mm$, put inside a 70 mm long hollow aluminum cylinder, with a diameter $d_{\text{cell}} = 21\ mm$ (the aluminum cylinders had the same dimensions of the 21700 cylindrical Li-ion cells). The units cartridge-cylinder were in turn put into a PET support the job of which was keeping together all the cells. All the cylindrical holes of this PET support presented an inner surface covered by a 1 mm thick aluminum liner (Figure 3.18 (a)) which better dissipated the heat generated by the cartridges with respect to the PET.

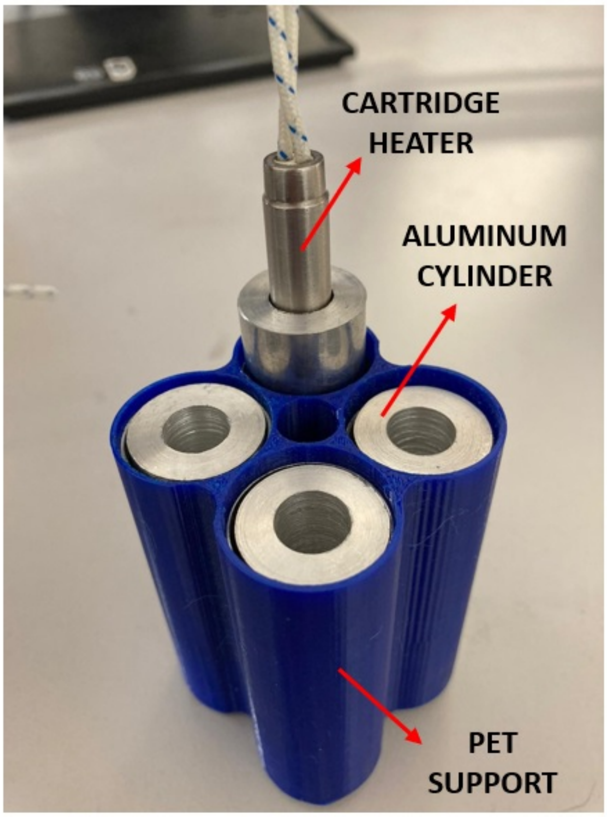

Figure 3.16. *The main parts of the 4-cells element.*

Due to the backlashes between the hollows of the cylinders and the cartridges and between the cylinder outer surfaces and the liners (necessary to slide every single part over each other), it was important to fill the air cavities with a thermal paste, reducing the insulation effect of the air. The selected thermal paste was the *LOCTITE*

SI 100, chosen for its high thermal conductivity ($\lambda_{\text{air}} = 0.026\ W/m\ K < \lambda_{\text{paste}} = 3.4\ W/m\ K$ [175]). Hence, all the cartridge heaters were coated with the thermal paste (Figure 3.17 (a)) so that they were ready to be inserted into the cylinders hollows (Figure 3.17 (b)).

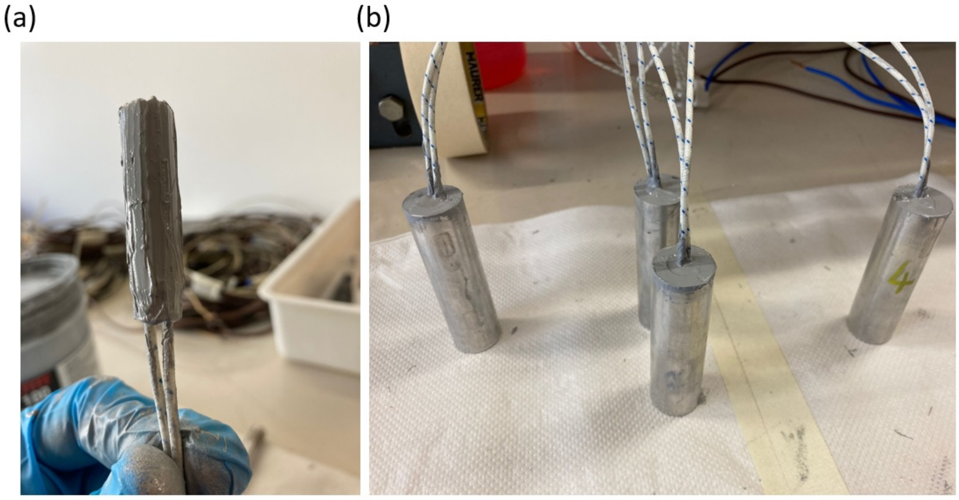

Figure 3.17. *A cartridge heater coated with the thermal paste (a); the four paste-coated cartridge heaters inserted into the hollows of the aluminum cylinders (b).*

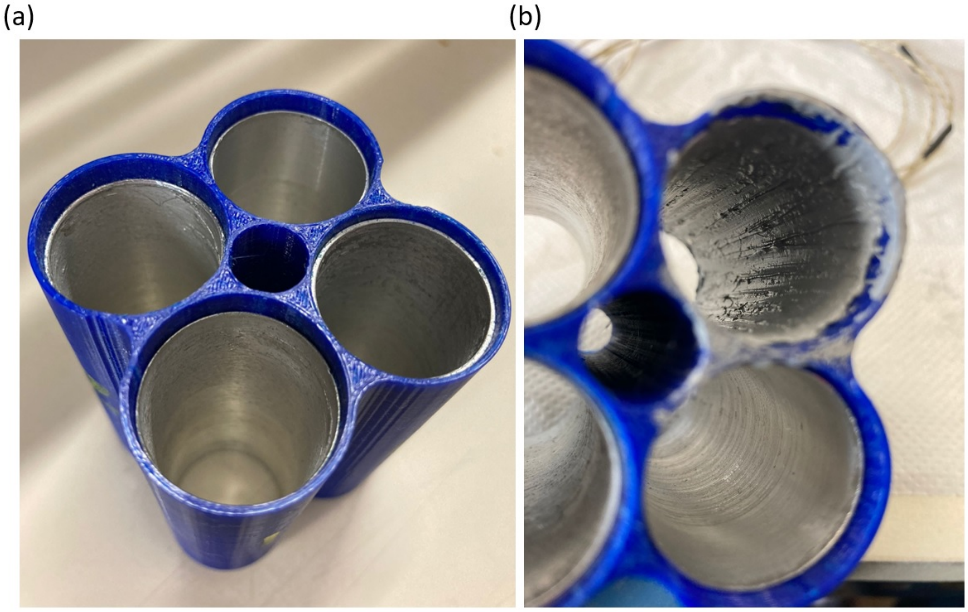

Figure 3.18. *The PET support with the aluminum liners covering the inner surfaces of its holes (a); the inner surface of an aluminum liner coated with the thermal paste (b).*

The same coating process was done for the liner inner surfaces (Figure 3.18) but, before inserting the cylinders into them, the thermocouples were placed. 12 T-type TCs were fixed all along the aluminum cylinders (3 TCs per cylinder), in the thin gap between the cylinders and the liners (Figure 3.19) to monitor the cell temperatures over time: independently from the z-quote, all the TCs were fixed at three precise x-quotes. Considering these positions, it was possible to identify top, middle and bottom thermocouples (TC_{TOP}, TC_{MID}, TC_{BOT}), obtaining four TCs with the x-quote in common for each of these groups. In Figure 3.20 the 4-cells element equipped with all the TCs is shown.

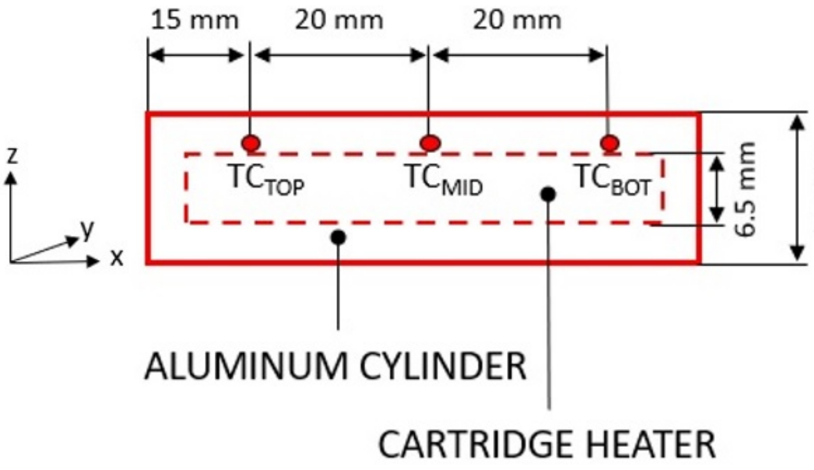

Figure 3.19. *Scheme representing one of the four units which composes the 4-cells element.*

Figure 3.20. *The 4-cells element equipped with 12 T-type TCs.*

The experimental setup showed in Figure 3.9 was used again for this research campaign but some changes and upgrades were done. The power supply was indirectly linked to the cartridge heaters (in order to impose a heat flux generated by Joule effect [161]) as the circuit was equipped with an *Arduino* board put between them. With an electric relay managed by *Arduino* it was possible to remote control the power supply circuit, making the work easier when the longer experiments had to be carried on.

The choice of the power with which supplying the heating source (the 4-cells element) was done on the basis of thermal evaluations and considering that the maximum operating temperature above which a BTMS starts to work is around 40 °C. A voltage tuning was carried out using the power supply of the experimental setup: the cells temperatures were constantly monitored and the voltage was slowly increased or decreased until the cells reached temperature values $2 \div 5$ °C higher than the upper bound of the optimal working range for lithium cells. For a voltage value $V = 34.5\ V$ the cells reached the maximum temperature $T = 45$ °C, so the related voltage value was chosen for the tests. For that voltage value the current delivered by the digital power supply was $i = 0.137\ A$, that is $i_{\text{cell}} = 0.0343\ A$ for each cell. Consequently, the power supplied to the whole 4-cells element was $P = V \cdot i = 4.73\ W$ and the power supplied to each of the cartridge heaters was $P_{\text{cell}} = V \cdot i_{\text{cell}} = 1.18\ W$.

This experimental setup represented the starting point for all the tests: it was a common configuration from which all the experiments started and, proceeding with the research work, the setup was upgraded both in terms of hardware and software (from the first to the last test the *LabVIEW* project was deeply improved and adapted to the acquisition needs).

3.4.2 *Forced ventilation*

Before starting with the tests about the PCM-based BTMSs, a forced ventilation cooling experiment was conducted with the aim of understanding the effectiveness of an ordinary air-based BTMS compared to the performance of an innovative cooling system without insulation.

To proceed with the forced ventilation test series a scaled wind gallery was built: an 85 mm^2 section duct was put in front of a fan which, in turn, was linked to the power supply (the set voltage was $V = 12\ V$) and blew air into the gallery. As it is possible to see in Figure 3.21, the 4-cells module was horizontally placed in correspondence of the longitudinal axis of the duct and it was hung up in this position (so that the PET support could not touch the duct inner surfaces), opposite to the fan. In this configuration there were two levels of cells: a lower level with cells number 1 and 4, an upper level with cells number 2 and cell 3. The air flow blown by the fan was $\dot{m}_{\text{air}} = 0.0236\ m^3/s = 84.96\ m^3/h$ and it was measured by a Pitot probe. In Figure 3.22 the final experimental setup is shown.

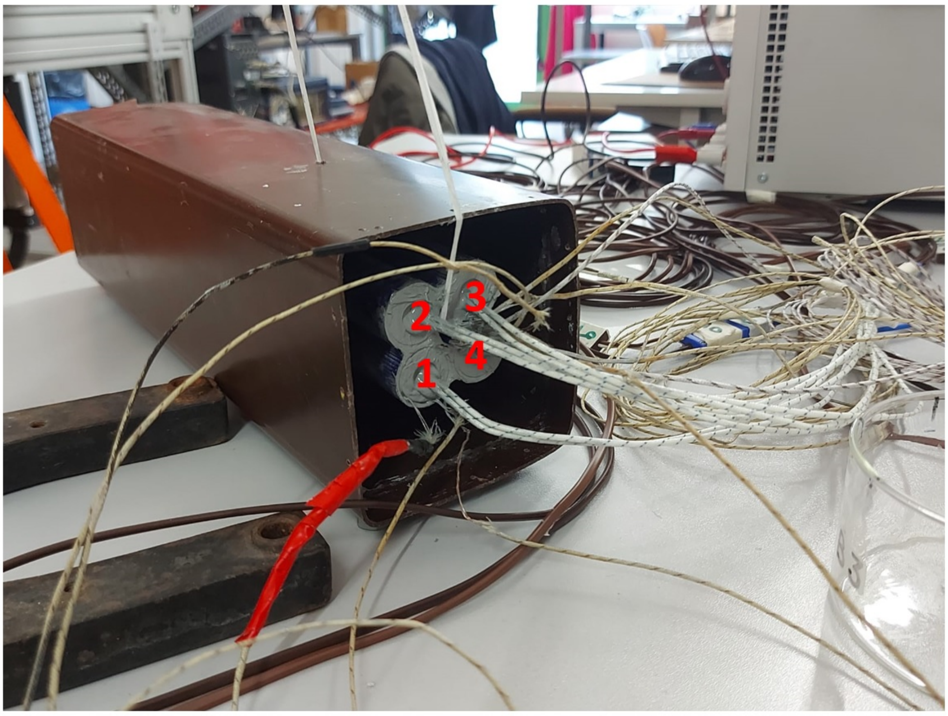

Figure 3.21. *The 4-cells module hung up in correspondence of the duct longitudinal axis: cells number 1 and 4 are the lower ones, cells number 2 and 3 are the upper ones.*

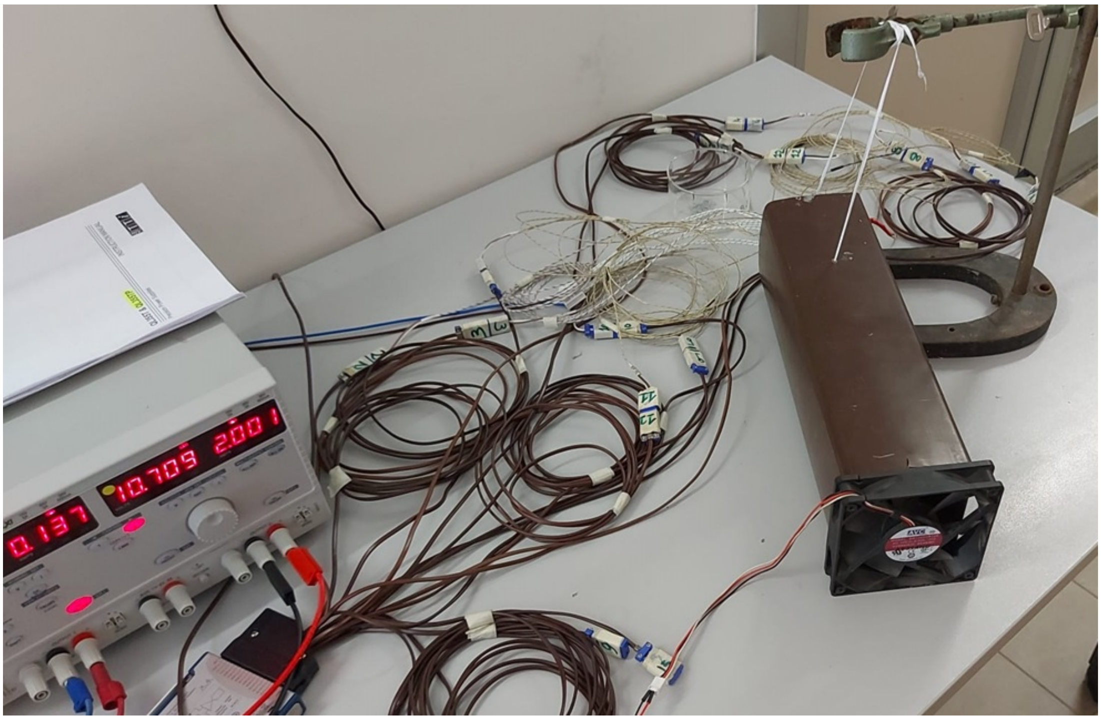

Figure 3.22. *The final setup for the forced ventilation tests.*

3.4.2.1 *Results*

The cooling process started as the 4-cells element reached the maximum temperature possible for the fixed power value (around $T = 45$ °C as previously explained in Section 3.4.1) and lasted until a temperature balance was achieved. The test was repeated for three times to demonstrate the repeatability of the experiment. The air temperature was constant during all the acquisitions with a value $T_{\mathrm{AIR}} = 22.5$ °C. Firstly, as it is possible to see in Figure 3.23, Figure 3.24, Figure 3.25 and Figure 3.26, the cell temperature was homogeneous for all the cells during the whole cooling process of Test 0.1 (as well as during Test 0.2 and Test 0.3). This means that the cell temperature was not influenced by the position of the TCs along the single cell.

Instead, a temperature difference was evident between the upper and the lower cells and this is highlighted by the left graphs in Figure 3.27, Figure 3.28 and Figure 3.29: for all the x-values fixed along the cells (top, middle, bottom) the temperature trends are not overlapped for all the cells but overlapped in couples. The temperature trend recorded for Cell 1 is always coincident with that of Cell 4 and so do the trends of Cell 2 and Cell 3: this is due to the air convective motions which cause higher temperatures on the higher levels.

In Table 3.5 there are the average temperatures recorded at the beginning and at the end of Test 0.1 for all the cells, calculated as the means of T_{TOP}, T_{MID} and T_{BOT}: the values show that the convective motions influenced the temperature difference more when the cells temperature was higher, that is at the beginning of the cooling process, and this is because at that point the air around the cells was hotter, too.

In the right graphs in Figure 3.27, Figure 3.28 and Figure 3.29 it is possible to see the temperature difference ($\Delta T_{\mathrm{UP\text{-}LOW}}$) trends recorded between the upper and the lower cells at different x-values. An interesting result regards the values of $\Delta T_{\mathrm{UP\text{-}LOW,\,max}}$ visible in these graphs and showed in Table 3.6: the closer the temperature acquisition was made to the duct outlet, the lower was the temperature difference. This happened because the bottom of the cells was closer to a colder environment (the one outside the duct) compared to the top of the cells which was in a hotter environment. Supplementary results related to Test 0.2 and Test 0.3 are reported in Appendix 4.

The overall results of Test 0.1÷0.3 are shown in Figure 3.30, Figure 3.31, Figure 3.32 and Figure 3.33, showing the temperature trends recorded by TC_{MID} (as it was already demonstrated that the x-value does not influence the temperature along the cell) for the single cells. Considering Cell 1, as well as all the other cells, it is evident the repeatability of the experiment. This forced-air cooling system demonstrated that, with the described conditions (no insulation, constant air temperature), it is possible to cool a battery until its proper working temperature.

Table 3.3. *T_{max} reached by the cells at the beginning of Test 0.1÷0.3 with forced ventilation.*

	Unit	Cell 1	Cell 2	Cell 3	Cell 4
$T_{\text{max, Test 0.1}}$	[°C]	44.81	45.71	45.55	44.66
$T_{\text{max, Test 0.2}}$	[°C]	44.83	45.73	42.60	44.72
$T_{\text{max, Test 0.3}}$	[°C]	44.93	45.86	45.66	44.90
$\widetilde{T}_{\text{max}}$	[°C]	44.86	45.77	45.60	44.76

Table 3.4. *T_{min} reached by the cells at the end of Test 0.1÷0.3 with forced ventilation.*

	Unit	Cell 1	Cell 2	Cell 3	Cell 4
$T_{\text{min, Test 0.1}}$	[°C]	29.35	29.69	29.46	29.22
$T_{\text{min, Test 0.2}}$	[°C]	29.29	29.64	29.42	29.17
$T_{\text{min, Test 0.3}}$	[°C]	29.25	29.53	29.37	29.06
$\widetilde{T}_{\text{min}}$	[°C]	29.30	29.62	29.42	29.15

Table 3.5. *Test 0.1: cell average temperatures at the beginning and at the end of the cooling process.*

	Unit	Cell 1	Cell 2	Cell 3	Cell 4
$\widetilde{T}_0$	[°C]	44.78	45.63	45.64	44.60
$\widetilde{T}_{\text{end}}$	[°C]	29.35	29.66	29.52	29.20

Table 3.6. *$\Delta T_{\text{UP-LOW, max}}$ recorded at a precise x-value along the cells for all the tests and $\widetilde{\Delta T}_{\text{UP-LOW, max}}$*

	Unit	TOP	MID	BOT
$\Delta T_{\text{UP-LOW, max, 1}}$	[K]	1.687	1.423	1.270
$\Delta T_{\text{UP-LOW, max, 2}}$	[K]	1.662	1.402	1.288
$\Delta T_{\text{UP-LOW, max, 3}}$	[K]	1.688	1.375	1.320
$\widetilde{\Delta T}_{\text{UP-LOW, max}}$	[K]	1.679	1.400	1.292

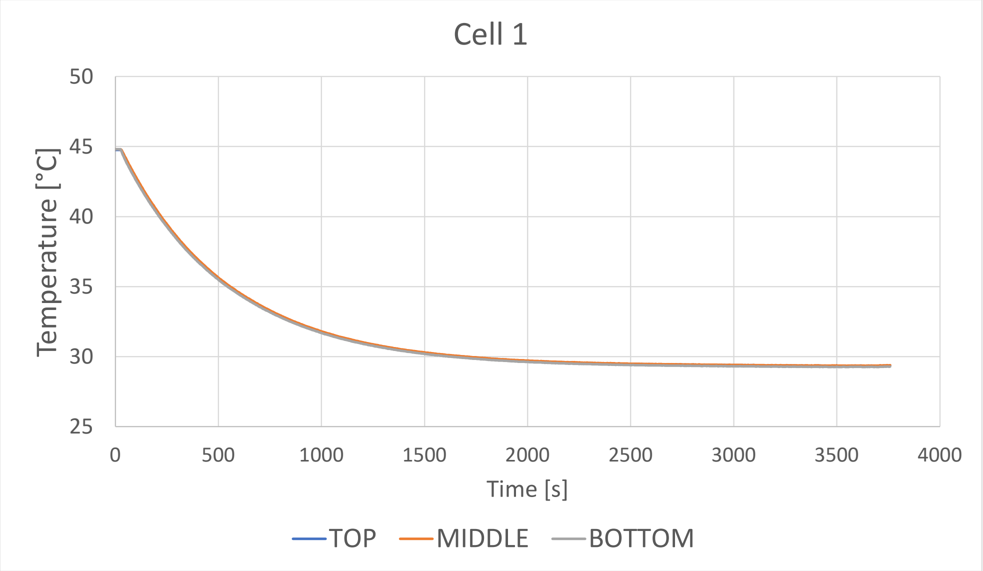

Figure 3.23. *Forced ventilation, Test 0.1: temperature trends recorded by* TC_{TOP}, TC_{MID} *and* TC_{BOT} *along Cell 1.*

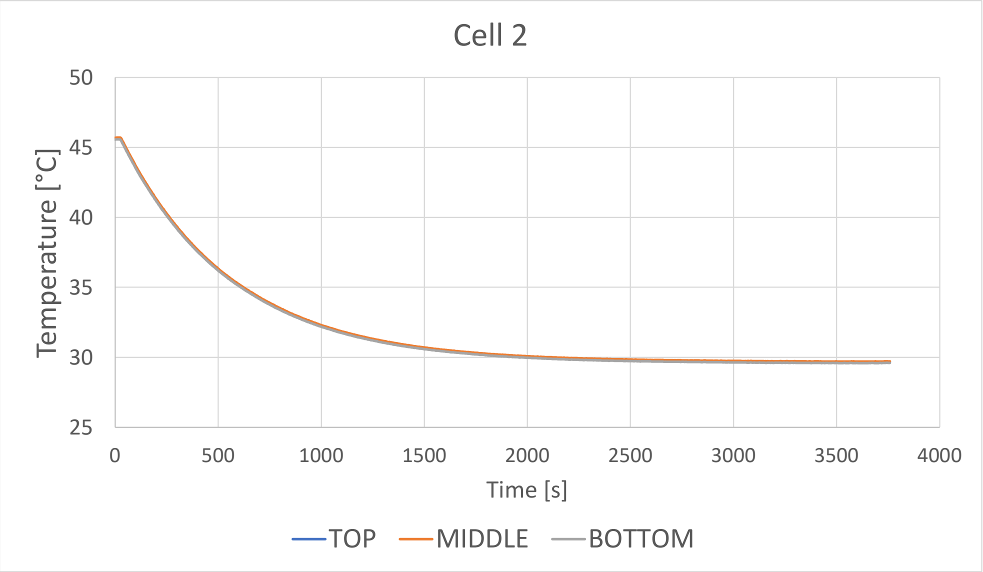

Figure 3.24. *Forced ventilation, Test 0.1: temperature trends recorded by* TC_{TOP}, TC_{MID} *and* TC_{BOT} *along Cell 2.*

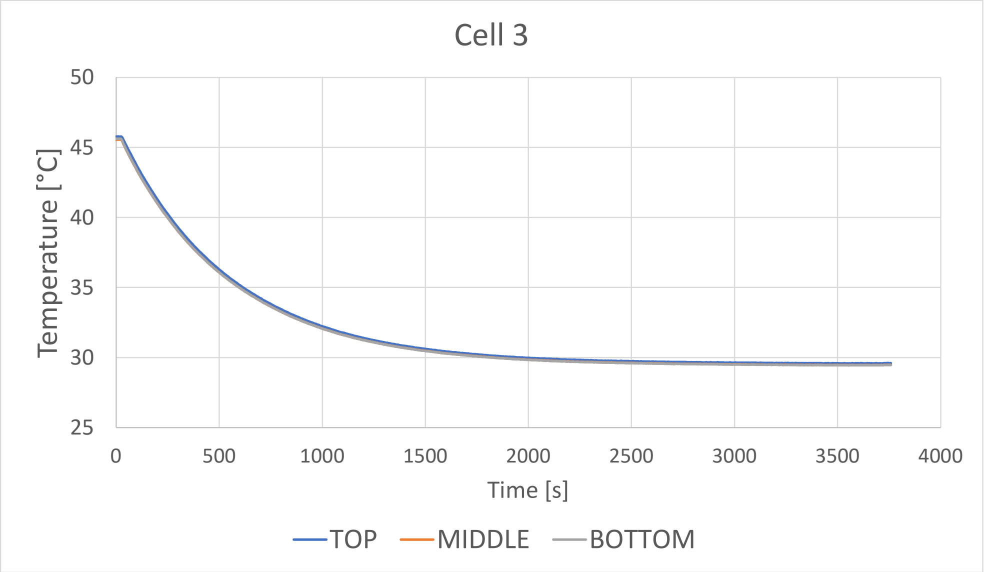

Figure 3.25. *Forced ventilation, Test 0.1: temperature trends recorded by* TC_{TOP}, TC_{MID} *and* TC_{BOT} *along Cell 3.*

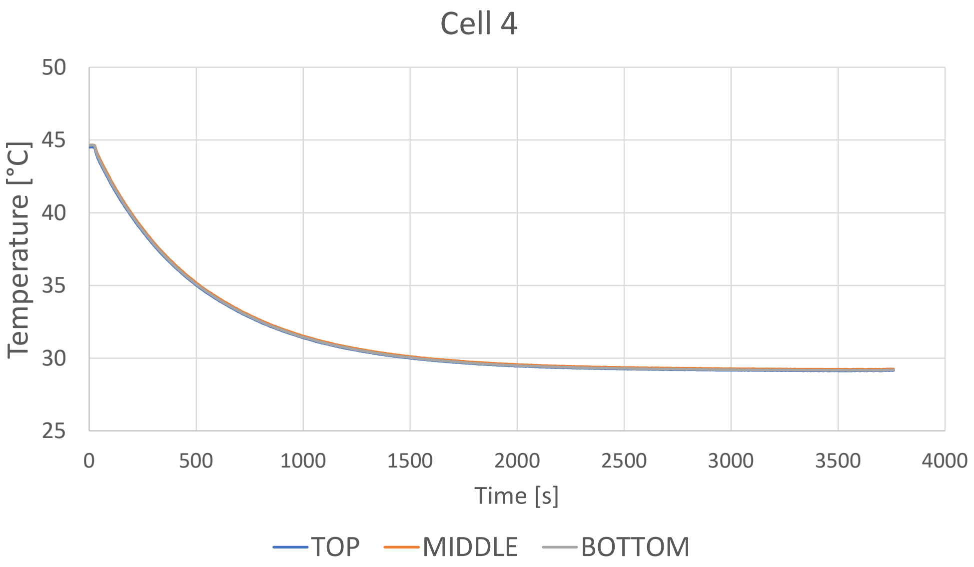

Figure 3.26. *Forced ventilation, Test 0.1: temperature trends recorded by* TC_{TOP}, TC_{MID} *and* TC_{BOT} *along Cell 4.*

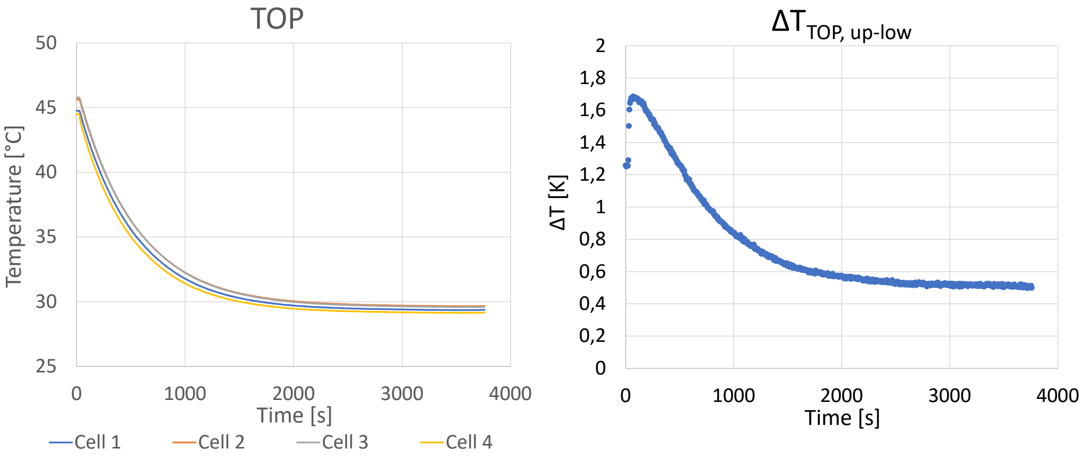

Figure 3.27. *Forced ventilation, Test 0.1: temperature trends recorded on the top of all the cells (left) and* ΔT *trend between the top of the upper and the lower cells (right).*

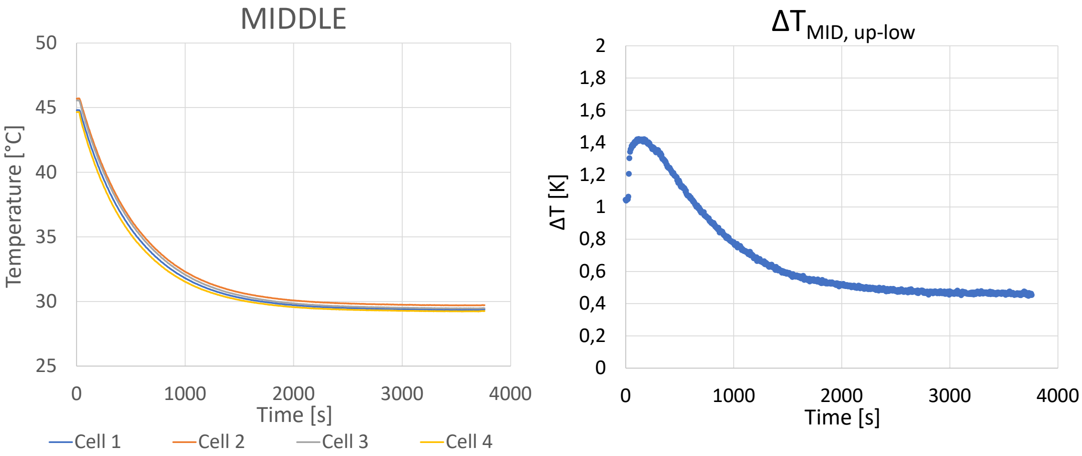

Figure 3.28. *Forced ventilation, Test 0.1: temperature trends recorded in the middle of all the cells (left) and* ΔT *trend between the middle of the upper and the lower cells (right).*

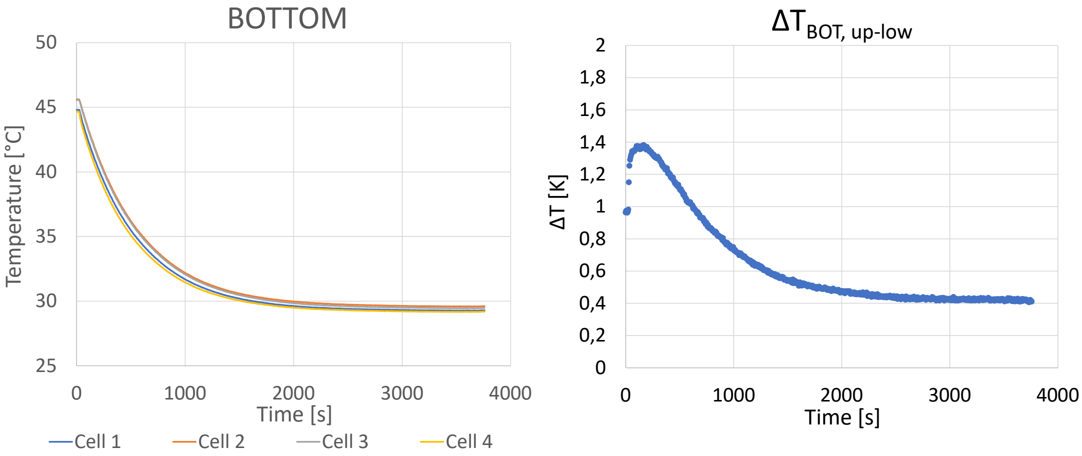

Figure 3.29. *Forced ventilation, Test 0.1: temperature trends recorded on the bottom of all the cells (left) and* ΔT *trend between the bottom of the upper and the lower cells (right).*

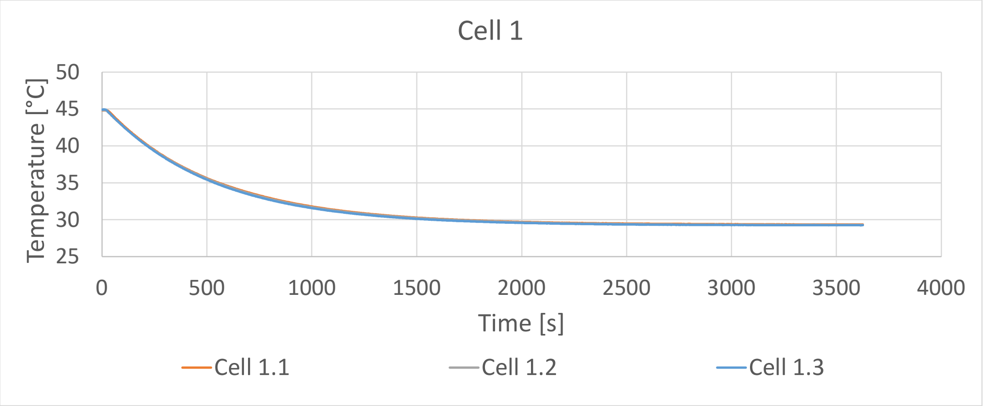

Figure 3.30. *Forced ventilation, Test 0.1÷0.3: temperature trends recorded by* TC_{MID} *on Cell 1.*

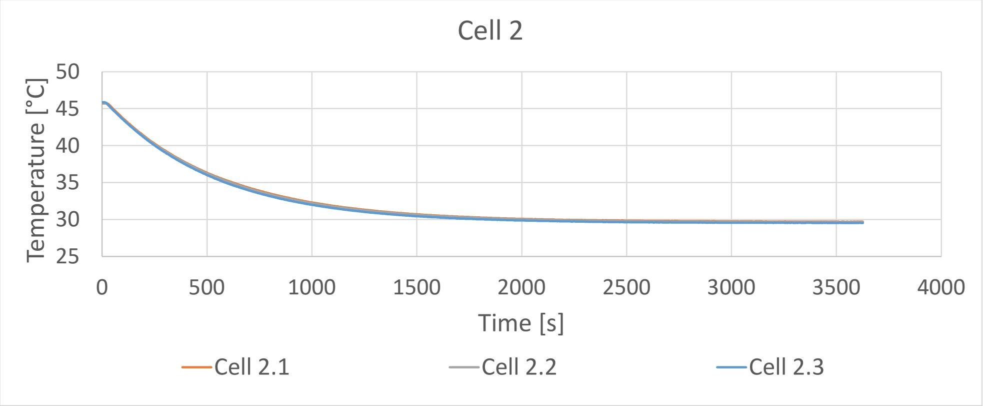

Figure 3.31. *Forced ventilation, Test 0.1÷0.3: temperature trends recorded by* TC_{MID} *on Cell 2.*

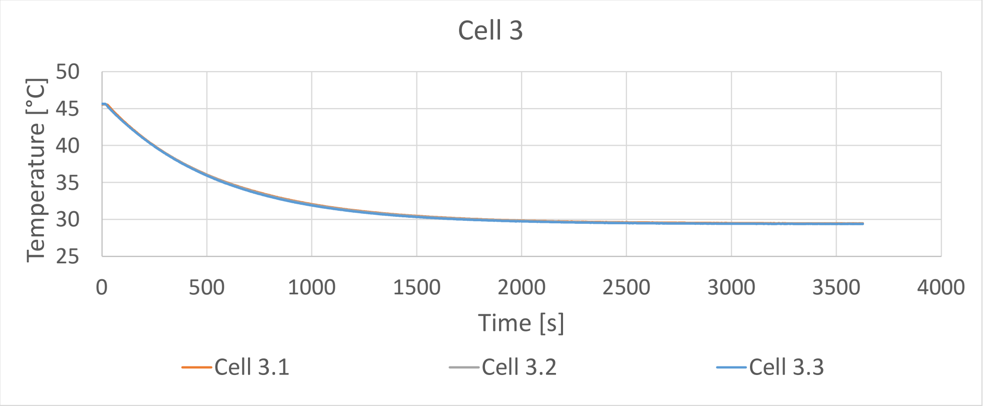

Figure 3.32. *Forced ventilation, Test 0.1÷0.3: temperature trends recorded by* TC_{MID} *on Cell 3.*

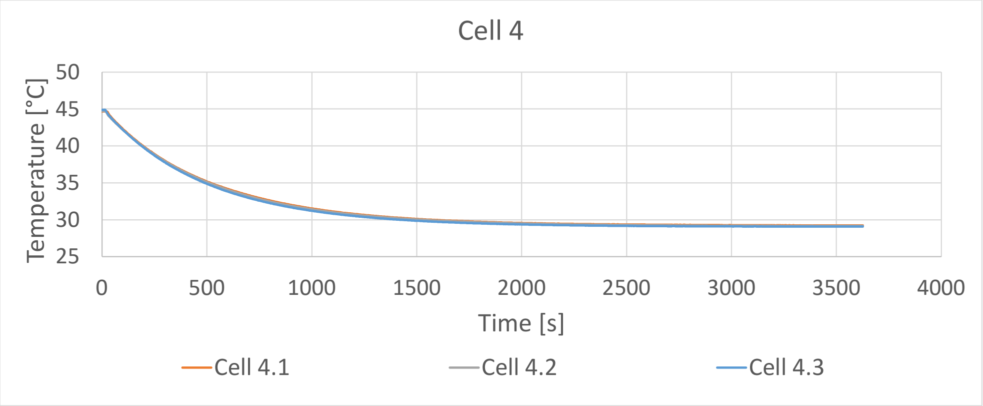

Figure 3.33. *Forced ventilation, Test 0.1÷0.3: temperature trends recorded by* TC_{MID} *on Cell 4.*

3.4.3 *Pure PCM*

To start with the tests regarding the PCM-based BMTSs, the experimental setup was properly modified. A new case with 5 mm thick polycarbonate walls and a final volume $V_{\text{case}} = 8.28 \cdot 10^5\ mm^3$ was built (as described in Section 3.3.2.1), milling polycarbonate sheets and gluing the resulting walls with a specific acrylic glue for polycarbonate (Figure 3.34). The case was filled with pure PCM and it was used as PCM container for all the experiments. The 4-cells battery module was immersed into the PCM and put horizontally into the polycarbonate case (Figure 3.35), so that the TCs configuration with upper and bottom levels (already seen in Section 3.4.2) was kept the same for all the experiments about the PCM-based BTMSs. Besides the 12 T-type TCs placed along the cells (as shown in Figure 3.19) three other TCs were used to monitor the air temperature (T_{AIR}) and the PCM temperature above and under the 4-cells module ($T_{\text{PCM, UP}}$ and $T_{\text{PCM, DOWN}}$, Figure 3.36): these TCs were named TC_{AIR}, $TC_{\text{PCM, UP}}$ and $TC_{\text{PCM, DOWN}}$, respectively.

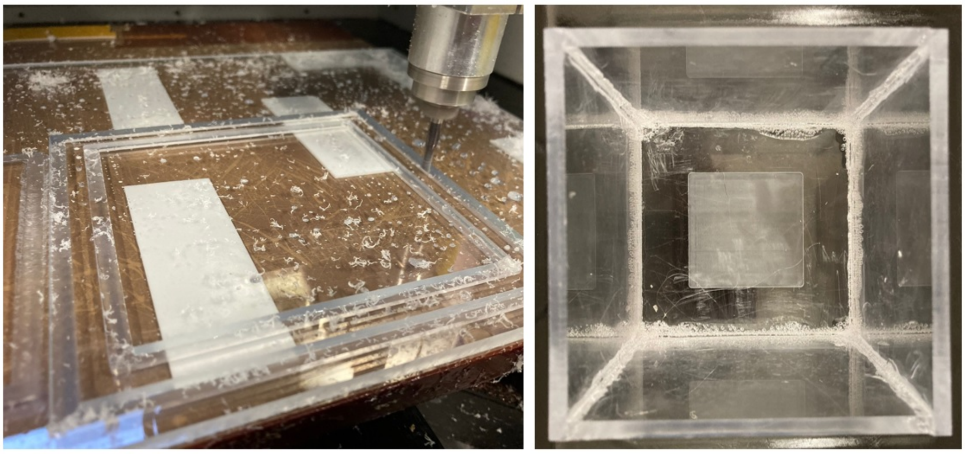

Figure 3.34. *The milling process (left) to obtain the polycarbonate walls, gluing them to realize the case (right).*

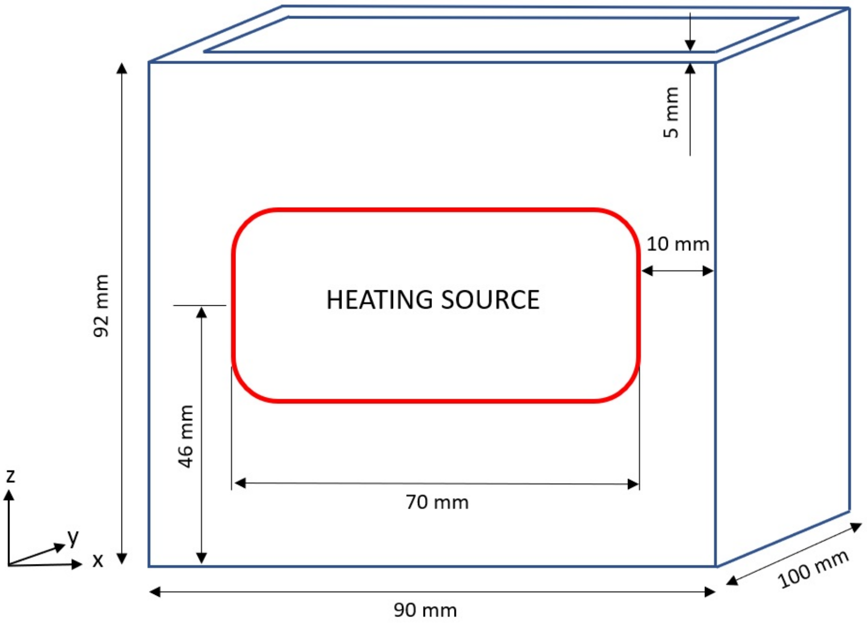

Figure 3.35. *Scheme of the polycarbonate case with the heating source inside.*

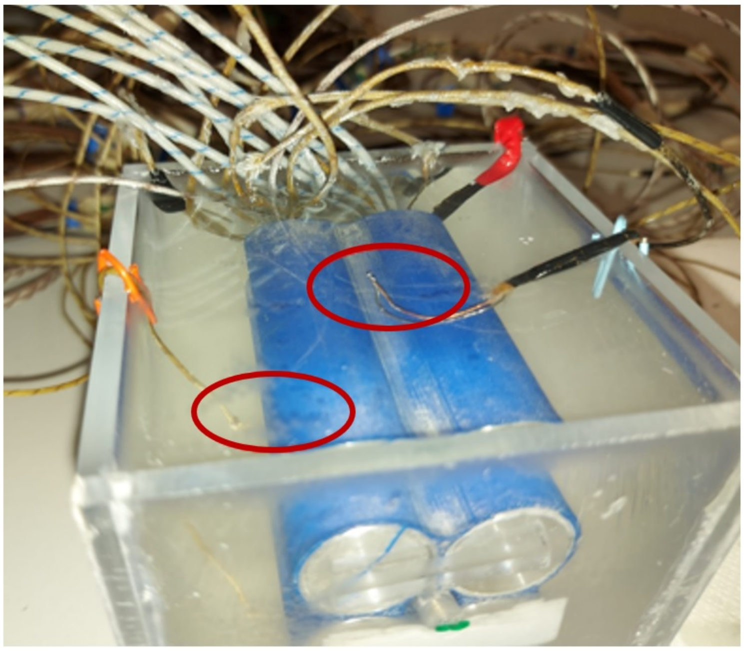

Figure 3.36. *The polycarbonate case filled with pure PCM:* $TC_{PCM,\ UP}$ *and* $TC_{PCM,\ DOWN}$ *put above and under the 4-cells module.*

One series of experiments was carried out to investigate the performance of a pure PCM-based BMTS, later comparing it to the effectiveness of a copper-foam-loaded-based BTMS. Finally, both of these two innovative cooling systems were compared with the forced-air BTMS, evaluating if without an insulation box it is necessary to use a cutting-edge technology anyway or an ordinary cooling system is enough.

The tests concerned charging cycles: at the beginning the power supply was turned on, the cells started to be heated (as in a real Li-ion cells charging cycle) thanks to the heat flux generated by Joule effect and the temperatures were recorded. The power supply was turned off, the system was left free to cool down to the initial temperature and, once that temperature was reached, another charging test started. For the first series of tests (Test 1.1÷1.6) described here below the filler of the polycarbonate case was just pure PCM.

3.4.3.1 *Results*

Six experimental tests (Test 1.1÷1.6) simulating charging cycles were carried on, with a constant environmental temperature $T_{\text{AIR}} = 23.5\ °C$ and a power supplied to the 4-cells element $P = 4.73\ W$ ($P_{\text{cell}} = 1.18\ W$ for each cell).

Since Test 1.1 a $\Delta T_{\text{UP-LOW}}$ was measured (between Cell 2 and Cell 3 and between Cell 1 and Cell 4). The left graphs in Figure 3.41, Figure 3.42 and Figure 3.43 show the results of Test 1.1 with pure PCM: the blue and the orange curves show the temperatures of the upper cells, the grey and the yellow curves show the temperatures of the lower cells. The temperature difference is constantly present, its value is independent from the x-quote and increases over time: in the right graphs in Figure 3.41, Figure 3.42 and Figure 3.43 the trends of the temperature differences during Test 1.1 at different x-values (top, middle and bottom areas of the cells) are shown.

This ΔT was visible during all the six tests with pure PCM. Considering Test 1.1÷1.6, the averages of the maximum temperature differences recorded by the top, the middle and the bottom TCs were $\widetilde{\Delta T}_{\text{TOP, max}} = 0.91\ K$, $\widetilde{\Delta T}_{\text{MID, max}} = 0.90\ K$, $\widetilde{\Delta T}_{\text{BOT, max}} = 0.87\ K$. In Figure 3.37, Figure 3.38, Figure 3.39 and Figure 3.40 the blue, the orange and grey curves (representing the temperature trends of the top, the middle and the bottom areas of the cells during Test 1.1) are overlapped, meaning that the temperature was homogeneous all along each unit of the 4-cells element. As there were no important differences among the temperatures recorded by the three TCs placed on each single cell, from now on only the values recorded by TC_{MID} will be considered. Supplementary results related to Test 1.2÷1.6 are reported in Appendix 4.

In Figure 3.44, Figure 3.45, Figure 3.46 and Figure 3.47 the overall results of Test 1.1÷1.6 (all made with pure PCM) are presented: the cells temperatures considered are those recorded by each of the TC_{MID} in contact with all the cells and there are also shown the temperature trends recorded by $TC_{\text{PCM, UP}}$ and $TC_{\text{PCM, DOWN}}$ which were immersed into the PCM, put above and under the 4-cells element. As seen in Figure 3.41, Figure 3.42 and Figure 3.43, for each of these six tests there is a ΔT between the upper (Figure 3.45 and Figure 3.46) and lower cells (Figure 3.44 and Figure 3.47).

For $t = 12000 \div 16000\ s$, $T_{\text{PCM, UP}}$ has not a constant trend and shows sudden temperature dips and rises: this is due to convective motions which developed in the upper PCM volume and, in turn, this could be a cause of the $\Delta T_{\text{UP-LOW}}$. As a matter of facts, in the time interval when the PCM above the 4-cells element was involved into the convection process, the cells temperature trends do not exactly overlap. However, the more the time passes, the more they tend to a common temperature value (getting very close at $t = 40000$ s). By comparing the maximum values of $\Delta T_{\text{UP-LOW}}$ for all the 4 cells (Table 3.7), it is possible to see that at $t = 15000$ s, when the effect of the convection was the highest, and at $t = 40000$ s, when the PCM previously involved into the convection process reached the equilibrium, it seems that the convection plays a key role in cells temperature. To verify this, it was necessary to damp the convective motions and re-analyse the temperature results (see Section 3.4.4.1).

Table 3.7. *Maximum temperature difference at $t = 15000$ s and $t = 40000$ s for a fixed cell, obtained in the Test 1.1÷1.6 with pure PCM.*

Cell	Unit	$\Delta T_{15000\text{ s}}$	$\Delta T_{40000\text{ s}}$
1	[K]	1.11	0.56
2	[K]	1.04	0.47
3	[K]	1.08	0.46
4	[K]	1.30	0.54

The maximum temperatures reached by the cells during Test 1.1÷1.6 and their averages ($\widetilde{T}_{\text{max}}$) are summarized in Table 3.8. Although all these temperatures are in the proper working range for Li-ion cells (which is about 15 ÷ 40 °C [69]), lower values and a more homogeneous distribution in the areas close to the cells would be appreciable, avoiding those temperature fluctuations typical of the convective processes. In a typical automotive BP, with a high number of modules one close each other and packed in a safety box, such fluctuations could lead to runaway problems.

Table 3.8. *Maximum temperatures reached by the cells during Test 1.1÷1.6 with pure PCM.*

	Unit	Cell 1	Cell 2	Cell 3	Cell 4
$T_{\text{max, Test 1.1}}$	[°C]	36.52	36.40	36.16	36.48
$T_{\text{max, Test 1.2}}$	[°C]	36.83	37.68	37.43	36.81
$T_{\text{max, Test 1.3}}$	[°C]	36.88	37.68	37.43	36.87
$T_{\text{max, Test 1.4}}$	[°C]	37.14	37.90	37.64	37.12
$T_{\text{max, Test 1.5}}$	[°C]	36.51	37.36	37.11	36.51
$T_{\text{max, Test 1.6}}$	[°C]	36.53	37.41	37.17	36.50
$\widetilde{T}_{\text{max}}$	[°C]	36.73	37.57	37.32	36.71

In conclusion, a temperature difference between the lower and the upper cells was always observed. This $\Delta T_{\text{UP-LOW}}$ presented wide fluctuations, in particular in the first 16000 s when convective motions developed (in the PCM area above the 4-cells element), influencing the heat fluxes and so the temperatures values. The maximum temperature averages reached by the cells during Test 1.1÷1.6 were $\widetilde{T}_{\text{max, UP, pure}} = 37.57$ °C for the upper cells and $\widetilde{T}_{\text{max, LOW, pure}} = 36.73$ °C for the lower ones.

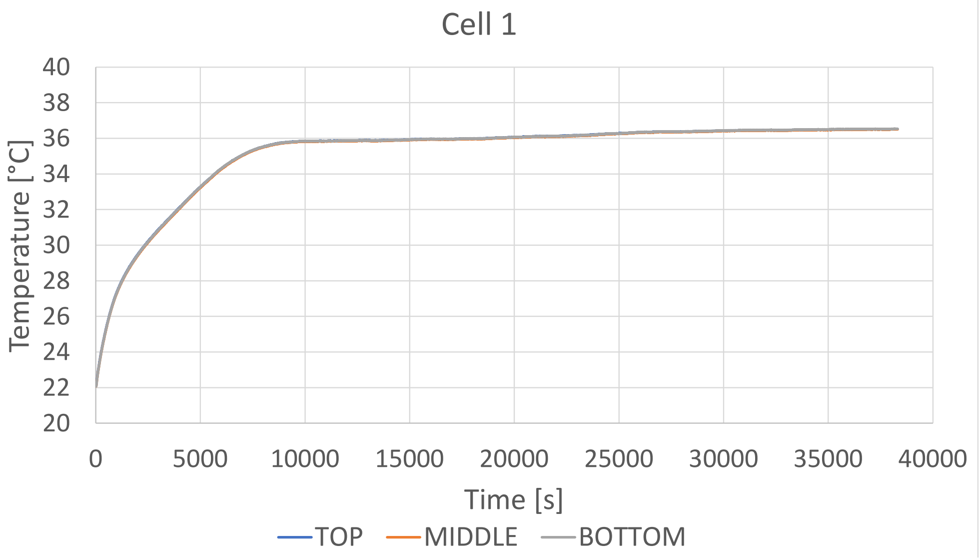

Figure 3.37. *Pure PCM, Test 1.1: temperature trends recorded by TC_{TOP}, TC_{MID} and TC_{BOT} along Cell 1.*

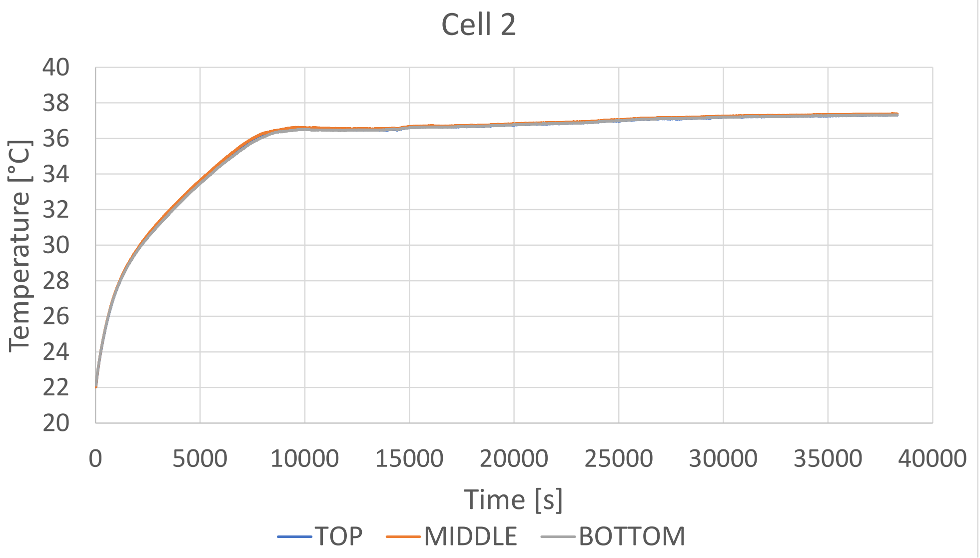

Figure 3.38. *Pure PCM, Test 1.1: temperature trends recorded by TC_{TOP}, TC_{MID} and TC_{BOT} along Cell 2.*

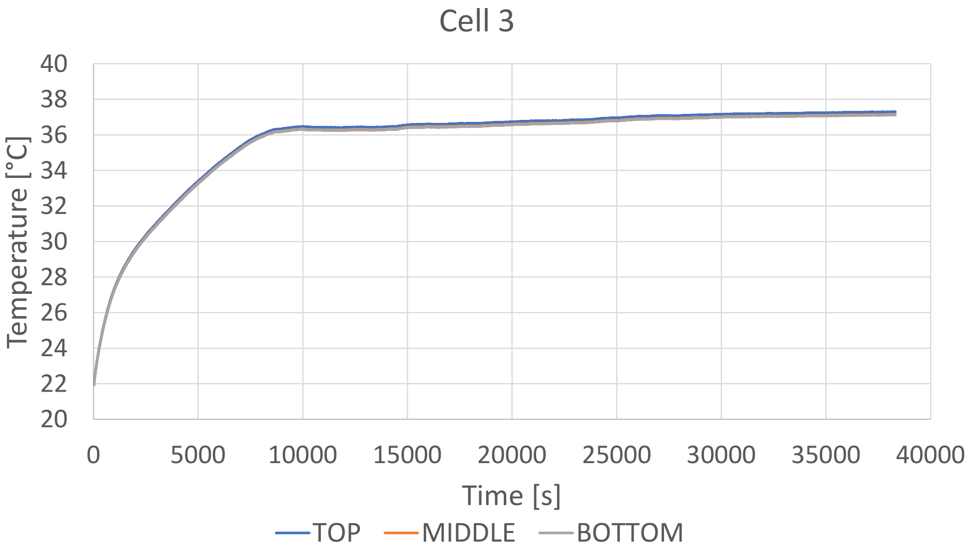

Figure 3.39. *Pure PCM, Test 1.1: temperature trends recorded by* TC_{TOP}, TC_{MID} *and* TC_{BOT} *along Cell 3.*

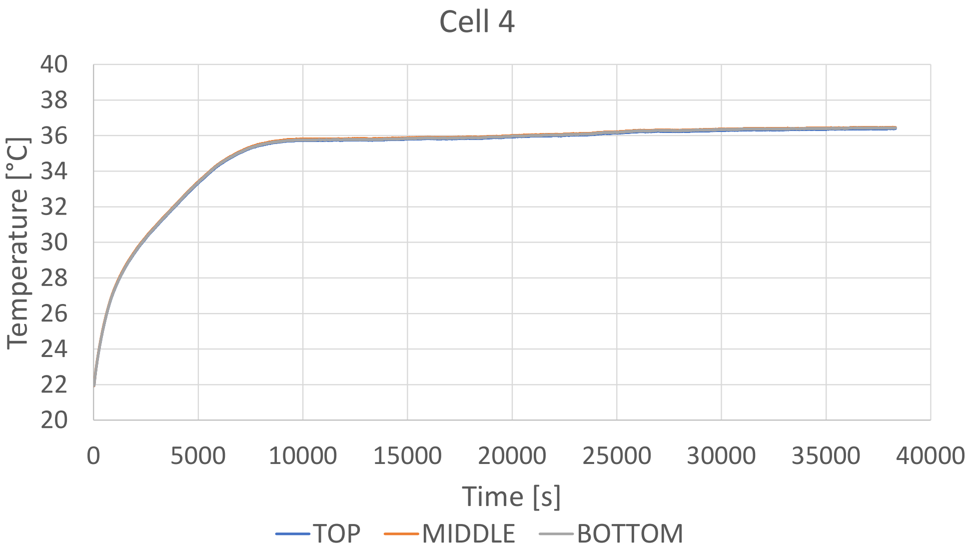

Figure 3.40. *Pure PCM, Test 1.1: temperature trends recorded by* TC_{TOP}, TC_{MID} *and* TC_{BOT} *along Cell 4.*

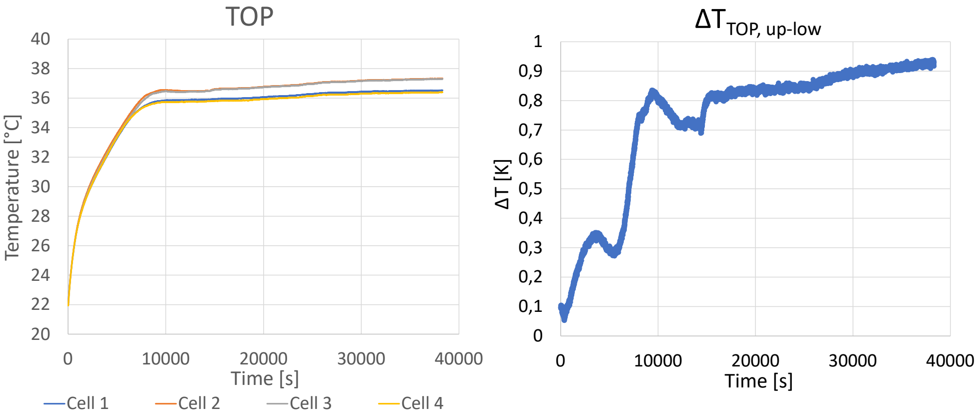

Figure 3.41. *Pure PCM, Test 1.1: temperature trends recorded on the top of all the cells (left) and* ΔT *trend between the top of the upper and the lower cells (right).*

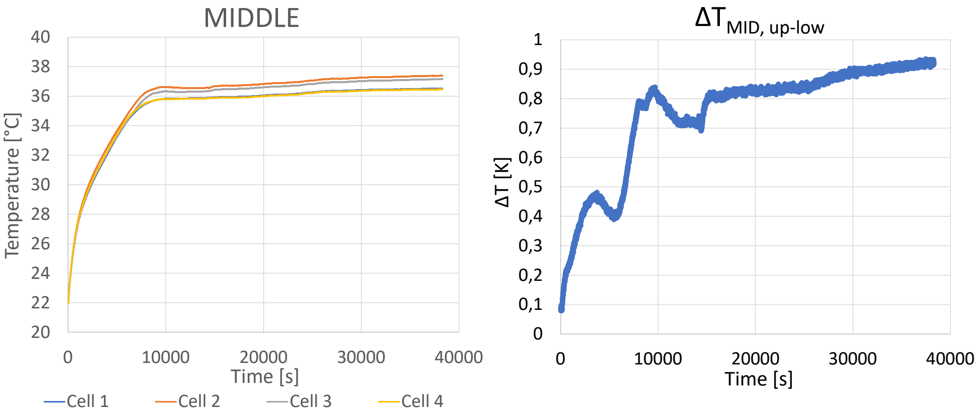

Figure 3.42. *Pure PCM, Test 1.1: temperature trends recorded in the middle of all the cells (left) and* ΔT *trend between the middle of the upper and the lower cells (right).*

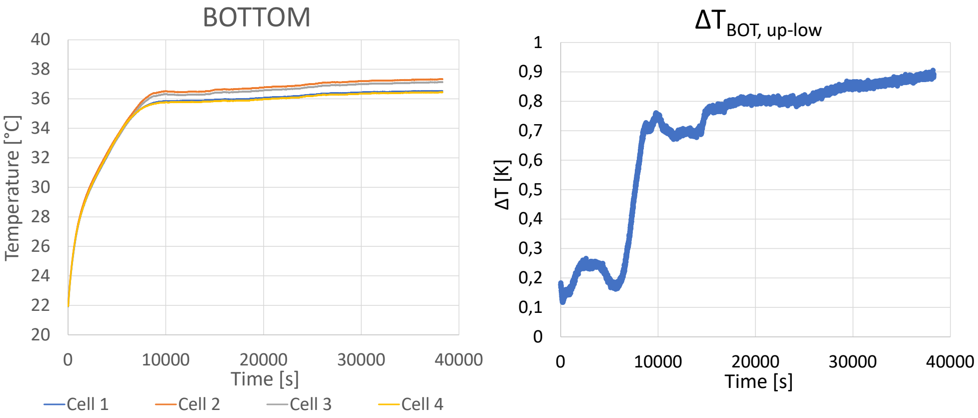

Figure 3.43. *Pure PCM, Test 1.1: temperature trends recorded on the bottom of all the cells (left) and* ΔT *trend between the bottom of the upper and the lower cells (right).*

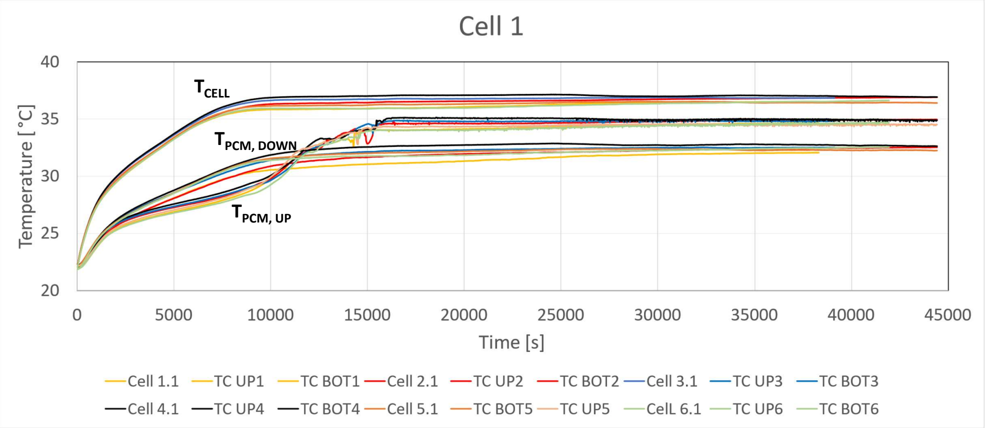

Figure 3.44. *Pure PCM, Test 1.1÷1.6: temperature trends recorded by* TC_{MID} *on Cell 1.*

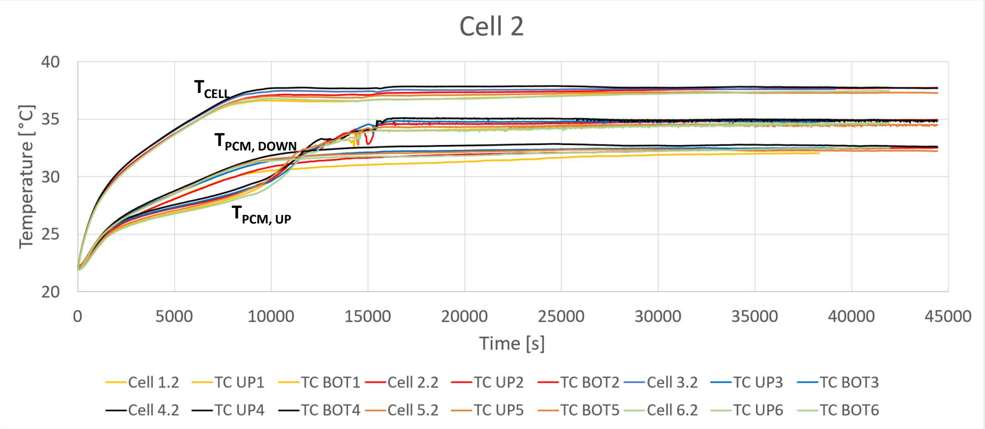

Figure 3.45. *Pure PCM, Test 1.1÷1.6: temperature trends recorded by* TC_{MID} *on Cell 2.*

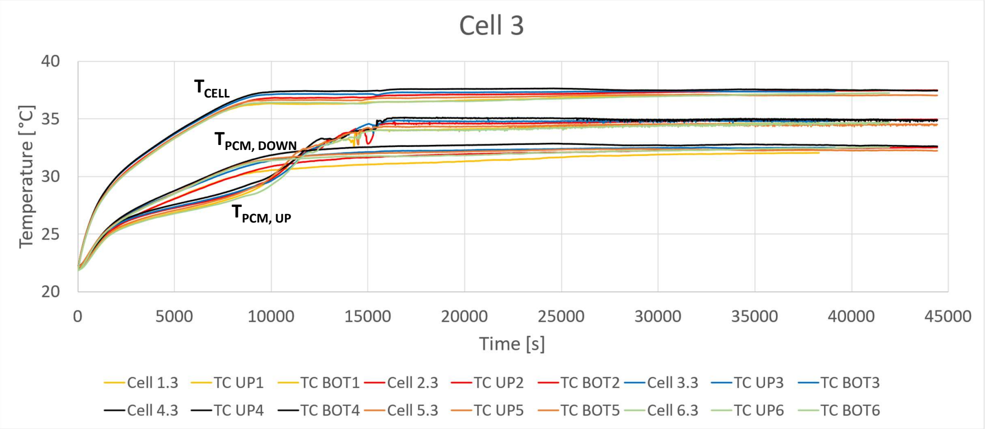

Figure 3.46. *Pure PCM, Test 1.1÷1.6: temperature trends recorded by* TC_{MID} *on Cell 3.*

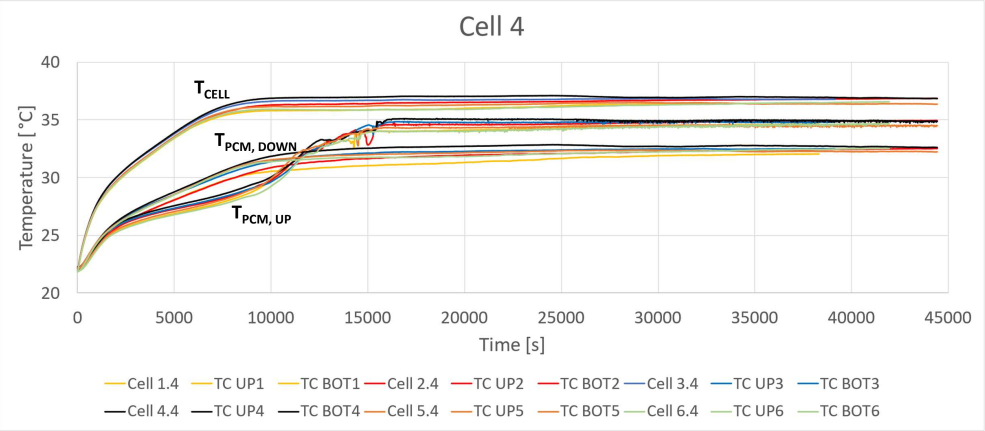

Figure 3.47. *Pure PCM, Test 1.1÷1.6: temperature trends recorded by* TC_{MID} *on Cell 4.*

3.4.4 *Copper-foam-loaded PCM*

As an inhomogeneous temperature distribution is one of the major causes for non-uniform and accelerated degradation both at a cell and at a battery pack level [176], for the second series of tests the PCM was loaded with a 95% porous copper foam (Table 3.1) to avoid the development of the convective motions and improve the temperature homogeneity [161] around the 4-cells element. The tests with the copper foam were carried on with the experimental rig used with the pure PCM tests: considering the polycarbonate case dimensions, the copper foam was properly milled and then immersed into the PCM inside the case (Figure 3.48).

Six tests (Test 2.1÷2.6) were performed with the same environmental temperature T_{AIR} and power P supplied to the 4-cells element as in Test 1.1÷1.6. To verify the metal foam capability to damp the convective motions, a confirmation test was done putting a TC inside the upper copper foam layer, at the same height where the convective motions had been observed during Test 1.1÷1.6. Results (Figure 3.49) show that with a copper-foam-loaded PCM there was still a temperature difference between the upper and the lower cells but there were not temperature fluctuations anymore and the 4-cells element reached lower temperatures.

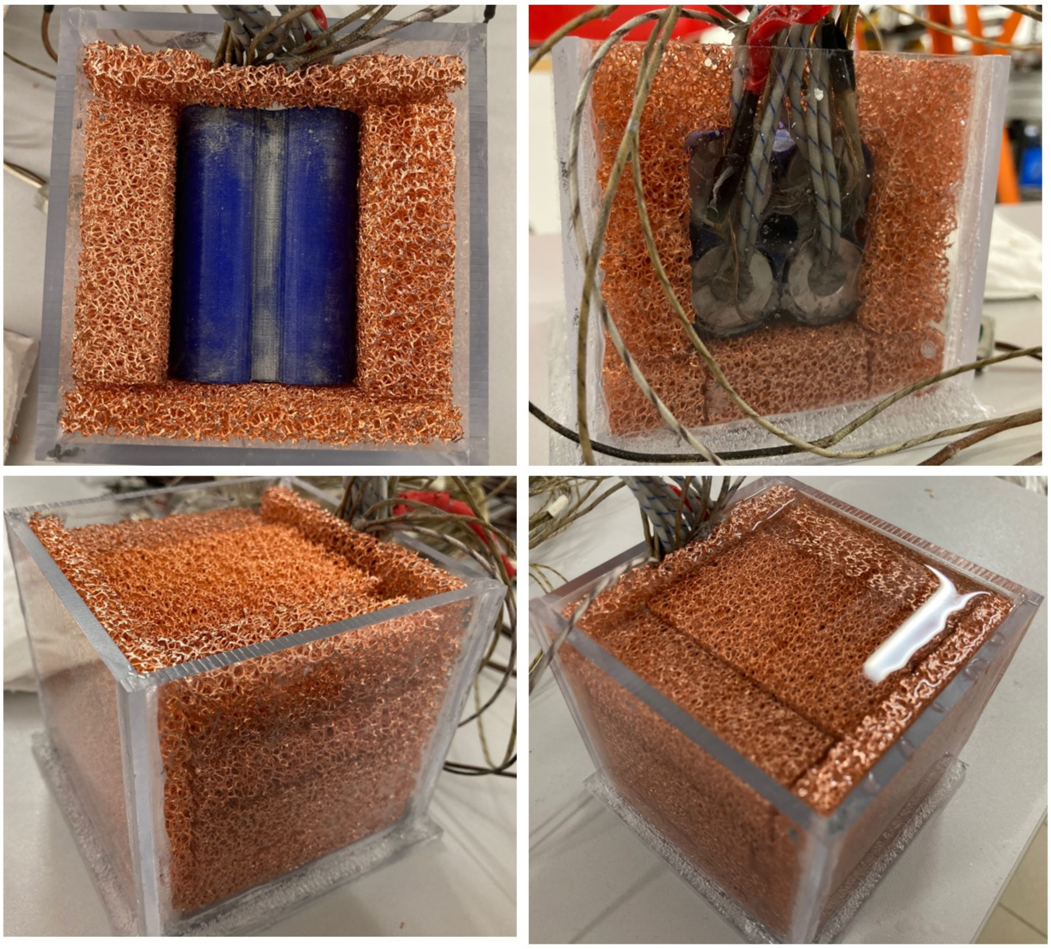

Figure 3.48. *Assembly of the experimental rig used for the tests with copper-foam-loaded PCM.*

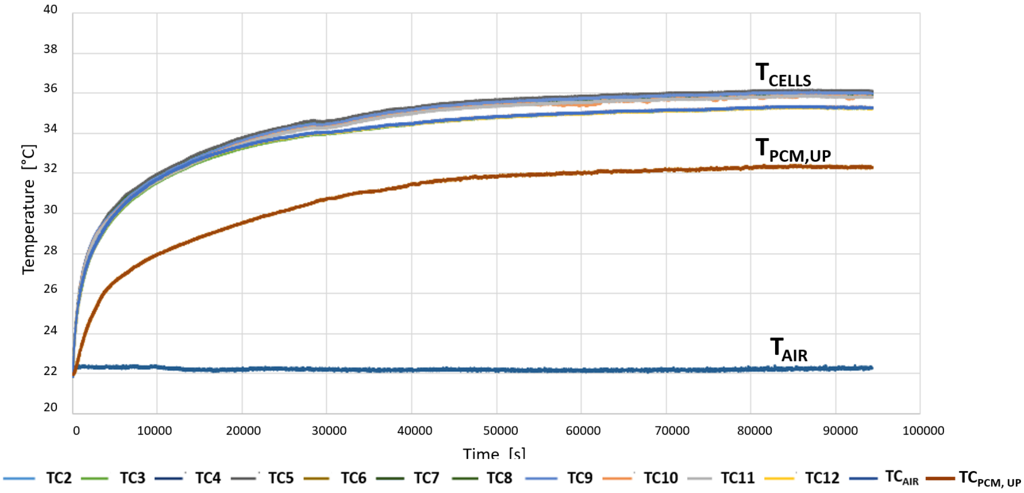

Figure 3.49. *Analysis of the convective motions in presence of the copper foam.*

3.4.4.1 *Results*

The left graphs in Figure 3.54, Figure 3.55 and Figure 3.56 show the results of Test 2.1 which was carried on with the copper-loaded PCM: the blue and the orange curves show the temperature of the upper cells, the grey and the yellow curves show the temperature of the lower cells. As in Test 1.1 (Figure 3.41, Figure 3.42 and Figure 3.43), with the copper-foam-loaded PCM $\Delta T_{\text{UP-LOW}}$ is constantly present and it is visible in all the five tests (Test 2.1÷2.5), its value is independent from the x-value along the cell and increases over time: in the right graphs of Figure 3.54, Figure 3.55 and Figure 3.56 it is possible to see the trends of the temperature differences during Test 2.1 at different x-values (top, middle and bottom areas). This ΔT is visible during all the five tests when the copper-foam-loaded PCM was used. The averages of the maximum temperature differences recorded by the top, the middle and the bottom TCs are $\Delta T_{\text{TOP, max}} = 0.98\ K$, $\Delta T_{\text{MID, max}} = 1.00\ K$, $\Delta T_{\text{BOT, max}} = 0.95\ K$. Taking into account the typical uncertainty value of the TCs which is estimated to be $Er \simeq 0.75 \div 1\ K$ [161], the values of the temperature difference between the upper and the lower cells are close to those obtained in Test 1.1÷1.6. Supplementary results related to Test 2.2÷2.5 are reported in Appendix 4.

As said, the presence of the metal foam does not influence the $\Delta T_{\text{UP-LOW}}$ but it works efficiently in lowering the highest temperatures reached by the cells. In Figure 3.57, Figure 3.58, Figure 3.59 and Figure 3.60 the results of Test 2.1÷2.5 with the copper-loaded PCM are presented: as mentioned in Section 3.4.3.1, the cells temperatures considered are those recorded by TC_{MID}.

Comparing these results with those related to the pure PCM tests in Figure 3.44, Figure 3.45, Figure 3.46 and Figure 3.47, it is possible to see how the presence of the copper foam was fundamental not to have a fast increase in temperature. As a matter of fact, with pure PCM the temperatures rose fast in a time interval of about $\Delta t_{\text{pure}} = 10000\ s$, then they tended to balance. Instead, with the copper-loaded PCM temperatures rose slower in about $\Delta t_{\text{load}} = 100000\ s$ (a value which is one order of magnitude higher than the previous one) until the moment they tended to balance. Table 3.10 shows the values of the maximum temperatures T_{max} measured on the cells for each test and their averages $\widetilde{T}_{\text{max}}$. Comparing the values obtained for the copper-foam-loaded PCM with those obtained for the pure PCM (Table 3.8) it can be observed that the maximum temperatures recorded for the copper-foam-loaded PCM are lower and so do their averages (Table 3.10).

In Table 3.9 all the maximum $\Delta T_{\text{UP-LOW}}$ values for all the cells are collected. This table shows that the effect of the copper foam in the system was to dampen the convective circulation observed in the case of pure PCM.

Table 3.9. *Maximum temperature differences at* $t = 15000$ *s and* $t = 70000$ *s for a fixed cell, obtained in Test 2.1÷2.5 with the copper-loaded PCM.*

Cell	Unit	$\Delta T_{15000\text{ s}}$	$\Delta T_{70000\text{ s}}$
1	[K]	1.61	0.76
2	[K]	1.37	0.43
3	[K]	1.42	1.24
4	[K]	1.60	1.26

Table 3.10. *Maximum temperatures reached by the cells during Test 2.1÷2.5 with the copper-foam-loaded PCM.*

	Unit	Cell 1	Cell 2	Cell 3	Cell 4
$T_{\text{max, Test 2.1}}$	[°C]	35.70	35.97	36.18	35.75
$T_{\text{max, Test 2.2}}$	[°C]	35.11	35.97	35.24	35.03
$T_{\text{max, Test 2.3}}$	[°C]	34.60	35.63	35.43	34.52
$T_{\text{max, Test 2.4}}$	[°C]	34.63	35.68	35.48	34.53
$T_{\text{max, Test 2.5}}$	[°C]	34.88	35.91	35.67	35.57
$\widetilde{T}_{\text{max}}$	[°C]	34.98	35.93	35.60	35.08

In conclusion, although the $\Delta T_{\text{UP-LOW}}$ was still present (independently from the x-value), there were no more temperature fluctuations in the PCM area above the 4-cells element and the temperature of the upper PCM layer ($T_{\text{PCM, UP}}$) followed that of the cells, not presenting peaks. As a matter of fact, for Test 1.1÷1.6 $\Delta T_{\text{UP-LOW}}$ is equal to 0.91 K on the top, 0.90 K in the middle and 0.95 K on the bottom; for Test 2.1÷2.5 the values are 0.98 K on the top, 1.00 K in the middle and 0.95 K on the bottom of the cells. Another interesting result achieved thanks to the copper-foam-loaded PCM was a lower cell temperature for all the cells. The maximum temperature averages reached by the cells during Test 2.1÷2.5 were $\widetilde{T}_{\text{max, UP, load}} = 35.93$ °C for the upper cells and $\widetilde{T}_{\text{max, LOW, load}} = 35.08$ °C for the lower ones.

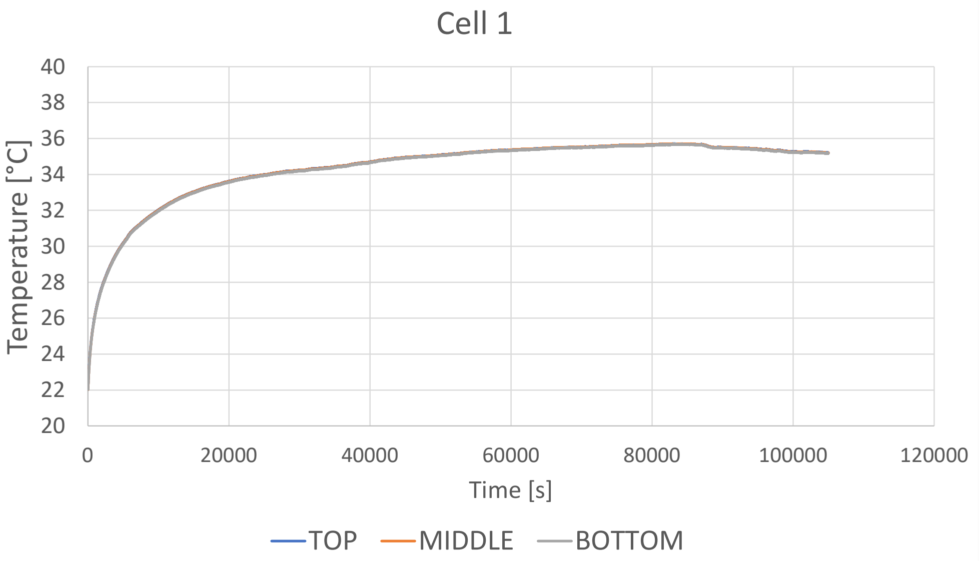

Figure 3.50. *Copper-foam-loaded PCM, Test 2.1: temperature trends recorded by* TC_{TOP}*,* TC_{MID} *and* TC_{BOT} *along Cell 1.*

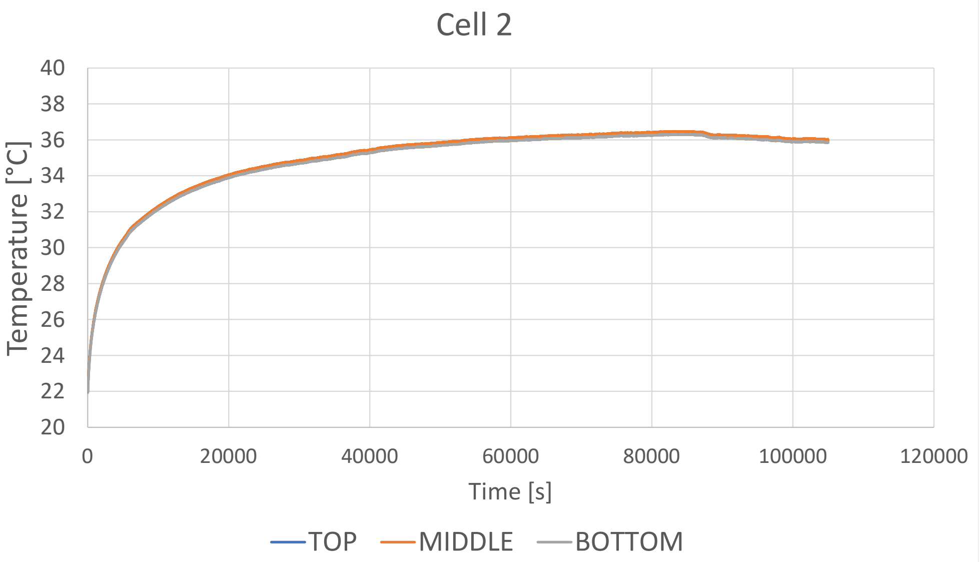

Figure 3.51. *Copper-foam-loaded PCM, Test 2.1: temperature trends recorded by* TC_{TOP}*,* TC_{MID} *and* TC_{BOT} *along Cell 2.*

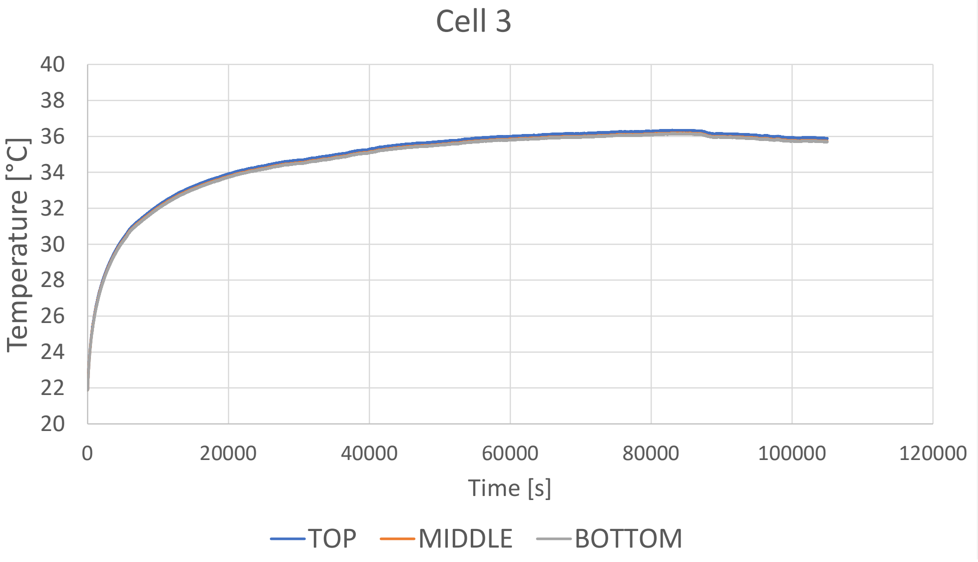

Figure 3.52. *Copper-foam-loaded PCM, Test 2.1: temperature trends recorded by* TC_{TOP}, TC_{MID} *and* TC_{BOT} *along Cell 3.*

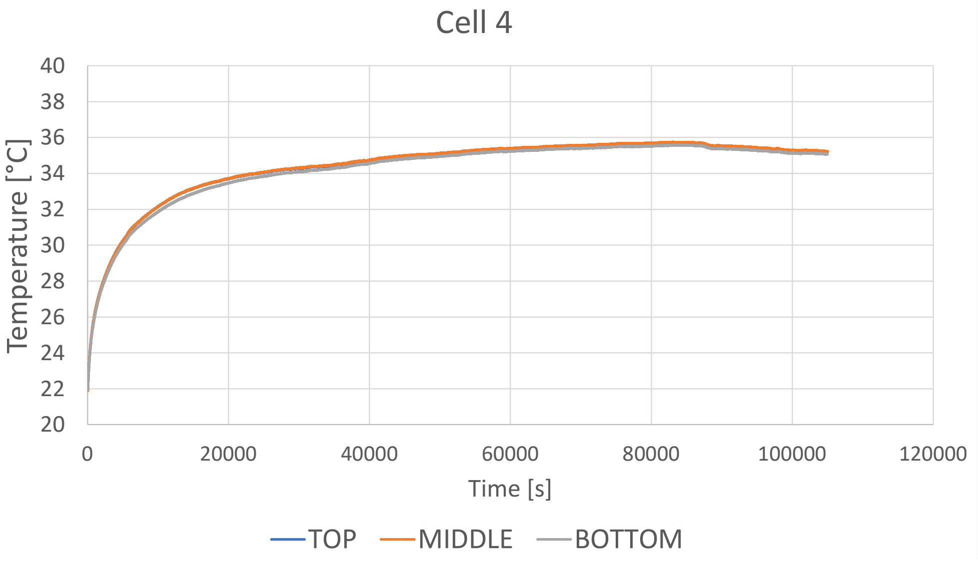

Figure 3.53. *Copper-foam-loaded PCM, Test 2.1: temperature trends recorded by* TC_{TOP}, TC_{MID} *and* TC_{BOT} *along Cell 4.*

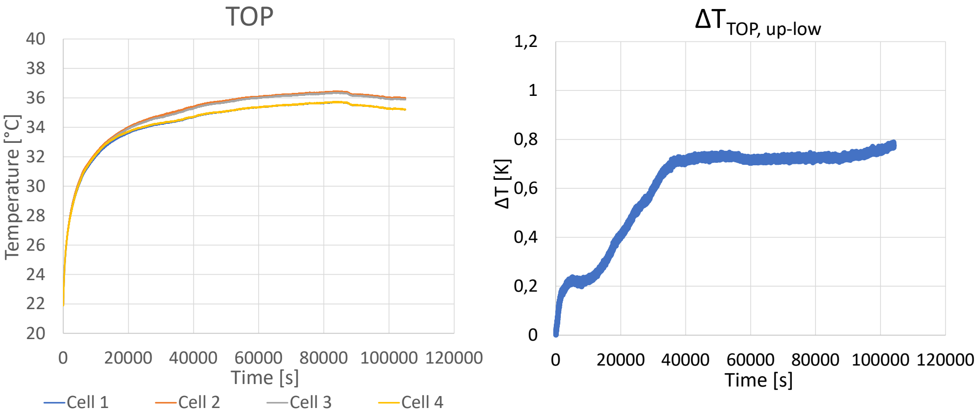

Figure 3.54. *Copper-foam-loaded PCM, Test 2.1: temperature trends recorded on the top of all the cells (left) and* ΔT *trend between the top of the upper and the lower cells (right).*

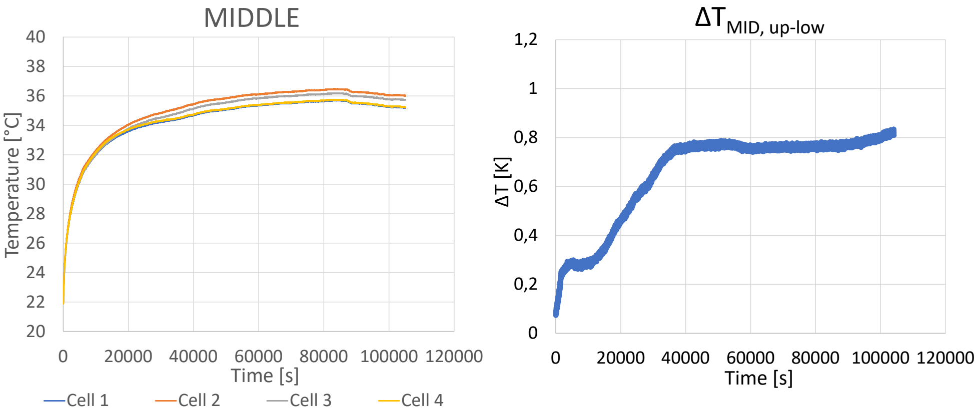

Figure 3.55. *Copper-foam-loaded PCM, Test 2.1: temperature trends recorded in the middle of all the cells (left) and* ΔT *trend between in the middle of the upper and the lower cells (right).*

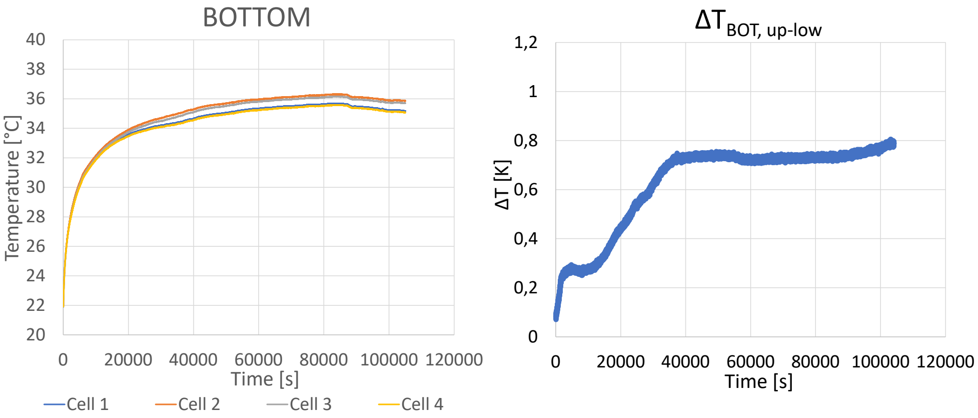

Figure 3.56. *Copper-foam-loaded PCM, Test 2.1: temperature trends recorded on the bottom of all the cells (left) and* ΔT *trend between the bottom of the upper and the lower cells (right).*

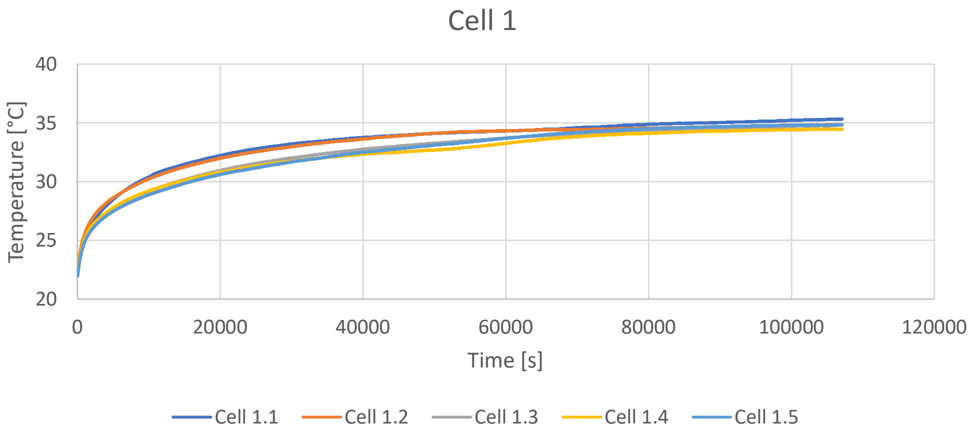

Figure 3.57. *Copper-foam-loaded PCM, Test 1.1÷1.5: temperature trends recorded by* TC_{MID} *on Cell 1.*

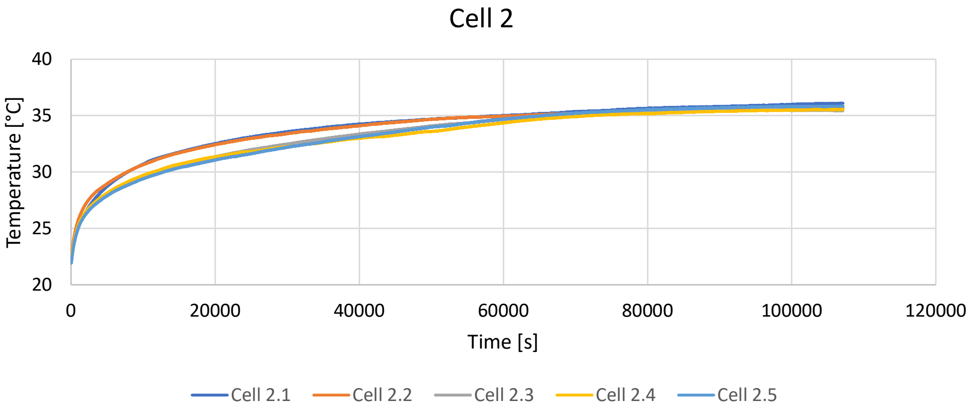

Figure 3.58. *Copper-foam-loaded PCM, Test 1.1÷1.5: temperature trends recorded by* TC_{MID} *on Cell 2.*

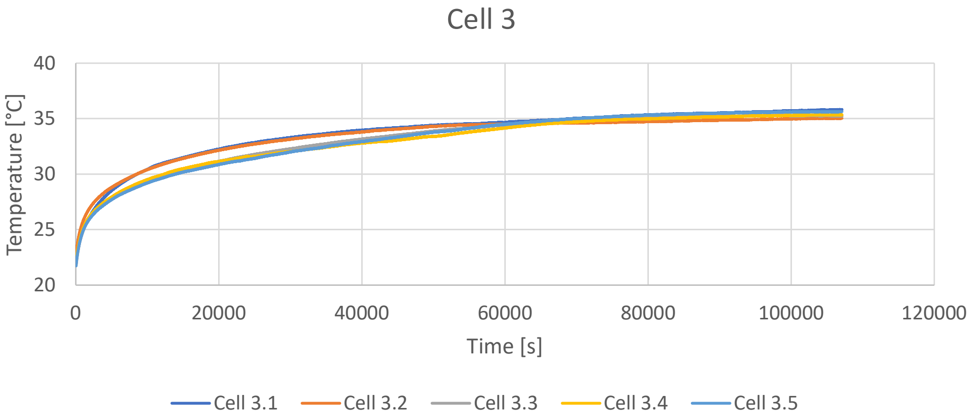

Figure 3.59. *Copper-foam-loaded PCM, Test 1.1÷1.5: temperature trends recorded by* TC_{MID} *on Cell 3.*

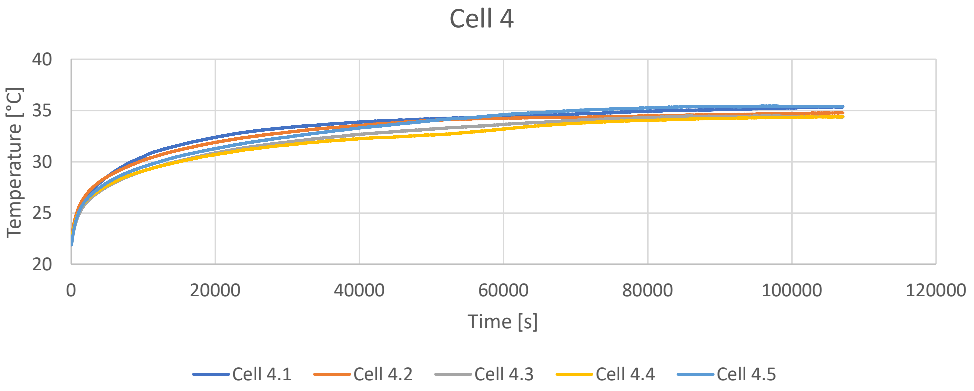

Figure 3.60. *Copper-foam-loaded PCM, Test 1.1÷1.5: temperature trends recorded by* TC_{MID} *on Cell 4.*

3.4.5 *Comparison between pure and copper-foam-loaded PCM*

The aim of these two first series of tests was to compare the performances of a pure PCM-based BTMS with those of a copper-foam-loaded-PCM-based one. With the pure PCM a $\Delta T_{\text{UP-LOW}}$ was recorded: wide fluctuations showed convective motions in the PCM area above the 4-cells element. This phenomenon influenced the heat fluxes and the temperature distribution within the system. The maximum temperature averages reached by the cells during these tests were in the interval $\widetilde{T}_{\text{max, pure}} = 36.7 \div 37.6$ °C. With the copper-foam-loaded PCM results showed that, although a $\Delta T_{\text{UP-LOW}}$ was still present, no temperature fluctuations were recorded in the PCM layer above the module and the temperature measured into the PCM was very close to the cell temperatures. The maximum temperatures reached by the cells were $1.63 \div 1.75$ K lower than those measured with pure PCM.

These results highlight the benefits of a copper-loaded-PCM-based BTMS compared to a pure-PCM-based one such as lower maximum temperatures on the cells and a better temperature homogeneity into the system: two important factors which contribute to the battery state of health (SOH)improvement.

3.4.6 *Insulated BTMS tests: experimental setup*

In all the automotive applications LIBs are enclosed in safety boxes which work both as fire emergency devices and to protect the cells from accidental impacts. Hence, these boxes are necessary but they also negatively influence the BP temperature, acting as an insulation container and making harder the heat dissipation process from the cells to the outer environment. For this reason it was important to proceed with deeper studies about insulated cooling systems, analysing the performances of several of them. Here below four series of tests are presented: each series deal with a different kind of insulated BTMS such as the PCM-based and the copper-loaded-PCM-based ones and those same BTMSs coupled with a liquid cooling system.

To proceed with the tests an insulation box was built, first drawing it on the *CATIA* CAD software and then milling it (the process was the same described in Section 3.3.2.1 for the polycarbonate case realization). The insulation box had 50 *mm* thick walls and it was composed of four polystyrene components: in this way it was possible to enclose the polycarbonate case into the final assembly (Figure 3.61) without leaving air cavities between the case and the box walls. All the thermal bridges were properly covered with EUROBATEX® (Table 3.1) and this insulation material was also inserted into the holes through which the cables of the cartridge heaters passed.

As explained in Section 3.4.1, for the uninsulated tests the choice of a precise value of power supplied to the 4-cells element was done considering that the typical temperature around which a BTMS starts to work is around 40 °C. With the addition of the insulation box it was necessary to lower the power supplied to the system as the heat losses were less: this means that for the same power the final temperature was higher. Hence, for the experimental campaign about the insulated cooling systems another voltage tuning process was done before proceeding with the tests: for a voltage value $V = 22.55\ V$ the cells reached the maximum temperature $T = 45\ °C$, so the related voltage was chosen for the tests. For that voltage value the current delivered by the digital power supply was $i = 0.089\ A$, that is $i_{\text{cell}} = 0.0223\ A$ for each cell. Consequently, the power supplied to the whole 4-cell element was $P = V \cdot i = 2\ W$ and the power supplied to each of the cartridge heaters was $P_{\text{cell}} = V \cdot i_{\text{cell}} = 0.50\ W$.

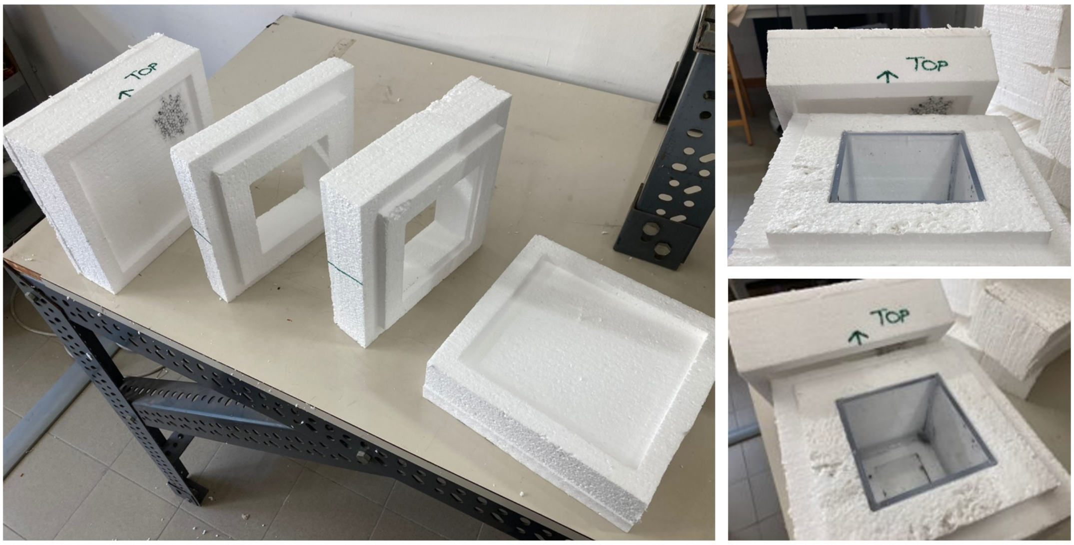

Figure 3.61. *The assembly process of the insulation box with the polycarbonate case inside.*

3.4.7 *Pure PCM: insulated*

A series of three tests (Test 3.1÷3.3) was carried on testing an insulated PCM-based BTMS. The experimental rig was the same used for the study of the uninsulated PCM-based BTMS (see Section 3.4.2) upgraded with the insulation box in Figure 3.62. As in the previous test series, several cell charging cycles were simulated monitoring the temperatures reached by the 4-cells element and the temperature homogeneity of its four units.

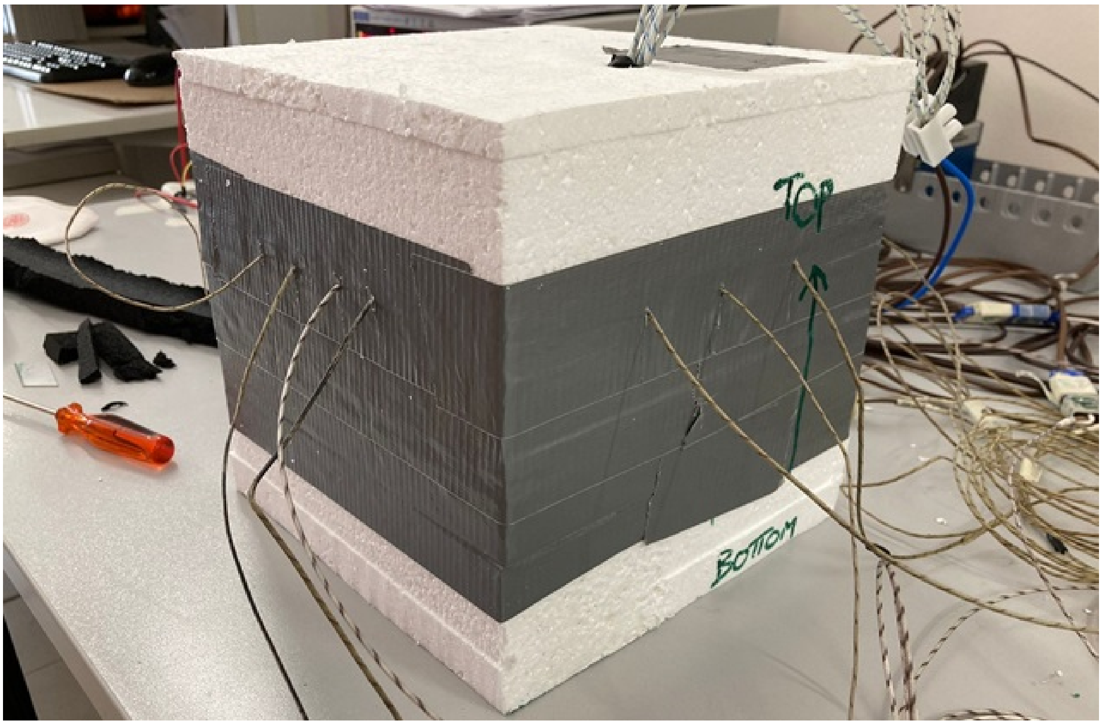

Figure 3.62. *The final assembly of the insulation box.*

3.4.7.1 *Results*

The temperature difference $\Delta T_{\text{UP-LOW}}$ was constantly present and its value was independent from the x-quote. In the right graphs of Figure 3.67, Figure 3.68 and Figure 3.69 it is possible to see the trends of the temperature differences during Test 3.1 at different x-values: $\Delta T_{\text{UP-LOW}}$ has a peak at $t = 6000\ s$ and this happens when the phase change occurs. Looking at the left graphs of the same figures, as well as at the graphs in Figure 3.63, Figure 3.64, Figure 3.65 and Figure 3.66, at $t = 6000\ s$ the temperature curves tend to flatten (their slope decreases before increasing again) and this is a typical temperature behaviour during a phase change process. This temperature trend was here more clearly visible than in the case of uninsulated systems as the studied environment was closer to an ideal adiabatic one.

The said $\Delta T_{\text{UP-LOW}}$ was visible during all the three tests when pure PCM was used in the insulated configuration. Considering Test 3.1÷3.3, the averages of the maximum temperature differences recorded by top, the middle and the bottom TCs were $\widetilde{\Delta T}_{\text{TOP, max}} = 1.06\ K$, $\widetilde{\Delta T}_{\text{MID, max}} = 1.09\ K$, $\widetilde{\Delta T}_{\text{BOT, max}} = 0.98\ K$. In Figure 3.63, Figure 3.64, Figure 3.65 and Figure 3.66 the curves showing the temperature trends along the cells are overlapped: there is thermal homogeneity all along each unit of the 4-cells element. As there were no great differences among the temperatures recorded by the three TCs placed on each single cell, from now on only the values recorded by TC_{MID} will be considered. Supplementary results related to Test 3.2 and Test 3.3 are reported in Appendix 4.

In Figure 3.70, Figure 3.71, Figure 3.72 and Figure 3.73 the overall results of Test 3.1÷3.3 are illustrated. Thanks to the insulation box, no temperature fluctuations were recorded during the heating processes as previously seen in Section 3.4.3.1 for an uninsulated PCM-based BTMS. Convective motions did not negatively influence the cells temperatures as much as they did without insulation, when they caused temperature dips and rises. However, a precise repeatability of the experiment was not fully achieved: with the pure PCM the melting material had a low thermal conductivity and, although the starting temperature was the same for all the tests of the series, the internal convective motions influenced the first part of the heating processes so that the whole volume of PCM did not always go through the same melting cycle in terms of phase change temperature. In particular, in the time interval $t = 15000 \div 60000\ s$, when the phase change happened and the convection was more developed, the temperature trends of the cells recorded during Test 3.1÷3.3 are not exactly overlapped. After the complete melting of the PCM ($t > 60000\ s$) the same thermal situation occurred in all the tests.

In the automotive LIBs, much more bigger than the 4-cells element studied, such a situation could lead to an inhomogeneous temperature distribution inside the battery pack and this is not a desired situation considering the SOH of the Li-ion cells.

The maximum temperatures reached by the cells during Test 3.1÷3.3 and their averages ($\widetilde{T}_{\text{max}}$) are summarized in Table 3.11. As the proper working range for Li-ion cells is about $15 \div 40$ °C [69], lower temperatures are required: this means that in an insulated environment a pure PCM-based BTMS is not able to satisfy the optimal thermal requirements for LIBs.

Table 3.11. *Maximum temperatures reached by the cells during Test 3.1÷3.3 with pure PCM in an insulated system.*

	Unit	Cell 1	Cell 2	Cell 3	Cell 4
$T_{\text{max, Test 3.1}}$	[°C]	44.19	44.84	44.62	43.96
$T_{\text{max, Test 3.2}}$	[°C]	45.33	45.97	45.77	45.11
$T_{\text{max, Test 3.3}}$	[°C]	45.79	46.33	46.04	45.54
$\widetilde{T}_{\text{max}}$	[°C]	45.10	45.71	45.44	44.87

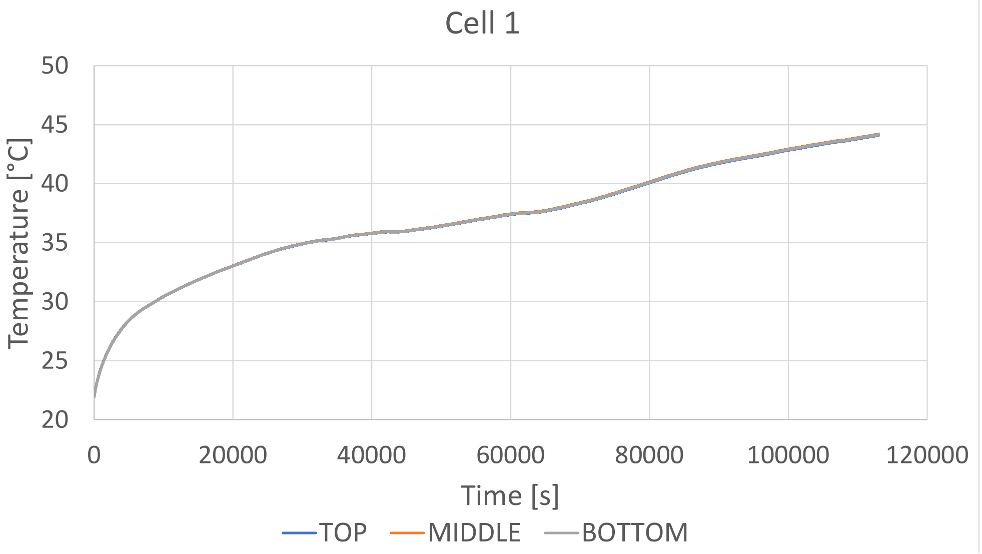

Figure 3.63. *Insulated system, pure PCM, Test 3.1: temperature trends recorded by* TC_{TOP}, TC_{MID} *and* TC_{BOT} *along Cell 1.*

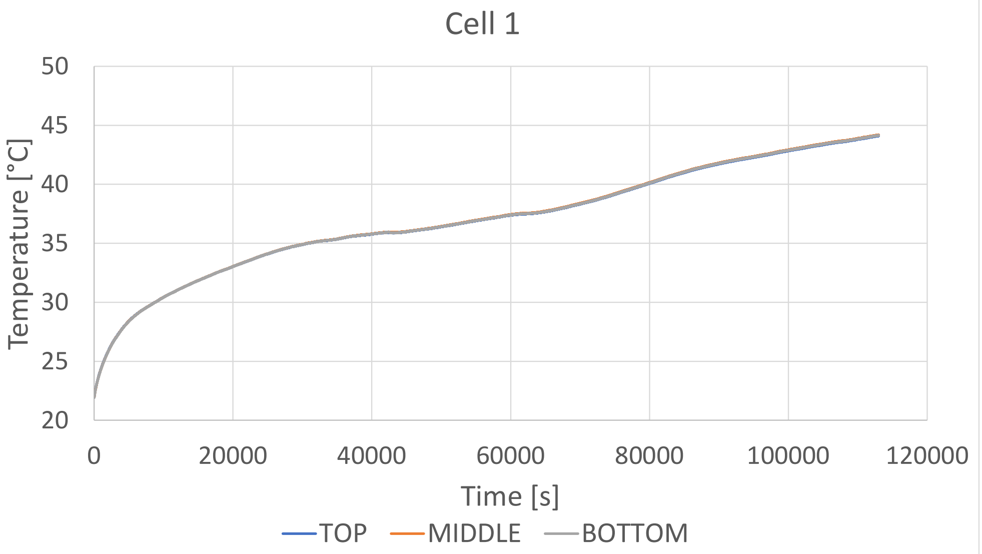

Figure 3.64. *Insulated system, pure PCM, Test 3.1: temperature trends recorded by* TC_{TOP}, TC_{MID} *and* TC_{BOT} *along Cell 2.*

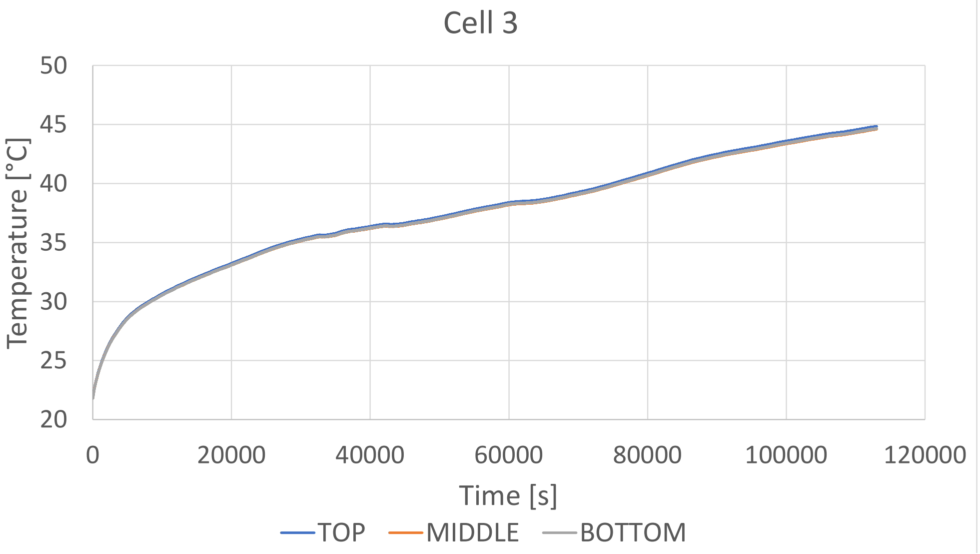

Figure 3.65. *Insulated system, pure PCM, Test 3.1: temperature trends recorded by* TC_{TOP}, TC_{MID} *and* TC_{BOT} *along Cell 3.*

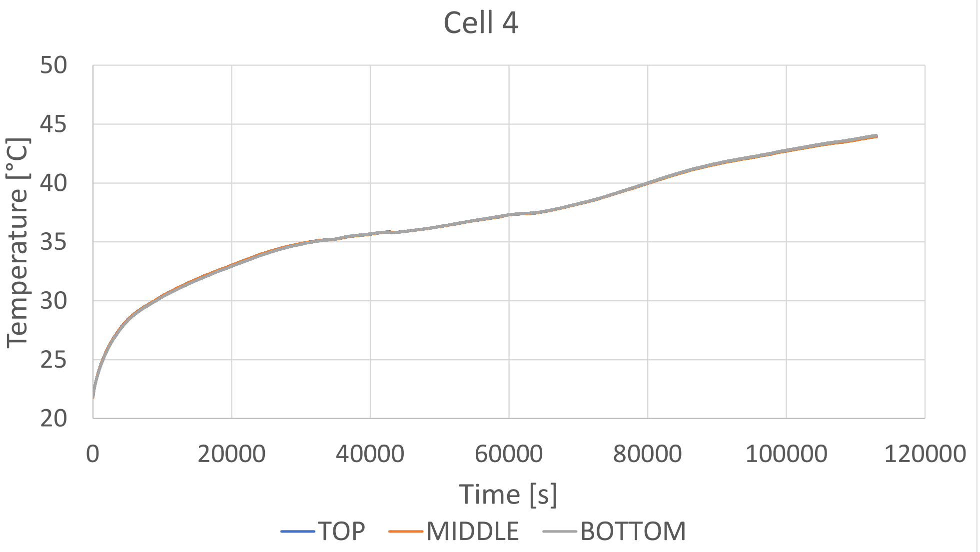

Figure 3.66. *Insulated system, pure PCM, Test 3.1: temperature trends recorded by* TC_{TOP}, TC_{MID} *and* TC_{BOT} *along Cell 4.*

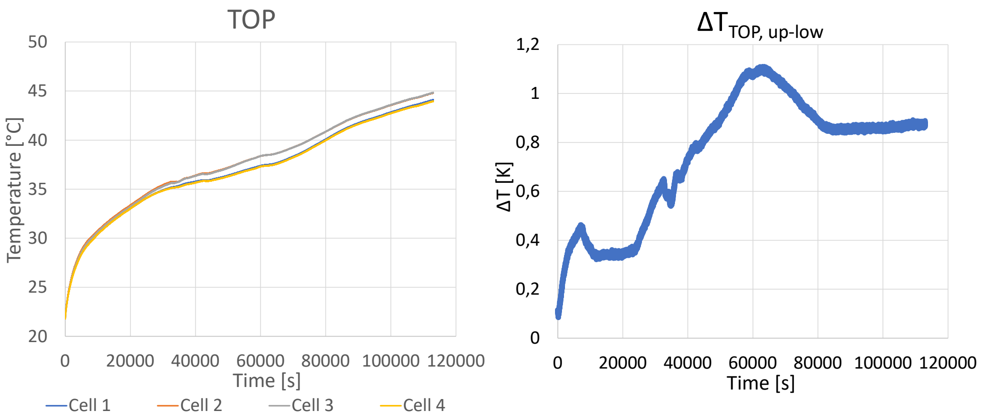

Figure 3.67. *Insulated system, pure PCM, Test 3.1: temperature trends recorded on the top of all the cells (left) and* ΔT *trend between the top of the upper and the lower cells (right).*

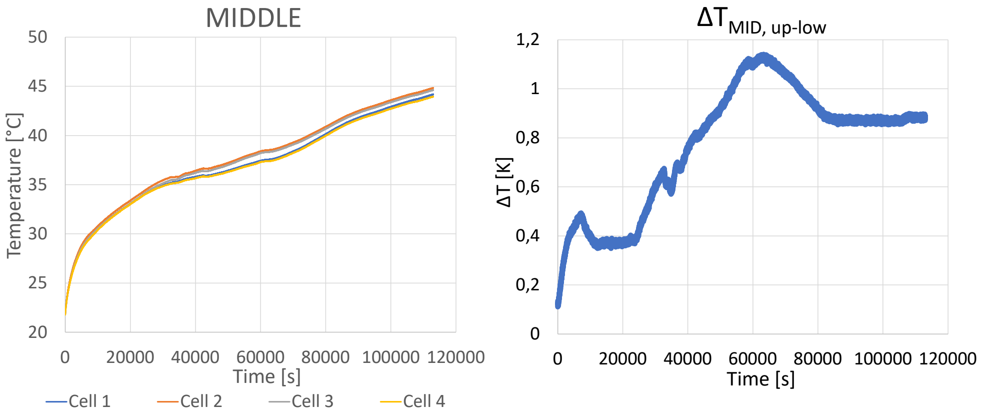

Figure 3.68. *Insulated system, pure PCM, Test 3.1: temperature trends recorded in the middle of all the cells (left) and* ΔT *trend between the middle of the upper and the lower cells (right).*

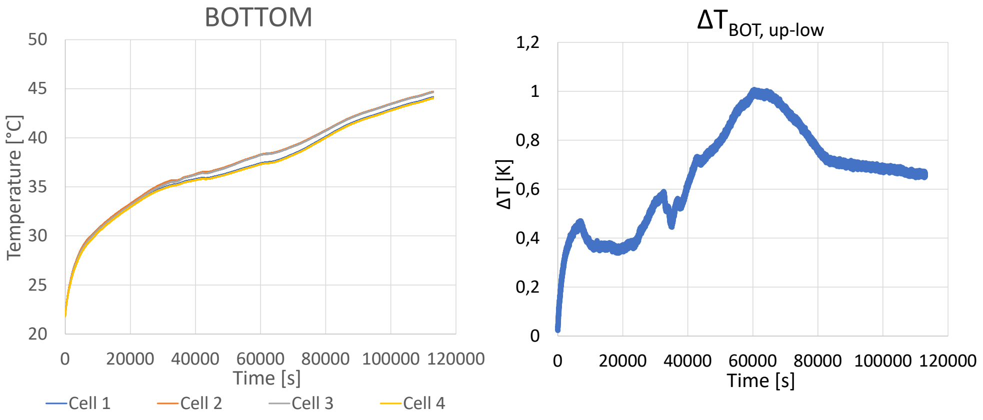

Figure 3.69. *Insulated system, pure PCM, Test 3.1: temperature trends recorded on the bottom of all the cells (left) and* ΔT *trend between the bottom of the upper and the lower cells (right).*

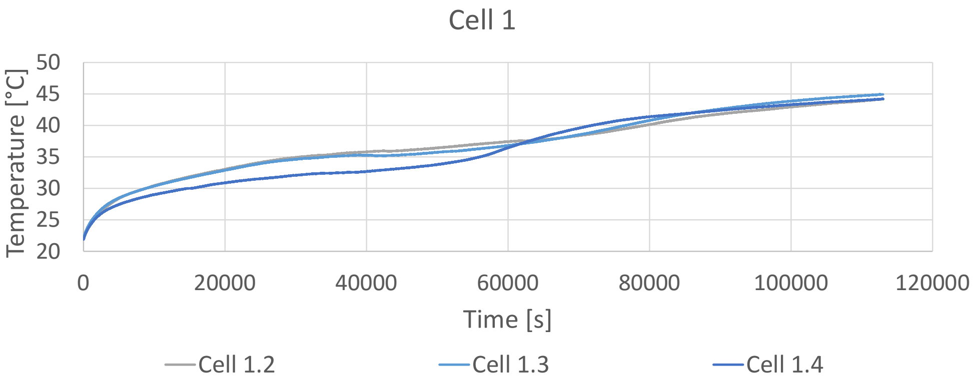

Figure 3.70. *Insulated system, pure PCM, Test 3.1÷3.3: temperature trends recorded by* TC_{MID} *on Cell 1.*

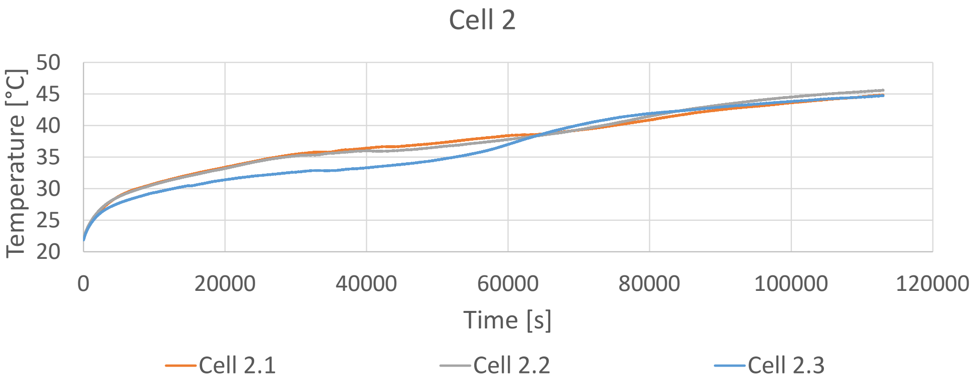

Figure 3.71. *Insulated system, pure PCM, Test 3.1÷3.3: temperature trends recorded by* TC_{MID} *on Cell 2.*

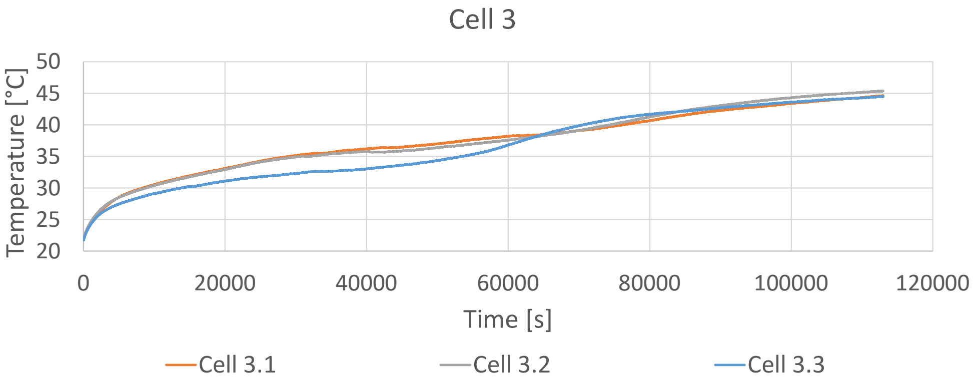

Figure 3.72. *Insulated system, pure PCM, Test 3.1÷3.3: temperature trends recorded by* TC_{MID} *on Cell 3.*

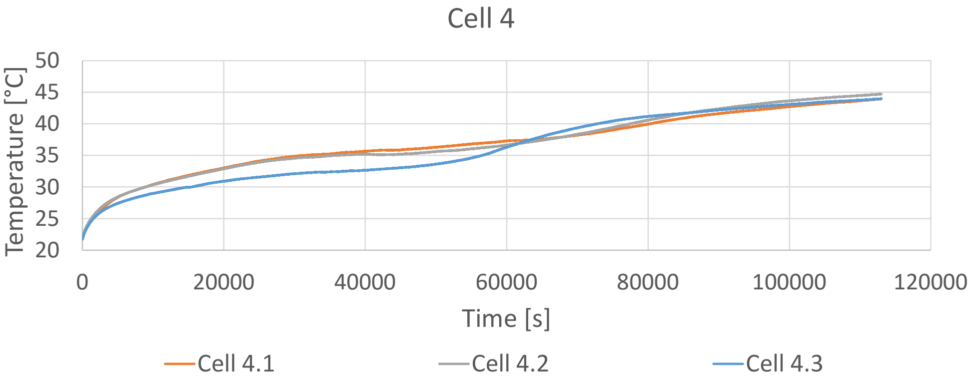

Figure 3.73. *Insulated system, pure PCM, Test 3.1÷3.3: temperature trends recorded by TC_{MID} on Cell 4.*

3.4.8 *Copper-foam-loaded PCM: insulated*

Three tests (Test 4.1÷4.3) were conducted exploiting almost the same experimental setup used for Test 3.1÷3.3 (see Section 3.4.7) but, this time, the investigations dealt with the temperature trends and the temperature distribution inside an insulated BP thermally managed by a copper-foam-loaded PCM. In Figure 3.74 the copper foam immersed into the PCM and the insulated experimental setup are shown.

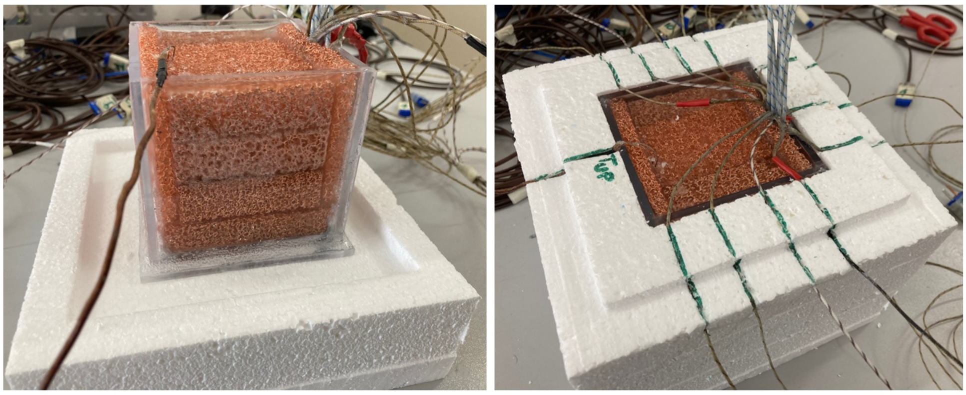

Figure 3.74. *The copper metal foam immersed into the PCM which fills the case (left) before the system is insulated with the polystyrene box (right).*

3.4.8.1 *Results*

Focusing the attention on Test 4.1, a $\Delta T_{\text{UP-LOW}}$ was measured and showed in Figure 3.79, Figure 3.80 and Figure 3.81. On the left graphs it is possible to see that the temperatures have almost the same trend for all the four cells, independently from the x-value. However, analysing the right graphs, it clearly appears that a temperature difference is always present with this setup configuration, too. As with the insulated PCM-based BTMS (Section 3.4.7.1), the peak of $\Delta T_{\text{UP-LOW}}$ is still at around $t = 6000\ s$ (during the phase change process) but, in this case, the trend of the increase in less steep. This happens thanks to the copper foam which keeps the temperatures more stable and homogeneous: soon after the heating process begins the $\Delta T_{\text{UP-LOW}}$ stabilizes on a value and retains it until the increase, before reaching the peak. This $\Delta T_{\text{UP-LOW}}$ was visible during the whole experimental campaign carried on with the copper-foam-loaded PCM used in the insulated configuration. Considering Test 4.1÷4.3, the averages of the maximum temperature differences recorded by the top, the middle and the bottom TCs were $\widetilde{\Delta T}_{\text{TOP, max}} = 0.86\ K$, $\widetilde{\Delta T}_{\text{MID, max}} = 0.83\ K$, $\widetilde{\Delta T}_{\text{BOT, max}} = 0.67\ K$ resulting in slightly lower values than those obtained with the insulated PCM-based BTMS (Section 3.4.7.1).

In Figure 3.75, Figure 3.76, Figure 3.77 and Figure 3.78 the curves showing the temperature trends along the cells are overlapped: this confirms that the temperature homogeneity all along each unit of the 4-cells element was achieved with this setup configuration, too. As there were no important differences among the temperatures recorded by the three TCs placed on each single cell, from now on only the values recorded by TC_{MID} will be considered. Supplementary results related to Test 4.2 and Test 4.3 are reported in Appendix 4.

In Figure 3.82, Figure 3.83, Figure 3.84 and Figure 3.85 the overall results of Test 4.1÷4.3 are shown. As in the case with the insulated PCM-based BTMS, no temperature dips and rises were recorded and, moreover, an important improvement came from the addition of the copper foam. As a matter of fact, the graphs show temperature trends exactly overlapped (the repeatability of the test is demonstrated), meaning that there were no more convective motions influencing the temperature during the phase change processes (Section 3.4.7.1).

However, although the $\Delta T_{\text{UP-LOW}}$ values were better (slightly lower) than those obtained in Test 3.1÷3.3 and the experiments showed a higher temperature stability during the phase change (a better temperature distribution in case of a huge real BP), the copper-foam-loaded-PCM-based BTMS did not satisfy the optimal thermal requirements for LIBs due to the maximum temperatures reached by the cells. These values and their averages are shown in Table 3.12.

Comparing the $\widetilde{T}_{\text{max}}$ values recorded during Test 3.1÷3.3 (insulated PCM-based BTMS) and Test 4.1÷4.3 (insulated copper-foam-loaded-PCM-based BTMS) it is clear that the two cooling systems reached almost the same temperatures and the benefits brought by the copper foam are not sufficient enough to preserve the cell SOH.

Table 3.12. *Maximum temperatures reached by the cells during Test 4.1÷4.3 with copper-foam-loaded PCM in an insulated system.*

	Unit	Cell 1	Cell 2	Cell 3	Cell 4
$T_{\text{max, Test 4.1}}$	[°C]	45.02	45.54	45.38	44.83
$T_{\text{max, Test 4.2}}$	[°C]	45.25	45.77	45.67	45.03
$T_{\text{max, Test 4.3}}$	[°C]	45.38	45.89	45.69	45.17
$\widetilde{T}_{\text{max}}$	[°C]	45.22	45.73	45.58	45.01

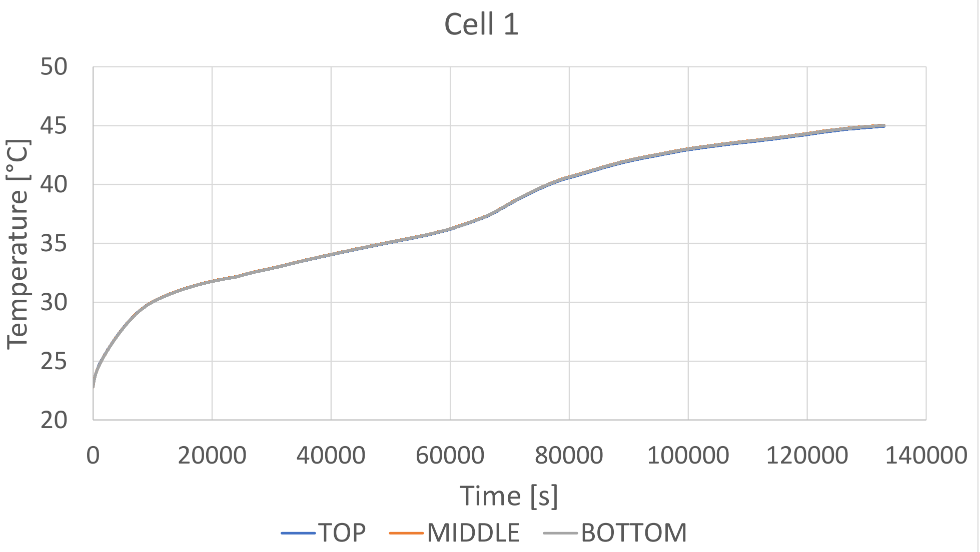

Figure 3.75. *Insulated system, copper-foam-loaded PCM, Test 4.1: temperature trends recorded by* TC_{TOP}, TC_{MID} *and* TC_{BOT} *along Cell 1.*

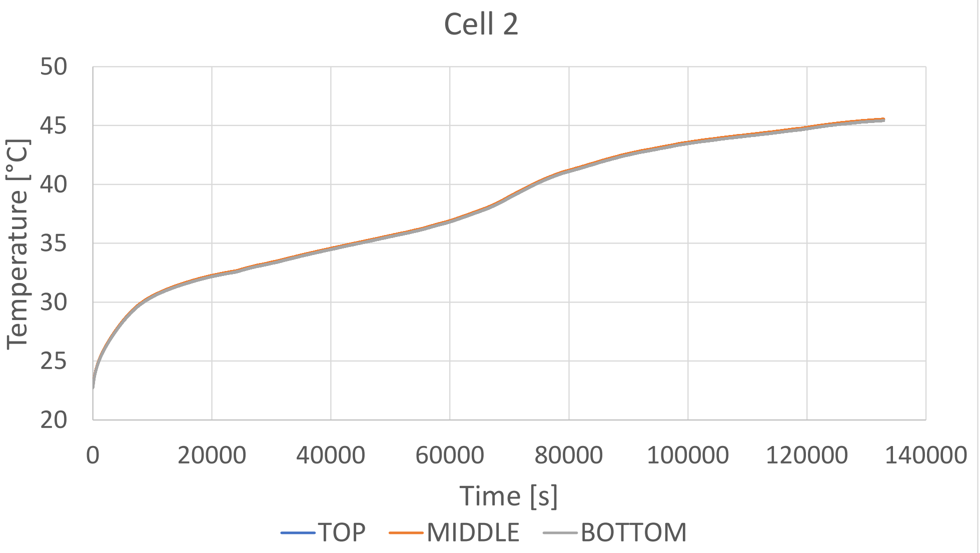

Figure 3.76. *Insulated system, copper-foam-loaded PCM, Test 4.1: temperature trends recorded by* TC_{TOP}, TC_{MID} *and* TC_{BOT} *along Cell 2.*

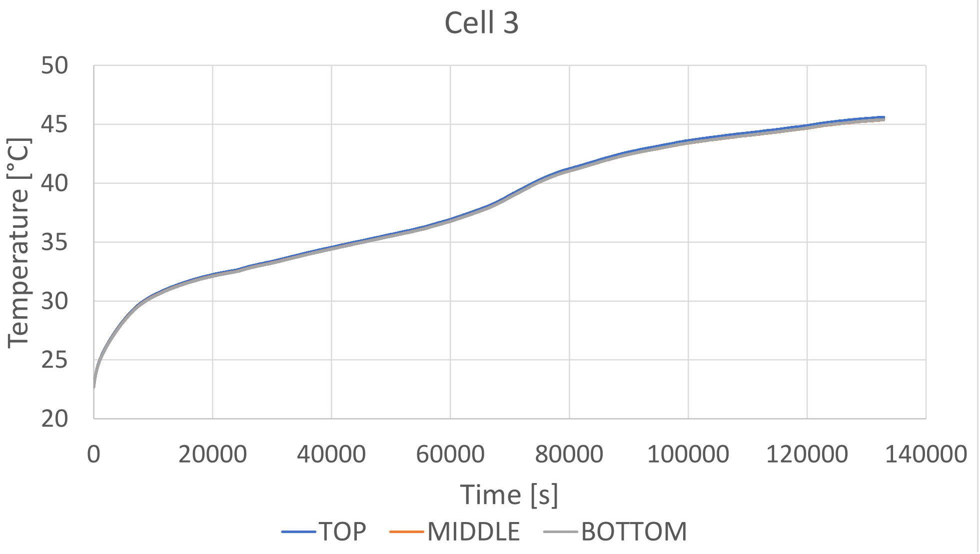

Figure 3.77. *Insulated system, copper-foam-loaded PCM, Test 4.1: temperature trends recorded by* TC_{TOP}, TC_{MID} *and* TC_{BOT} *along Cell 3.*

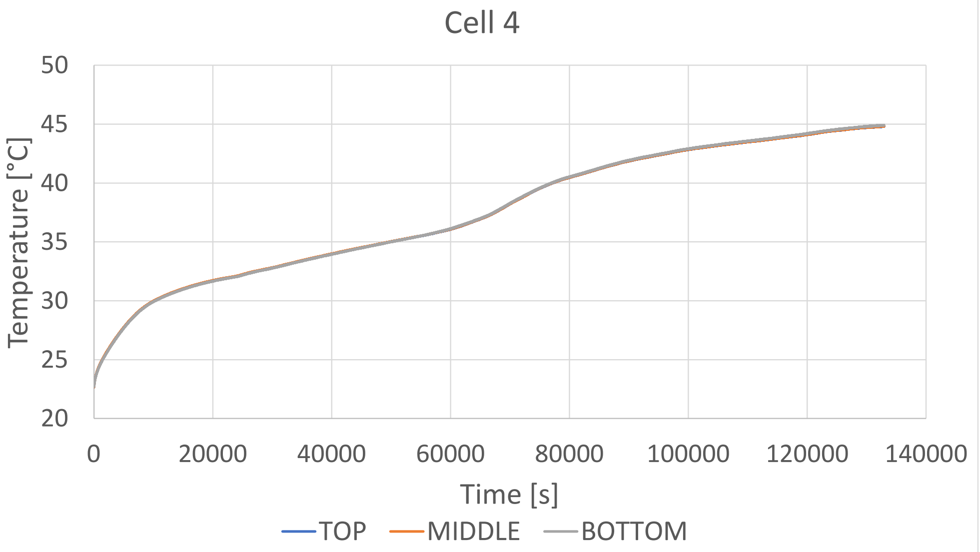

Figure 3.78. *Insulated system, copper-foam-loaded PCM, Test 4.1: temperature trends recorded by* TC_{TOP}, TC_{MID} *and* TC_{BOT} *along Cell 4.*

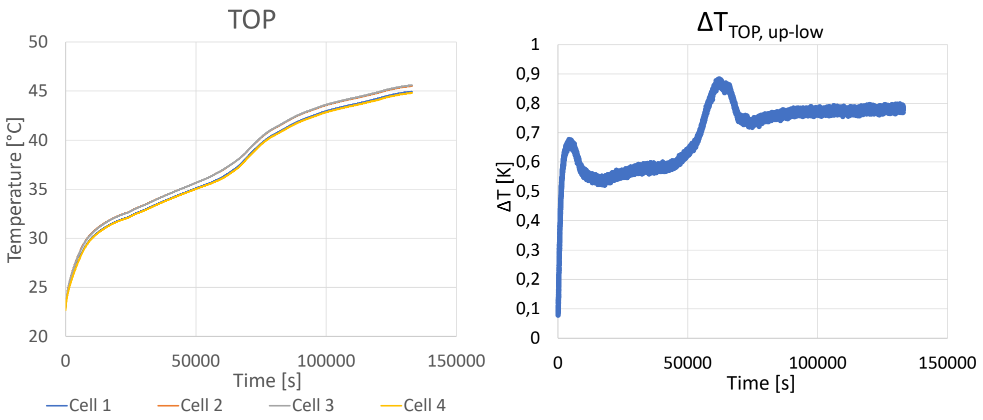

Figure 3.79. *Insulated system, copper-foam-loaded PCM, Test 4.1: temperature trends recorded on the top of all the cells (left) and ΔT trend between the top of the upper and the lower cells (right).*

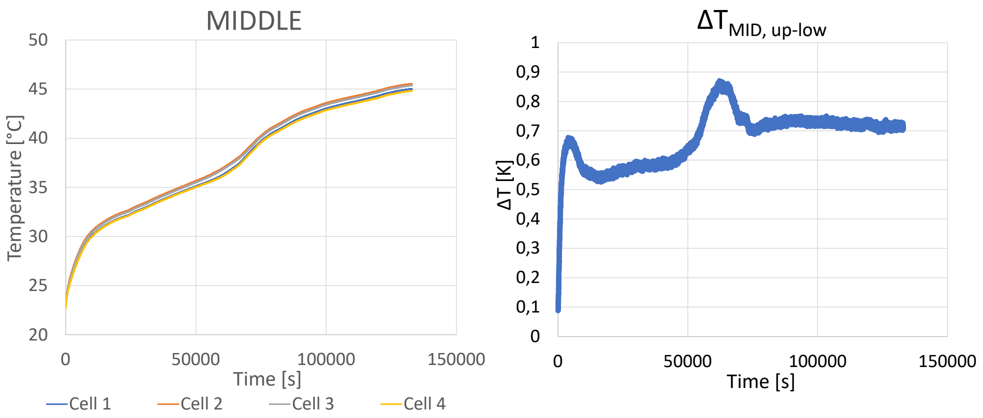

Figure 3.80. *Insulated system, copper-foam-loaded PCM, Test 4.1: temperature trends recorded in the middle of all the cells (left) and ΔT trend between the middle of the upper and the lower cells (right).*

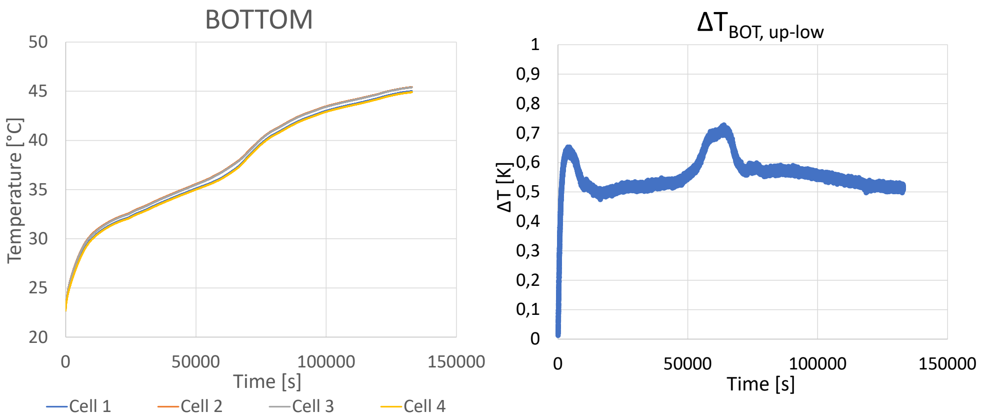

Figure 3.81. *Insulated system, copper-foam-loaded PCM, Test 4.1: temperature trends recorded on the bottom of all the cells (left) and ΔT trend between the bottom of the upper and the lower cells (right).*

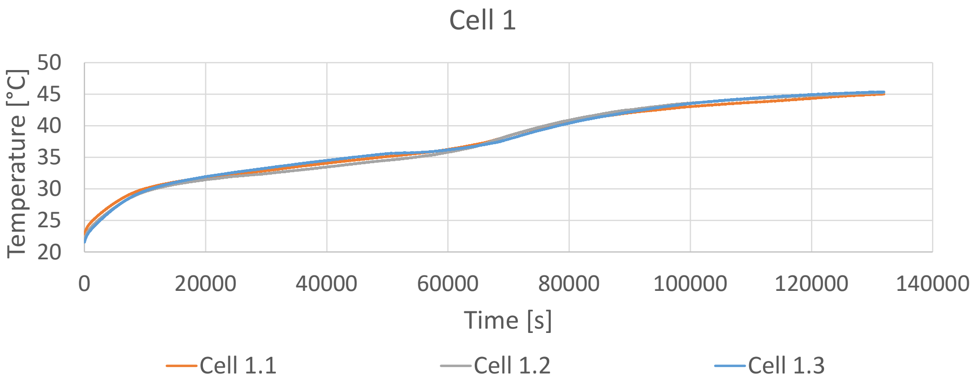

Figure 3.82. *Insulated system, copper-foam-loaded PCM, Test 4.1÷4.3: temperature trends recorded by* TC_{MID} *on Cell 1.*

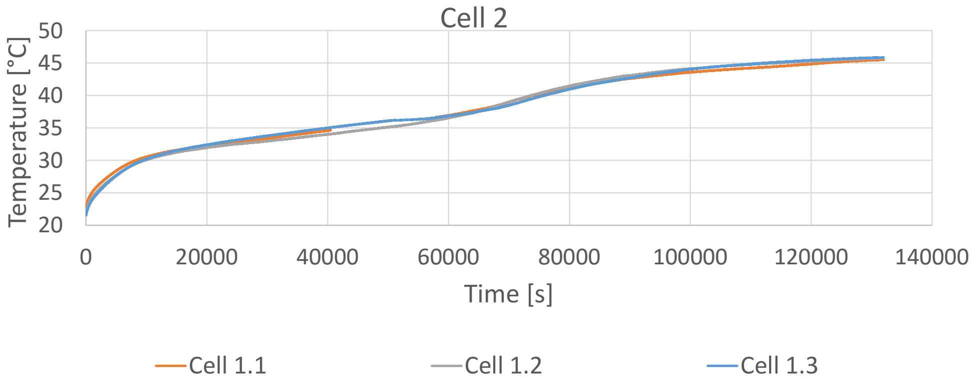

Figure 3.83. *Insulated system, copper-foam-loaded PCM, Test 4.1÷4.3: temperature trends recorded by* TC_{MID} *on Cell 2.*

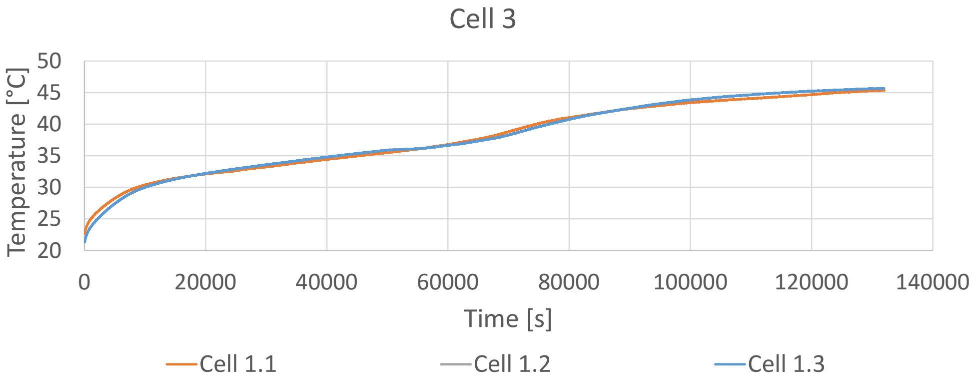

Figure 3.84. *Insulated system, copper-foam-loaded PCM, Test 4.1÷4.3: temperature trends recorded by* TC_{MID} *on Cell 3.*

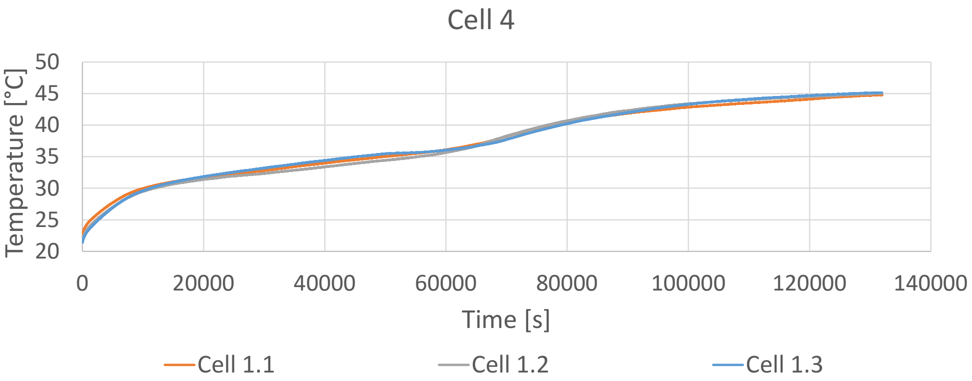

Figure 3.85. *Insulated system, copper-foam-loaded PCM, Test 4.1÷4.3: temperature trends recorded by* TC_{MID} *on Cell 4.*

3.4.9 *PCM and liquid cooling: insulated*

The aim of this new series of tests was to analyse the performances of a PCM-based BTMS coupled with a liquid cooling system which, in turn, used water as a coolant. To do this it was necessary to modify the previous experimental setup, updating it with the cooling circuit. A thermal bath was used to circulate the water along the circuit and to keep the water temperature at the chosen fixed value $T_w = 20$ °C. A flexible silicon tube was chosen to be the channel where the coolant would have flown. As it had to pass through the central hole of the 4-cells element PET support whose diameter was $d_{\text{PET}} = 10\ mm$, the selected tube had an internal diameter $d_{\text{tube, int}} = 8\ mm$ and a thickness $s_{\text{tube}} = 1\ mm$, resulting in a tube whose external diameter was equal to d_{PET}. The tube was inserted into the PET support hole so that the cold-water inlet and the hot-water outlet were in correspondence of the cells bottom and top, respectively (Figure 3.86).

Both the polycarbonate case and the polystyrene box had to be properly adapted for the new cooling system configuration (Figure 3.87): the case was milled and a hole was made to allow the tube to pass through; the insulation box was modified so that the tube could go in and out from it.

An analog flowmeter was inserted into the cooling circuit line to monitor the water flow rate. The chosen flowmeter gave a frequency output signal so a converter was used to transform the frequency into a current output signal which, in turn, was acquired by another NI module (NI-9203). To correlate the acquired current value with the initial flow rate, a flowmeter calibration process was done before starting with the tests (see Appendix 3): thanks to this preliminary work it was possible to determine the flow rate used for Tests 5.1÷5.3 which resulted to be $\dot{m} = 0.058\ kg/s$.

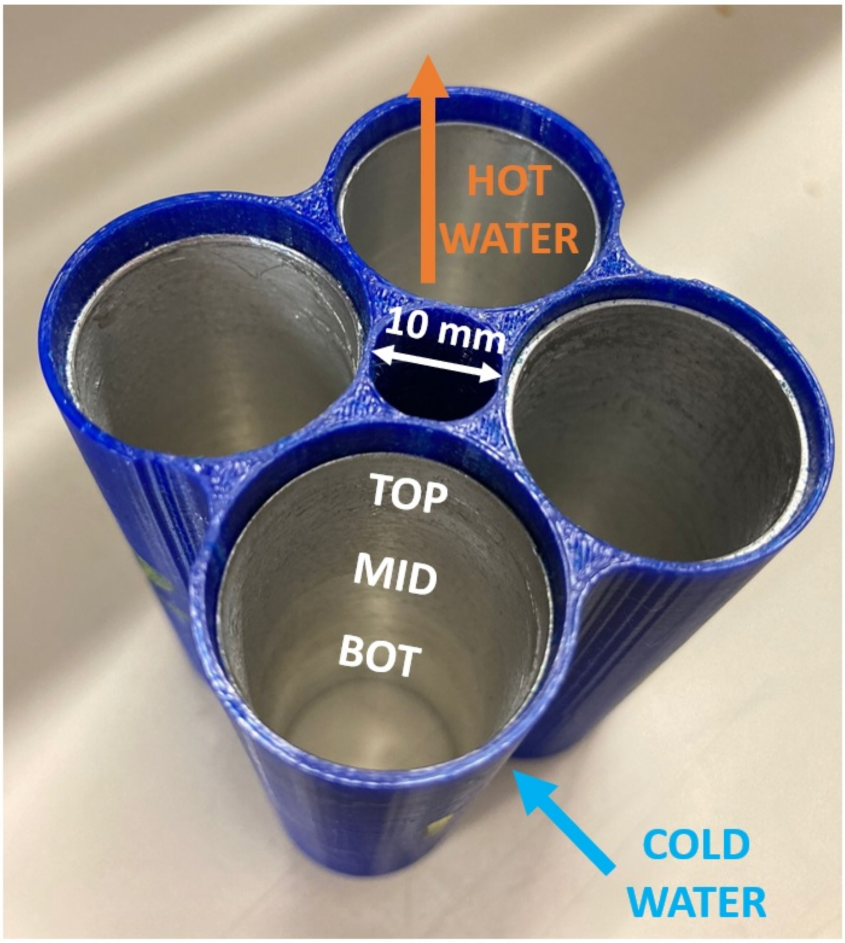

Figure 3.86. *Indications regarding the cold-water inlet and the hot-water outlet of the liquid cooling system.*

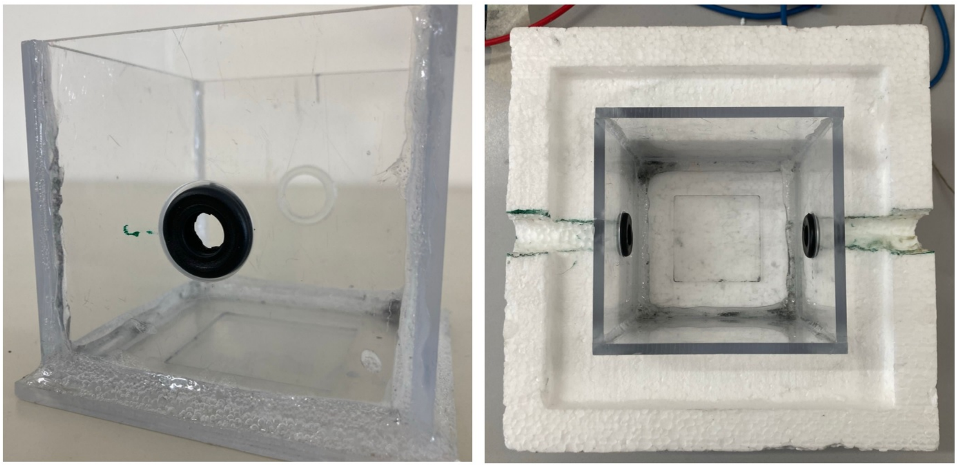

Figure 3.87. *The polycarbonate case and the polystyrene box modified for the water cooling system addition.*

The scheme of the final experimental setup is shown in Figure 3.88: starting from the thermal bath (A), the cold water (light blue line, B) flows out from it to pass through the flowmeter (C), the polystyrene box (dashed line, D), the polycarbonate case (E), then it flows all along the 4-cells element (F) and, finally, it goes out from the box as hot water (red line, G) and enters into the thermal bath again. The signal converter (H) receives the output signals from the flowmeter and sends them to the NI current module (I). Both the current signals and the temperature ones acquired by the NI temperature module (L) are sent to the computer (M) to be elaborated. As seen before, the 4-cells element is linked to a digital power supply (N). With this new configuration another series of tests (Test 5.1÷5.3) was carried on.

With these experiments a passive-active BTMS was tested: the passive section was represented by the PCM-based one, the active section was the water cooling circuit. The 4-cells element was heated until it reached the maximum temperature possible and, once it stabilized on that $T_{\max}$, the cooling system was turned on. The cooling process was stopped when a thermal balance was reached.

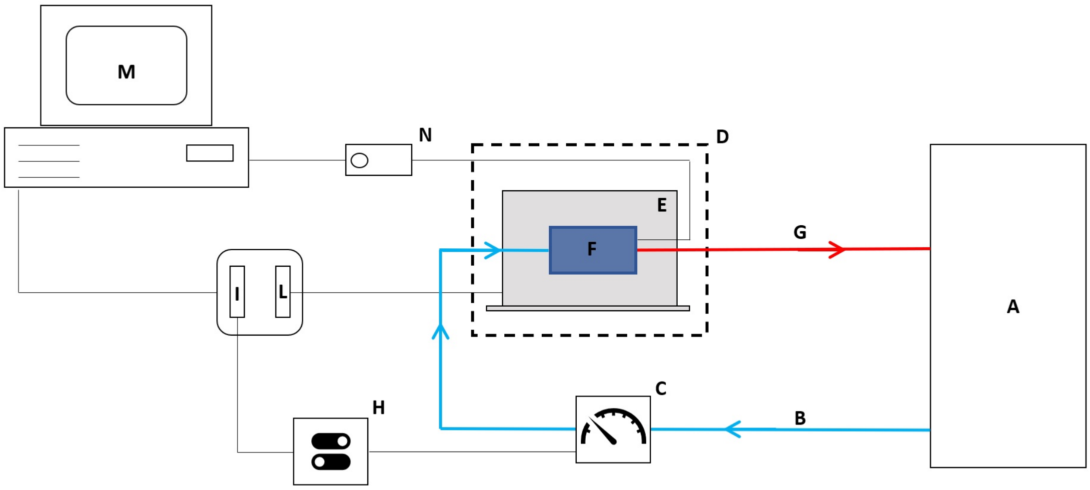

Figure 3.88. *Scheme of the PCM-based BTMS coupled with the water cooling system.*

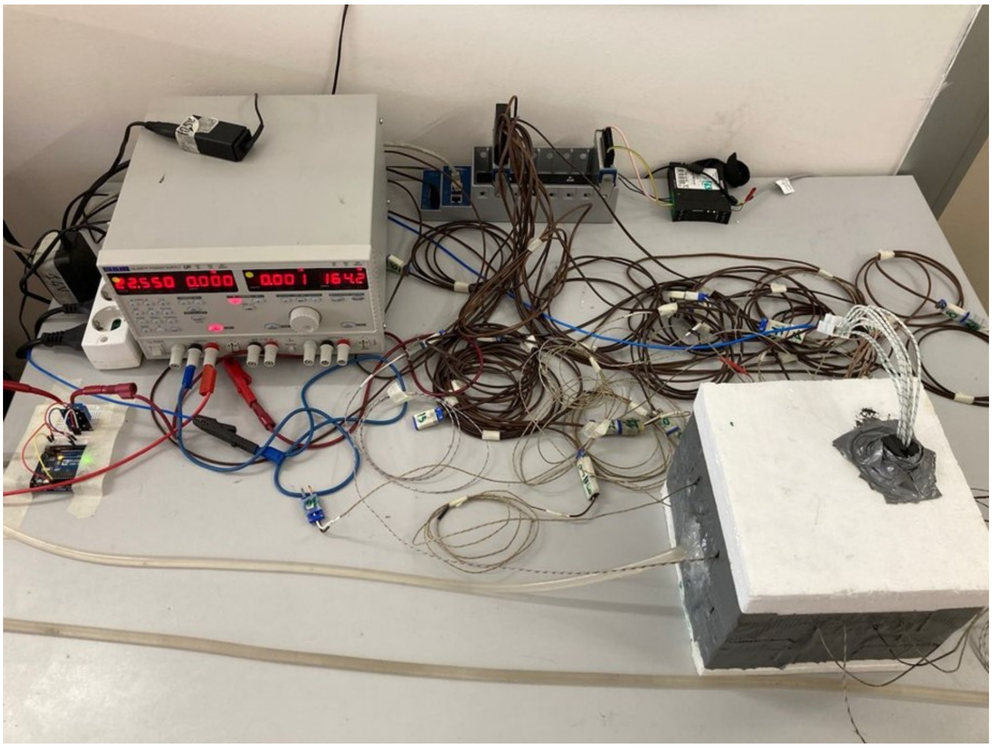

Figure 3.89. *The experimental setup used to test the PCM-based BTMS coupled with the water cooling system.*

3.4.9.1 *Results*

Focusing the attention on Test 5.1 results, looking at Figure 3.94, Figure 3.95 and Figure 3.96 it soon appears that the $\Delta T_{\text{UP-LOW}}$ shows a trend never recorded with the previous experiments. Analyzing the left graphs of the figures and moreover the right ones, it is evident how the $\Delta T_{\text{UP-LOW}}$ does not vary a lot during the cooling process except for a cooling time interval in correspondence of the top of the cells. From $t = 0\ s$ to $t = 5000\ s$ ΔT_{TOP} has a steep decrease starting from about $\Delta T_{\text{TOP, 0}} = 0.85\ K$ which is a higher initial value compared to $\Delta T_{\text{MID, 0}} = 0.47\ K$ and $\Delta T_{\text{BOT, 0}} = 0.31\ K$.

The reason of this phenomenon is that when the experimental setup was realized, to avoid PCM leakages both from the polystyrene box and from the polycarbonate case, all the holes through which the cooling tube passed were sealed with a silicon paste (it is visible in Figure 3.88). After Test 5.1÷5.3, opening the experimental box, it was discovered that some silicon paste was in contact with the top of the upper cells, acting as an insulator and slightly hindering the heat dissipation. The result (Figure 3.94) was that on the top of the 4-cells element, the upper cells were at a higher temperature than the lower ones.

As soon as the liquid cooling system was turned on and the water started to flow, the coolant acted to balance the temperatures all along the cells. As a matter of fact, although the silicon paste issue, looking at the graphs of Test 5.1 $\Delta T_{\text{UP-LOW}}$ tends to zero over time independently from the x-value. Considering Test 5.1÷5.3, the averages of the maximum temperature differences recorded by the top, the middle and the bottom TCs were $\widetilde{\Delta T}_{\text{TOP, max}} = 0.86\ K$, $\widetilde{\Delta T}_{\text{MID, max}} = 0.42\ K$, $\widetilde{\Delta T}_{\text{BOT, max}} = 0.33\ K$ but, considering the aforementioned issue about the silicon paste, the most realistic $\widetilde{\Delta T}_{\text{UP-LOW}}$ value assumable for the whole cell is $\widetilde{\Delta T}_{\text{BOT, max}}$. This is also confirmed by the left graphs in Figure 3.94, Figure 3.95 and Figure 3.96 for Test 5.1 as well as by those related to Test 5.2 and Test 5.3 (see Appendix 4). In Figure 3.90, Figure 3.91, Figure 3.92 and Figure 3.93 the temperature trends show a thermal homogeneity situation all along the cells so, from now on, only the values recorded by TC_{MID} will be considered. Supplementary results related to Test 5.2 and Test 5.3 are reported in Appendix 4.

In Figure 3.97, Figure 3.98, Figure 3.99 and Figure 3.100 the overall results of Test 5.1÷5.3 are presented. The temperature trends do not show dips and rises and exactly overlap for all the cells: this means that the addition of the liquid circuit was functional to overcome the thermal inhomogeneity issues caused by the convective motions (still present with the insulated PCM-based BTMS, see Section 3.4.7.1) whose influence, in this case, is hindered by the more effective liquid cooling effect.

Further, looking at Table 3.13 and comparing these T_{max} values with those showed in Table 3.11, the benefit brought by the coolant is evident: it worked absorbing a part of the cells heat when the liquid system was not turned on yet. As a matter of fact, although at $t = 0\ s$ the cooling process had not yet begun, the averages of the maximum temperatures reached by the cells ranged from 42.05 °C to 42.87 °C, lower values compared to those in Table 3.11 which ranged from 44.87 °C to 45.71 °C. These values recorded in Test 5.1÷5.3 are also lower than those recorded in Test 4.1÷4.3, with the insulated copper-foam-loaded-PCM-based BTMS, when $\widetilde{T}_{\text{max}}$ (Table 3.12) ranged from 45.01 °C to 45.73 °C.

Anther interesting result deals with the lowest temperatures reached by the cells at the end of the cooling process: analysing the data in Table 3.14 it is clear that this BTMS successfully satisfied the thermal requirements for LIBs.

Table 3.13. *Maximum temperatures reached by the cells at the beginning of Test 5.1÷5.3 with pure PCM, in an insulated system coupled with a water cooling circuit.*

	Unit	Cell 1	Cell 2	Cell 3	Cell 4
$T_{\text{max, Test 5.1}}$	[°C]	42.99	42.64	42.44	42.16
$T_{\text{max, Test 5.2}}$	[°C]	42.82	42.37	42.27	42.00
$T_{\text{max, Test 5.3}}$	[°C]	42.79	42.34	42.24	41.98
$\widetilde{T}_{\text{max}}$	[°C]	42.87	42.56	42.32	42.05

Table 3.14. *Minimum temperatures reached by the cells at the end of Test 5.1÷5.3 with pure PCM, in an insulated system coupled with a water cooling circuit.*

	Unit	Cell 1	Cell 2	Cell 3	Cell 4
$T_{\text{min, Test 5.1}}$	[°C]	28.75	29.07	28.97	29.09
$T_{\text{min, Test 5.2}}$	[°C]	28.62	28.80	28.62	28.84
$T_{\text{min, Test 5.3}}$	[°C]	28.90	29.07	28.91	29.07
$\widetilde{T}_{\text{min}}$	[°C]	28.76	28.98	28.83	29.00

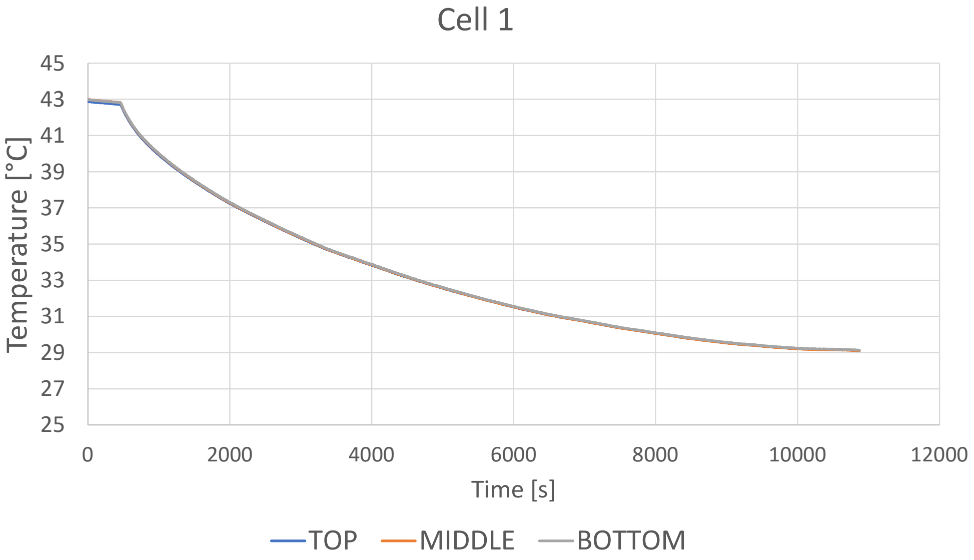

Figure 3.90. *Insulated system, pure PCM and water cooling, Test 5.1: temperature trends recorded by* TC_{TOP}, TC_{MID} *and* TC_{BOT} *along Cell 1.*

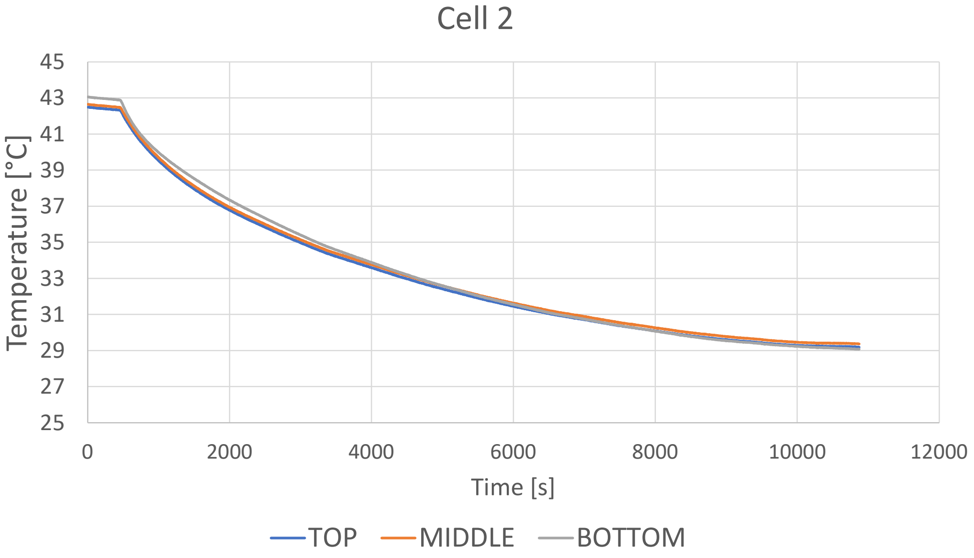

Figure 3.91. *Insulated system, pure PCM and water cooling, Test 5.1: temperature trends recorded by* TC_{TOP}, TC_{MID} *and* TC_{BOT} *along Cell 2.*

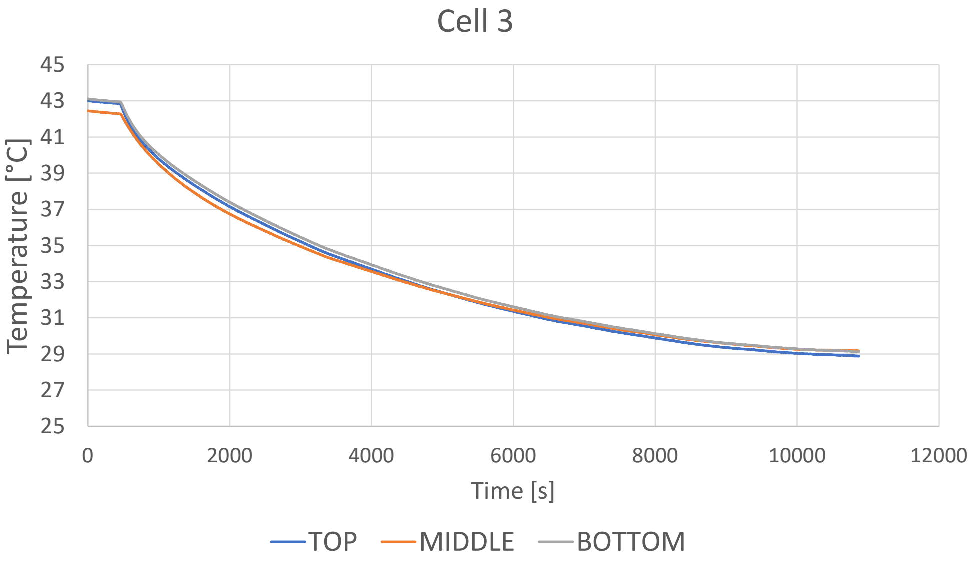

Figure 3.92. *Insulated system, pure PCM and water cooling, Test 5.1: temperature trends recorded by* TC_{TOP}, TC_{MID} *and* TC_{BOT} *along Cell 3.*

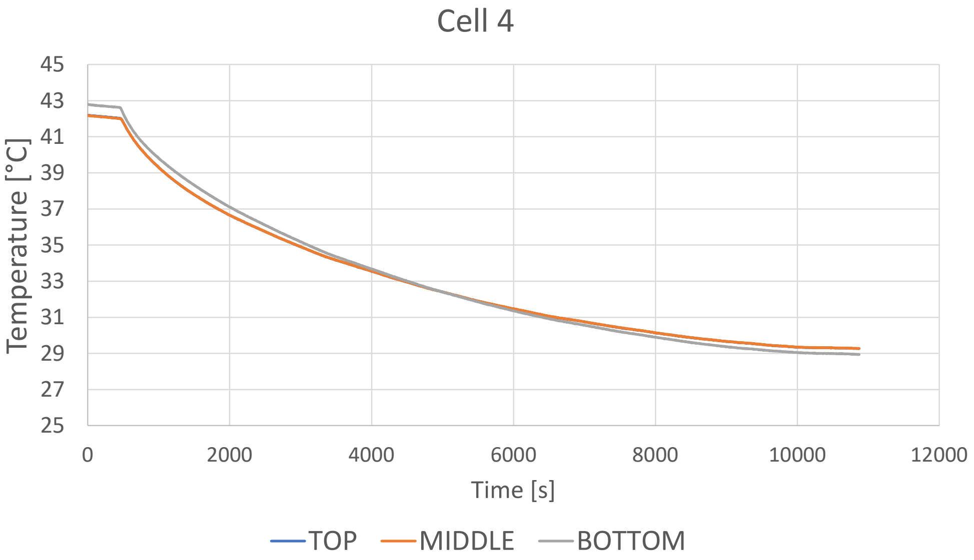

Figure 3.93. *Insulated system, pure PCM and water cooling, Test 5.1: temperature trends recorded by* TC_{TOP}, TC_{MID} *and* TC_{BOT} *along Cell 4.*

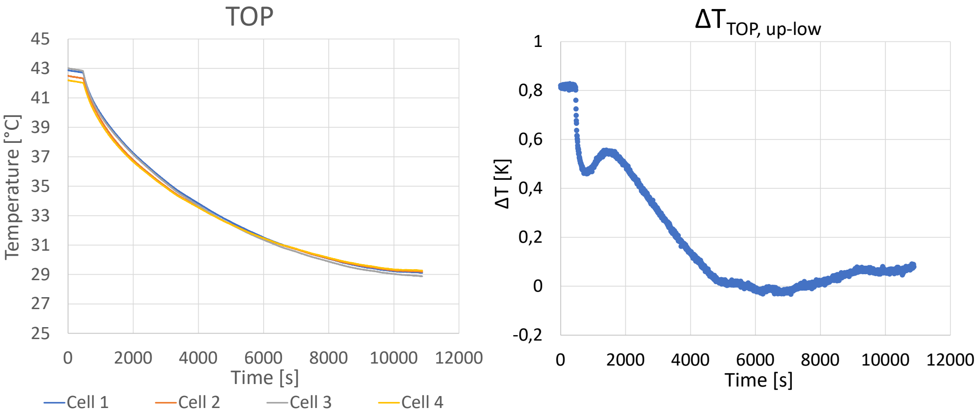

Figure 3.94. *Insulated system, pure PCM and water cooling, Test 5.1: temperature trends recorded on the top of all the cells (left) and* ΔT *trend between the top of the upper and the lower cells (right).*

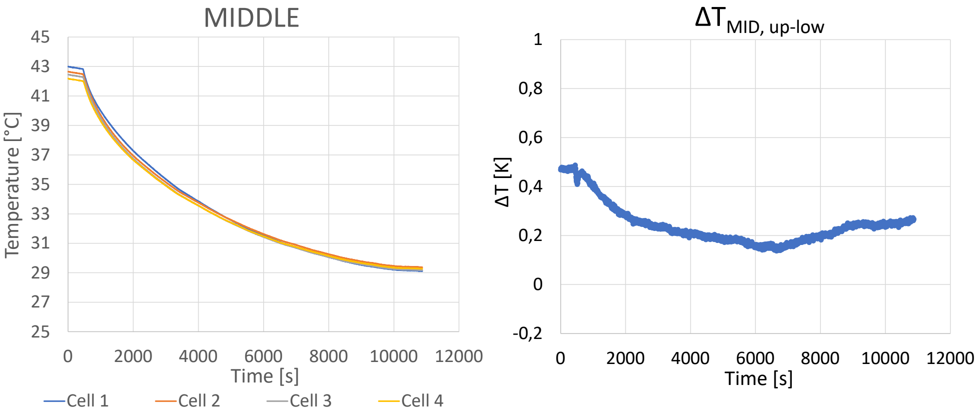

Figure 3.95. *Insulated system, pure PCM and water cooling, Test 5.1: temperature trends recorded in the middle of all the cells (left) and* ΔT *trend between the middle of the upper and the lower cells (right).*

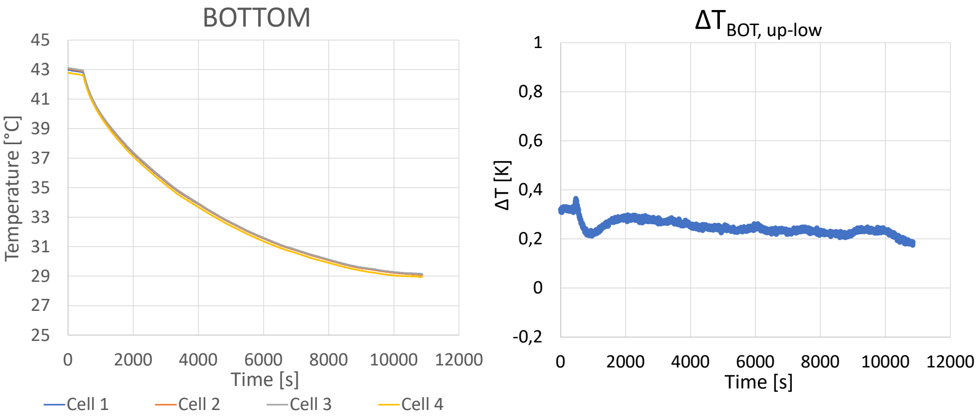

Figure 3.96. *Insulated system, pure PCM and water cooling, Test 5.1: temperature trends recorded on the bottom of all the cells (left) and* ΔT *trend between the bottom of the upper and the lower cells (right).*

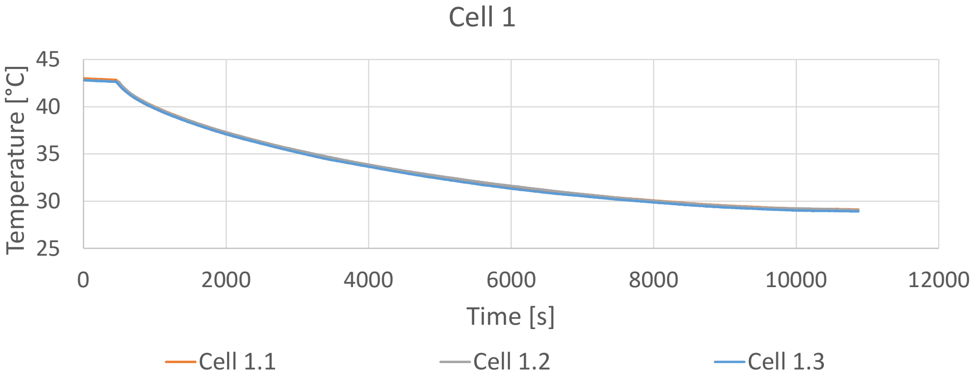

Figure 3.97. *Insulated system, pure PCM and water cooling, Test 5.1÷5.3: temperature trends recorded by* TC_{MID} *on Cell 1.*

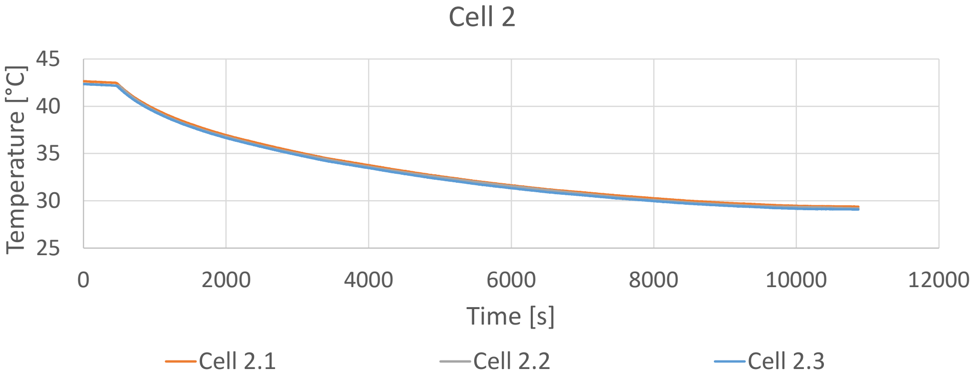

Figure 3.98. *Insulated system, pure PCM and water cooling, Test 5.1÷5.3: temperature trends recorded by* TC_{MID} *on Cell 2.*

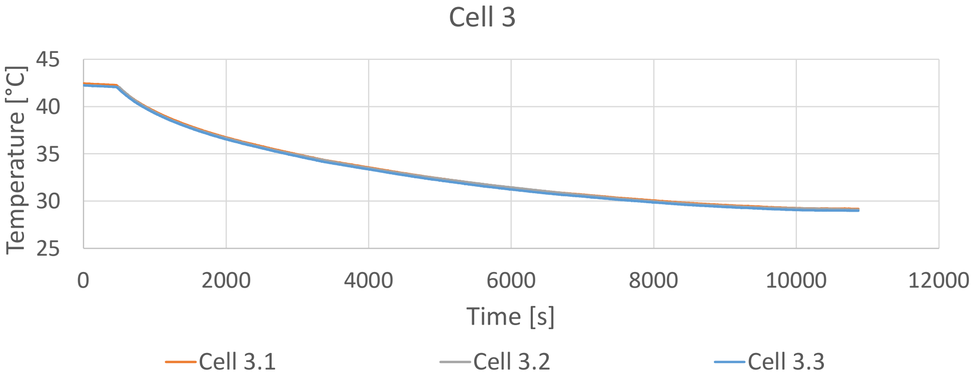

Figure 3.99. *Insulated system, pure PCM and water cooling, Test 5.1÷5.3: temperature trends recorded by* TC_{MID} *on Cell 3.*

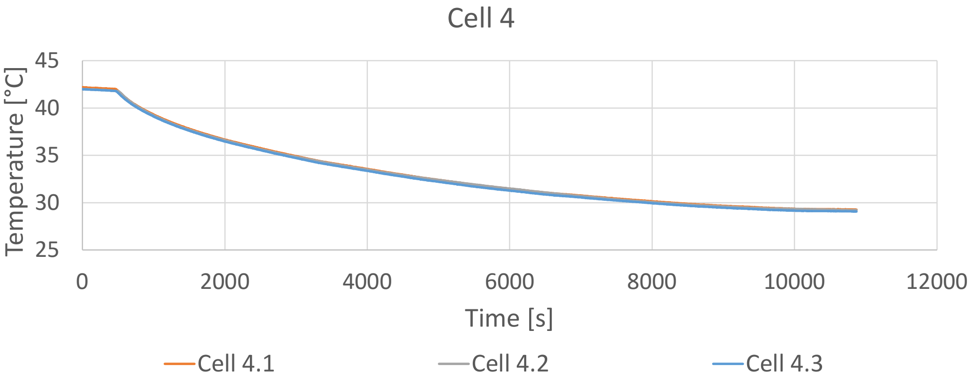

Figure 3.100. *Insulated system, pure PCM and water cooling, Test 5.1÷5.3: temperature trends recorded by* TC_{MID} *on Cell 4.*

3.4.10 *Copper-foam-loaded PCM and liquid cooling: insulated*

For this last series of tests (Test 6.1÷6.3) the experimental rig exploited in Test 5.1÷5.3 was used again, the excess of silicon paste was removed not to create the same issues discussed in Section 3.4.9.1 and the metal foam was added to the system to load the PCM. No other changes were done and three other heating/cooling cycles were analysed.

3.4.10.1 *Results*

Taking into consideration Test 6.1, the first test of this series, and looking at the graphs in Figure 3.105, Figure 3.106 and Figure 3.107, a $\Delta T_{\text{UP-LOW}}$ is visible but the more the time passes and the cooling proceeds, the more it tends to a common value for all the x-values. On the left graphs it is possible to see that the temperatures have almost the same trend for all the four cells, independently from the x-quote: the slight detachment among the temperature curves is completely negligible until $t = 5000\ s$, then the $\Delta T_{\text{UP-LOW}}$ starts to increase very slowly until it reaches its maximum value at the end of the cooling process. However, considering how low the cells temperatures were when the cooling circuit was turned off, this $\Delta T_{\text{UP-LOW}}$ did not represent a big issue.

In particular, during Test 6.1÷6.3, the averages of the maximum temperature differences recorded by the top, the middle and the bottom TCs were $\widetilde{\Delta T}_{\text{TOP, max}} = 0.66\ K$, $\widetilde{\Delta T}_{\text{MID, max}} = 0.68\ K$, $\widetilde{\Delta T}_{\text{BOT, max}} = 0.50\ K$. Considering what it was said in Section 3.4.9.1 about the realistic value of $\widetilde{\Delta T}_{\text{UP-LOW}}$, in this case the temperature difference between the upper and the lower cells was $0.1 \div 0.3\ K$ higher.

In Figure 3.101, Figure 3.102, Figure 3.103 and Figure 3.104 the curves showing the temperature trends along the cells are almost completely overlapped. Supplementary results related to Test 6.2 and Test 6.3 are reported in Appendix 4. As there were no important differences among the temperatures recorded by the three TCs placed on each single cell (not important considering the low temperatures reached, thanks to the liquid cooling), from now on only the values recorded by TC_{MID} will be considered.

In Figure 3.108, Figure 3.109, Figure 3.110 and Figure 3.111 the overall results of Test 6.1÷6.3 are shown. No temperature dips and rises were recorded and in the aforementioned figures it is possible to see that the temperature trends are almost exactly overlapped, except for the final parts of the curves: anyway, the temperatures were so low that such ΔT are negligible. Further, thanks to the addition of the copper foam there was an improvement regarding both the highest starting temperatures and the lowest final ones.

About the maximum temperatures reached by the cells at the beginning of the tests, comparing the results in Table 3.15 with those obtained without metal foam and collected in Table 3.13, it is possible to appreciate a slight decrease of the T_{max} and $\widetilde{T}_{\text{max}}$. The same magnitude of improvement regards the minimum temperatures reached by the cells at the end of Test 6.1÷6.3. In Table 3.16 are shown the T_{min} and the $\widetilde{T}_{\text{min}}$ recorded with the setup configuration tested in this section and, comparing these results with those obtained without metal foam in Table 3.14, it can be said that the insulated copper-foam-loaded-PCM-based BTMS coupled with a water cooling system is the one which allows reaching the lowest temperatures.

Table 3.15. *Maximum temperatures reached by the cells at the beginning of Test 6.1÷6.3 with copper-foam-loaded PCM, in an insulated system coupled with a water cooling circuit.*

	Unit	Cell 1	Cell 2	Cell 3	Cell 4
$T_{\text{max, Test 6.1}}$	[°C]	41.97	41.71	41.51	41.48
$T_{\text{max, Test 6.2}}$	[°C]	42.71	42.35	42.15	42.13
$T_{\text{max, Test 6.3}}$	[°C]	42.69	42.34	42.14	42.14
$\widetilde{T}_{\text{max}}$	[°C]	42.46	42.13	41.93	41.91

Table 3.16. *Minimum temperatures reached by the cells at the end of Test 6.1÷6.3 with copper-foam-loaded PCM, in an insulated system coupled with a water cooling circuit.*

	Unit	Cell 1	Cell 2	Cell 3	Cell 4
$T_{\text{min, Test 6.1}}$	[°C]	28.13	28.88	28.68	25.56
$T_{\text{min, Test 6.2}}$	[°C]	28.03	28.65	28.45	28.41
$T_{\text{min, Test 6.3}}$	[°C]	28.46	29.11	28.91	28.88
$\widetilde{T}_{\text{min}}$	[°C]	28.21	28.88	28.68	28.62

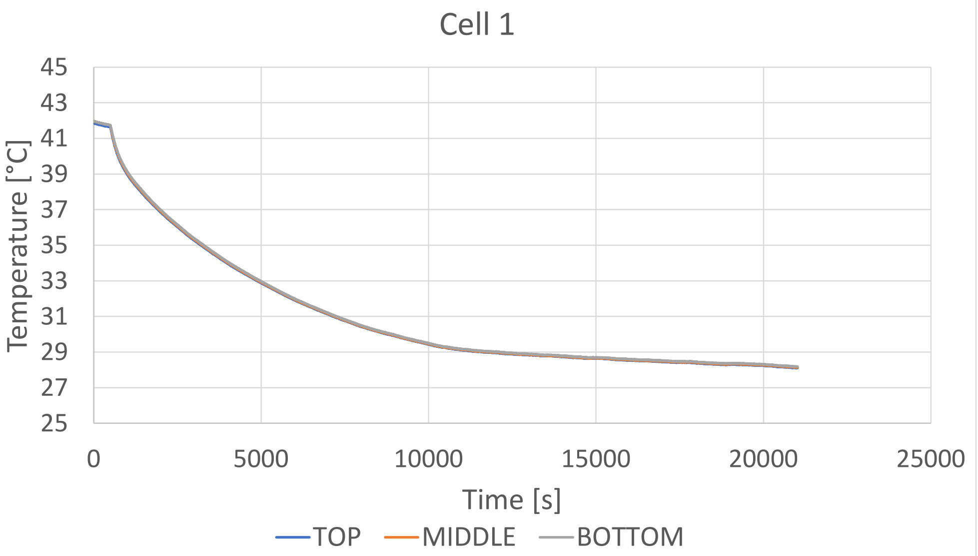

Figure 3.101. *Insulated system, copper-foam-loaded PCM and water cooling, Test 6.1: temperature trends recorded by* TC_{TOP}, TC_{MID} *and* TC_{BOT} *along Cell 1.*

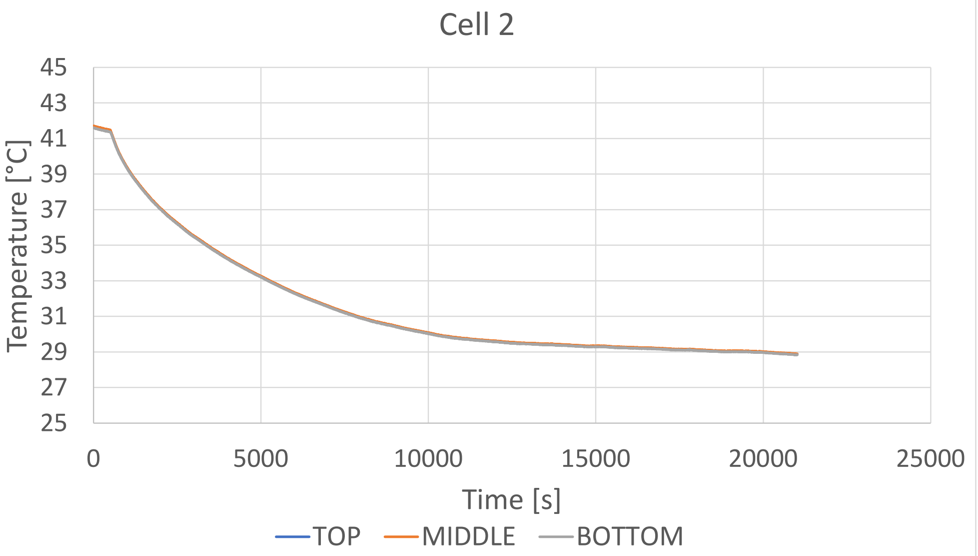

Figure 3.102. *Insulated system, copper-foam-loaded PCM and water cooling, Test 6.1: temperature trends recorded by* TC_{TOP}, TC_{MID} *and* TC_{BOT} *along Cell 2.*

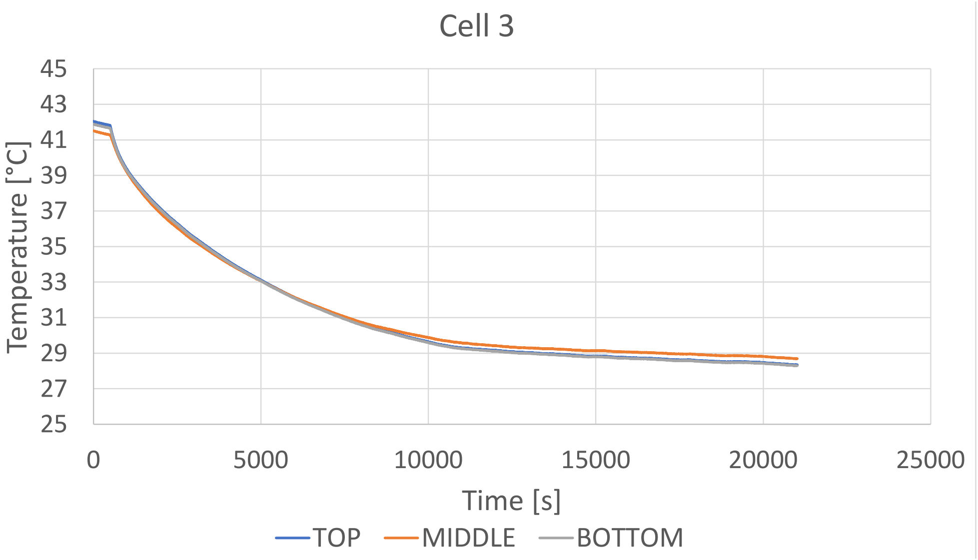

Figure 3.103. *Insulated system, copper-foam-loaded PCM and water cooling, Test 6.1: temperature trends recorded by* TC_{TOP}*,* TC_{MID} *and* TC_{BOT} *along Cell 3.*

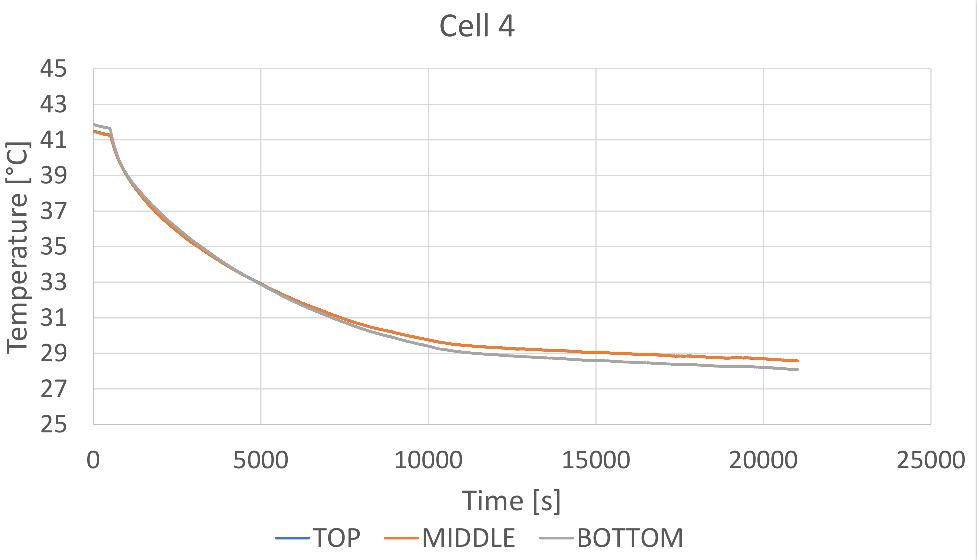

Figure 3.104. *Insulated system, copper-foam-loaded PCM and water cooling, Test 6.1: temperature trends recorded by* TC_{TOP}*,* TC_{MID} *and* TC_{BOT} *along Cell 4.*

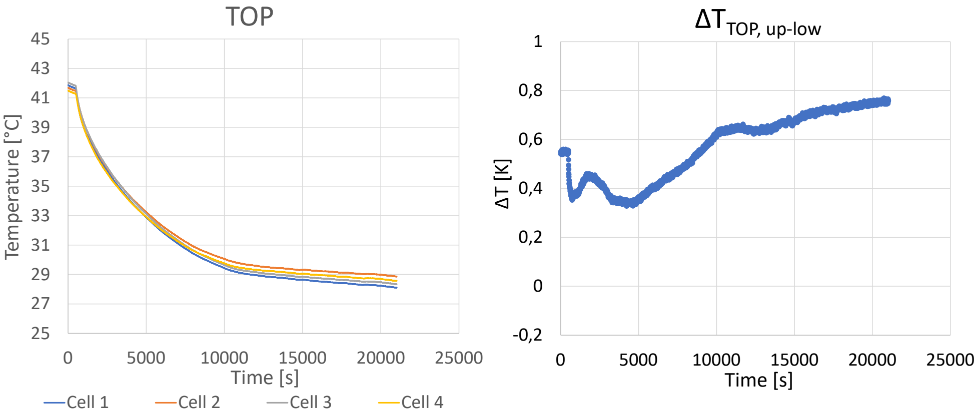

Figure 3.105. *Insulated system, copper-foam-loaded PCM and water cooling, Test 6.1: temperature trends recorded on the top of all the cells (left) and ΔT trend between the top of the upper and the lower cells (right).*

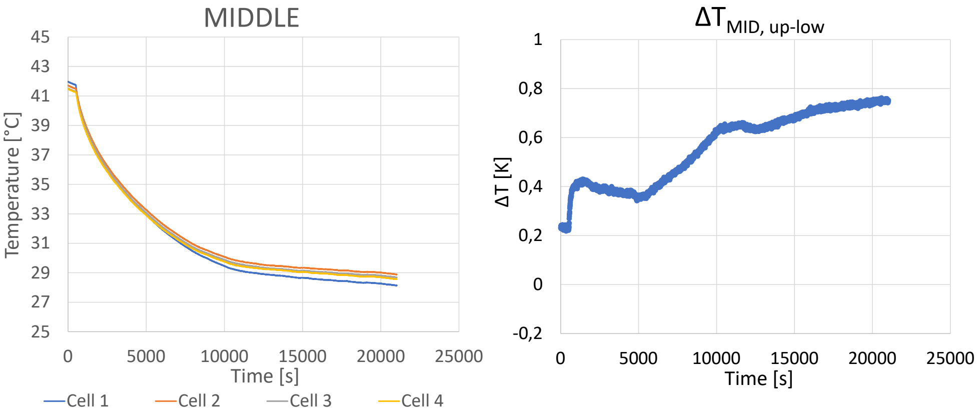

Figure 3.106. *Insulated system, copper-foam-loaded PCM and water cooling, Test 6.1: temperature trends recorded in the middle of all the cells (left) and ΔT trend between the middle of the upper and the lower cells (right).*

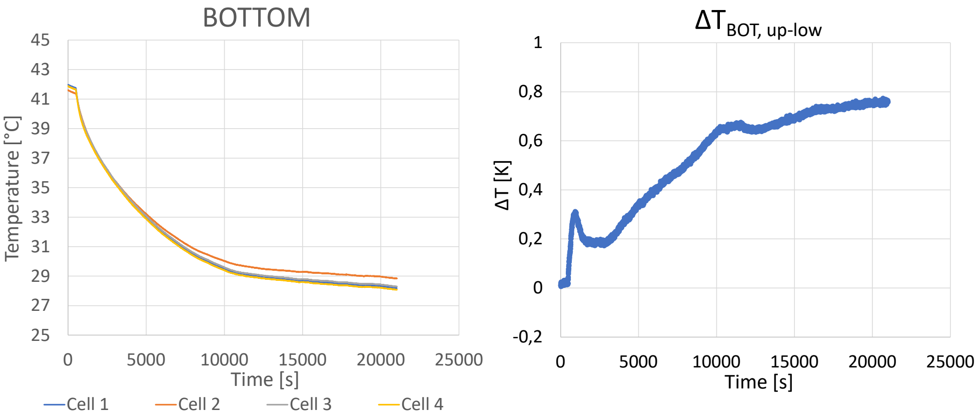

Figure 3.107. *Insulated system, copper-foam-loaded PCM and water cooling, Test 6.1: temperature trends recorded on the bottom of all the cells (left) and ΔT trend between the bottom of the upper and the lower cells (right).*

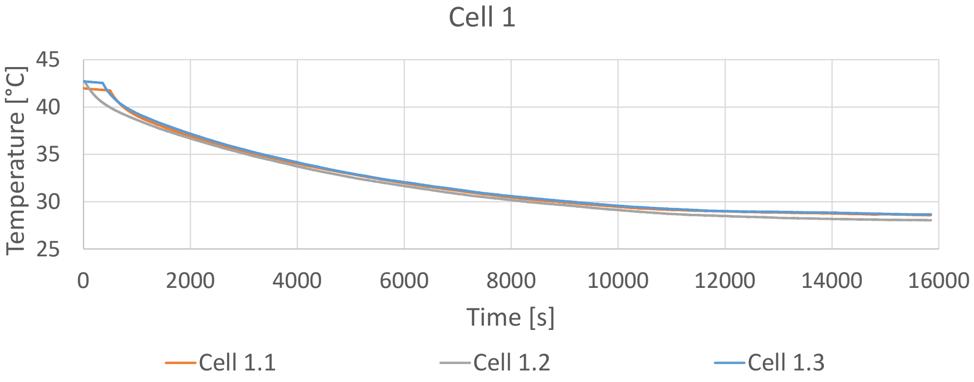

Figure 3.108. *Insulated system, copper-foam-loaded PCM and water cooling, Test 6.1÷6.3: temperature trends recorded by* TC_{MID} *on Cell 1.*

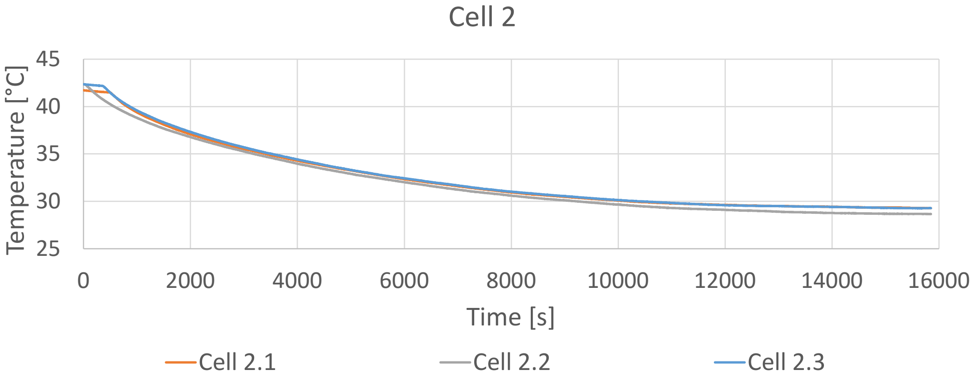

Figure 3.109. *Insulated system, copper-foam-loaded PCM and water cooling, Test 6.1÷6.3: temperature trends recorded by* TC_{MID} *on Cell 2.*

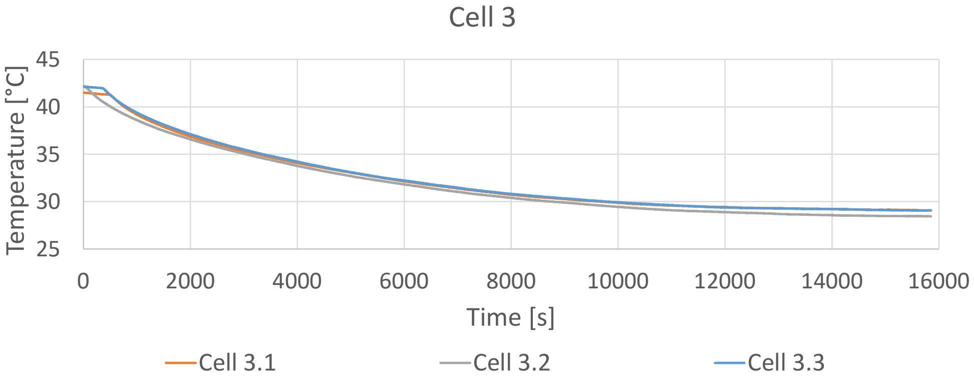

Figure 3.110. *Insulated system, copper-foam-loaded PCM and water cooling, Test 6.1÷6.3: temperature trends recorded by* TC_{MID} *on Cell 3.*

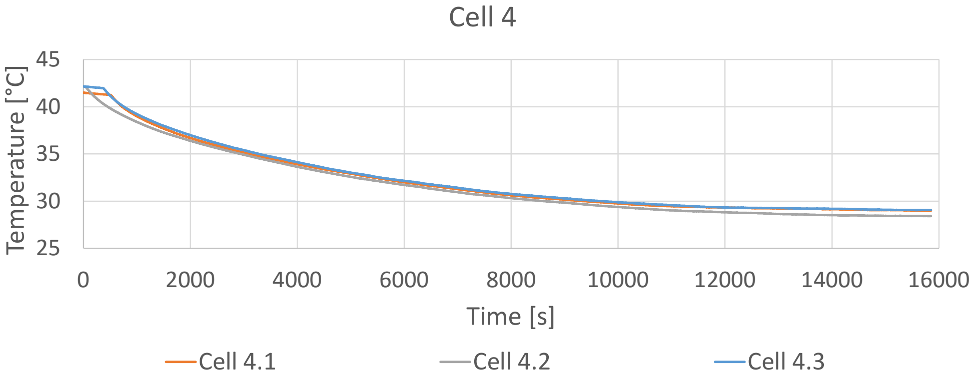

Figure 3.111. *Insulated system, copper-foam-loaded PCM and water cooling, Test 6.1÷6.3: temperature trends recorded by* TC_{MID} *on Cell 4.*

3.4.11 *Conclusions*

This complex experimental campaign was useful to compare the performances of different kinds of BTMSs and offers a valid overview on what is the proper cooling system to install considering the working conditions.

The most innovative BTMS is not always essential and sometimes ordinary cooling systems can be the best choice in terms of installation simplicity and economic investment. This is valid for those applications where a safety battery box is not provided: it is the case of the tests about the forced ventilation, the pure PCM and the copper-foam-loaded PCM cooling (Test 0.1÷0.3, Test 1.1÷1.6 and Test 2.1÷2.5, respectively), all carried on without the insulation box.

With a simple forced-air BTMS (Section 3.4.2.1) results showed that an air flow $\dot{m}_{\text{air}} = 0.0236\ m^3/s = 84.96\ m^3/h$ at a constant temperature $T_{\text{AIR}} = 22.5\ °\text{C}$ was able to cool the system until it reached the average temperature $\widetilde{T}_{\text{min, Test 0.1÷0.3}} = 29.37\ °\text{C}$ (calculated considering the data referred to TC_{MID} in Table 3.4) in an average time $\widetilde{t}_{T_{\text{min}}} = 2400\ s$. During Test 0.1÷0.3, before turning on the fan, the system was left free to heat till an average maximum temperature $\widetilde{T}_{\text{max, Test 0.1÷0.3}} = 45.28\ °\text{C}$ (considering Table 3.3) which is absolutely not a good thermal situation considering the battery SOH. However, this was obviously done for research purposes: in a real BP the forced-air system can be sat to start working at a desired cell temperature, before the batteries reach such high values.

So $\widetilde{T}_{\text{max, Test 0.1÷0.3}}$ does not represent a big issue for this kind of BTMSs. Instead, the measured $T_{\text{UP-LOW}}$ can represent a problem in the bigger real BPs: although the studied 4-cells element was not sealed in a box, it was surrounded by the scaled wind gallery and the temperature difference between the upper and the lower cells was influenced by the position of the cells inside the gallery, with respect to the outer environment. Proceeding towards the area of the 4-cells element closer to the gallery air-outlet (from the cells top to their bottom) $T_{\text{UP-LOW}}$ ranged from 1.68 K to 1.29 K

as, following that direction, the heat of the cells could be more easily dissipated . In huge battery packs such temperature differences have to be avoided. Further, it is not often available enough space to install the forced ventilation system: the pure PCM-based and the copper-foam-loaded-PCM-based BTMSs were considered as possible alternative options.

The power supplied to the tested 4-cells element in Test 1.1÷1.6 and Test 2.1÷2.5 without insulation was $P = 4.73\ W$ and the air temperature was constantly $T_{\text{AIR}} = 22.5\ °C$. After investigating these two systems (Section 3.3.3), results highlighted that with pure PCM there was the development of convective motions which negatively affected the temperature trends and, consequently, the thermal homogeneity. This means that in a real BP, there would be temperature distribution problems.

With this pure PCM-based BTMS the average of the maximum temperatures was $\widetilde{T}_{\text{max, Test 1.1÷1.6}} = 37.33\ °C$ (calculated using the data of Table 3.8) which is surely an appreciable result respect to $\widetilde{T}_{\text{max, Test 0.1÷0.3}}$ but, as said, this value would not be reached in a real application as the BTMS would be put into operation sooner than it was done in the laboratory. All results considered, with an uninsulated BTMS the pure PCM-based solution is not the best to choose. The copper-foam-loaded-PCM-based BTMS studied with Test 2.1÷ 2.5 showed best performances both in terms of average maximum temperatures and because no temperature fluctuations were recorded during all the heating cycles. As a matter of fact, $\widetilde{T}_{\text{max, Test 2.1÷2.5}} = 35.40\ °C$ (calculated with the data showed in Table 3.10) which is 1.93 K lower than $\widetilde{T}_{\text{max, Test 0.1÷0.3}}$. Further, as the convective motions were hindered by the porous structure of the copper metal foam, although all the recorded $T_{\text{UP-LOW}}$ had almost the same values compared to those acquired during Test 1.1÷1.6, with this cooling solution the temperature around the heat source (the cells) was more stable (Figure 3.49) and this represents a benefit for the cells SOH.

It should also be said that the use of metal foams is not so common in the automotive field due to the limited space but, on the other hand, all the automotive LIBs are enclosed in safety boxes. So the copper-foam-loaded-PCM-based BTMS studied in Test 2.1÷2.5 can be a valid solution to cool uninsulated batteries in applications where an ordinary forced-air BTMS cannot be installed due to geometrical issues or because it is not possible to generate air flows (possible powders pollution issues).

Test 3.1÷3.3, Test 4.1÷4.3, Test 5.1÷5.3 and Test 6.1÷6.3 were all carried on in the same insulated environment and with the studied 4-cells element supplied by a power $P = 2\ W$. In an insulated environment batteries dissipate heat worse. Hence, the use of just pure PCM (a good LTES material) resulted to be a self-defeating method to manage the temperature of the cells. As a matter of fact, analysing the data in Table 3.11 it is possible to calculate the average of the maximum temperatures recorded during the tests with the insulated PCM-based BTMS: in this case $\widetilde{T}_{\text{max, Test 3.1÷3.3}} = 45.28\ °C$, not low enough to satisfy the optimal thermal requirements for LIBs. In addition, convective motions into the PCMs could bring to an inhomogeneous temperature distribution inside the battery pack. This is not a good BTMS to take into account for automotive applications.

In Test 4.1÷4.3, the copper-foam-loaded PCM helped in obtaining a better temperature distribution, a higher thermal stability and there were also recorded lower $T_{\text{UP-LOW}}$ compared to the previous case with pure PCM (Test 3.1÷3.3). Unfortunately, in the insulated environment the addition of the copper foam was not enough to satisfy the thermal requirements for LIBs: $\widetilde{T}_{\text{max, Test } 4.1 \div 4.3} = 45.39$ °C, so nothing changed in terms of maximum temperatures respect to Test 3.1÷3.3. This kind of BTMS can be rejected, too.

Test 5.1÷5.3 and Test 6.1÷6.3 were both carried on coupling a liquid cooling circuit to the experimental setup used for Test 3.1÷3.3 and Test 4.1÷4.3, respectively. The liquid system worked with a water flow rate $\dot{m} = 0.058\ kg/s$ at a fixed temperature $T_w = 20$ °C. With the tested liquid-cooled BTMSs (the insulated pure PCM-based and the copper-foam-loaded-based one) there were no temperature fluctuations, it was always recorded a homogeneous thermal distribution and the values of $T_{\text{UP-LOW}}$ were low enough and acceptable considering the lowest temperatures reached by the cells. The averages of the maximum temperatures $\widetilde{T}_{\text{max, Test } 5.1 \div 5.3} = 42.45$ °C and $\widetilde{T}_{\text{max, Test } 6.1 \div 6.3} = 42.11$ °C (calculated thanks to the values showed in Table 3.15 and Table 3.16) were both lower than in the experiments without the liquid cooling system. Further, although these values could seem not acceptable in terms of SOH, it has to be considered that having those setup configurations it is possible to exploit an active cooling method (the liquid cooling). As in Test 0.1÷0.3 with the forced ventilation, the liquid cooling system can be turned on before arriving at such high temperatures.

About the averages of the minimum temperatures, $\widetilde{T}_{\text{min, Test } 5.1 \div 5.3} = 28.89$ °C and $\widetilde{T}_{\text{min, Test } 6.1 \div 6.3} = 28.60$ °C (calculated with the data in Table 3.13 and Table 3.14) were great results which make both of these setups suitable in terms of thermal requirements. However, as there were not important performance differences between these two systems and considering the already mentioned lack of space in the automotive LIBs, the pure PCM-based BTMS coupled with the water cooling system proved to be the best choice for automotive applications. Further, considering the high LTES capability of the PCMs, this kind of BTMS represents a good solution against extremely low temperature environments, too.

In Table 3.17 the overall results regarding all the six series of tests are shown. The averages of T_{min} are given just for the active cooling methods, whereas with the passive cooling methods it was only possible to obtain the averages of T_{max}.

Table 3.17. *Averages of T_{max} and T_{min} recorded during all the six series of tests.*

		$\widetilde{T}_{\mathrm{max}}$ [°C]	$\widetilde{T}_{\mathrm{min}}$ [°C]
NO INSULATION	Forced-air	45.25	29.37
	PCM	37.08	–
	Cu-loaded PCM	35.40	–
INSULATED	PCM	45.28	–
	Cu-loaded PCM	45.39	–
	PCM + water	42.45	28.90
	Cu-loaded PCM + water	42.11	28.60

4

LIFE CYCLE ASSESSMENT

4.1 INTRODUCTION

In a society where the energy demand is constantly growing hand in hand with the technological development and, at the same time, the environmental issue awareness is rising, studies about the life cycle assessment (LCA) have become fundamental. Before 2015, when the EU Circular Economy Action Plan had not come into play yet [177], the LCA was already a discussion topic but in particular in the research environments. The outdated and most common way of approaching goods production was mainly focused on performances and costs, in a "linear life thinking" which caused dramatic results in terms of raw materials usage. The United Nations Environment Programme (UNEP) stated that in the last 40 years the raw material consumption tripled, going from 27 billions of tons in 1970 to 98 billions of tons in 2018 [178].

In the last decade, the LCA is acquiring interest involving not only the academic world but also the industry stakeholders who began to change their mindset, switching to the new "circular life thinking" or life cycle thinking (LCT) [179]. Both private realities (industries, companies) and public ones (governments) started to embrace the green economy principles, establishing and regulating business models so that both materials and products could keep their highest value throughout their whole life cycles [180, 181]. The new way of thinking about the product impact does not only consider its disposal stages [182] but also all the production phases, from the extraction of the raw materials to the manufacturing processes, not neglecting the use of energy and water, the wastes and the transportation emissions.

Finally, the disposal of the product is investigated taking into account the possibility to recycle all or part of it. This last consideration is the key-point which distinguishes the two different approaches to the product impact:

- Cradle-to-grave
- Cradle-to-cradle

The cradle-to-grave approach dates from the '90s [182] and increased the producers awareness about the real consumption related to their production, teaching the LCT and motivating them not to waste resources.

It was in 2002 when the definition of cradle-to-cradle came out thanks to the chemist Michael Braungart and the architect William McDonough: making a parallelism with nature where "the waste of one system becomes food for another" [183], they suggested a product impact approach where the products arrived at the end of their lives would have become a sort of raw material to produce something of equal or even better quality. As it is possible to see in Figure 4.1, this innovative LCT implied recycling processes which, in the last decades, have been developed and improved a lot in every field.

The International Organization for Standardization (ISO) includes widely recognized procedures to conduct valid and deepen LCA studies [184]. In particular ISO 14040 and ISO 14044 represent the basis of the International Reference Life Cycle Data System (ILCD), a technical guidance to carry on accurate LCAs considering product-specific criteria [179].

Figure 4.1. *A scheme of the cradle-to-cradle LCT.*

To complete a detailed and useful LCA, ISO 14040 and ISO 14044 suggest to proceed following four different phases which are often interdependent one from each other. Nevertheless, none of these stages should be considered as concluded until the entire study is complete. The aforementioned stages are the following:

- Goal and scope;
- Life cycle inventory (LCI);
- Life cycle impact assessment (LCIA);
- Interpretation.

During the goal and scope stage the intended application and audience have to be defined, as well as the reason of the study and whether the results will be used in a comparative dissertation publicly released. This is a fundamental preliminary phase which helps not to waste time during the following ones, focusing the attention on the real core of the investigation.

The LCI is the data collecting phase resulting from an input and output analysis and quantification: this is the moment when a real inventory is compiled considering raw materials, energy and water requirements, atmospheric emissions, resources usage and all the other flows involved in a product or process life cycle. Flow charts as the Sankey diagram are very helpful during this phase.

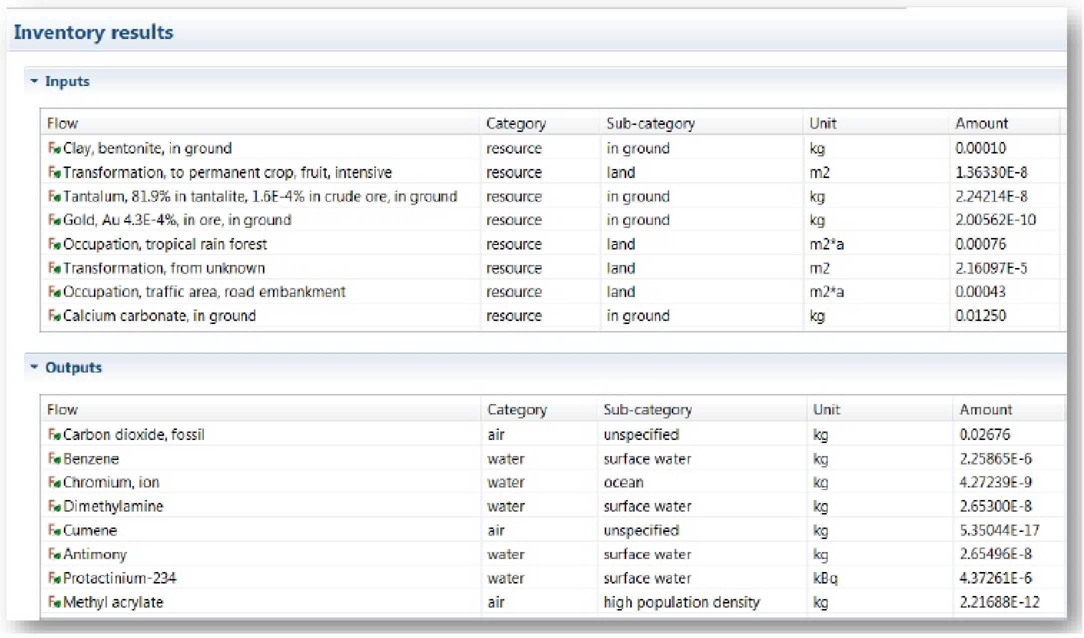

Inventory results

Inputs

Flow	Category	Sub-category	Unit	Amount
Clay, bentonite, in ground	resource	in ground	kg	0.00010
Transformation, to permanent crop, fruit, intensive	resource	land	m2	1.36330E-8
Tantalum, 81.9% in tantalite, 1.6E-4% in crude ore, in ground	resource	in ground	kg	2.24214E-8
Gold, Au 4.3E-4%, in ore, in ground	resource	in ground	kg	2.00562E-10
Occupation, tropical rain forest	resource	land	m2*a	0.00076
Transformation, from unknown	resource	land	m2	2.16097E-5
Occupation, traffic area, road embankment	resource	land	m2*a	0.00043
Calcium carbonate, in ground	resource	in ground	kg	0.01250

Outputs

Flow	Category	Sub-category	Unit	Amount
Carbon dioxide, fossil	air	unspecified	kg	0.02676
Benzene	water	surface water	kg	2.25865E-6
Chromium, ion	water	ocean	kg	4.27239E-9
Dimethylamine	water	surface water	kg	2.65300E-8
Cumene	air	unspecified	kg	5.35044E-17
Antimony	water	surface water	kg	2.65496E-8
Protactinium-234	water	surface water	kBq	4.37261E-6
Methyl acrylate	air	high population density	kg	2.21688E-12

Figure 4.2. *An example of LCI showing input and output flows [185].*

Knowing the methods to extract or machine the materials, it is possible to work on the impact assessment. First it is necessary to classify the kind of impact associated to the considered material (climate change, ozone depletion, human toxicity). Then, all the inventory items (flows) have to be characterized: this means that every flow related to a certain kind of impact has to be classified under a common unit of comparison [184]. For instance, considering the Global Warming Potential (*GWP*) as impact, the unit is the equivalent CO_2 weight which has to be assigned to all the items in the inventory. This procedure is usually done with the help of databases. Finally there is the interpretation of the collected data: the LCI and the LCIA are checked, evaluated and all the issues coming from the investigation of these two previous phases are identified and faced, choosing among a broad repertoire of methodological alternatives [186]. A series of limitations and recommendations represents the final result of the interpretation phase.

4.2 LCA OF THE LIBER BATTERY PACK

Nowadays the LCA is a powerful weapon to achieve important goals such as the waste reduction and a clearer awareness about energy consumption. It is exploited in several fields such as packaging [187], food processes [188, 189] and drink consumption [190, 191], tourism [192], textile industry [193] and so on. Automotive is another huge sector where the LCA analysis are applied, studying the car lightening effects [194], the benefits of using recycled natural materials [195] and, when it talks about EVs, the attention is often focused on the LIBs [196, 197, 198].

About this, a LCA study on a battery pack unit is presented here below. The chosen product is the *LiBER* (Lithium Battery for Emilia-Romagna) battery pack whose prototype was installed on the solar car *Emilia 4* (see Section 1.5). To the present date, the modular *LiBER* BP has not been commercialized yet but there are only the final steps to do before the industrialization and marketing phases [199]. The entire BP is made of 2 modules composed of 15 bricks each and all the bricks are, in turn, realized with 48 Li-ion cells. One of this brick is the BP unit taken into consideration for this LCA analysis. For the *LiBER* LCA study it was chosen to divide the analysis into three main research macro-topics usually taken into consideration in this field [200]:

- Cells support
- Li-ion cells
- Liquid-cooled BTMS

The LCA was conducted as a cradle-to-gate analysis (a partial cradle-to-grave without the study of the product disposal) and concerning the kind of resultant impact it was chosen to consider both the energy demand (*ED*) and the *GWP*.

The transportation impact was evaluated considering a diesel powered *IVECO ECOSTRALIS Active AS* truck for the road transport and a HFO powered *MAN S90ME-C9.2-GI* ship for the sea transport, a 8000 *TEU* (Twenty-foot Equivalent Unit) cargo provided with a two-stroke marine engine. 1 *TEU* represents the dimension of an ordinary container whose maximum payload is 24000 *kg*.

As the *LiBER* headquarter is based in Bologna (Emilia-Romagna, Italy) this influenced the choice of where to stock up the materials, aiming to obtain as low transport emissions as possible. All the data related to the impact of the transportation means are shown in Table 4.1 and Table 4.2.

Table 4.1. *Impact evaluation data of a diesel powered IVECO ECOSTRALIS Active AS truck considering a payload of* 10200 *kg.*

	Unit	Value
Emissions	[kg_{CO_2}/l]	2.65
Fuel consumption	[l/km]	0.3
Fuel calorific value	[MJ/kg]	45
Fuel density	[kg/l]	0.83

Table 4.2. *Impact evaluation data of a HFO powered MAN S90ME-C9.2-GI cargo ship considering an average speed* $\widetilde{v}_{cargo} = 23.5\ kn = 43.6\ km/h$ *[201] .*

	Unit	Value
Emissions	$[g_{CO_2}/\mathrm{km\ t}]$	12.5
Fuel consumption	[t/d]	206.8
Fuel calorific value	[MJ/kg]	42.7

4.2.1 *Cells support impact*

In Figure 4.3 the *LiBER* cells support is shown: it is a plastic structure with 48 holes for the Li-ion cells arranged in a 6x8 configuration: an aluminum liner in each hole works to better dissipate the heat generated by the cells. This configuration is the same of the scaled 4-cells element discussed in Section 3.4.1.

About the aluminum it was assumed to be all primary aluminum as the majority of literature data about the impact evaluations (*ED* and *GWP*) deal with that kind of metal. The LCA about the plastic part of the support involved the analysis of two different materials: the polyoxymethylene (POM) used in the manual production line and the acrylonitrile butadiene styrene (ABS) used in the automatic production line. Following, both the aluminum and the plastic impact evaluations are presented.

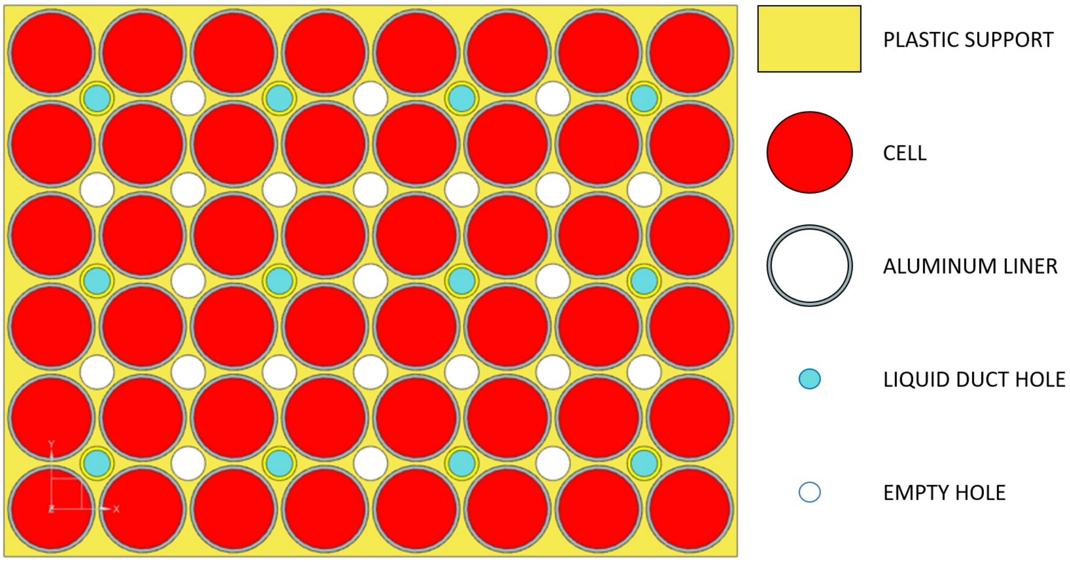

Figure 4.3. *A scheme of the LiBER brick plastic support.*

4.2.1.1 *Raw material extraction and processing*

ALUMINUM The production processes involving the primary aluminum are the bauxite extraction, the Bayer process (the conversion from bauxite to alumina), the Hall–Héroult process (the smelting of the alumina into molten cryolite followed by the electrolysis of the molten salt bath) [202]. Then it comes the T6 temper, a heat treatment which consists in two phases: the quenching (a heating process followed by a sudden cooling) and the artificial ageing [203]. The *ED* and the *GWP* values related to the aluminum processes are shown in Table 4.3 (the cutting process *ED* was considered negligible) and Table 4.4.

POM Talking about the POM, a block of material is obtained starting from the coarse powder, thanks to a molding process [204]. Then, the block is machined with a CNC miller, removing the chips. During the machining process there is an 87% volume reduction: in order to obtain a realistic analysis, the overall machining process was split into a coarse machining for the 65% of the removed volume and a fine machining for the 17% of it. The *ED* and the *GWP* values related to the POM processes are shown in Table 4.5 and Table 4.6.

ABS Regarding the ABS it was chosen the UL 94 V0 according to the Standard for Safety of Flammability of Plastic Materials: this kind of ABS shows great performances in case of fire emergency, succeeding in stopping the burning process on a vertical specimen within 10 seconds [205]. The ABS processes deal with a coarse powder molding phase carried on with a hot chamber injection molding method [204]: this means that before the process the ABS gross mass is equal to the ABS net mass after the injection. The *ED* and the *GWP* values related to the POM processes are shown in Table 4.7 and Table 4.8.

4.2.1.2 *Extraction and processing impact: results*

All the results regarding the extraction and the processing impact related to the materials needed for the cells support are collected in the tables here below.

Table 4.3. *Average ED related to the aluminum processes [206, 207].*

Process	ED [MJ/kg_{Al}]
Extraction	1.04
Processing	148.42
Heat treatments	21
Coarse machining	1.47
Total	171.93

Table 4.4. *Average GWP related to the aluminum processes [207].*

Process	GWP [kg_{CO_2}/kg_{Al}]
Extraction	0.07
Processing and heat treatments	8.46
Total	8.53

Table 4.5. *Average ED related to the POM processes [208, 209, 210].*

Process	ED [MJ/kg_{POM}]
Primary production	86.00
Block molding	16.00
Coarse machining	1.29
Fine machining	8.38
Total	109.67

Table 4.6. *Average GWP related to the POM processes [208, 209, 210].*

Process	GWP [kg_{CO_2}/kg_{POM}]
Primary production	3.20
Block molding	1.20
Coarse machining	0.10
Fine machining	0.63
Total	5.13

Table 4.7. *Average ED related to the ABS processes [208, 209, 210].*

Process	ED [MJ/kg_{ABS}]
Primary production	104.80
Injection molding	19.05
Total	123.85

Table 4.8. *Average GWP related to the ABS processes [208, 209, 210].*

Process	GWP [kg_{CO_2}/kg_{ABS}]
Primary production	3.89
Injection molding	1.43
Total	5.32

4.2.1.3 *Material transportation*

Regarding the aluminum transportation impact, two options were considered. The first one involved the transport of the Al6065: this kind of metal has been chosen for the real *LiBER* brick but it gives a remarkable negative contribution to the emissions due to the distance of its current stocking up site (Jiangsu, China). The second option was the Al6063: with almost the same mechanical and physical characteristics of the Al6065, this metal is a good substitute as it is available in Italy (San Colombano al Lambro). The transportation impacts related to the POM and the ABS are presented in this section, too. Here below, the calculations for the transport emissions are shown step by step so that they can be taken as example for all the other transport contributions.

ALUMINUM 6065 Choosing the Al6065 it was necessary to consider both the cargo ship and the truck. The cargo covers a distance $s_{\text{cargo}} = 19535\ km$ at an average speed $\tilde{v}_{\text{cargo}} = 43.6\ km/h$, meaning that it takes $t_{\text{cargo}} = 448.05\ h = 18.669\ d$ to travel the whole path. As the daily fuel consumption is $F_{\text{day, cargo}} = 206.8\ t/d$ (Table 4.2), the total fuel consumption results $F_{\text{TOT, cargo}} = 3860.7\ t$. Knowing that the emission factor for cargo ships related to the grams of CO_2 emitted per kilometer and ton is $f_{\text{CO}_2\text{, cargo}} = 12.5\ g_{\text{CO}_2}/km\ t$ [201], the specific emission (GWP_{s}) can be calculated as $GWP_{\text{s, cargo}} = f_{\text{CO}_2\text{, cargo}} \cdot s_{\text{cargo}}$ which, in numbers, becomes $GWP_{\text{s, cargo}} = 12.5\ g_{\text{CO}_2}/km\ t_{\text{Al}} \cdot 19535\ km \cdot 10^{-3}\ kg_{\text{CO}_2}/g_{\text{CO}_2} \cdot 10^{-3}\ t_{\text{Al}}/kg_{\text{Al}} = 0.244\ kg_{\text{CO}_2}/kg_{\text{Al}}$. As said, the chosen cargo ship was a 8000 TEU with a maximum payload for each container $Pl_{\text{cargo}} = 24000\ kg$. Hence, the total emissions are $GWP_{\text{TOT, cargo}} = GWP_{\text{s, cargo}} \cdot (8000 \cdot Pl_{\text{cargo}}) = 46848000\ kg_{\text{CO}_2}$.

The transport ED takes into consideration the fuel calorific value for HFO (H_{HFO}, Table 4.2) so that $CED_{\text{cargo}} = F_{\text{TOT, cargo}} \cdot H_{\text{HFO}} = 164851890\ MJ = 164851.89\ GJ$. Finally, it is possible to calculate the specific energy demand as $ED_{\text{s, cargo}} = CED_{\text{cargo}}/(8000 \cdot Pl) = 0.859\ MJ/kg_{\text{Al}}$.

Talking about the Al6065 road transportation, the calculations were easier. The truck covers a distance $s_{\text{truck}} = 1565\ km$ with a total fuel consumption $F_{\text{TOT, truck}} = 469.5\ l$ (considering the average fuel consumption of the truck, Table 4.1). Taking into account the emission factor for trucks ($f_{\text{CO}_2\text{, truck}}$, Table 4.1), the total emissions are $GWP_{\text{TOT, truck}} = F_{\text{TOT, truck}} \cdot f_{\text{CO}_2\text{, truck}} = 1244.18\ kg_{\text{CO}_2}$ and the specific emissions are $GWP_{\text{s, truck}} = GWP_{\text{TOT, truck}}/Pl_{\text{truck}} = 0.122 kg_{\text{CO}_2}/kg_{\text{Al}}$.

As the diesel density is $\rho_{\text{d}} = 0.83\ kg/l$, converting the fuel consumption $F_{\text{TOT, truck}} = 469.5\ l = 389.685\ kg$ and considering the diesel calorific value (Table 4.1) it is possible to calculate $CED_{\text{truck}} = F_{\text{TOT, truck}} \cdot H_{\text{d}} = 17535.825\ MJ = 17.54\ GJ$. Dividing this value by the truck payload the result is $ED_{\text{s, truck}} = CED_{\text{truck}}/Pl_{\text{truck}} = 1.72\ MJ/kg_{\text{Al}}$.

Once all the contributions coming from the cargo and the truck transportation are found, it is possible to obtain the overall ED and GWP specific values for the Al6065: $GWP_{\text{s, Al6065}} = 0.366\ kg_{\text{CO}_2}/kg_{\text{Al}}$, $ED_{\text{s, Al6065}} = 2.579\ MJ/kg_{\text{Al}}$.

ALUMINUM 6063 With the same logic, the ED and GWP values are calculated for the Al6063, considering a travel distance $s_{\text{truck}} = 175\ km$. In this case $GWP_{\text{s, Al6063}} = 0.013\ kg_{\text{CO}_2}/kg_{\text{Al}}$, $ED_{\text{s, Al6063}} = 0.196\ MJ/kg_{\text{Al}}$.

POM For the transportation impact of both kinds of plastics it was just considered the road transport emission contribute as the materials are available in Italy at a relative short distance from Bologna. Regarding the POM, the common trade routes were studied and finally it was assumed that the material came from Brescia (Italy) and travelled along the route Brescia-Minerbio-Bologna ($s_{\text{POM}} = 238\ km$).

Considering this, the specific and the overall ED and GWP values are $GWP_{\text{TOT, POM}} = 189\ kg_{\text{CO}_2}$, $GWP_{\text{s, POM}} = 0.018\ kg_{\text{CO}_2}/kg_{\text{POM}}$, $CED_{\text{POM}} = 2723.4\ MJ$, $ED_{\text{s, POM}} = 0.267\ MJ/kg_{\text{POM}}$.

ABS Brescia was chosen as stocking up site for the ABS too but, this time, following the route Brescia-Ravenna-Bologna ($s_{\text{ABS}} = 353\ km$). Results for ABS are: $GWP_{\text{TOT, ABS}} = 280.63\ kg_{\text{CO}_2}$, $GWP_{\text{s, ABS}} = 0.028\ kg_{\text{CO}_2}/kg_{\text{ABS}}$, $CED_{\text{ABS}} = 3978\ MJ$, $ED_{\text{s, ABS}} = 0.390\ MJ/kg_{\text{ABS}}$.

4.2.1.4 *Transportation impact: results*

All the results regarding the transportation impact related to the materials needed for the cells support are collected in Table 4.9.

Table 4.9. *Average ED and GWP related to the transportation impact of the cells support materials.*

		ED [MJ/$kg_{material}$]		GWP [kg_{CO_2}/$kg_{material}$]	
		TRUCK	CARGO	TRUCK	CARGO
Materials	Al6065	1.72	0.86	0.12	0.24
	Al6063	0.20	–	0.01	–
	POM	0.27	–	0.02	–
	ABS	0.40	–	0.03	–

4.2.2 *Li-ion cells impact*

The cells chosen for the LCA analysis were the *INR* 21700 *P42A* produced by *Molicel* [211]: these are cylindrical NMC batteries ($LiNiMnCoO_2$ cathode) whose electrochemical properties are similar to those of the *LiBER* BP. This kind of cells is a quite common choice in the BP mass production when frequent charging/discharging cycles are required (energy storage, automotive): the reason is the that the low cobalt content brings to lower costs [212].

Besides the anode and the cathode components, the study of a cell initially deals with many other materials such as the binder constituents, the separator ones, the electrolyte salt and its additives and, enclosing the whole assembly, the nickel-plated steel cell casing.

More in details, the binder works as an electrode coating having a safety function: during the chemical reactions it keeps the active material (cathode) in the right position, also enabling a great connection between the electrodes and the cell terminals. The separator prevents the cell short-circuit and facilitates the Li-ions diffusion process, the electrolyte salt plays a key role in the Li-ions transport between the cathode and the anode and the electrolyte solvent improves the salt stability, preventing the dendrite formation. Finally, the external nickel-plated steel casing keeps all the elements of the cells together and protects them from impacts and moisture corrosion issues thanks to the high chemical resistance of *Ni*.

As the cells are composed of several materials (much more than the cells support), before starting with the impact evaluation, some assumptions were done: it was decided not to take into consideration the binder as its constituent material (polyvinylidene fluoride, PVDF) represents a negligible mass percentage (< 1%) [211] in the chosen NMC cells [200]; the chosen separator composition was equal to 50% of polypropylene (PP) and 50% of polyethylene (PE) (several composition percentages can be found in the literature); the electrolyte solvent was considered as 50% dimethyl carbonate (DMC) made and 50% ethylene carbonate (EC) made as the other carbonates which usually compose the NMC cell solvent are in much lower and negligible percentages. Also the cell casing was not considered as in the overall CO_2 emissions balance its impact is lower than 1% [200]. Once these assumptions were done, the following inventory was prepared [211]:

- **Anode**: graphite coating on a copper foil;
- **Cathode**: $CoLiO_2$, Mn, Ni coating on an Al foil;
- **Separator**: 50% PP, 50% PE;
- **Electrolyte salt**: lithium hexafluorophosphate ($LiPF_6$);
- **Electrolyte solvent**: 50% DMC, 50% EC.

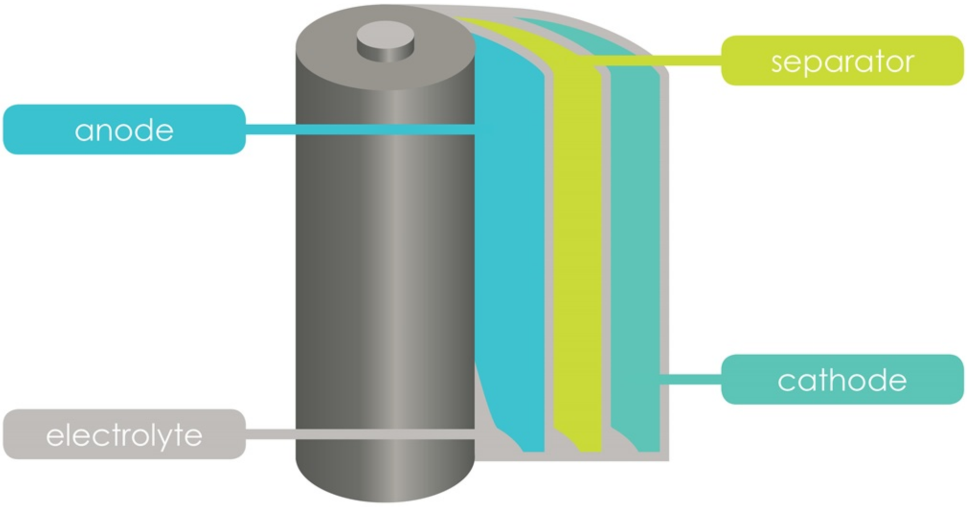

Figure 4.4. *The scheme of a BP cell [213].*

In this LCA study the assembly process was not taken into consideration as its impact is negligible in terms of ED and GWP. Researches demonstrated that the cell assembly energy demand and the CO_2 emissions are much lower than those related to the impact coming from the cell processing (in particular from the processes involving the anode and the cathode) [197]. Other studies highlighted how reasonable is this assumption comparing the extremely low emissions for the entire battery pack assembly and those associated with the overall LCA ($GWP_{\text{ASS}} \simeq 0.7 \cdot GWP_{\text{TOT}}$) [214] .

4.2.2.1 *Raw material extraction*

The ED and GWP evaluations were conducted as previously seen for the elements of the cells support, so the calculations are not shown step by step as done before. Here below, the specific extraction impact values for each element are reported.

ALUMINUM For the aluminum extraction results are $GWP_{\text{s, Al}} = 0.078\ kg_{\text{CO}_2}/kg_{\text{Al}}$; $ED_{\text{s, Al}} = 1.040\ MJ/kg_{\text{Al}}$ [207].

COPPER The extraction copper process first involves sulphide ores which, then, are processed to become pure copper (these processes have been discussed below). For the copper (sulphide ores) extraction results are $GWP_{\text{s, Cu}} = 1.20\ kg_{\text{CO}_2}/kg_{\text{Cu}}$; $ED_{\text{s, Cu}} = 28.3\ MJ/kg_{\text{Cu}}$ [215].

LITHIUM Lithium is usually obtained via brine evaporation or it is extracted mining a pegmatite rock (spodumene or petalite) [216]. A brine extraction is possible in presence of saline lakes, seawater, saline sedimentary basins and wherever high-$NaCl$-concentration solutions are available. This extraction method is based on the natural ores leaching from the Andes mountain range, accumulated underground as brines [217] and then pumped to the surface [218]. The brine is stored inside open pools under the sun (Figure 4.5), so that the salt concentration increases thanks to the evaporation. The Chilean brines located in the Atacama desert are natural water solutions characterized by the highest content of Li and P and representing the largest lithium extraction site in the world [217]. The exploitation of spodumene or petalite ores happens in open-pit mines and it is more common in countries such as Bolivia, Zimbawe, Australia, Canada and Portugal.

Figure 4.5. *Brine evaporation pools in the Atacama desert, Chile.*

Both of these extraction methods lead to obtain lithium carbonate and they are not so different in terms of environmental impact [216, 219] considering favorable weather conditions. On the contrary, Stamp et al. [219] demonstrate that unfavorable conditions such as solar discontinuity and the consequent inefficient evaporation make the ore extraction choice the best one. As a matter of fact, mines are not afflicted by the weather changes as the brine sites.

In this LCA study, a brine extraction carried on with favorable conditions was considered. For the brine extraction results are $GWP_{\text{s, Li}} = 4.50\ kg_{\text{CO}_2}/kg_{\text{Li}}$ [218, 220]; $ED_{\text{s, Li}} = 31.15\ MJ/kg_{\text{Li}}$ [219].

COBALT This element is produced worldwide as a byproduct of copper, nickel and silver and copper-cobalt ores are the most common source where to extract these materials [221]. The cobalt is never used alone but it is needed to produce NMC powder, starting from $CoSo_4$ which is then mixed with $NiSo_4$, $MnSO_4$ and other chemical compounds present in lower quantities. For the cobalt extraction $GWP_{\text{s, Co}} = 38\ kg_{\text{CO}_2}/kg_{\text{Co}}$; $ED_{\text{s, Co}} = 653\ MJ/kg_{\text{Co}}$ [222].

MANGANESE This is a very abundant element on Earth, available in more than 30 countries. The manganese is extracted from open-pit mines where there is usually a mixture of several manganese oxides such as pyrolusite, romanechite, manganite: considering the battery cells, the manganese is used as MnO_2, that is the pyrolusite composition. After the extraction, several steps follow (beneficiation, smelting, refining [216]) before obtaining the manganese. The final results for the extraction are: $GWP_{\text{s, Mn}} = 6.20\ kg_{\text{CO}_2}/kg_{\text{Mn}}$ [216]; $ED_{\text{s, Mn}} = 16.5\ MJ/kg_{\text{Mn}}$ [223].

NICKEL Nickel is the most important material in terms of cathode mass: as a matter of fact, a NMC cathode is 80% nickel made [224]. Further, it is a natural source and so fully recyclable, not showing quality and performance decrease issues. For the nickel extraction results are $GWP_{\text{s, Ni}} = 8.84\ kg_{\text{CO}_2}/kg_{\text{Ni}}$; $ED_{\text{s, Ni}} = 155\ MJ/kg_{\text{Ni}}$ [225].

GRAPHITE This is the most stable form of coal (in standard conditions) and it is possible the extract it from open-pit mines or from the underground. There are two kinds of graphite: the natural and the synthetic one, both producing almost the same CO_2 emissions [226]. Considering the *Molicel* datasheet [211], it was chosen to consider the synthetic graphite as anode constituent. For the synthetic graphite extraction results are $GWP_{\text{s, C}} = 1.80 \div 8.20\ kg_{\text{CO}_2}/kg_{\text{C}}$ [216]; $ED_{\text{s, C}} = 4.80 \div 5.20\ MJ/kg_{\text{C}}$ [221].

4.2.2.2 *Extraction impact: results*

All the results regarding the extraction impact related to the materials needed for the cells are collected in Table 4.10 which shows the values of both ED and GWP.

Table 4.10. *Average EP and GWP related to the extraction of the raw materials for the cells.*

Materials	ED [MJ/$kg_{material}$]	GWP [kg_{CO_2}/$kg_{material}$]
Al	1.04	0.08
Cu	28.30	1.20
Li	31.15	4.50
Co	653.00	38.00
Mn	16.50	6.20
Ni	155.00	8.84
Graphite	5.00	5.00
Total	889.99	55.82

4.2.2.3 *Material processing*

Once obtained all the raw materials, the majority of them have to be processed in one or more phases, achieving the final form to be useful for the needed product. For this LCA study several production lines were evaluated in terms of environmental impact, in particular those referred to the production of the lithium carbonate (Li_2CO_3), the synthetic graphite and the copper current collector for the anode, the *Co-Mn-Ni* powder and the aluminum current collector for the cathode, the separator manufacturing, the electrolyte salt and solvent, the nickel plated steel casing.

LITHIUM CARBONATE Once the brine is stored into the open pools (Section 4.2.2.1) the purification occurs (it takes about one year): this is the phase when the lithium concentration increases [218]. Then, a carbonation process follows [219]: this chemical reaction involves lithium and sodium carbonate (Na_2CO_3), producing Li_2CO_3. The lithium carbonate production chain ends with the compound filtration and washing and, finally with the packaging phases. For the Li_2CO_3 processing results are: $GWP_{\mathrm{s,\,Li_2CO_3}} = 2.02\ kg_{\mathrm{CO_2}}/kg_{\mathrm{Li_2CO_3}}$; $ED_{\mathrm{s,\,Li_2CO_3}} = 28.43\ MJ/kg_{\mathrm{Li_2CO_3}}$ [219]. Li_2CO_3 is then used in the chemical processes to obtain the cathode powders.

ANODE GRAPHITE POWDER The synthetic graphite preparation process deals with several phases such as the initial petroleum coke grinding and sizing and the following mixing where the coke is blended with pitch in the desired proportion. After an extrusion process, the mixture is heated at $800 \div 1000\ °C$ in a natural-gas-fired furnace. This baking phase is often doubled, putting in the middle a further impregnation phase during which the mixture is blended with more pitch to improve the final graphite properties. Finally, the graphitization occurs: this fully electricity-powered phase slowly brings the product until $3000\ °C$, so the graphite crystal formation can start [221]. Results for the anode graphite processing are $GWP_{\mathrm{s,\,gr}} = 4.86\ kg_{\mathrm{CO_2}}/kg_{\mathrm{gr}}$; $ED_{\mathrm{s,\,gr}} = 89.87\ MJ/kg_{\mathrm{gr}}$ [226].

COPPER ANODE CURRENT COLLECTOR After the extraction of sulphide ores, a beneficiation phase ($GWP_{\text{s, Cu}} = 2.40\ kg_{\text{CO}_2}/kg_{\text{Cu}}$ [216]) is necessary to transform the ores into a slurry from which skimming the copper minerals. These minerals are then dried and sent to the smelter ($GWP_{\text{s, Cu}} = 1.8 \div 7.4\ kg_{\text{CO}_2}/kg_{\text{Cu}}$ [216]). To obtain a copper anode collector it is finally required a refining phase, processing the metal and obtaining $4 \div 12\ \mu m$ thick foils [227]. First, an aqueous solution of copper sulfate ($CuSO_4$) has to be prepared, dissolving electrolytic copper or waste copper in a sulfuric acid (H_2SO_4) solution. Then, the metallic copper is electrodeposited on a cathodic roller surface thanks to an electrolytic reaction. At the same time, one side of the resulting copper foil is peeled to achieve the desired thickness, so that the final product is a foil having one rough side and one smooth side [228, 229].

In general, two main methods can be followed for the copper processing: a pyrometallurgical technique ($ED_{\text{s, Cu}} = 33\ MJ/kg_{\text{Cu}}$) or a hydrometallurgical one ($ED_{\text{s, Cu}} = 64\ MJ/kg_{\text{Cu}}$) [230, 229]. For this LCA study, pyrometallurgy was chosen as more related literature data were available. For the copper current collector processing results are $GWP_{\text{s, Cu}_{\text{anod}}} = 4.1\ kg_{\text{CO}_2}/kg_{\text{Cu}_{\text{anod}}}$; $ED_{\text{s, Cu}_{\text{anod}}} = 47\ MJ/kg_{\text{Cu}_{\text{anod}}}$ [229].

CATHODE *NI-MN-CO* POWDERS The most common cathode composition in NMC cells is that of the NMC111 cells (also known as NMC333) so called because the *Ni-Mn-Co* blend is in the ratio 1:1:1 (or 3:3:3) [231, 232]. Regarding the impact evaluation of the cathode powder, discordant results are present in the literature if considering analytical [233] or experimental investigations [226]. In this LCA study the experimental results were taken into account.

The cathode powders production begins with a reaction among $NiSO_4$, $MnSO_4$ and $CoSO_4$, all mixed in a co-precipitate with $NaOH$ and NH_4OH. The product of this reaction is $Ni_{1/3}3Mn_{1/3}3Co_{1/3}$ and then it follows a multi-stage reaction called calcination. This is a high temperature heating process where the co-precipitation product reacts with Li_2CO_3 producing cathode powders. For the cathode *Ni-Mn-Co* powder processing results are $GWP_{\text{s, Ni-Mn-Co}} = 16.11\ kg_{\text{CO}_2}/kg_{\text{Ni-Mn-Co}}$; $ED_{\text{s, Ni-Mn-Co}} = 231.28\ MJ/kg_{\text{Ni-Mn-Co}}$ [226].

ALUMINUM CATHODE CURRENT COLLECTOR After the extraction, the raw aluminum is processed (the main phases are discussed in Section 4.2.1.1) till reaching the ingot casting [216]. Then, the ingot has to be machined as the thickness of the final product has to decrease until about $10 \div 20\ \mu m$ [234]. To do this multiple rolling processes are necessary.

The aluminum rolling method exploits steel rolls to dramatically reduce the ingot thickness which usually ranges from $0.46\ m$ to $0.76\ m$ [207]. Operations start with a hot rolling phase during which ingots are pre-heated at $500\ °C$. The process energy demand is strictly related to the ingot temperature which, in turn, influences the time process: the higher is the ingot temperature, the lower is the energy needed to deform the aluminum block, as well as the processing time. Partial results for the hot rolling are $GWP_{\text{s, Al}_{\text{hot}}} = 0.41\ kg_{\text{CO}_2}/kg_{\text{Al}_{\text{hot}}}$; $ED_{\text{s, Al}_{\text{hot}}} = 7.06\ MJ/kg_{\text{Al}_{\text{hot}}}$ [207]. After the hot rolling, a cold rolling follows: the product thickness continues to decrease and the environment temperature is kept around 80 °C. Partial results for the cold rolling are $GWP_{\text{s, Al}_{\text{cold}}} = 0.41\ kg_{\text{CO}_2}/kg_{\text{Al}_{\text{cold}}}$; $ED_{\text{s, Al}_{\text{cold}}} = 7.92\ MJ/kg_{\text{Al}_{\text{cold}}}$ [207].

Considering all the processes which come after the mining until the rolling operations (included), results are the following: $GWP_{\text{s, Al}_{\text{cath}}} = 8.86\ kg_{\text{CO}_2}/kg_{\text{Al}_{\text{cath}}}$; $ED_{\text{s, Al}_{\text{cath}}} = 137.06\ MJ/kg_{\text{Al}_{\text{cath}}}$ [207].

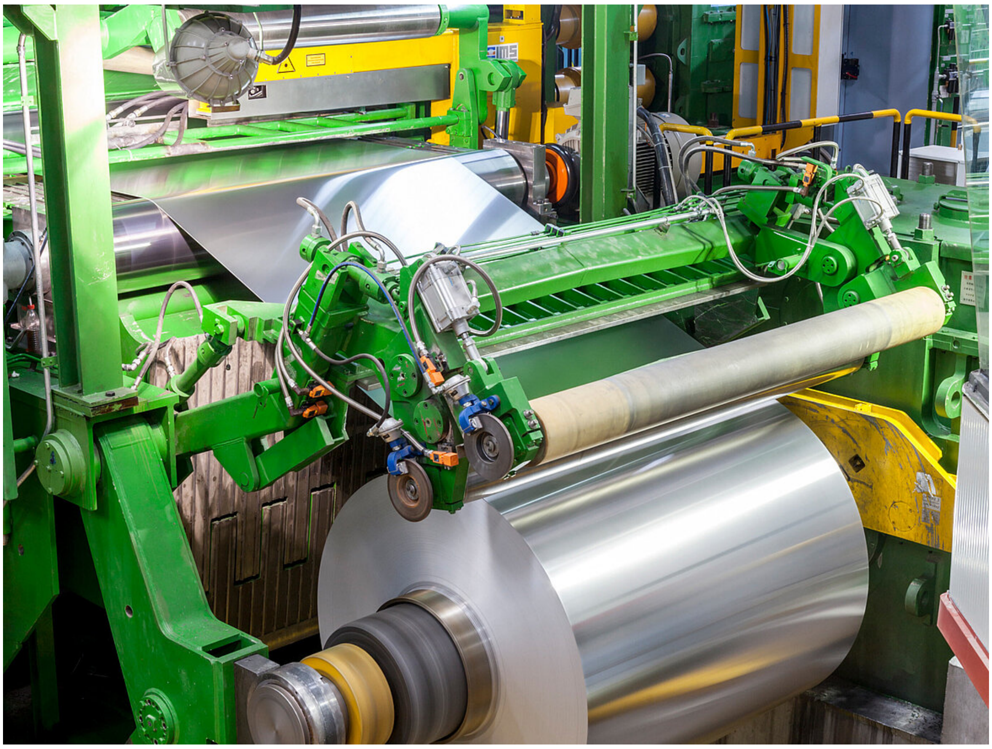

Figure 4.6. *A rolling mill processing an aluminum foil.*

PP AND PE SEPARATORS As the separator was considered to be 50% PP and 50% PE made, the processes of both kinds of materials were considered in the analysis. Results are the following: $GWP_{\text{s, PP}} = 2.53\ kg_{\text{CO}_2}/kg_{\text{PP}}$; $ED_{\text{s, PP}} = 78.59\ MJ/kg_{\text{PP}}$; $GWP_{\text{s, PE}} = 2.93\ kg_{\text{CO}_2}/kg_{\text{PE}}$; $ED_{\text{s, PE}} = 80.96\ MJ/kg_{\text{PE}}$ [226].

ELECTROLYTE SALT The electrolyte salt is made of lithium hexafluorophosphate ($LiPF_6$): it is the product of the reaction between the phosphorous pentafluoride (PF_5) and the lithium fluoride (LiF) previously dissolved in hydrogen fluoride (HF) [235]. For the electrolyte salt processing results are $GWP_{\text{s, LiPF}_6} = 12.15\ kg_{\text{CO}_2}/kg_{\text{LiPF}_6}$; $ED_{\text{s, LiPF}_6} = 179.07\ MJ/kg_{\text{LiPF}_6}$ [226].

DMC AND EC ELECTROLYTE SOLVENTS As said, the electrolyte solvent composition chosen for this LCA study was 50% DMC and 50% EC: these elements have the capability to increase the $LiPF_6$ permittivity if mixed with it [236]. For the electrolyte solvents processing results are $GWP_{s,\,DMC} = 1.72\ kg_{CO_2}/kg_{DMC}$; $ED_{s,\,DMC} = 37.44\ MJ/kg_{DMC}$; $GWP_{s,\,EC} = 0.47\ kg_{CO_2}/kg_{EC}$; $ED_{s,\,EC} = 10.19\ MJ/kg_{EC}$ [226].

4.2.2.4 *Processing impact: results*

All the results regarding the processing impact related to the materials transformations needed for the cells are collected in Table 4.11.

Table 4.11. *Average EP and GWP related to the processing of the materials for the cells.*

Materials	ED [$MJ/kg_{material}$]	GWP [$kg_{CO_2}/kg_{material}$]
Li_2CO_3	28.43	2.02
Anode graphite powder	89.87	4.86
Cu anode collector	47.00	4.10
Cathode Ni-Mn-Co powder	231.28	16.11
Al cathode collector	137.06	8.86
PP separator	78.59	2.53
PE separator	80.96	2.93
Electrolyte salt	179.07	12.15
DMC electrolyte solvent	37.44	1.72
EC electrolyte solvent	10.19	0.47
Total	919.99	55.75

4.2.2.5 *Product transportation*

The transportation impact regarding the cells components was found with the same logic followed for the *ED* and *GWP* evaluation about the cells support (see Section 4.2.1.3). As said, the chosen lithium extraction process was the brine evaporation and the selected site was the Atacama desert in Chile (see Section 4.2.2.1). As this choice alone represented an important contribution in terms of transportation impact, to minimize the other emissions coming from the transport of all the other raw materials for the cells, two assumptions were formulated.

Firstly, all the elements were considered available in Chile and this is a reasonable hypothesis considering how rich is the Chilean land in terms of ores and metals [237, 238, 239, 240]. Secondly, also the cell assembly process was intended as completely carried out in Chile, so that the transportation would have only involved the final products: the Li-ion cells.

Studying the most common trade routes, the chosen one for the cells transportation was Santiago de Compostela (Chile)-Rio Grande do Sul (Brasil)-Antwerp (Belgium)-Bologna (Italy), with the first and the third road stages and one sea stage in the middle. For the first truck stage Santiago de Compostela-Rio Grande do Sul (2435 km): $GWP_{\text{s, cells, T1}} = 2.108\ kg_{\text{CO}_2}/kg_{\text{cells}}$; $ED_{\text{s, cells, T1}} = 29.721\ MJ/kg_{\text{cells}}$. For the cargo stage Rio Grande do Sul-Antwerp (7289 km and 167.18 h of sailing): $GWP_{\text{s, cells, C}} = 0.091\ kg_{\text{CO}_2}/kg_{\text{cells}}$; $ED_{\text{s, cells, C}} = 0.320\ MJ/kg_{\text{cells}}$. For the second truck stage Antwerp-Bologna (1259 km): $GWP_{\text{s, cells, T2}} = 1.090\ kg_{\text{CO}_2}/kg_{\text{cells}}$; $ED_{\text{s, cells, T2}} = 15.367\ MJ/kg_{\text{cells}}$. The overall results for the whole cells transportation are the following: $GWP_{\text{s, cells}} = 3.289\ kg_{\text{CO}_2}/kg_{\text{cells}}$; $ED_{\text{s, cells}} = 45.408\ MJ/kg_{\text{cells}}$.

4.2.2.6 *Transportation impact: results*

All the results regarding the transportation impact related to the cells are collected in Table 4.12 considering all the stages travelled by truck or cargo: the first road stage T1, the second sea stage C and the third road stage T2.

Table 4.12. *Average EP and GWP related to the transportation of the cells considering all the stages travelled by truck (T) or cargo (C).*

Route	ED [$\text{MJ}/\text{kg}_{\text{material}}$]	GWP [$\text{kg}_{\text{CO}_2}/\text{kg}_{\text{material}}$]
T1	29.72	2.11
C	0.32	0.09
T2	15.37	1.09
Total	45.41	3.29

4.2.3 *Liquid-cooled BTMS impact*

The LCA analysis about the BTMS was based on the real liquid cooling system installed on the *LiBER* BP prototype: it is a water-based BTMS with a coolant circuit made of a silicone rubber tube which passes through several holes of the brick. As seen in the brick scheme of Figure 4.3, among the bigger holes for the cells there are smaller holes: the cooling circuit passes through 12 of them while the coolant flows along the tube. As in the 4-cells element used for the experiments in Section 3.4, the liquid duct holes have a diameter $d_{\text{hole}} = 10\ mm$, so the chosen silicone rubber tube has an external diameter $d_{\text{tube, ext}} = 10\ mm$ and an internal diameter $d_{\text{tube, int}} = 8\ mm$, resulting in a thickness $s_{\text{tube}} = 1\ mm$. The LCA regarding the BTMS was facilitated considering the raw materials extraction, processing and transportation just concerning the silicon rubber tube.

4.2.3.1 *Raw material extraction and processing*

The state of the art about the silicone rubber production impact does not provide many *ED* and *GWP* data which specifically regards the transformation of the raw materials. The majority of the papers deals with the energy demand and the emission values related to the extraction of the materials and their processing together.

There are lots of phases before arriving to the silicone rubber tube production: the whole process starts with a thermal phase which involves the silicon dioxide (SiO_2) and allows obtaining metal silicon; then several other chemical and mechanical processes occur with a descending energy requirement [241]. One of the final products is the silicone rubber, the material used to produce the silicone rubber tubes by extrusion. This LCA analysis focuses on the SiO_2 reaction phase as it is the most energy-intensive process and then it deals with the final silicone rubber extrusion. However, the overall *ED* and *GWP* reported at the end of this section regard the whole silicone rubber tube production process.

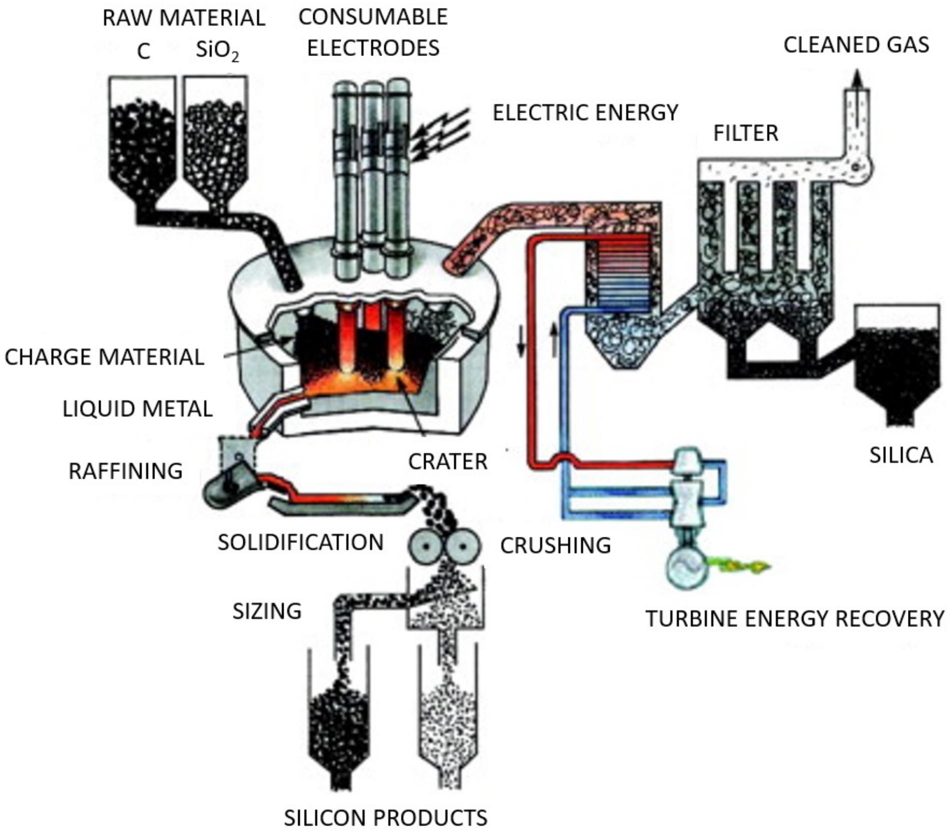

Figure 4.7. *Scheme of a SAF used for the silicon production [242].*

The silicon production is based on the SiO_2 reduction which occurs in a submerged arc furnace (SAF, Figure 4.7) in presence of carbonaceous raw materials. In the SAF body all the raw materials (the charge) are put together with a continuous addition of carbon (inserted into the furnace when the SAF Söderberg electrodes have been consumed too much) and small quantities of limestone. The charge is mainly composed of quartz, coke, coal, charcoal and woodchips [242] and the reduction reactions ($SiO_2 + 2C \rightarrow Si + 2CO$) represent one of the two main SAF energy requirements. The other one is the electric energy to supply the electrodes. The product of the SAF reactions is metal silicon which then undergoes a grinding phase, several other chemical reactions, a distillation phase and other chemical processes such as the hydrolysis and the stripping [241]. The resulting product is a silicone rubber which becomes the raw material for the next extrusion phase during which the rubber is forced through a die, finally obtaining the desired shape.

To facilitate the energy demand and the CO_2 emissions data research it was decided to use *openLCA*, an open source software useful to conduct LCA studies both for company evaluations and for academy aims [243]. The chosen databases were the ELCD and the Idemat ones. Considering the final silicone rubber tube results are $GWP_{\text{s, tube}} = 3.745\ kg_{\text{CO}_2}/kg_{\text{tube}}$; $ED_{\text{s, tube}} = 118.920\ MJ/kg_{\text{tube}}$.

4.2.3.2 *Product transportation*

The transportation impact regarding the silicone rubber tube was found with the same logic followed for the *ED* and *GWP* evaluation about the cells support (see Section 4.2.1.3). In this case the chosen supplier was in Milan (Italy) so it was just necessary a road transport by truck (216 *km*). For the route Milano-Bologna results are $GWP_{\text{s, tube}} = 0.017\ kg_{\text{CO}_2}/kg_{\text{tube}}$; $ED_{\text{s, tube}} = 0.237\ MJ/kg_{\text{tube}}$.

4.2.3.3 *Extraction, processing, transportation impact: results*

All the impact results regarding the materials extraction, the materials processing and the transportation related to the silicone rubber tube for the BP liquid cooling system are collected in Table 4.13.

Table 4.13. *Average EP and GWP related to the extraction, processing and transportation for the silicone rubber tube of the BP liquid cooling system.*

Impact	ED [MJ/kg$_{\text{material}}$]	GWP [kg$_{\text{CO}_2}$/kg$_{\text{material}}$]
Extraction + processing	118.92	3.75
Transportation	0.24	0.02
Total	119.16	3.77

4.2.4 *Interpretation*

A LCA study is not an exact calculation of the energy demand and the CO_2 emissions but, stating reasonable assumptions, the aim is to estimate ED and GWP, getting as closer as possible to their real values. As seen in Section 4.1, the interpretation is one of the most important phases of the study: thanks to the results regarding the whole production cycle (from the raw materials extraction to the final product transportation), it is possible to understand how to save energy and what can be the best effective strategy to reduce the CO_2 emissions.

Looking at the results obtained for the extraction and production of the aluminum needed to realize the cells support (Table 4.3 and Table 4.4) it is clear that innovative technologies to process the aluminum could represent an efficient solution to lower the ED instead proceeding with the ordinary and energy-intensive methods (Bayer and Hall–Héroult processes, Section 4.2.1.1). Cutting-edge technologies would be also promising to reduce the CO_2 emissions.

Regarding the plastic material for the cells support, the choice is driven more by the ED than by the GWP value. As a matter of fact, comparing the GWP for POM and ABS in Table 4.6 and Table 4.8, results show just a slight difference between the two values: 5.13 $kg_{\mathrm{CO_2}}/kg_{\mathrm{POM}}$ for POM and 5.32 $kg_{\mathrm{CO_2}}/kg_{\mathrm{ABS}}$ for ABS, with a percentage decrease $\Delta GWP = -3.57\%$. Instead, considering the ED results in Table 4.5 and Table 4.7 the obtained values 109.67 MJ/kg_{POM} for POM and 123.85 MJ/kg_{ABS} result in a percentage decrease $\Delta ED = -12\%$. The POM is definitely the best choice both in terms of GWP and ED.

Analysing the transportation impact for the materials of the cells support, regarding the aluminum it clearly appears that choosing Al6063 instead of Al6065 represents the more convenient option considering both the energy demand and the emissions. Indeed, the overall Al6063 ED results to be 0.2 MJ/kg_{Al6063} instead of 2.58 MJ/kg_{Al6065} for Al6065, with a percentage decrease $\Delta ED = -92.25\%$ and the overall Al6063 GWP results to be 0.01 $kg_{\mathrm{CO_2}}/kg_{\mathrm{Al6063}}$ instead of 0.36 $kg_{\mathrm{CO_2}}/kg_{\mathrm{Al6065}}$ for Al6065, with a percentage decrease $\Delta GWP = -97.22\%$.

However, it has to be highlighted how convenient is the cargo transport respect to the truck one. Focusing on the Al6065 impact values, it results that the GWP for the cargo stage is higher by 50% than that related to the truck stage, but the distance travelled by the truck is just the 8.01% of the cargo distance. Further, although this the ED for the cargo stage is lower by 50% than that related to the truck stage. Hence, if it is possible to choose between a road or a sea transportation, it should be better to go for the second option.

Looking at the results obtained for the extraction of the raw materials for the cells (Table 4.10) it is evident how the cobalt has a deep impact both in terms of ED and GWP, followed by the nickel which has a high ED value, too. These are two fundamental elements to produce the NMC111 cells cathode powder, so it is not possible to lower this contribution if the use of this kind of cells is mandatory for the considered application. However, when it is possible to use another type of NMC cells, the more innovative NMC622 or NMC811 cells represent better choices. The NMC622 cathode is composed of 60% of Ni, 20% of Mn and 20% of Co, the NMC811 cathode is composed of 80% of Ni, 10% of Mn and 10% of Co (Figure 4.8): both of them have a lower weight (lower transport impact) and a higher energy density respect to the NMC111. The extremely reduced quantity of Co in NMC811 cells, their lowest weight and highest energy density may suggest that this is the best choice at all. On the other hand, the high Ni percentage of the the NMC811 cells is responsible for a more sensitive chemistry and, consequently, the need of additional post-processing phases and a more expensive manufacturing process [232]. Plus, NMC811 cells are sensitive to moisture and air so, in an automotive application, it would be necessary a further sealed structure to insulate them from the outside. All these additional processes and components would increase the ED and GWP values, nullifying the benefits brought by the lower Co percentage. From this point of view, the NMC622 cells represent a good compromise.

About the processing of the cells materials, looking at Table 4.11 results show high values of ED and GWP for several processed materials but it is possible to lower only some of them. One of the initial assumption was to consider the separator as 50% PP-made and 50% PE-made but, looking at the related ED and GWP, it results that the use of a PP separator brings to a decrease of both energy demand ($\Delta ED = -2.93\%$) and CO_2 emissions ($\Delta GWP = -13.65\%$).

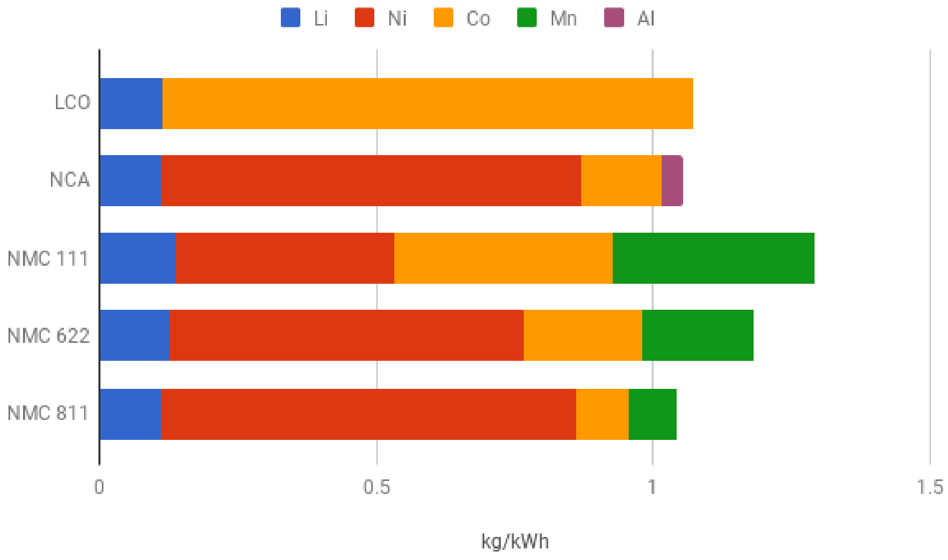

Figure 4.8. *The chemical cathode composition of different Li-ion cells [232].*

A similar evaluation can be done regarding the electrolyte solvent which was considered 50% DMC-made and 50% EC-made. The use of an EC electrolyte solvent brings to a great decrease of both energy demand ($\Delta ED = -72.78\%$) and CO_2

emissions ($\Delta GWP = -72.67\%$).

The processes regarding the anode and the cathode powders and collectors as well as the electrolyte salt production are very energy-intensive as they include several thermal, chemical and electrochemical phases. As these treatments are fundamental for the quality of the final components, the only possible choice to lower the *ED* values is the exploitation of the most efficient available industrial plants.

Considering the assumption of the cells assembled in Chile (the same place were the raw materials extraction takes place) the transportation impact includes both truck and cargo stages. As seen before, the sea transport results to be better than the road one: although the total distance travelled by the truck (3694 km) represents the 50.68% of the distance travelled by the cargo (7289 km), the sea transport results in a great *ED* decrease $\Delta ED = -99.29\%$ and *GWP* decrease $\Delta GWP = -97.19\%$. Hence, the more it is possible to exploit the sea transport, the better is in terms of impact.

High values of *ED* and *GWP* are shown in Table 4.13 regarding the material extraction and processing to realize the silicone rubber tube. As said for the processes involving several cell components, in this case energy-intensive thermal and chemical processes are exploited to obtain the final product, so the aim of reducing the energy demand represents a hard challenge. Further, the use of the SAF does not help in lower the *GWP*: to face this problem, some effectiveness cutting-edge filters [244] can be used both to reduce CO_2 emissions and to recycle it, transforming this end-of-life product in feeding material for the life cycle of a new product.

4.3 CONCLUSIONS

This LCA study focused the attention on the real *LiBER* BP which will be soon put on the market. Several literature researches were consulted, compared and then exploited for the *ED* and *GWP* estimations. To achieve the most accurate results as possible, not only analytical but also experimental evaluations were taken into account and different databases were considered via *OpenLCA*.

The importance of this research lies in the fact that, analysing the interpretation of the data (Section 4.2.4), different valid measures could be taken to lower the overall energy demand and emissions values in the production of a more environmentally friendly second generation of *LiBER* BPs. It is intuitive that actions such as the choice of less energy-intensive processes, the use of higher advanced technologies, the introduction of recovery energy systems and the implementation of the production line with final recycling stages are all good solutions in terms of energy saving. A LCA study not only quantifies the energy consumption and the emissions related to a precise product but also reveals the magnitude of the benefits brought by the changes that can be done to improve its production, showing the effects in terms of *ED* and *GWP* decrease (as seen in this chapter).

CONCLUSIONS

The results presented in this PhD thesis offer a great overview regarding several cutting-edge technologies and methods to reduce both the energy consumption and the greenhouse gas emissions in the sustainable mobility field. The main topics dealt with the car building materials, focusing the attention on the carbon fiber composites which bring evident benefits in terms of lightening and, consequently, energy consumption decrease. Then, the ordinary BTMSs were analysed and a complex and detailed experimental campaign about innovative PCM-based BTMSs was presented, investigating on which is the best system to cool a battery pack, improving its SOH and extending its life. Finally, the whole life cycle of a battery pack unit was studied, carrying on a LCA evaluation which resulted in a series of estimations and suggestions useful to lower both the ED and the GWP of the entire production line.

Regarding the composites, the carbon fiber ones were deepened: several lamination processes were discussed and the lamination process optimization achieved with the help of the PLM software *Fibersim* was discussed. Thanks to this program, it was possible to complete two lamination design projects, the first one regarding the sides and the air intakes of a *Bugatti Divo* and the second one about the pillars of a *Lamborghini Aventador*. A proper lamination design can bring to a following manufacturing process characterized by an almost total absence of wastes. Plus, this previous lamination modeling allows not to use more material than the needed and this represents a benefit in terms of lightening, a key-word in the EVs field.

A case study about the carbon fiber composites was *Emilia 4*, the competitive solar car fully made of carbon fiber and realized by the university sport team *Onda Solare*. Experimental evidences showed that the substitution of Ergal upper front and rear brackets with carbon fiber ones resulted in a 71.54% weight reduction.

This work did not only deal with innovative materials but, as said, also with novel solutions to preserve the battery SOH. Concerning the BTMSs, once the ordinary cooling systems (forced-air, cooling plates, heat pipes) were discussed, the PCM-based BTMSs were introduced. The first part of this dissertation regarded the characterization of the PCMs conducted both with qualitative and quantitative tests. With the qualitative tests the comparison between the heating cycles of pure and aluminum-foam-loaded PCM and that between pure and copper-foam-loaded PCM showed how the presence of the metal foam is fundamental to highly increase the thermal conductivity of the PCMs.

Then, the experimental campaign proceeded with quantitative test series. With the first one, the temperature distribution inside a PCM volume during a heating cycle was studied: under the analysed experimental heating conditions, results highlighted that the heat transfer into the PCM can be considered as mono-dimensional and the temperature results homogeneous on the plane. The second group of quantitative characterization tests dealt with the PCM thermal conductivity enhancement: comparing the heating cycles of a pure PCM volume and a copper-foam-loaded PCM one, a more uniform temperature distribution along the vertical direction was observed, testifying a lower thermal resistance of the metal-foam-loaded PCM layers. Further, a lower maximum temperature of the system was recorded as well as a melting time reduction by 32%, putting in evidence how the addition of metal foam can be a great energy-saving strategy in the thermal storage applications.

The core of the thesis involved the PCM-based BTMSs. Seven series of tests were carried on: the first three series investigated the effectiveness of uninsulated cooling systems, whereas the other four series analyzed insulated BTMSs. Among the studied uninsulated systems there were a forced-air BTMS, a pure PCM-based and a copper-foam-loaded-PCM-based BTMS. The insulated cooling systems concerned a pure PCM-based and a copper-foam-loaded-PCM-based BTMS, equipped or not with a water cooling system. Results showed that with an uninsulated system the most innovative BTMSs are not always needed and, under certain conditions, a forced-air cooling system can be sufficient in terms of optimal working temperature for the Li-ion cells. Another important factor which has to be taken into consideration is the temperature homogeneity inside the BP: although the forced-air and the pure PCM-based cooling systems succeeded in keeping the cells in the proper working temperature range, they were not able to face the issue of the convective motions developed inside the analysed systems. The addition of the copper foam inside the pure PCM resulted to be the perfect choice to hinder the development of the convective motions, to obtain a more homogeneous thermal distribution inside the BP and to keep the system at the proper working temperature.

The insulated test series (the closest ones to the real automotive applications) show that both PCM based and copper-foam-loaded-based-PCM BTMSs are not effectiveness enough to satisfy the thermal requirements for LIBs. In this case it turned out that coupling the system with a liquid cooling circuit is mandatory to preserve the cells. With the cooling circuit the LIBs thermal requirements were satisfied with and without the copper foam loading of the pure PCM. However, considering the automotive final application and the well known issue regarding the lack of space into the BPs, the pure PCM-based BTMS coupled with the water cooling system was considered as the best choice both for the cooling and for the heating of the cells in extremely low temperature environments.

The final part of this thesis showed a LCA study regarding a brick of the *LiBER* BP. Three main research macro-topics were considered: the cells support, the Li-ion cells, the liquid cooling BTMS. After discussing about reasonable assumptions useful for the assessment, the impact evaluations were carried on focusing the attention on the raw materials extraction, the processing of these materials and the transportation of the final products. The resulting interpretation proposed alternative methods and choices that can be done to lower the energy demand and the CO_2 emissions such as using the POM instead of the ABS as material for the cells support, preferring the sea transport with respect to the road one, choosing low-cobalt cells, using the PP instead of the PE for the separator and the EC instead of the DMC for the electrolyte salt.

Finally, another suggestion came out from the interpretation of the LCA results: a good practice would be trying to avoid the extraction and processing of the materials by means of obsolete machines. The majority of the thermal, chemical and electrochemical processes are characterized by energy-intensive phases but the choice of cutting-edge technologies could represent the turning point against the high values of ED and GWP. In this perspective there are not only practical changes in terms of technology that can be done but it is also fundamental a mindset switch towards a new life cycle thinking, considering the end-of-life products as feedstock for the life cycle of new products.

This PhD thesis gives its contribution to the sustainable mobility research field, in particular in the sectors of the innovative materials, the BTMSs and the BPs LCA analysis. All the topics covered in this work offer solid bases from which future researchers could start to deepen and improve the results presented.

Regarding the vehicle building materials, further studies can be done to compare mechanical pieces made of carbon fiber composites with other ones made of different kinds of composite materials. The strength, the stiffness, the weight and other mechanical and physical characteristics could be the factors to be investigated, aiming to find new more performing composites in terms of energy saving.

Considering the field of BTMSs, the studies here reported could be pursued designing and testing more other innovative hybrid cooling systems realized with a PCM-based BTMS coupled with other kinds of technologies such as cold plates, heat pipes, TEC systems. The focus of the tests would deal with the efficiency of these BTMSs both in terms of maximum temperatures reached by the Li-ion cells and considering the temperature homogeneity inside the BP. Other ways to enrich the research started in this thesis could be the investigation of the already studied BTMSs in an extremely low temperature environment or the analysis of the PCM-based cooling systems working with several kinds of PCMs (characterized by other phase change temperature ranges with respect to the RT35) or loads (different from the aluminum and copper metal foams for their material, shape and structure). A final comparison of these tests with the forced-air BTMS reference experiment and all the other tests would be helpful in better understanding which is the best performing cooling system in operating conditions different from those already investigated.

Further improvements to carry on this work can also be done deepening the BP LCA study and trying to obtain increasingly precise estimations of ED and GWP. Some neglected processes or choices can be analyzed in terms of energy demand and CO_2 emissions: the assembly phase, the goods transport from different places, the use of other transportation means (besides trucks and cargo ships). An exhaustive LCA analysis could involve a more detailed liquid-based BTMS, not only considering the rubber silicone tube but also taking into account any pumps, valves and all the other components usually part of that kind of cooling system. Finally, the presented cradle-to-gate LCA could be turned into a cradle-to-cradle one, adding the contributions of any recycling stages at the end of the production lines. This kind of research would put in evidence the importance of recycling in terms of energy saving and could represent a push also for the more reluctant stakeholders.

APPENDICES

1. THERMOCOUPLES CALIBRATION

In the research field one of the most common methods to make temperature measurements is by means of thermocouples (TCs). A TC is composed of two filaments made of two different materials and joined together in the so called hot junction: this is one of the two ends of a TC and its temperature is the one to be measured. The other end is called cold junction and it is always related to a reference temperature. The returned temperature value of a TC is a comparison between the temperatures of the two junctions and, more precisely, it is not a direct temperature evaluation but it regards the voltage difference between the junctions generated by Seebeck effect [245].

The calibration process consists in the comparison between the output of the instrument or sensor under test with that of a high-precision instrument when the same known input is applied to both. This procedure is carried out considering a range of inputs which covers the whole measurement range of the instruments under calibration. Further, the tools calibration has to be repeated after prescribed intervals as the characteristics of any instrument change over time [246].

To calibrate the TCs used for tests discussed in this thesis a resistance temperature detector (RTD) was used. The RTD was, in turn, previously calibrated comparing it (the secondary instrument) with a four-terminals platinum-resistance thermometer (the primary standard instrument). The platinum-resistance thermometer is a high-precision tool as well as delicate: this is why it usually used just for the initial calibration of the secondary instrument. Then, it is preferable to use more rugged tools such as the RTDs.

A RTD consists of a solid metal wire whose resistance increases with temperature. The wire is usually encased in an insulating support to prevent resistance alterations due to strains or surrounding fluid contamination. Once the RTD is calibrated it becomes the primary instrument to be used in the TCs calibration and the TCs become the secondary tools. The RTD temperature is not directly read: firstly, its resistance value is read by a Wheatstone bridge (a four-wire electrical circuit used to measure unknown resistances); secondly, the resistance value is converted into a temperature one. When the Wheatstone bridge reaches the balance, the related temperature value is the one to take into consideration for the TCs calibration.

To calibrate the TCs for the tests in Chapter 3, both the 16 TCs and the RTD were immersed into a water thermostatic bath equipped with a refrigeration unit: thanks to the thermostatic control unit it was possible to manage the temperature of the fluid. The temperatures of the TCs were always monitored, recorded during 10 *min* acquisition sessions and analyzed with *LabVIEW*. The temperature range considered for the calibration was $T_{\text{calib}} = 10 \div 65$ °C, focusing on the following temperatures: $T_1 = 10$ °C, $T_2 = 15$ °C, $T_3 = 20$ °C, $T_4 = 25$ °C, $T_5 = 30$ °C, $T_6 = 35$ °C, $T_7 = 40$ °C, $T_8 = 45$ °C, $T_9 = 55$ °C, $T_{10} = 65$ °C. For all of these values the average temperatures recorded by each of the 16 TCs and the average RTD temperatures were calculated (Figure 4.9). Finally, the temperatures of the RTD and the TCs were plotted and the interpolating curves were found: the second degree polynomials of these curves gave the temperature corrective coefficients which were used to have error-free acquisitions during the tests. In Figure 4.10 the plot $T_{\text{RTD}} - T_{\text{TC}_1}$ represents an example of the final interpolating curve found for the TC_1.

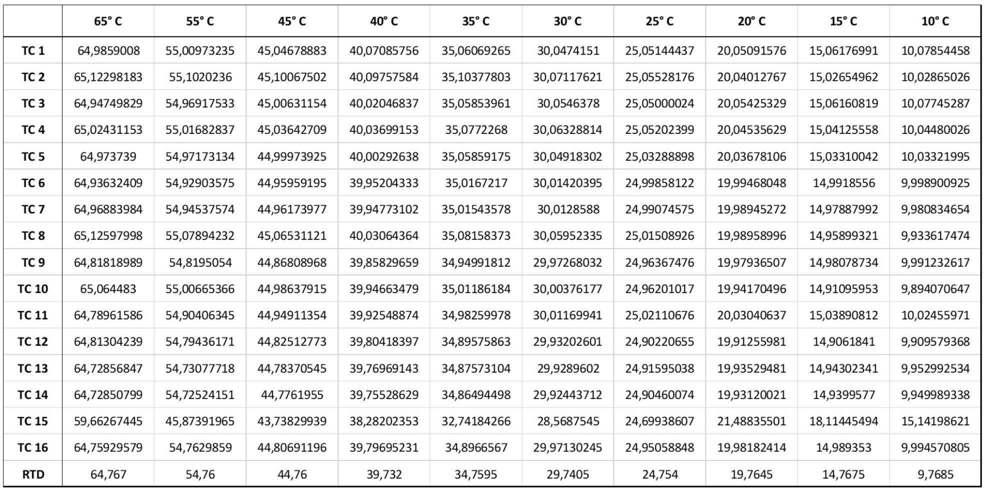

	65° C	55° C	45° C	40° C	35° C	30° C	25° C	20° C	15° C	10° C
TC 1	64,9859008	55,00973235	45,04678883	40,07085756	35,06069265	30,0474151	25,05144437	20,05091576	15,06176991	10,07854458
TC 2	65,12298183	55,1020236	45,10067502	40,09757584	35,10377803	30,07117621	25,05528176	20,04012767	15,02654962	10,02865026
TC 3	64,94749829	54,96917533	45,00631154	40,02046837	35,05853961	30,0546378	25,05000024	20,05425329	15,06160819	10,07745287
TC 4	65,02431153	55,01682837	45,03642709	40,03699153	35,0772268	30,06328814	25,05202399	20,04535629	15,04125558	10,04480026
TC 5	64,973739	54,97173134	44,99973925	40,00292638	35,05859175	30,04918302	25,03288898	20,03678106	15,03310042	10,03321995
TC 6	64,93632409	54,92903575	44,95959195	39,95204333	35,0167217	30,01420395	24,99858122	19,99468048	14,9918556	9,998900925
TC 7	64,96883984	54,94537574	44,96173977	39,94773102	35,01543578	30,0128588	24,99074575	19,98945272	14,97887992	9,980834654
TC 8	65,12597998	55,07894232	45,06531121	40,03064364	35,08158373	30,05952335	25,01508926	19,98958996	14,95899321	9,933617474
TC 9	64,81818989	54,8195054	44,86808968	39,85829659	34,94991812	29,97268032	24,96367476	19,97936507	14,98078734	9,991232617
TC 10	65,064483	55,00665366	44,98637915	39,94663479	35,01186184	30,00376177	24,96201017	19,94170496	14,91095953	9,894070647
TC 11	64,78961586	54,90406345	44,94911354	39,92548874	34,98259978	30,01169941	25,02110676	20,03040637	15,03890812	10,02455971
TC 12	64,81304239	54,79436171	44,82512773	39,80418397	34,89575863	29,93202601	24,90220655	19,91255981	14,9061841	9,909579368
TC 13	64,72856847	54,73077718	44,78370545	39,76969143	34,87573104	29,9289602	24,91595038	19,93529481	14,94302341	9,952992534
TC 14	64,72850799	54,72524151	44,7761955	39,75528629	34,86494498	29,92443712	24,90460074	19,93120021	14,9399577	9,949989338
TC 15	59,66267445	45,87391965	43,73829939	38,28202353	32,74184266	28,5687545	24,69938607	21,48835501	18,11445494	15,14198621
TC 16	64,75929579	54,7629859	44,80691196	39,79695231	34,8966567	29,97130245	24,95058848	19,98182414	14,989353	9,994570805
RTD	64,767	54,76	44,76	39,732	34,7595	29,7405	24,754	19,7645	14,7675	9,7685

Figure 4.9. *The average temperatures of the RTD and the TCs recorded during the calibration.*

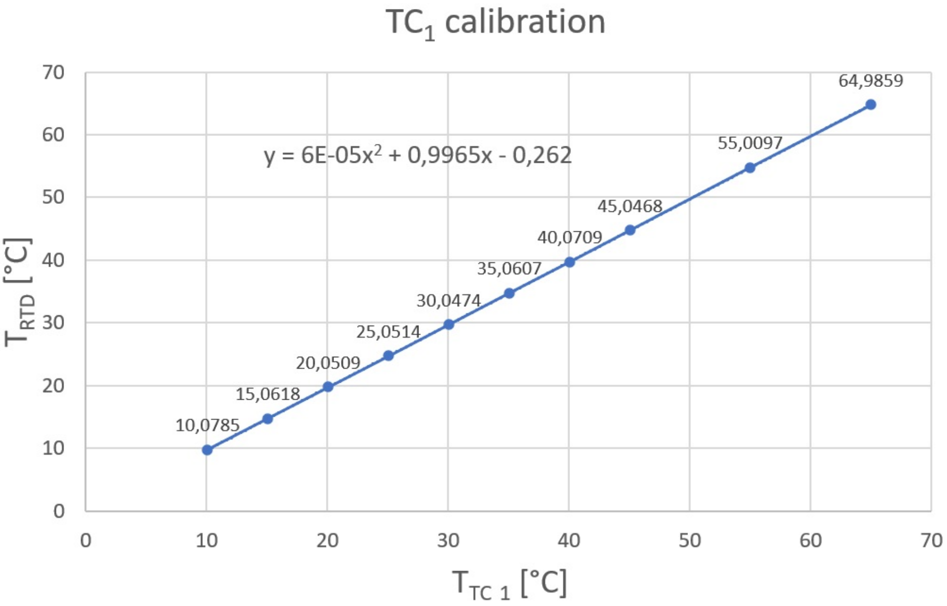

Figure 4.10. *Interpolating curve found for* TC_1.

2. GLOBAL HEAT TRANSFER COEFFICIENT CALCULATION

To calculate and compare the global heat transfer coefficients related to the insulation boxes of the tests in Section 3.3.2 and Section 3.3.3 the heat transfer coefficients had to be found before. The heat transfer coefficient k comes from the formula:

$$M\ c_p\ \frac{\partial\theta}{\partial t} = -\ k\ \theta$$

where M is the PCM mass contained in the case; c_p is the PCM specific heat capacity; $\theta = (\widetilde{T} - T_\mathrm{AIR})$ with $\widetilde{T}$ as the PCM average temperature and T_AIR as the average air temperature; t is time.

Considering $\theta(t = 0) = \theta_\mathrm{o} = 24.82$ °C (value measured during the tests), integrating the previous equation it becomes:

$$\int_{\theta_0}^{\theta} \frac{\partial\theta'}{\theta'} = -\int_0^t \left(\frac{k}{Mc_p}\right)\partial t' \rightarrow$$

$$\rightarrow\ \left[ln\theta - ln(24,82)\right] = -\ B\ t \rightarrow$$

$$\rightarrow\ -\ ln\left(\frac{\theta}{24{,}82}\right) = B\ t$$

with $B = \left(\frac{k}{M\ c_p}\right)$ which is the slope of the resulting line.

Before calculating k the value of θ had to be found and, consequently, the value of $\widetilde{T}$ which was considered as a weighted average related to the temperatures of the PCM sub-volumes placed at different heights (z) in the case. In Figure 4.11 and Figure 4.12 the division of the whole PCM volume ($V = 1.08 \cdot 10^6\ mm^3$) in sub-volumes is shown.

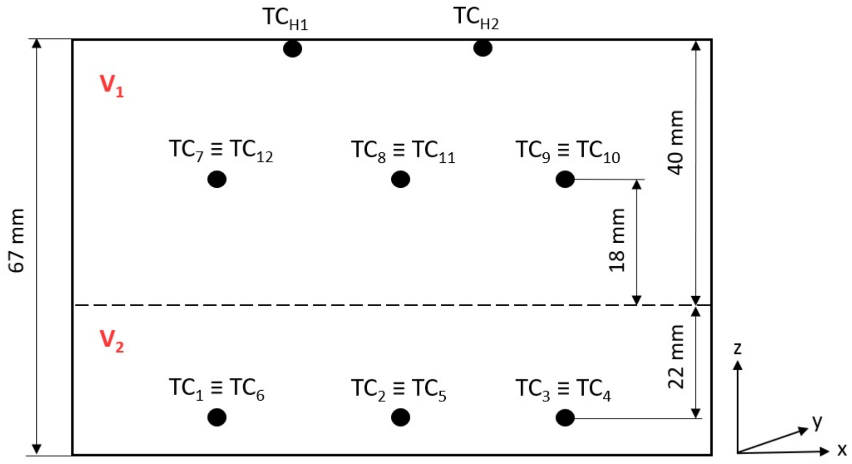

Figure 4.11. *Sub-volumes division in the worse insulated case (Section 3.3.2.1).*

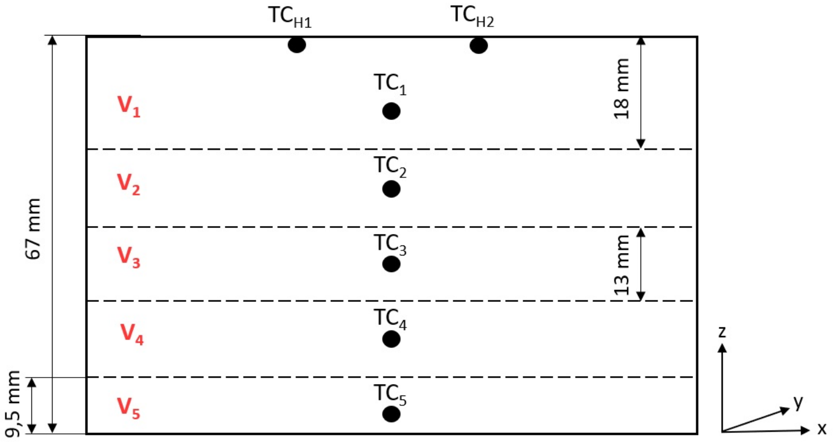

Figure 4.12. *Sub-volumes division in the better insulated case (Section 3.3.3.1).*

As each sub-volume V_{i} has a thermal weight depending from its mass M_{i} (the value of $c_{p_{\mathrm{i}}}$ is constant for each solid or liquid phase), $\widetilde{T}$ was calculated as the average temperature of the whole PCM volume, considering these weights. The formula used to calculate $\widetilde{T}$ is:

$$\widetilde{T} = \frac{\sum_i^n m_i \; c_{p_i} \; T_i}{\sum_i^n m_i \; c_{p_i}}$$

where T_{i} represents the temperature recorded by TC_{i} in the sub-volume V_{i} or the average temperature of V_{i} if in that sub-volume there is more than one TC. With this equation it is possible to calculate $\widetilde{T}$ for each instant of time, so obtaining θ over time. The value of $\widetilde{T}$ does not change if considering the whole PCM as liquid or solid (using the density ρ_{L} and the specific heat capacity $c_{p_{\mathrm{L}}}$ or using ρ_{S} and $c_{p_{\mathrm{S}}}$ in Table 3.1) and it appears clear while developing the formula of $\widetilde{T}$.

Further, it is not possible to take into account the period during which the PCM presents both solid and liquid phases because its physical characteristics (ρ, c_{p}) change in that interval. The choice was to focus the attention on a cooling process, when the whole PCM was still liquid and the solidification had not begun yet.

During the tests discussed in Section 3.3 it was chosen a precise temperature value ($T_{\mathrm{melt/solid}} = 35$ °C) reached which the phase change of the PCM was considered complete. This was obviously done for research purposes: in reality the PCM phase change process does not happen at a precise $T_{\mathrm{melt/solid}}$ as it occurs in a temperature range of about $5 \div 7$ K. Hence, to be sure not to examine the PCM when the solidification process had already begun, the considered values of $\widetilde{T}$ were those related to the time interval just before $T_{\mathrm{melt/solid}}$ was reached, in particular until $\widetilde{T} = 40$ °C (the part of the curve in the red oval of Figure 4.13).

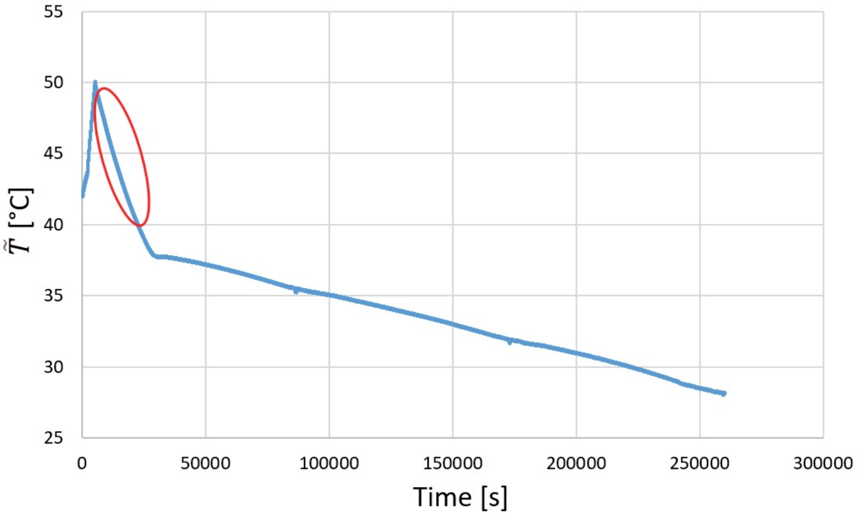

Figure 4.13. *$\widetilde{T}$ considered for the calculation of k during the studied PCM cooling process.*

As said before, $-ln\left(\frac{\theta}{24{,}82}\right) = B\ t$ is the equation of a line ($y = mx + q$) where, in this specific case:

$$y = -\ ln\left(\frac{\theta}{24{,}82}\right)$$

$$m = B$$

$$x = t$$

Knowing $\widetilde{T}$ and consequently θ, it was possible to calculate y, plotting it above time (the blue curve in Figure 4.14) and then extracting the slope from the regression line. Once obtained B it was also possible to plot the interpolating line (the red one in Figure 4.14) whose classical equation is $y = mx + q$, choosing a proper value of q which better matched the experimental regression line.

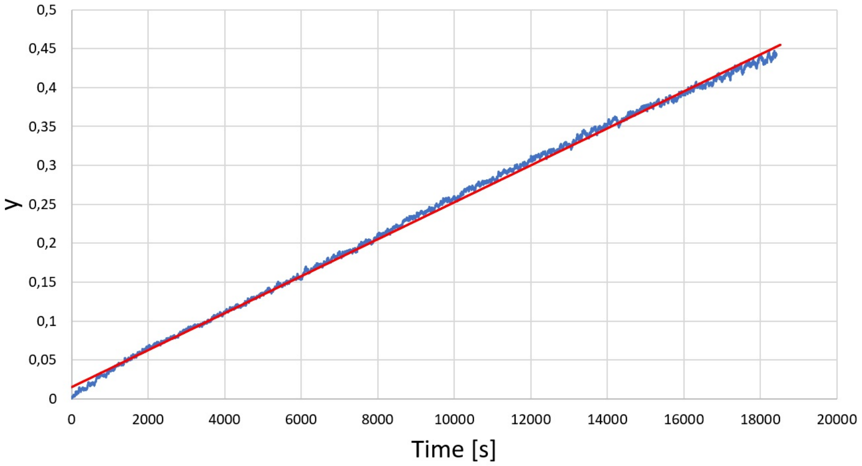

Figure 4.14. *The trend of y above time.*

The heat transfer coefficients were calculated with the inverse formula of B:

$$k = B\ M\ c_p$$

Finally, for the global heat transfer coefficients it was used the formula:

$$U = \frac{k}{A}$$

with A as the total external heat exchanging area.

In Table 4.14 the values of k and U related to the two insulation boxes discussed in Section 3.3.2 and Section 3.3.3 are presented. Results show that the insulation improvements brought to a global heat transfer coefficient decrease by 66.6%.

Table 4.14. *k and U calculated for the worse and the better insulated polystyrene boxes.*

	k [W/K]	U [W/m²K]
Worse insulation	0.079	0.132
Better insulation	0.026	0.044

3. FLOWMETER CALIBRATION

To properly calibrate the analog flowmeter used in Test 5.1 ÷ 5.3 and Test 6.1 ÷ 6.3 the liquid cooling circuit was linked to a digital flowmeter with which it was possible to directly read the flow rate and then associate it to an electric current value (the frequency-current converter output) acquired by the NI module.

After ten electric current acquisitions for each flow rate value, the average current was calculated and correlated to the average flow rate. This was repeated for several known flow rate values so that it was possible to plot a flow rate-current graph, finding a second degree polynomial. This interpolating curve allowed determining any flow rate for each current value acquired. In Figure 4.15 and Figure 4.16 the flowmeter calibration spreadsheet is shown.

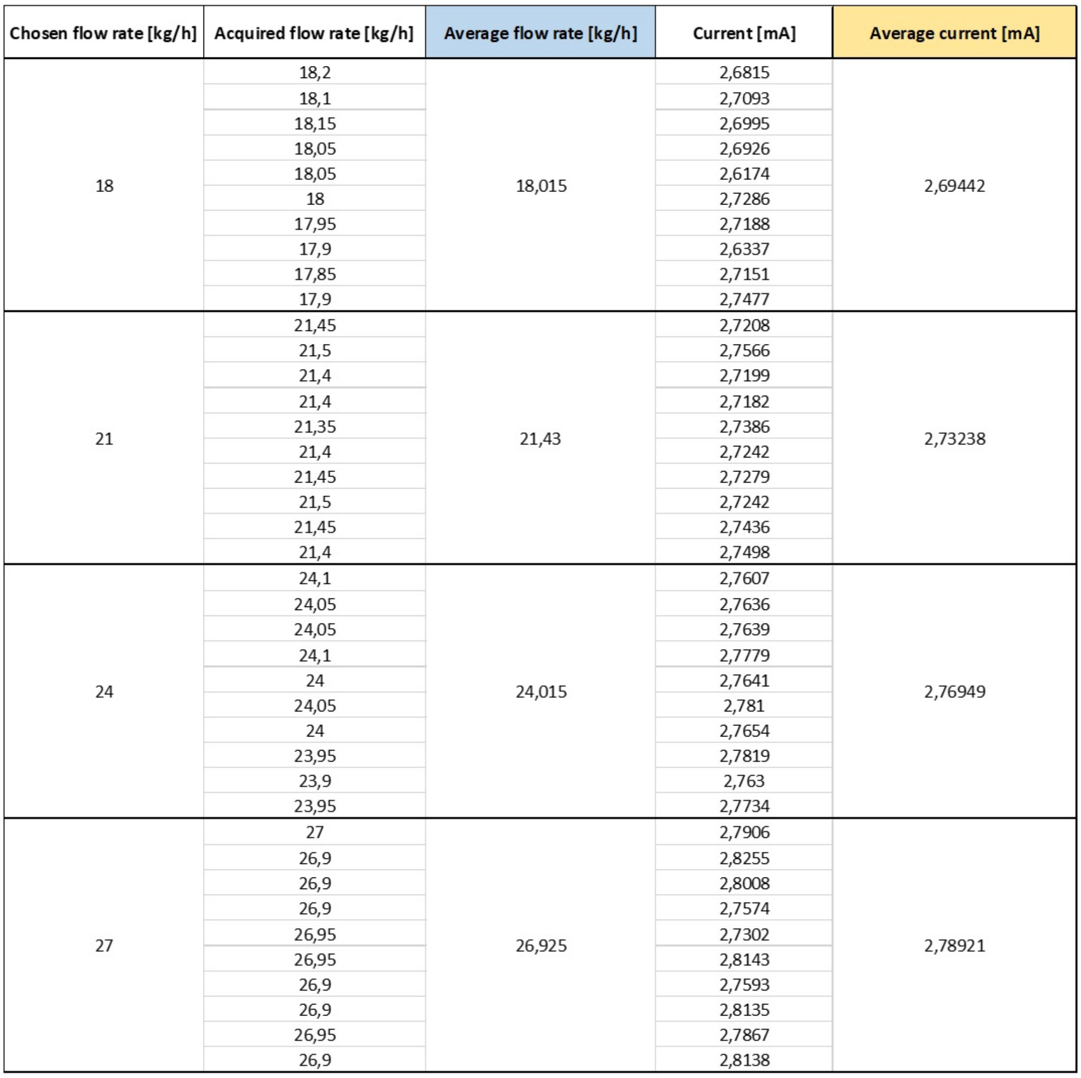

Chosen flow rate [kg/h]	Acquired flow rate [kg/h]	Average flow rate [kg/h]	Current [mA]	Average current [mA]
18	18,2	18,015	2,6815	2,69442
	18,1		2,7093	
	18,15		2,6995	
	18,05		2,6926	
	18,05		2,6174	
	18		2,7286	
	17,95		2,7188	
	17,9		2,6337	
	17,85		2,7151	
	17,9		2,7477	
21	21,45	21,43	2,7208	2,73238
	21,5		2,7566	
	21,4		2,7199	
	21,4		2,7182	
	21,35		2,7386	
	21,4		2,7242	
	21,45		2,7279	
	21,5		2,7242	
	21,45		2,7436	
	21,4		2,7498	
24	24,1	24,015	2,7607	2,76949
	24,05		2,7636	
	24,05		2,7639	
	24,1		2,7779	
	24		2,7641	
	24,05		2,781	
	24		2,7654	
	23,95		2,7819	
	23,9		2,763	
	23,95		2,7734	
27	27	26,925	2,7906	2,78921
	26,9		2,8255	
	26,9		2,8008	
	26,9		2,7574	
	26,95		2,7302	
	26,95		2,8143	
	26,9		2,7593	
	26,9		2,8135	
	26,95		2,7867	
	26,9		2,8138	

Figure 4.15. *A screenshot of the flowmeter calibration spreadsheet.*

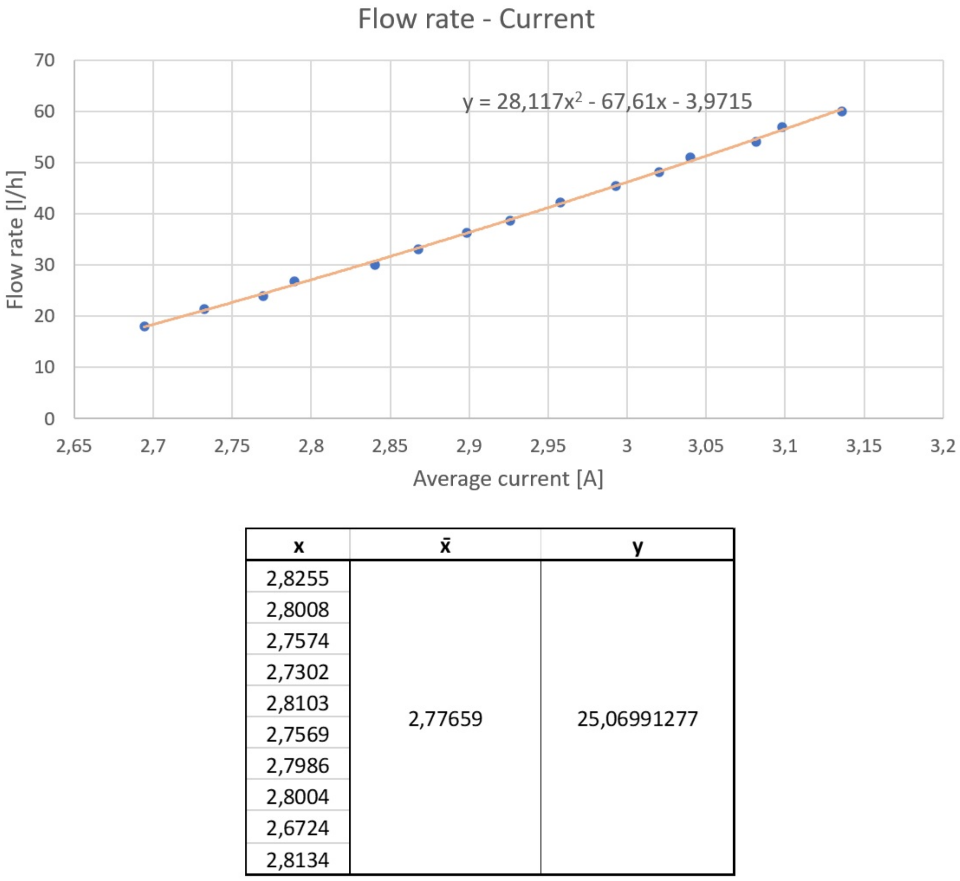

x	x̄	y
2,8255	2,77659	25,06991277
2,8008		
2,7574		
2,7302		
2,8103		
2,7569		
2,7986		
2,8004		
2,6724		
2,8134		

Figure 4.16. *A screenshot of the flowmeter calibration spreadsheet with the flow rate-current graph.*

4. SUPPLEMENTARY EXPERIMENTAL RESULTS

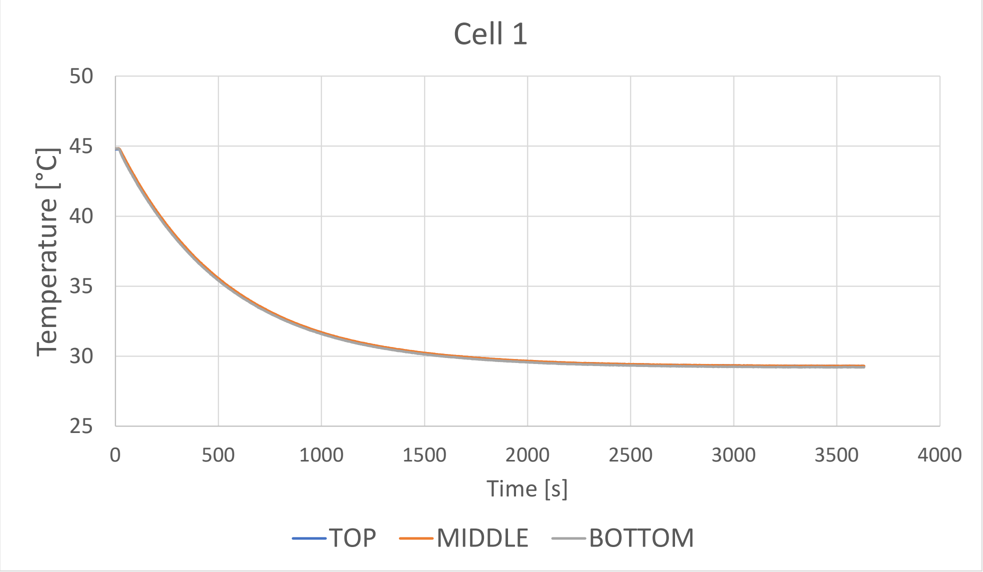

Figure 4.17. *Forced ventilation, Test 0.2: temperature trends recorded by* TC_{TOP}*,* TC_{MID} *and* TC_{BOT} *along Cell 1.*

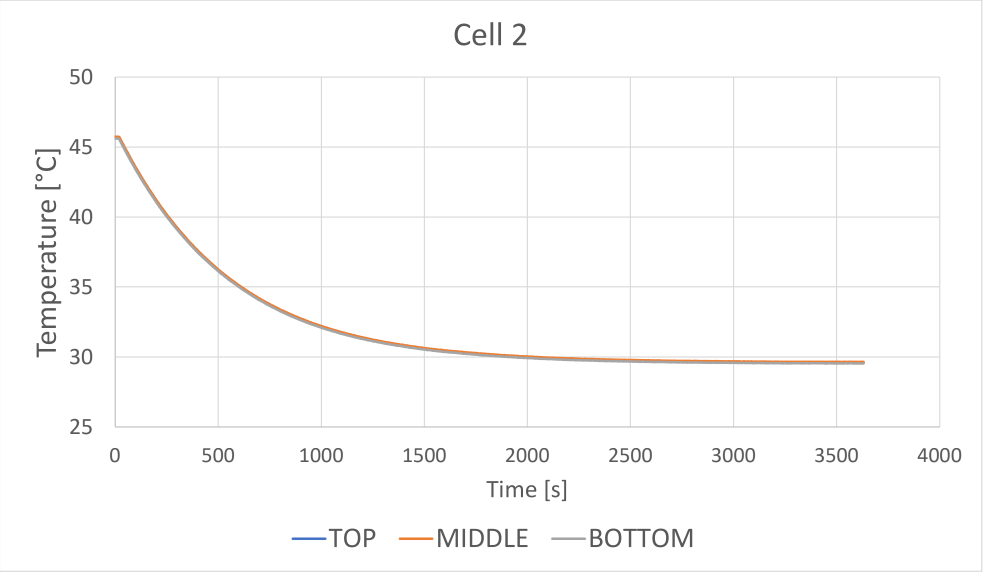

Figure 4.18. *Forced ventilation, Test 0.2: temperature trends recorded by* TC_{TOP}*,* TC_{MID} *and* TC_{BOT} *along Cell 2.*

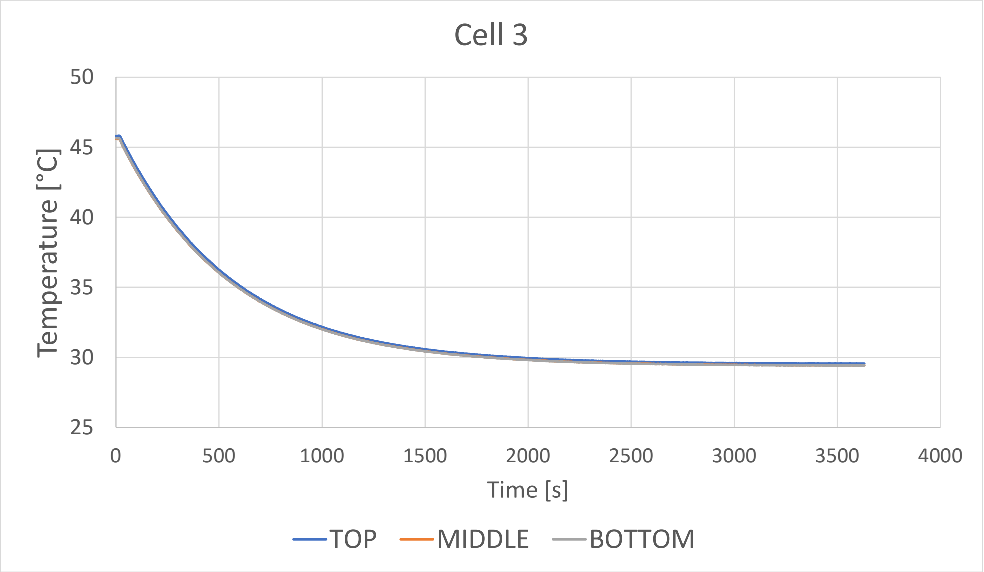

Figure 4.19. *Forced ventilation, Test 0.2: temperature trends recorded by* TC_{TOP}, TC_{MID} *and* TC_{BOT} *along Cell 3.*

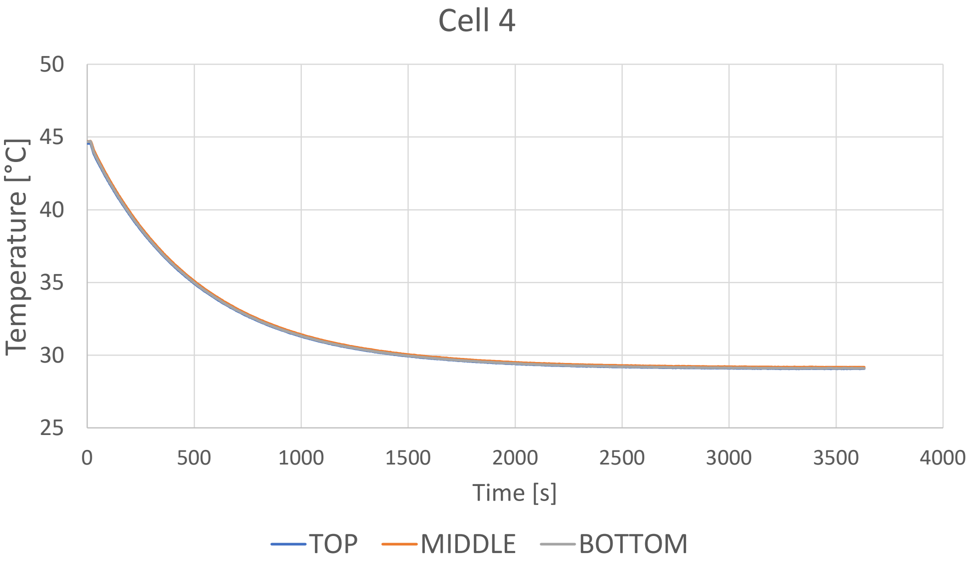

Figure 4.20. *Forced ventilation, Test 0.2: temperature trends recorded by* TC_{TOP}, TC_{MID} *and* TC_{BOT} *along Cell 4.*

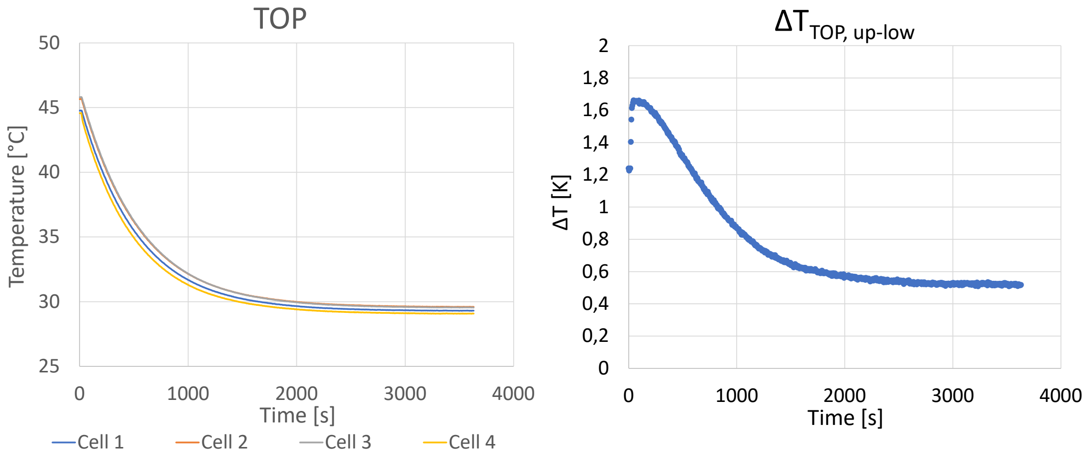

Figure 4.21. *Forced ventilation, Test 0.2: temperature trends recorded on the top of all the cells (left) and ΔT trend between the top of the upper and the lower cells (right).*

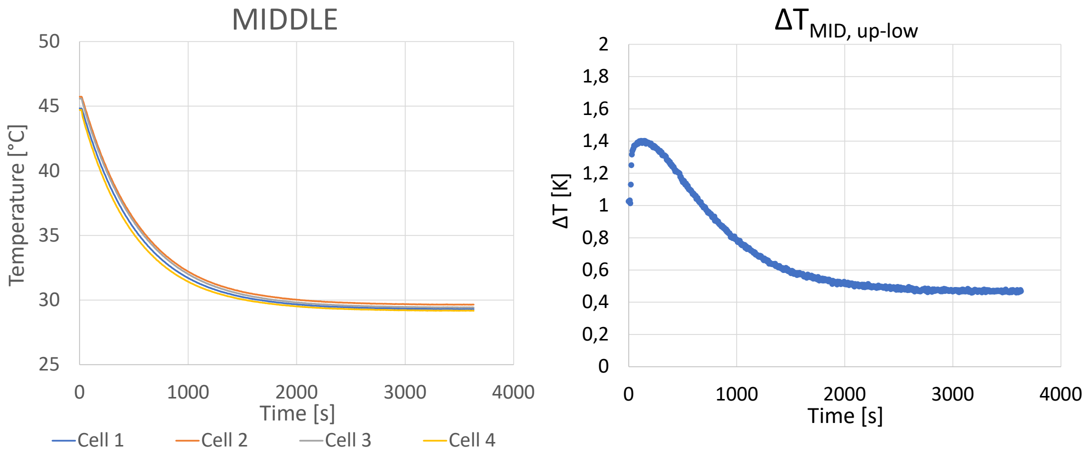

Figure 4.22. *Forced ventilation, Test 0.2: temperature trends recorded in the middle of all the cells (left) and ΔT trend between the middle of the upper and the lower cells (right).*

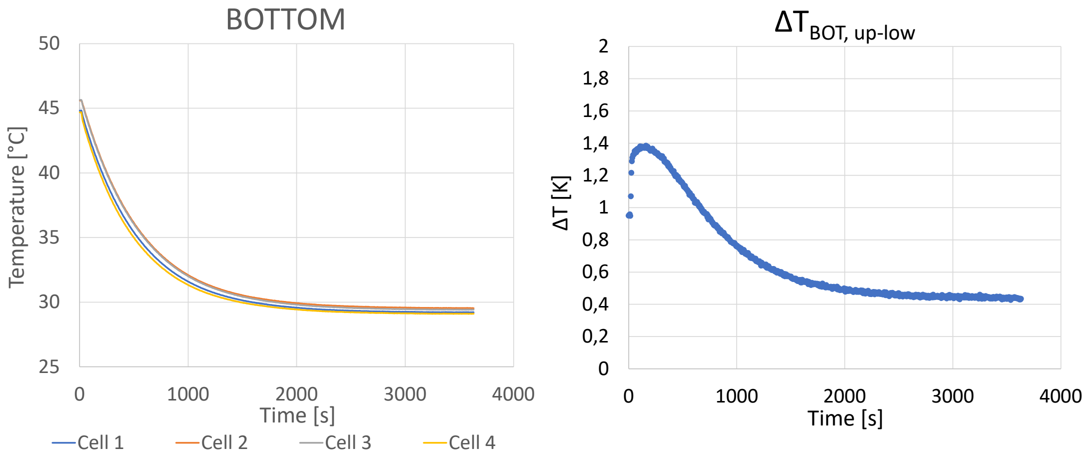

Figure 4.23. *Forced ventilation, Test 0.2: temperature trends recorded on the bottom of all the cells (left) and ΔT trend between the bottom of the upper and the lower cells (right).*

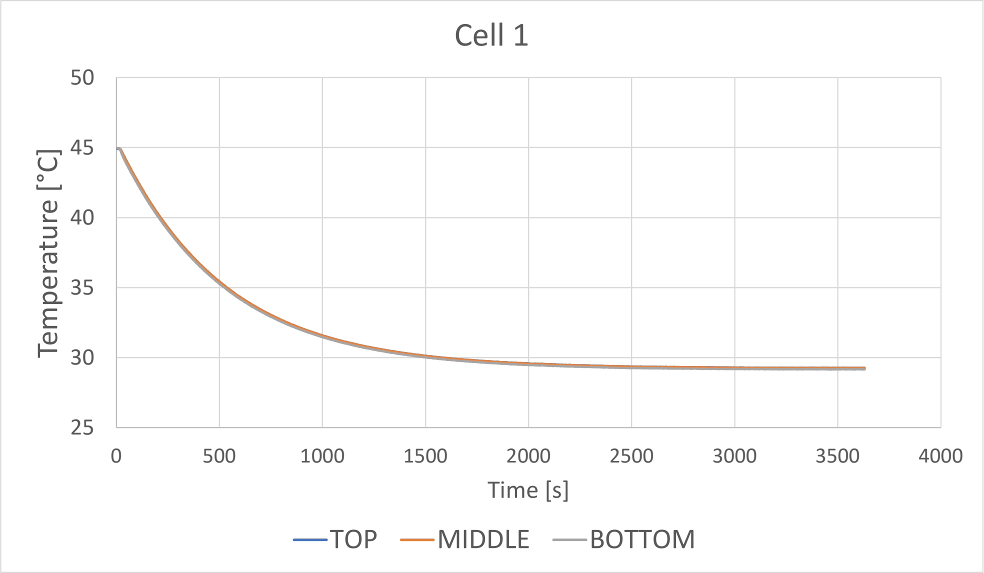

Figure 4.24. *Forced ventilation, Test 0.3: temperature trends recorded by* TC_{TOP}, TC_{MID} *and* TC_{BOT} *along Cell 1.*

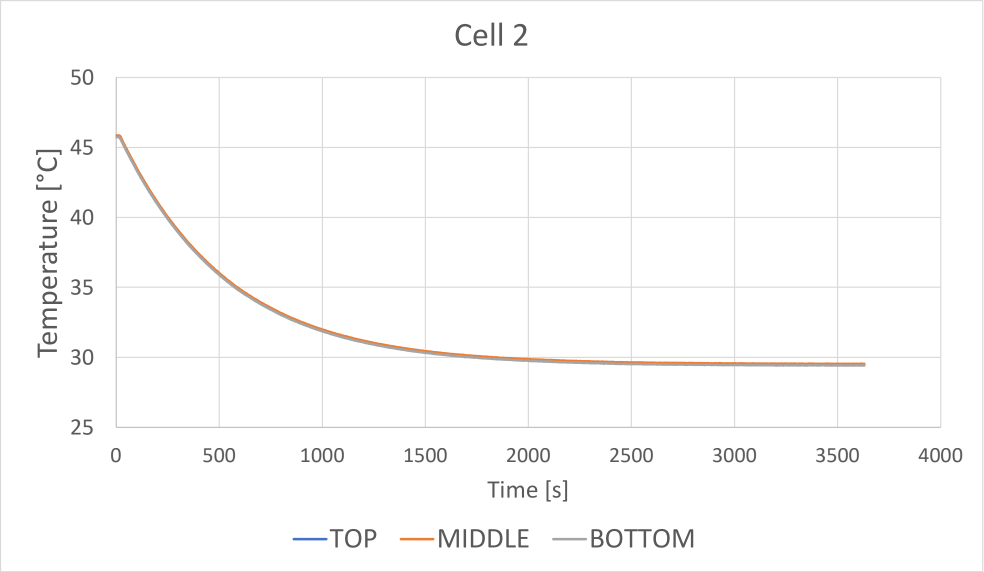

Figure 4.25. *Forced ventilation, Test 0.3: temperature trends recorded by* TC_{TOP}, TC_{MID} *and* TC_{BOT} *along Cell 2.*

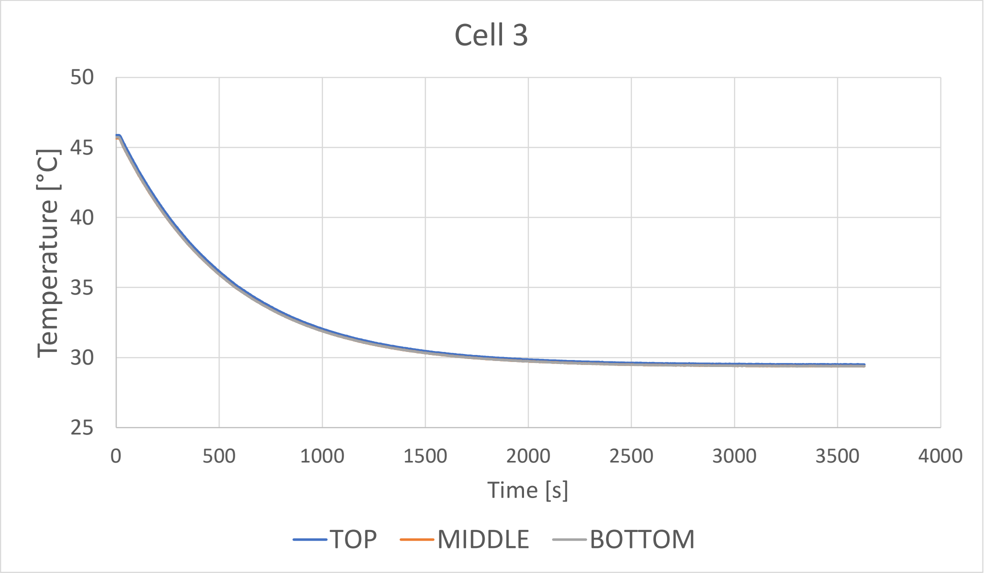

Figure 4.26. *Forced ventilation, Test 0.3: temperature trends recorded by* TC_{TOP}, TC_{MID} *and* TC_{BOT} *along Cell 3.*

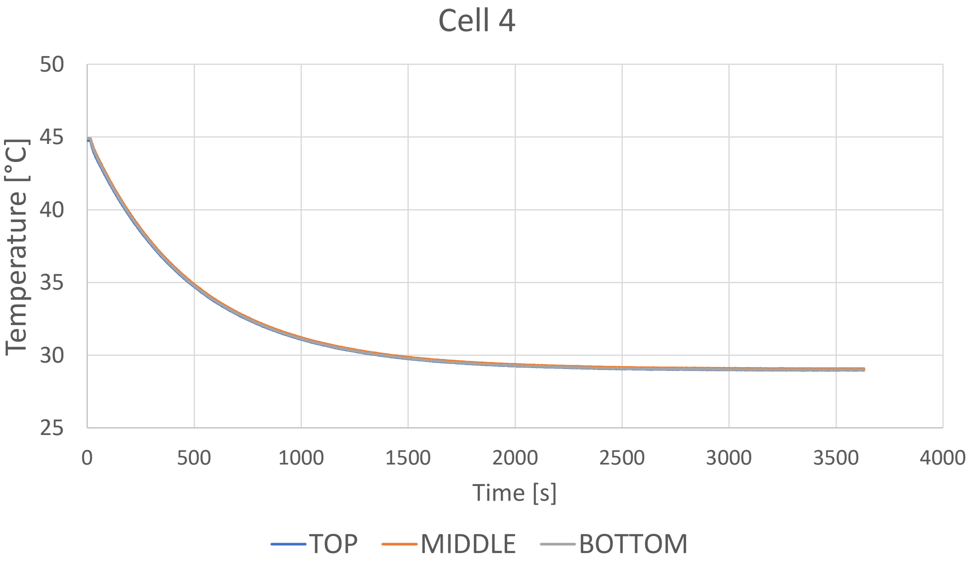

Figure 4.27. *Forced ventilation, Test 0.3: temperature trends recorded by* TC_{TOP}, TC_{MID} *and* TC_{BOT} *along Cell 4.*

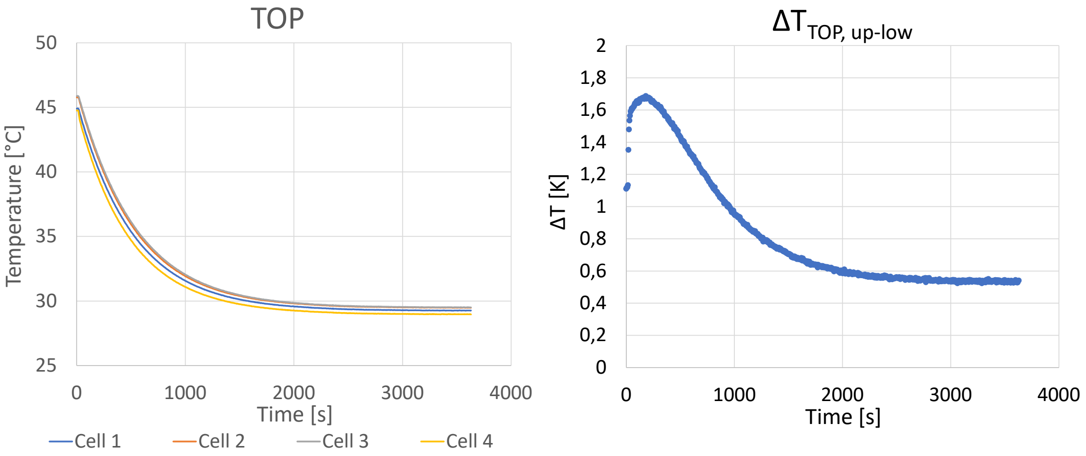

Figure 4.28. *Forced ventilation, Test 0.3: temperature trends recorded on the top of all the cells (left) and* ΔT *trend between the top of the upper and the lower cells (right).*

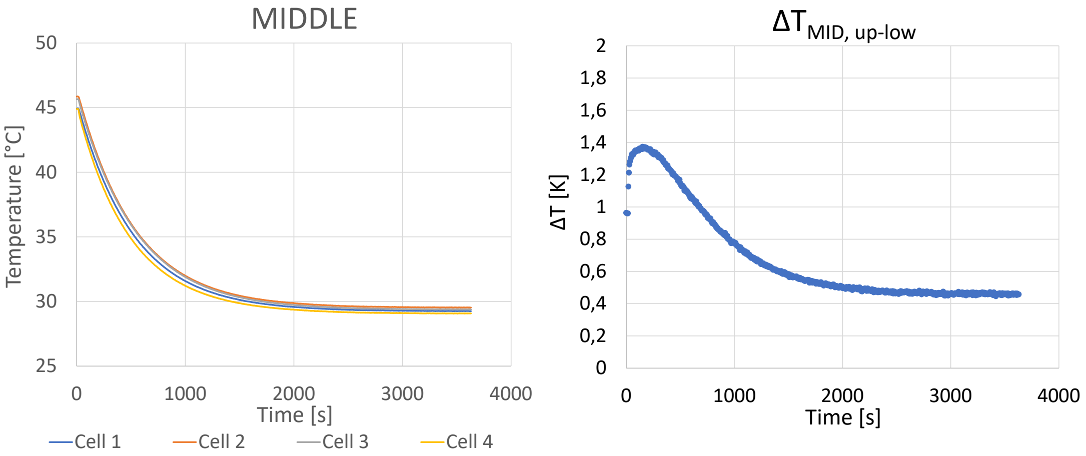

Figure 4.29. *Forced ventilation, Test 0.3: temperature trends recorded in the middle of all the cells (left) and* ΔT *trend between the middle of the upper and the lower cells (right).*

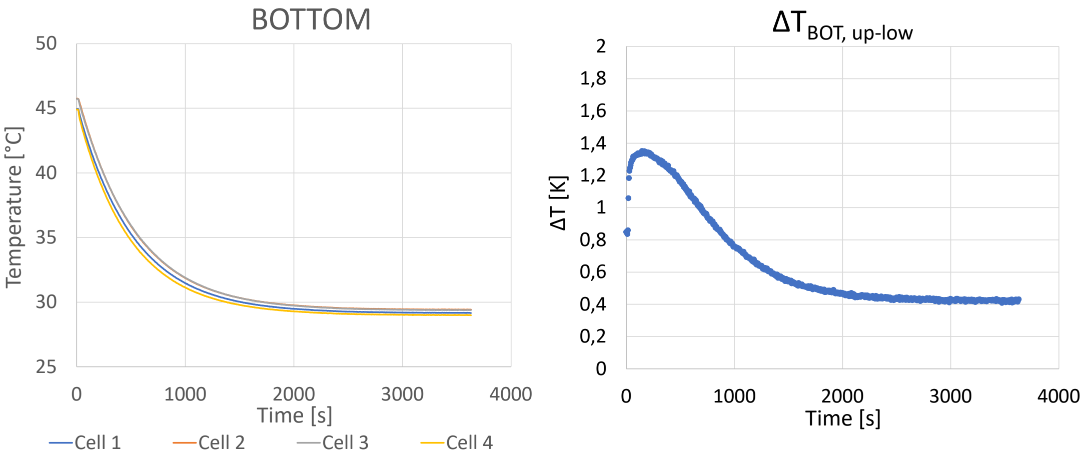

Figure 4.30. *Forced ventilation, Test 0.3: temperature trends recorded on the bottom of all the cells (left) and* ΔT *trend between the bottom of the upper and the lower cells (right).*

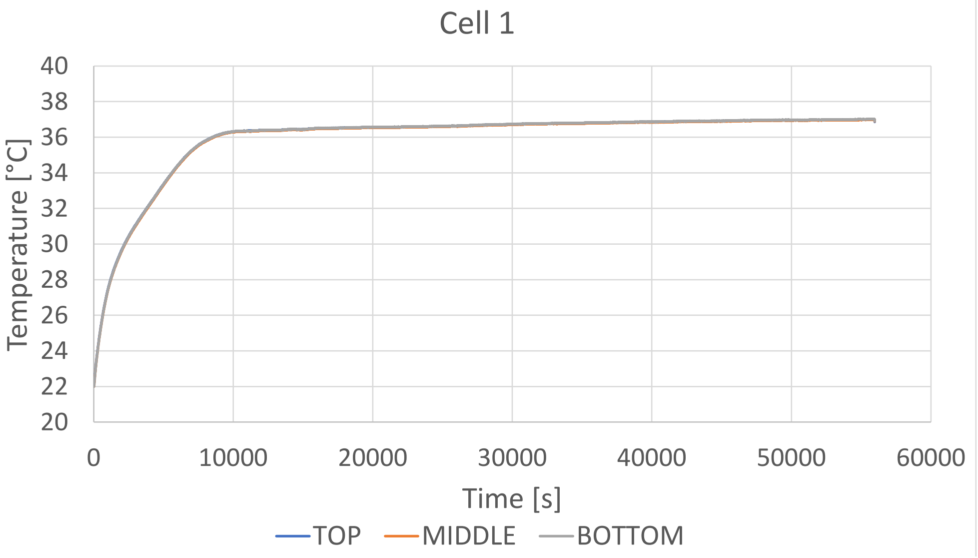

Figure 4.31. *Pure PCM, Test 1.2: temperature trends recorded by* TC_{TOP}, TC_{MID} *and* TC_{BOT} *along Cell 1.*

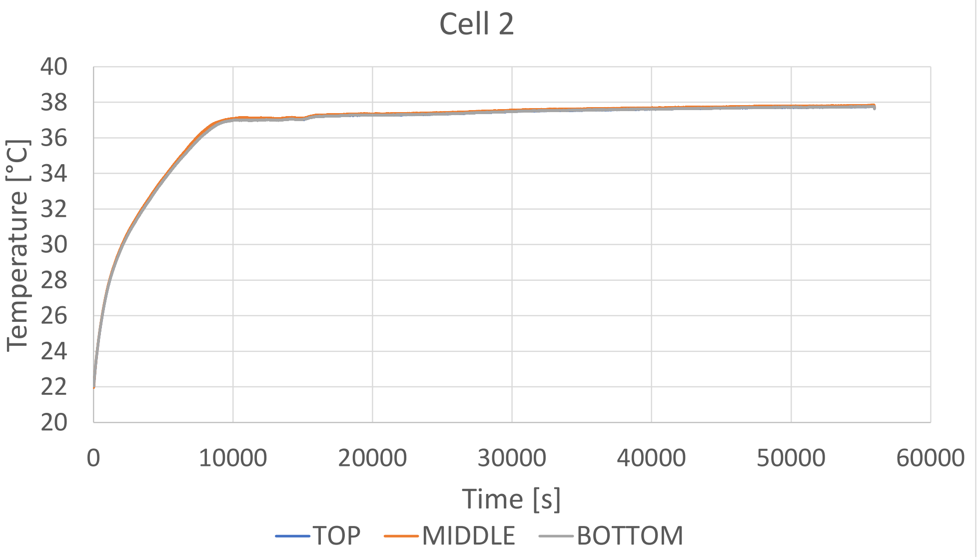

Figure 4.32. *Pure PCM, Test 1.2: temperature trends recorded by* TC_{TOP}, TC_{MID} *and* TC_{BOT} *along Cell 2.*

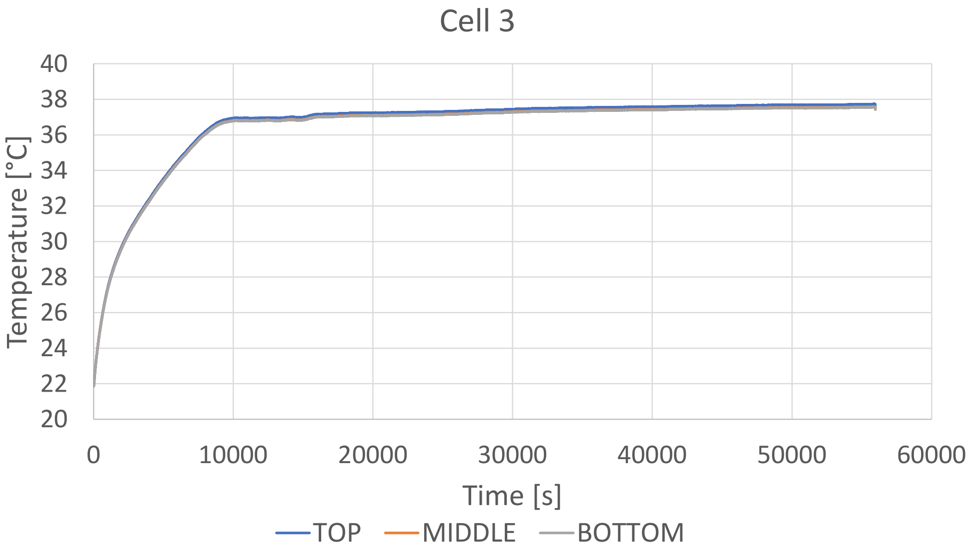

Figure 4.33. *Pure PCM, Test 1.2: temperature trends recorded by* TC_{TOP}*,* TC_{MID} *and* TC_{BOT} *along Cell 3.*

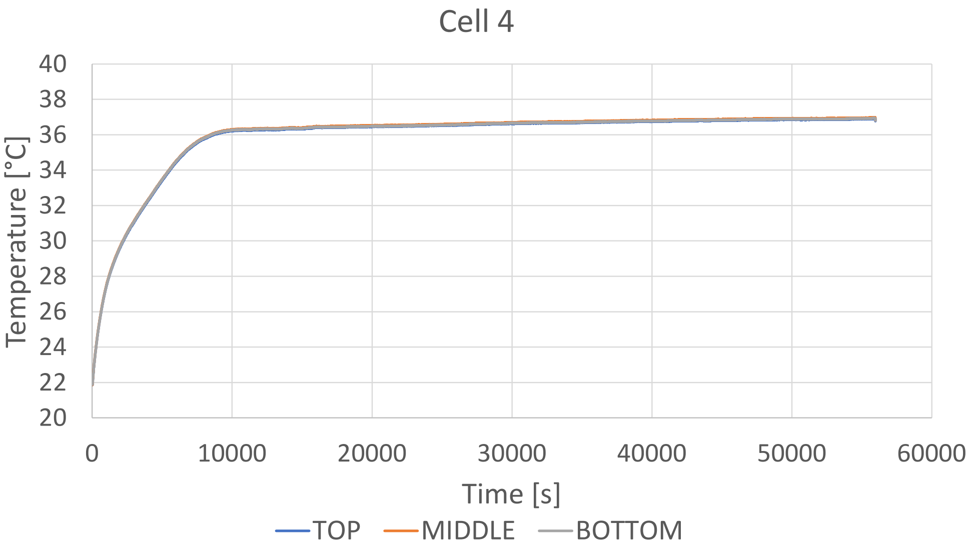

Figure 4.34. *Pure PCM, Test 1.2: temperature trends recorded by* TC_{TOP}*,* TC_{MID} *and* TC_{BOT} *along Cell 4.*

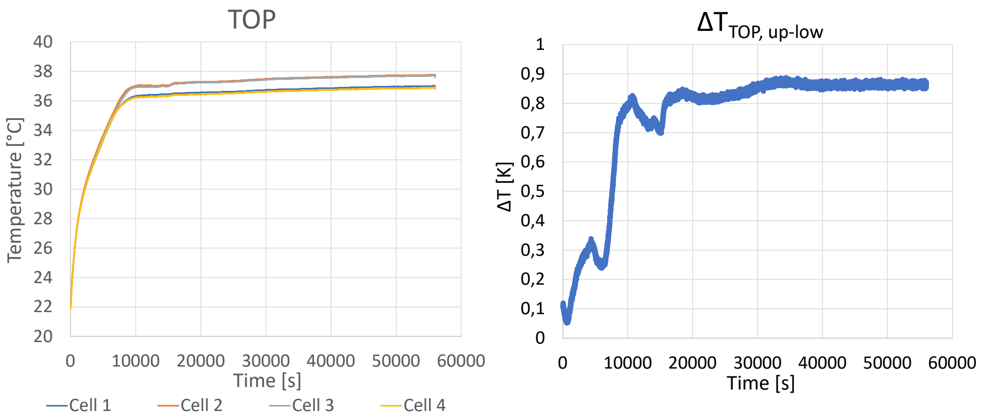

Figure 4.35. *Pure PCM, Test 1.2: temperature trends recorded on the top of all the cells (left) and ΔT trend between the top of the upper and the lower cells (right).*

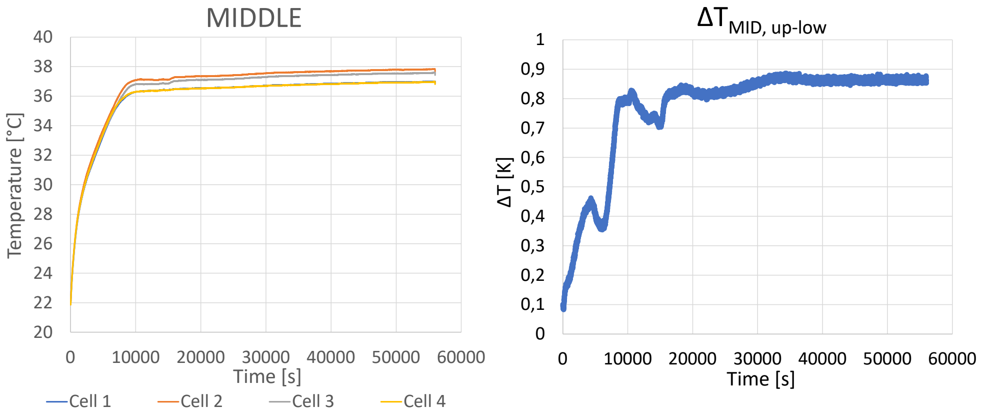

Figure 4.36. *Pure PCM, Test 1.2: temperature trends recorded in the middle of all the cells (left) and ΔT trend between the middle of the upper and the lower cells (right).*

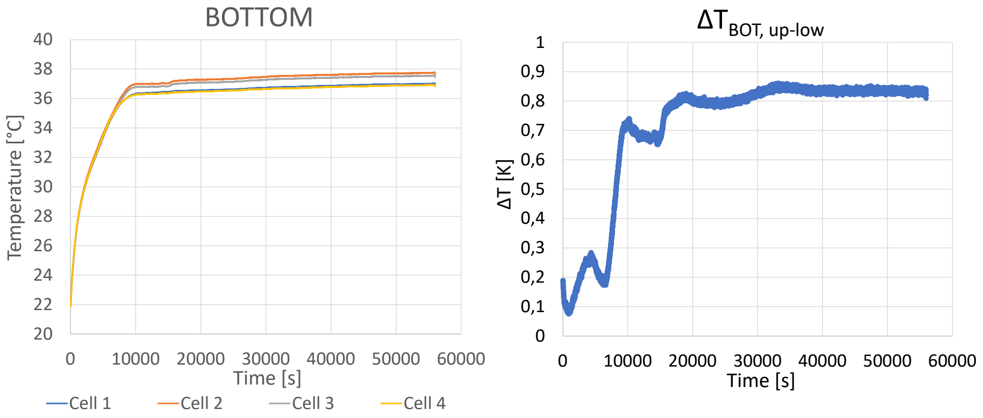

Figure 4.37. *Pure PCM, Test 1.2: temperature trends recorded on the bottom of all the cells (left) and ΔT trend between the bottom of the upper and the lower cells (right).*

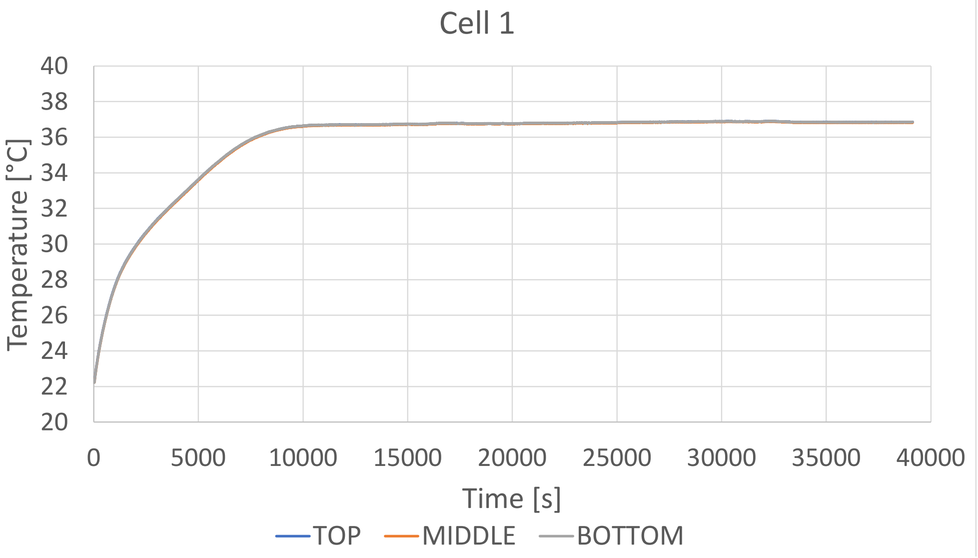

Figure 4.38. *Pure PCM, Test 1.3: temperature trends recorded by* TC_{TOP}, TC_{MID} *and* TC_{BOT} *along Cell 1.*

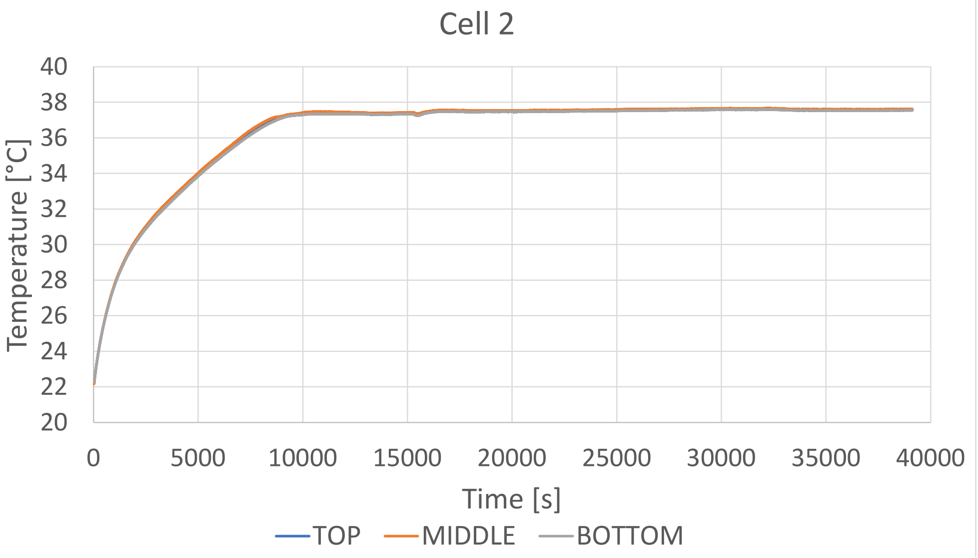

Figure 4.39. *Pure PCM, Test 1.3: temperature trends recorded by* TC_{TOP}, TC_{MID} *and* TC_{BOT} *along Cell 2.*

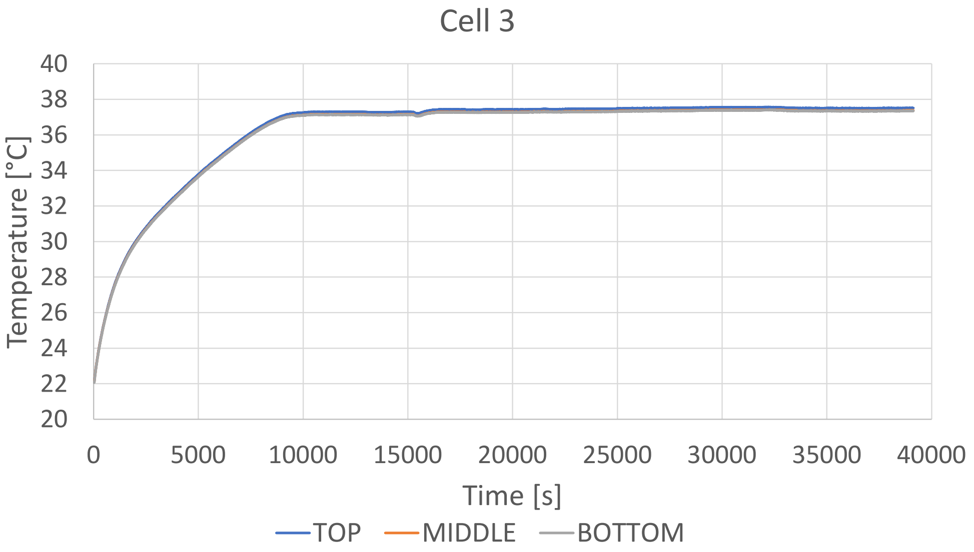

Figure 4.40. *Pure PCM, Test 1.3: temperature trends recorded by* TC_{TOP}, TC_{MID} *and* TC_{BOT} *along Cell 3.*

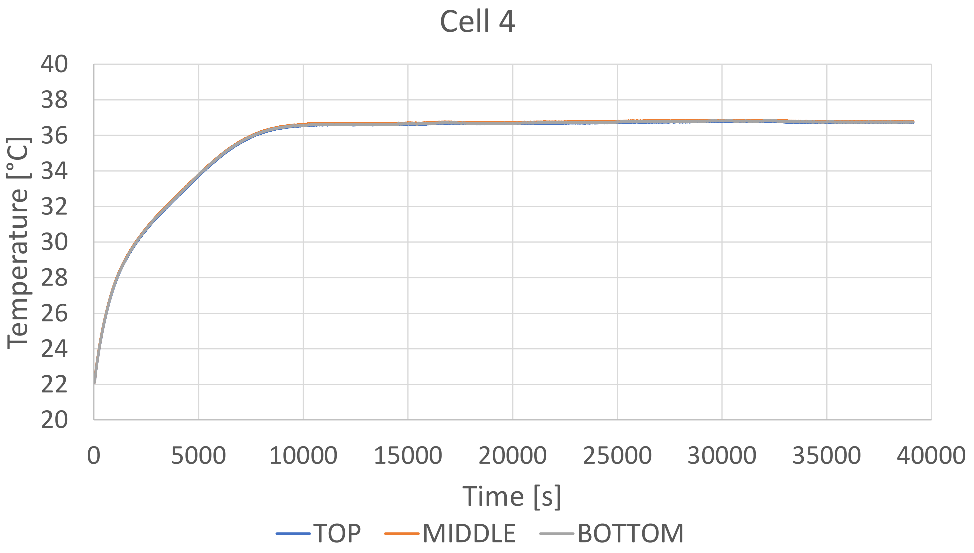

Figure 4.41. *Pure PCM, Test 1.3: temperature trends recorded by* TC_{TOP}, TC_{MID} *and* TC_{BOT} *along Cell 4.*

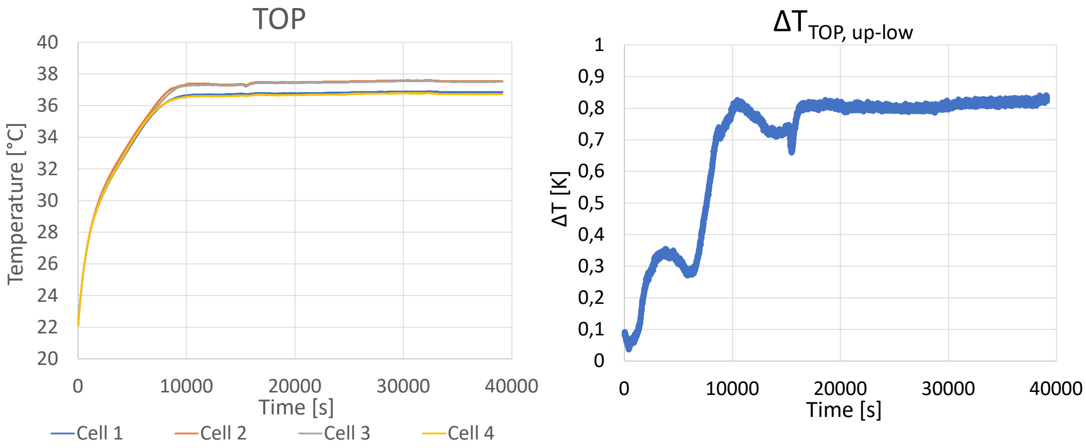

Figure 4.42. *Pure PCM, Test 1.3: temperature trends recorded on the top of all the cells (left) and ΔT trend between the top of the upper and the lower cells (right).*

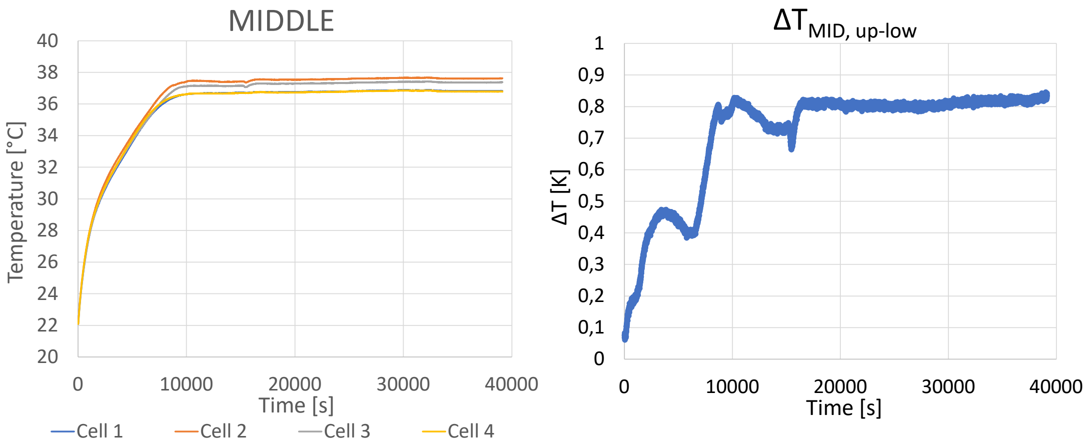

Figure 4.43. *Pure PCM, Test 1.3: temperature trends recorded in the middle of all the cells (left) and ΔT trend between the middle of the upper and the lower cells (right).*

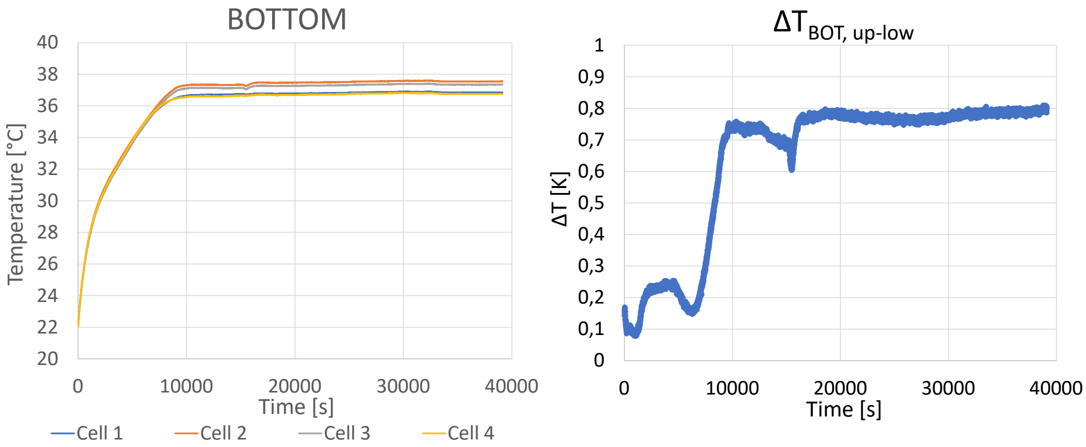

Figure 4.44. *Pure PCM, Test 1.3: temperature trends recorded on the bottom of all the cells (left) and ΔT trend between the bottom of the upper and the lower cells (right).*

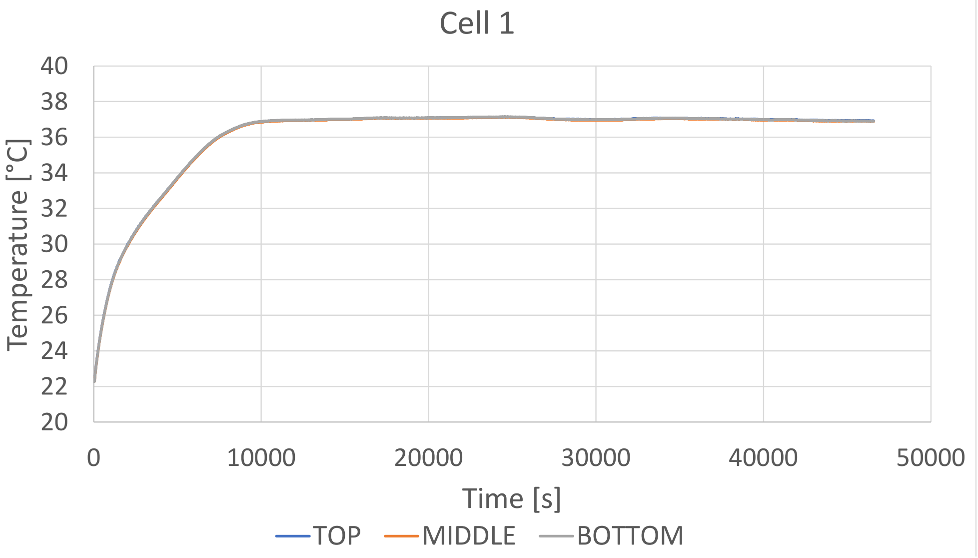

Figure 4.45. *Pure PCM, Test 1.4: temperature trends recorded by* TC_{TOP}, TC_{MID} *and* TC_{BOT} *along Cell 1.*

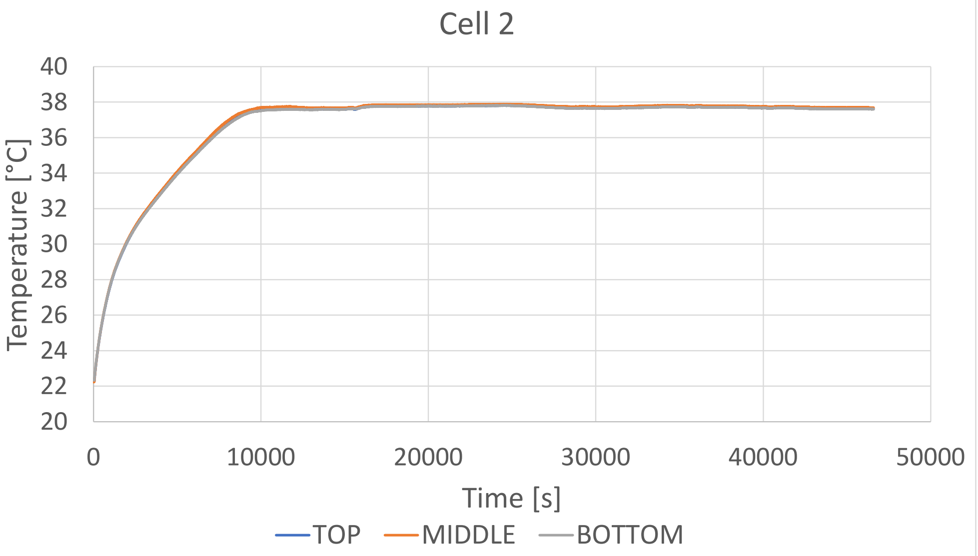

Figure 4.46. *Pure PCM, Test 1.4: temperature trends recorded by* TC_{TOP}, TC_{MID} *and* TC_{BOT} *along Cell 2.*

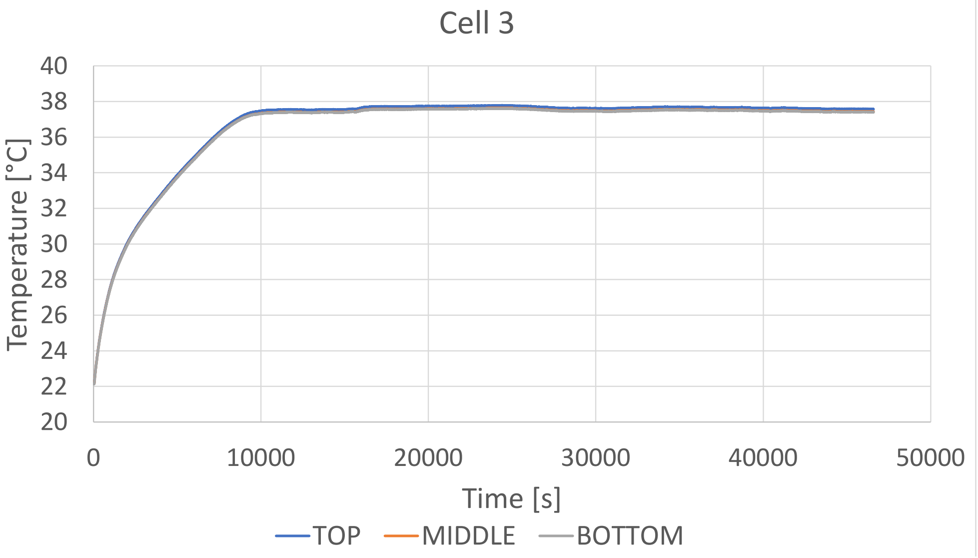

Figure 4.47. *Pure PCM, Test 1.4: temperature trends recorded by* TC_{TOP}, TC_{MID} *and* TC_{BOT} *along Cell 3.*

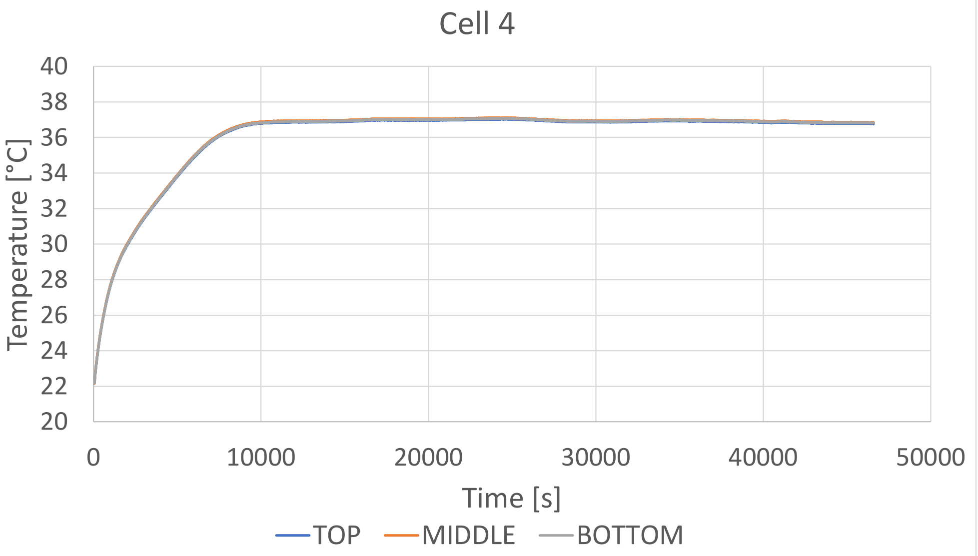

Figure 4.48. *Pure PCM, Test 1.4: temperature trends recorded by* TC_{TOP}, TC_{MID} *and* TC_{BOT} *along Cell 4.*

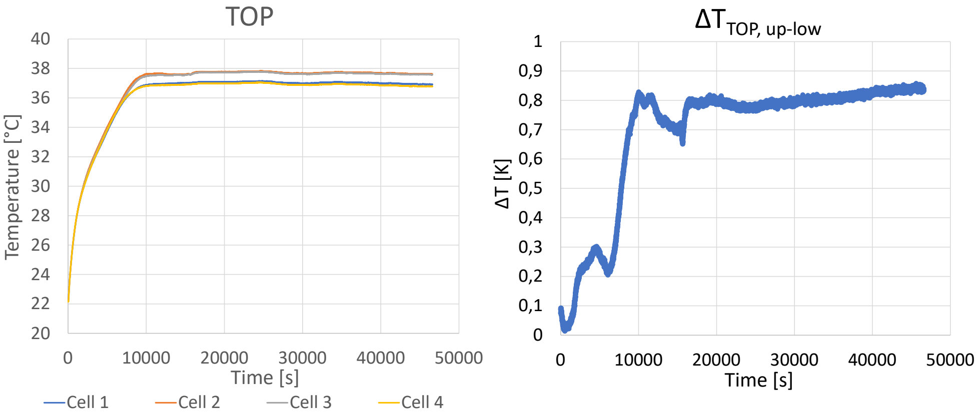

Figure 4.49. *Pure PCM, Test 1.4: temperature trends recorded on the top of all the cells (left) and* ΔT *trend between the top of the upper and the lower cells (right).*

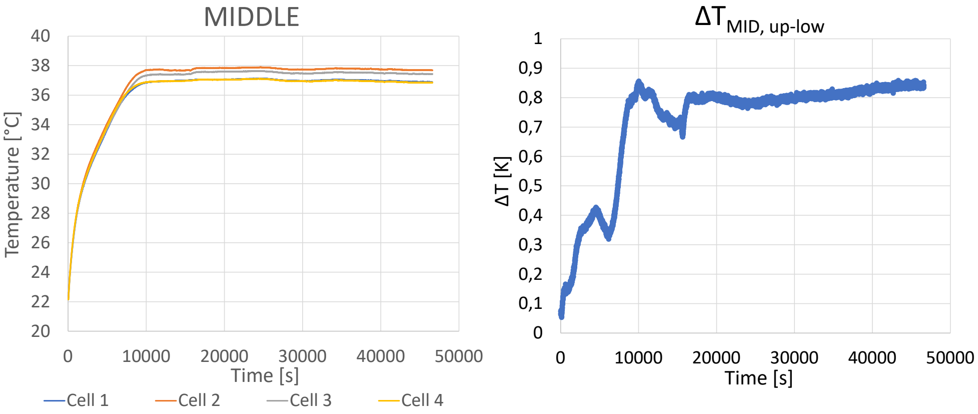

Figure 4.50. *Pure PCM, Test 1.4: temperature trends recorded in the middle of all the cells (left) and* ΔT *trend between the middle of the upper and the lower cells (right).*

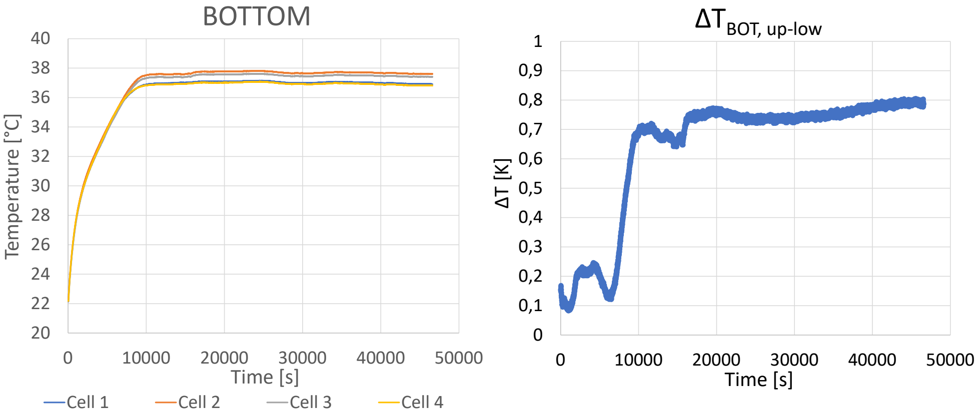

Figure 4.51. *Pure PCM, Test 1.4: temperature trends recorded on the bottom of all the cells (left) and* ΔT *trend between the bottom of the upper and the lower cells (right).*

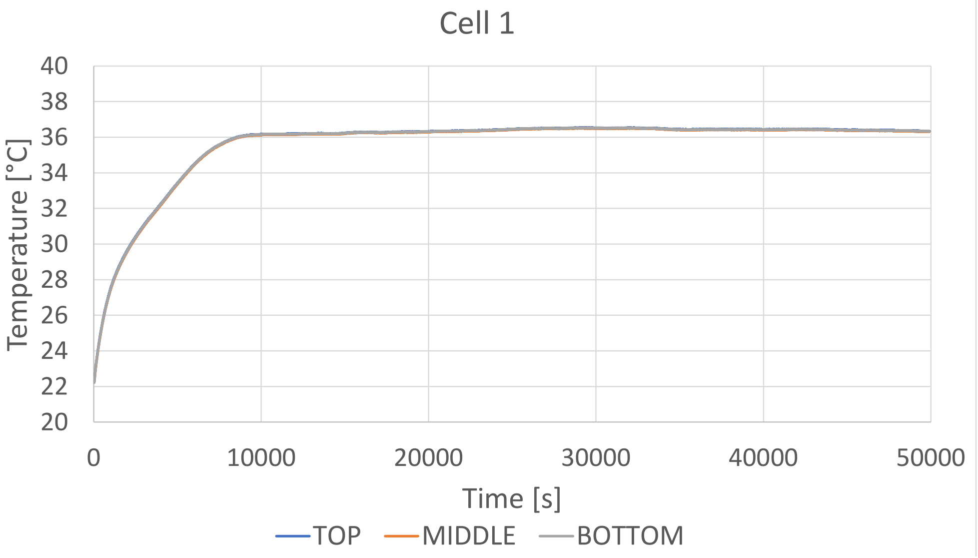

Figure 4.52. *Pure PCM, Test 1.5: temperature trends recorded by* TC_{TOP}, TC_{MID} *and* TC_{BOT} *along Cell 1.*

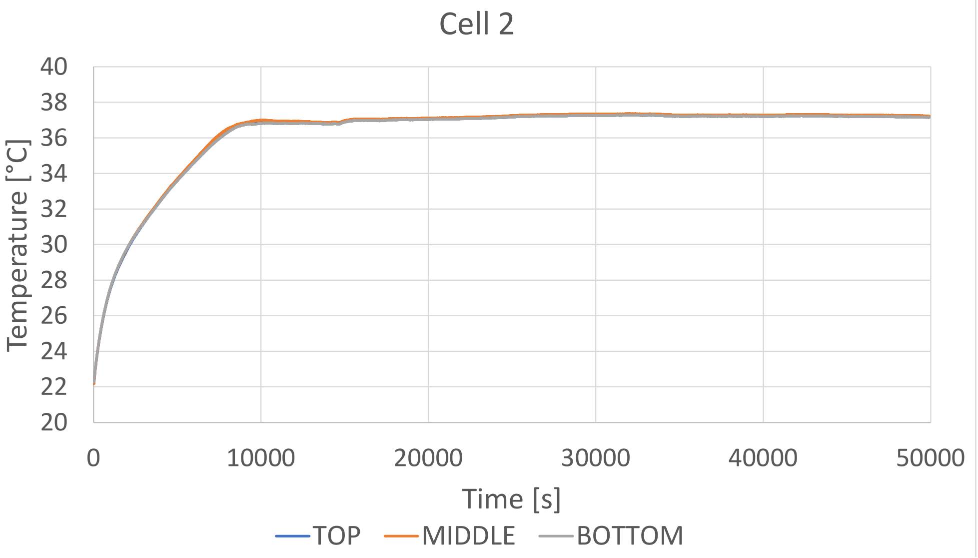

Figure 4.53. *Pure PCM, Test 1.5: temperature trends recorded by* TC_{TOP}, TC_{MID} *and* TC_{BOT} *along Cell 2.*

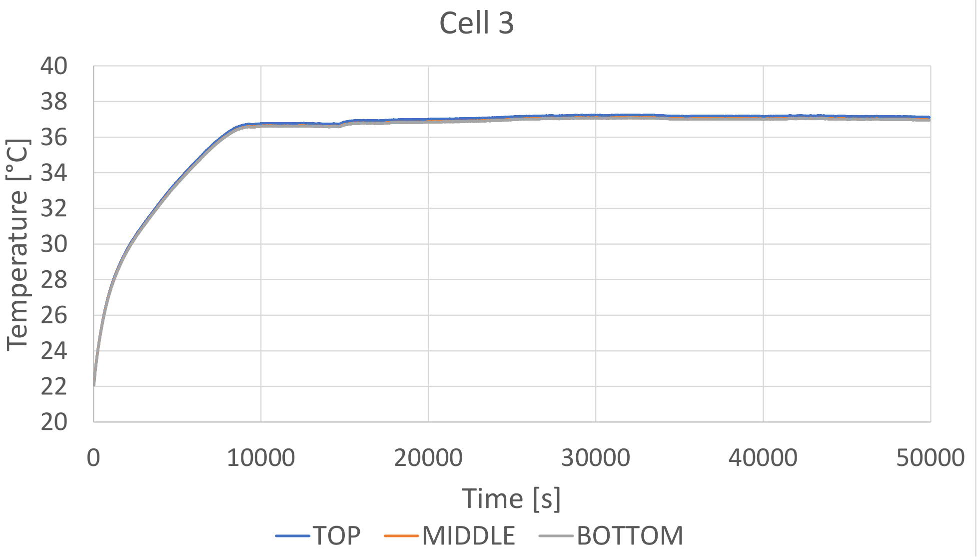

Figure 4.54. *Pure PCM, Test 1.5: temperature trends recorded by* TC_{TOP}, TC_{MID} *and* TC_{BOT} *along Cell 3.*

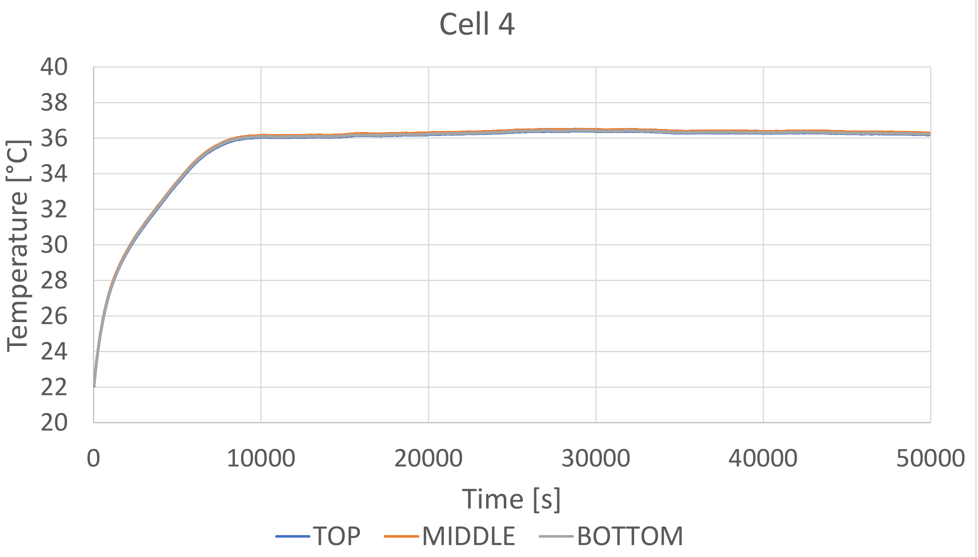

Figure 4.55. *Pure PCM, Test 1.5: temperature trends recorded by* TC_{TOP}, TC_{MID} *and* TC_{BOT} *along Cell 4.*

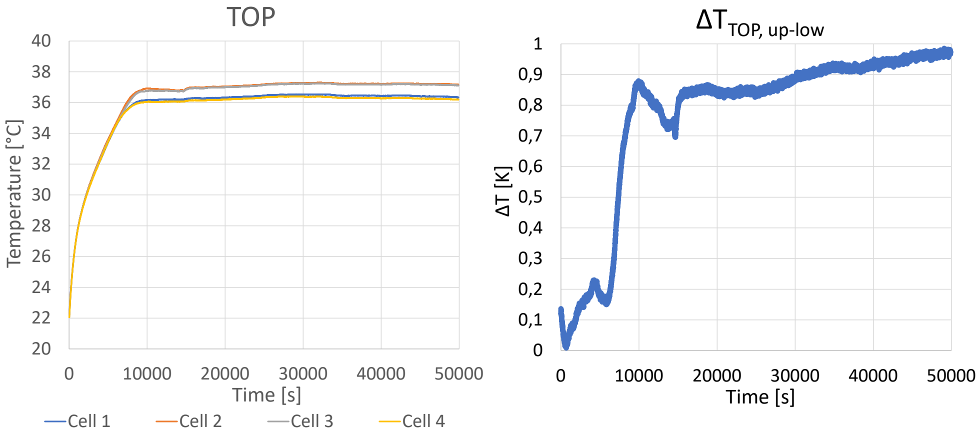

Figure 4.56. *Pure PCM, Test 1.5: temperature trends recorded on the top of all the cells (left) and* ΔT *trend between the top of the upper and the lower cells (right).*

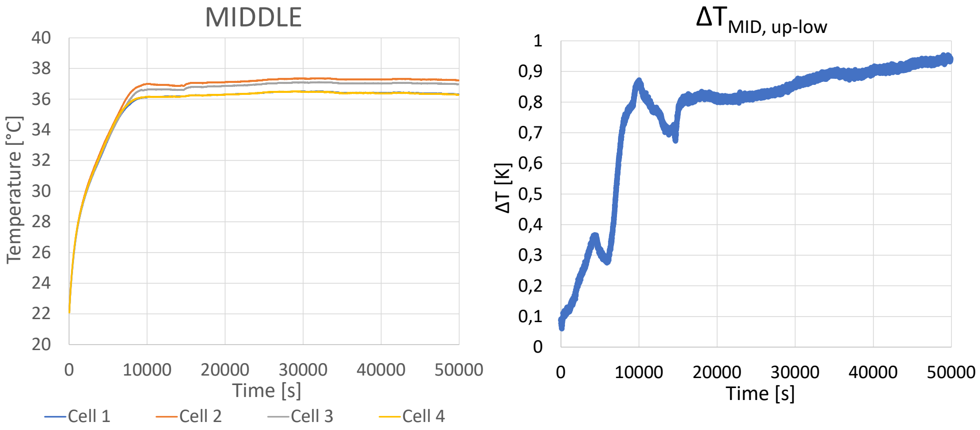

Figure 4.57. *Pure PCM, Test 1.5: temperature trends recorded in the middle of all the cells (left) and* ΔT *trend between the middle of the upper and the lower cells (right).*

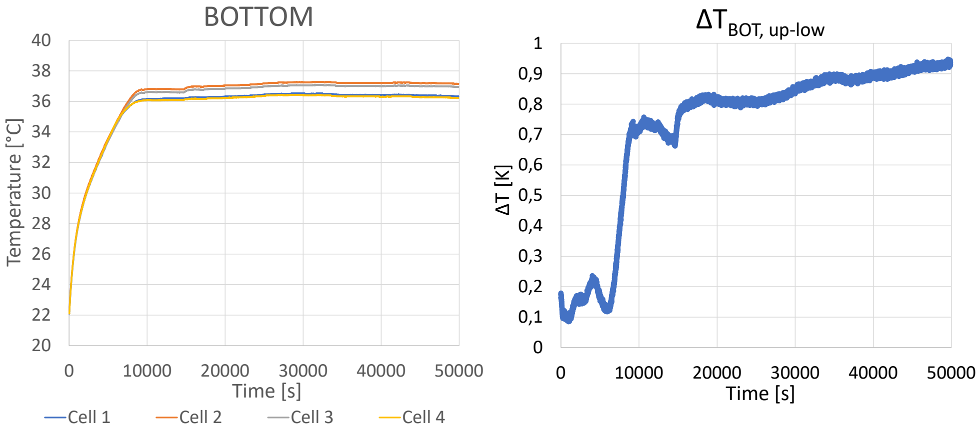

Figure 4.58. *Pure PCM, Test 1.5: temperature trends recorded on the bottom of all the cells (left) and* ΔT *trend between the bottom of the upper and the lower cells (right).*

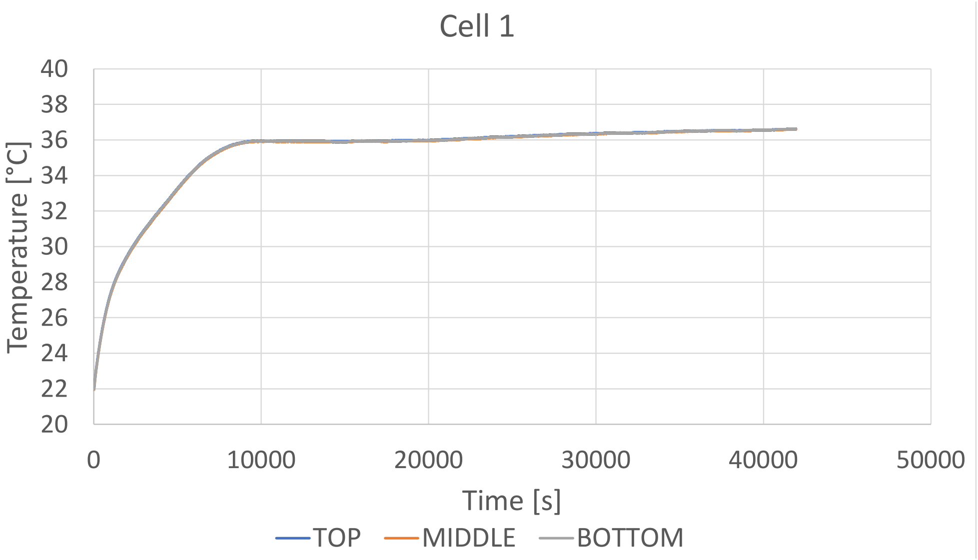

Figure 4.59. *Pure PCM, Test 1.6: temperature trends recorded by* TC_{TOP}*,* TC_{MID} *and* TC_{BOT} *along Cell 1.*

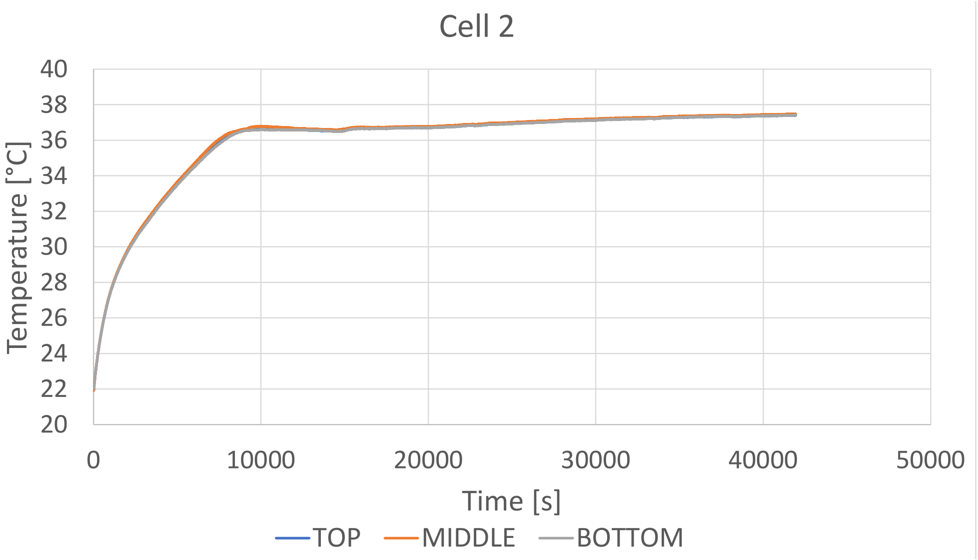

Figure 4.60. *Pure PCM, Test 1.6: temperature trends recorded by* TC_{TOP}*,* TC_{MID} *and* TC_{BOT} *along Cell 2.*

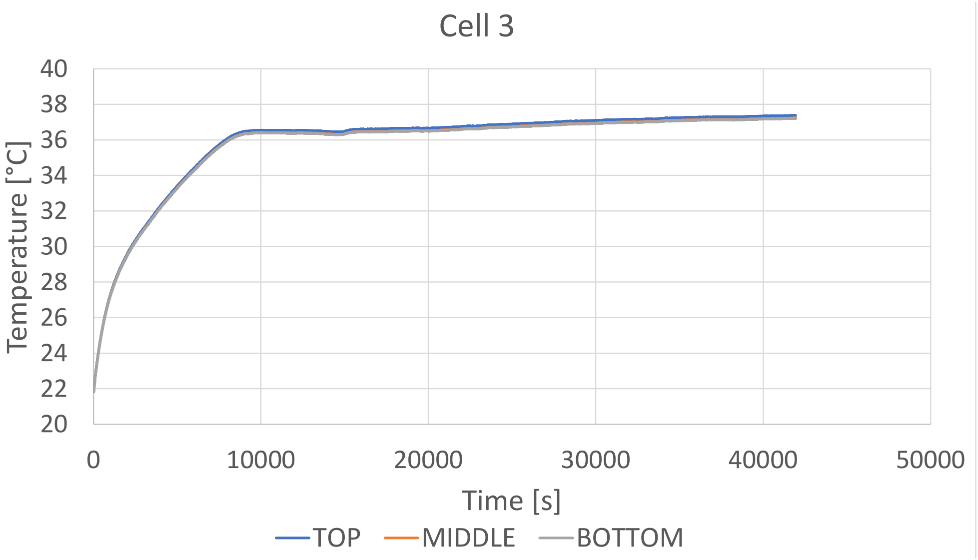

Figure 4.61. *Pure PCM, Test 1.6: temperature trends recorded by* TC_{TOP}, TC_{MID} *and* TC_{BOT} *along Cell 3.*

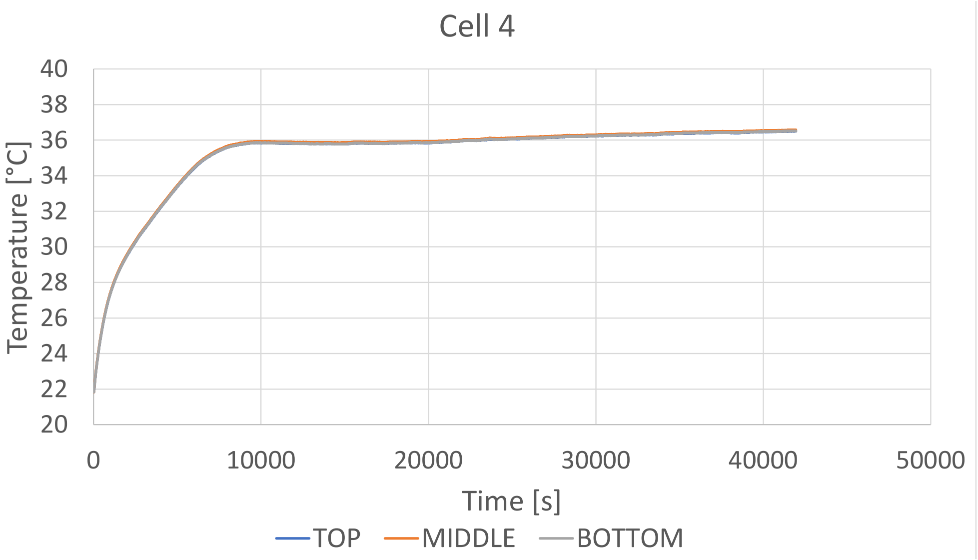

Figure 4.62. *Pure PCM, Test 1.6: temperature trends recorded by* TC_{TOP}, TC_{MID} *and* TC_{BOT} *along Cell 4.*

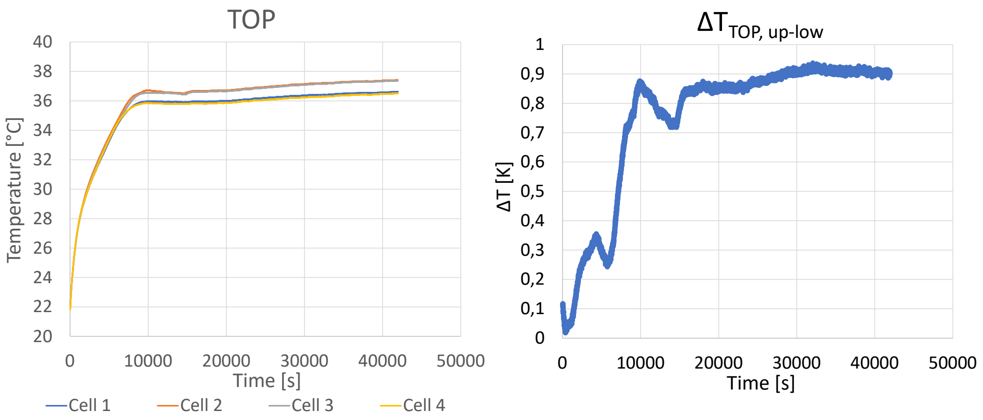

Figure 4.63. *Pure PCM, Test 1.6: temperature trends recorded on the top of all the cells (left) and* ΔT *trend between the top of the upper and the lower cells (right).*

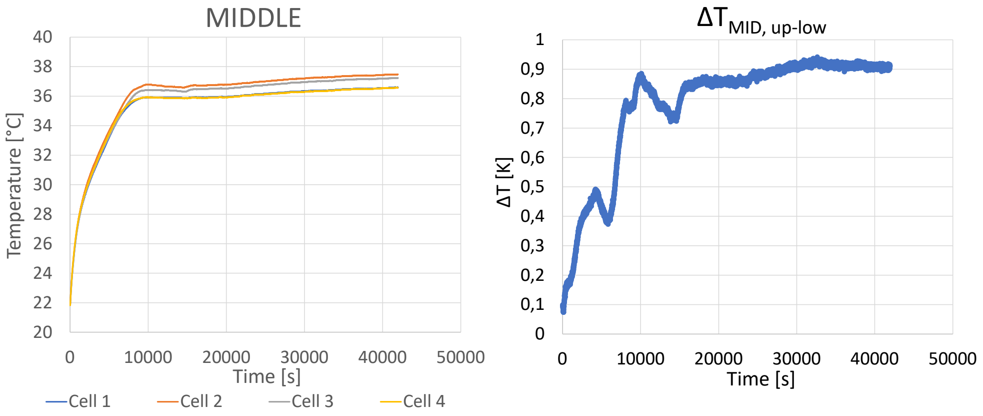

Figure 4.64. *Pure PCM, Test 1.6: temperature trends recorded in the middle of all the cells (left) and* ΔT *trend between the middle of the upper and the lower cells (right).*

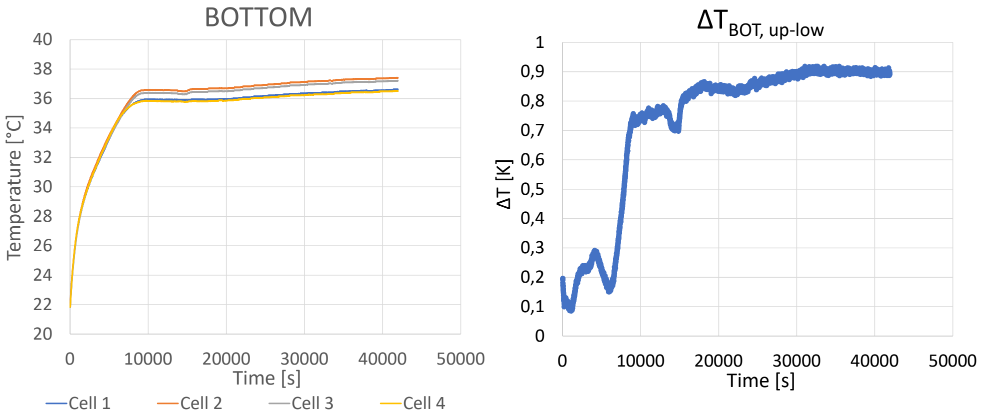

Figure 4.65. *Pure PCM, Test 1.6: temperature trends recorded on the bottom of all the cells (left) and* ΔT *trend between the bottom of the upper and the lower cells (right).*

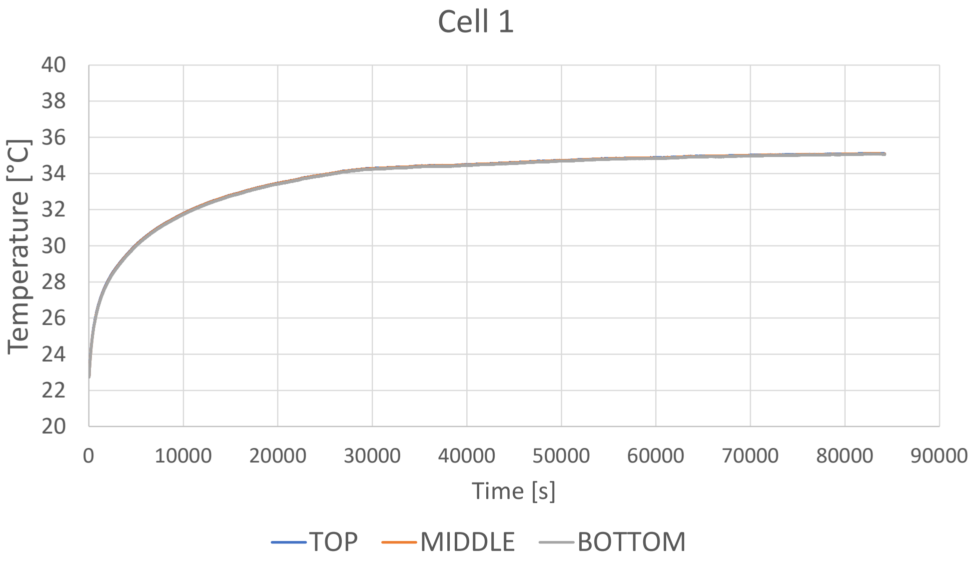

Figure 4.66. *Copper-foam-loaded PCM, Test 2.2: temperature trends recorded by* TC_{TOP}, TC_{MID} *and* TC_{BOT} *along Cell 1.*

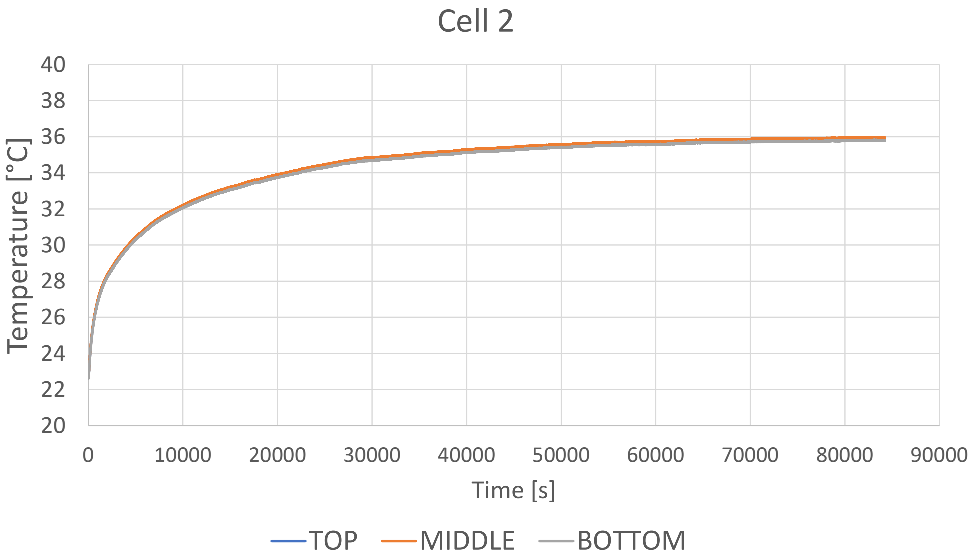

Figure 4.67. *Copper-foam-loaded PCM, Test 2.2: temperature trends recorded by* TC_{TOP}, TC_{MID} *and* TC_{BOT} *along Cell 2.*

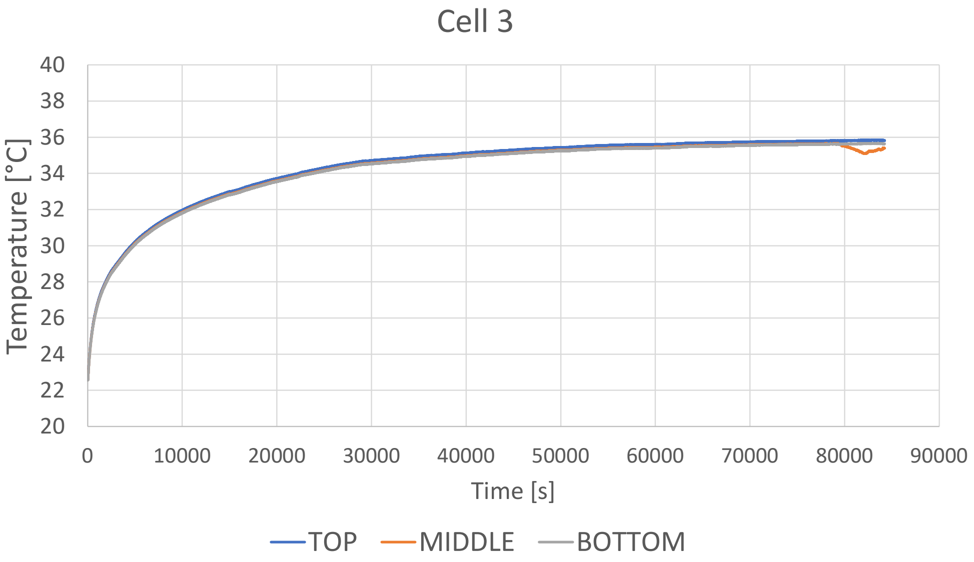

Figure 4.68. *Copper-foam-loaded PCM, Test 2.2: temperature trends recorded by* TC_{TOP}, TC_{MID} *and* TC_{BOT} *along Cell 3.*

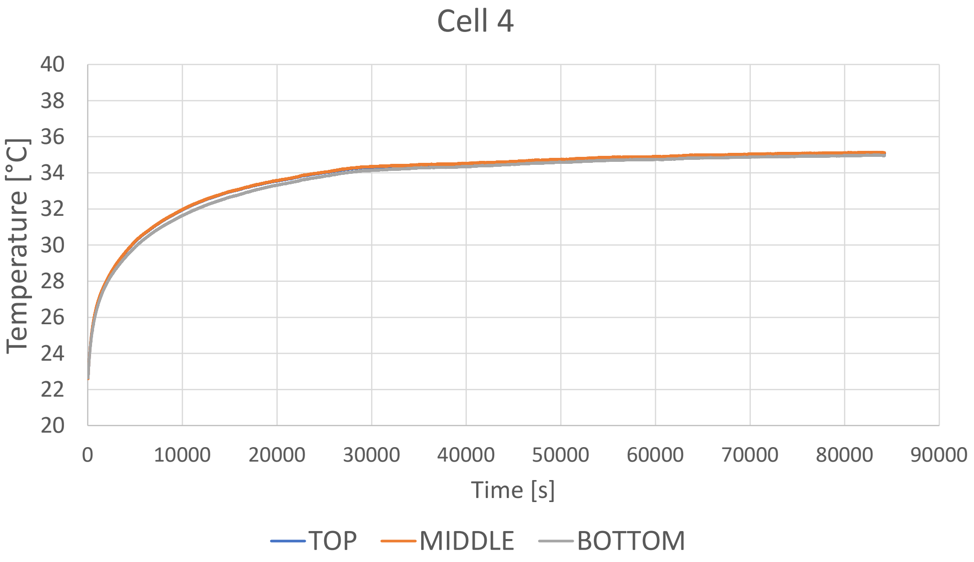

Figure 4.69. *Copper-foam-loaded PCM, Test 2.2: temperature trends recorded by* TC_{TOP}, TC_{MID} *and* TC_{BOT} *along Cell 4.*

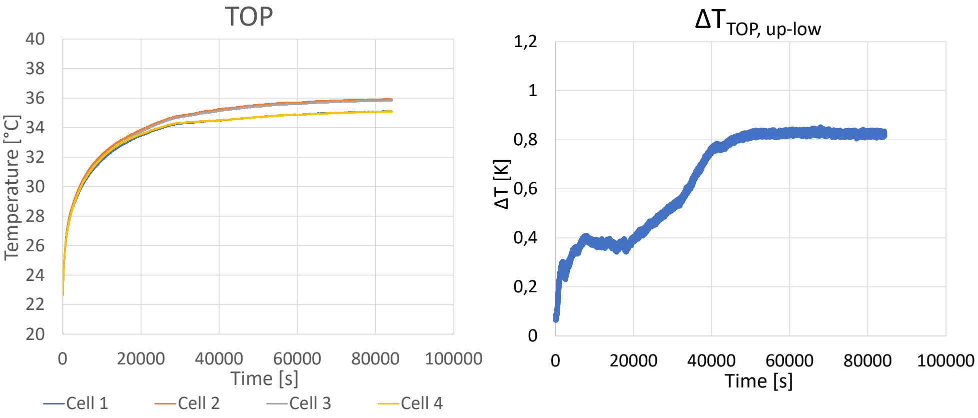

Figure 4.70. *Copper-foam-loaded PCM, Test 2.2: temperature trends recorded on the top of all the cells (left) and ΔT trend between the top of the upper and the lower cells (right).*

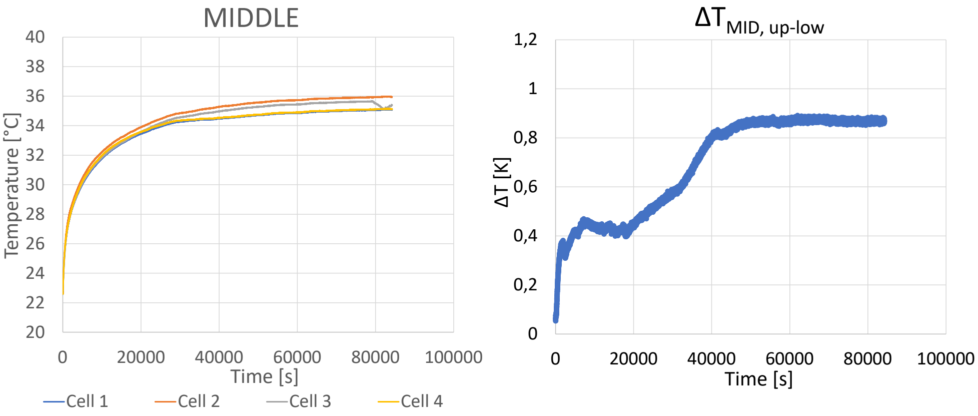

Figure 4.71. *Copper-foam-loaded PCM, Test 2.2: temperature trends recorded in the middle of all the cells (left) and ΔT trend between in the middle of the upper and the lower cells (right).*

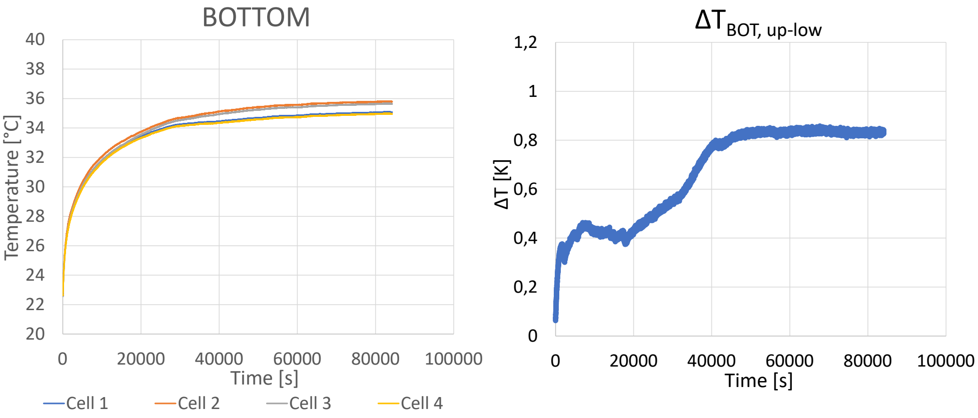

Figure 4.72. *Copper-foam-loaded PCM, Test 2.2: temperature trends recorded on the bottom of all the cells (left) and ΔT trend between the bottom of the upper and the lower cells (right).*

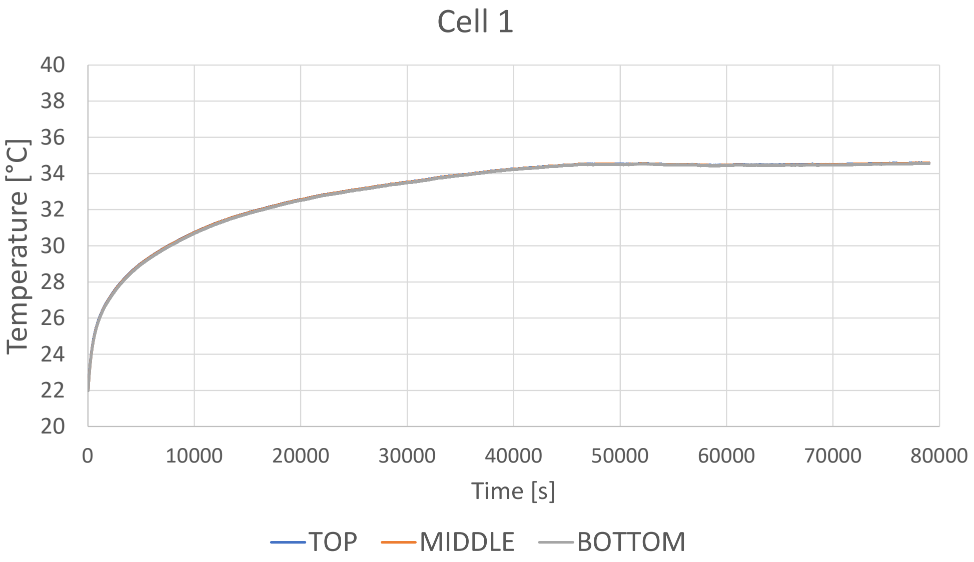

Figure 4.73. *Copper-foam-loaded PCM, Test 2.3: temperature trends recorded by* TC_{TOP}*,* TC_{MID} *and* TC_{BOT} *along Cell 1.*

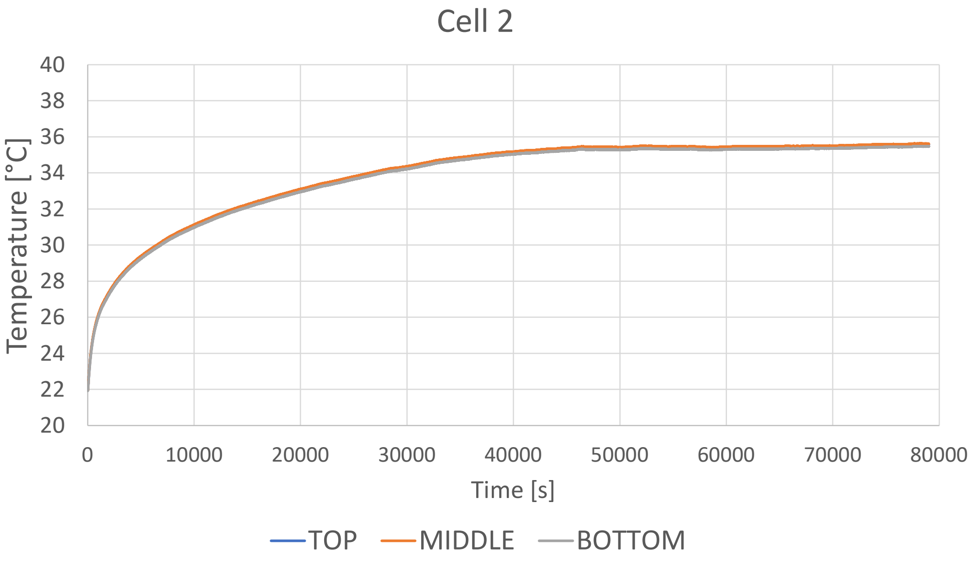

Figure 4.74. *Copper-foam-loaded PCM, Test 2.3: temperature trends recorded by* TC_{TOP}*,* TC_{MID} *and* TC_{BOT} *along Cell 2.*

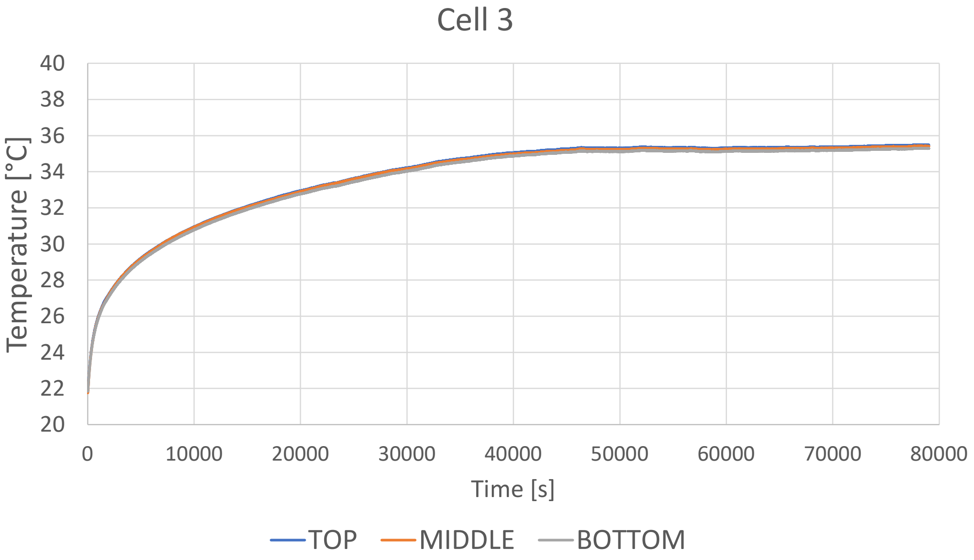

Figure 4.75. *Copper-foam-loaded PCM, Test 2.3: temperature trends recorded by* TC_{TOP}, TC_{MID} *and* TC_{BOT} *along Cell 3.*

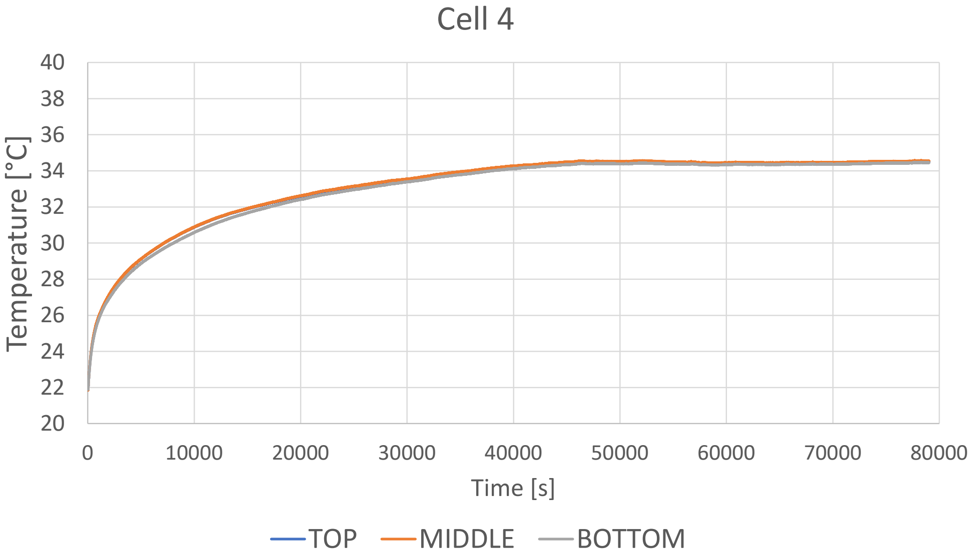

Figure 4.76. *Copper-foam-loaded PCM, Test 2.3: temperature trends recorded by* TC_{TOP}, TC_{MID} *and* TC_{BOT} *along Cell 4.*

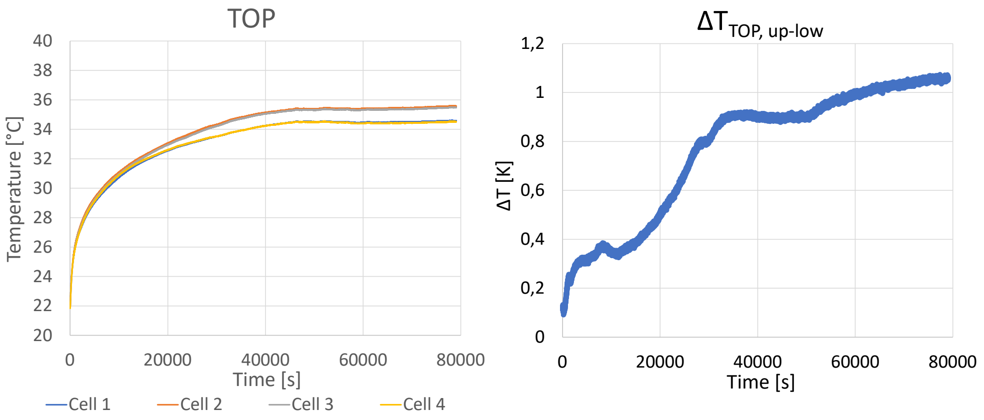

Figure 4.77. *Copper-foam-loaded PCM, Test 2.3: temperature trends recorded on the top of all the cells (left) and ΔT trend between the top of the upper and the lower cells (right).*

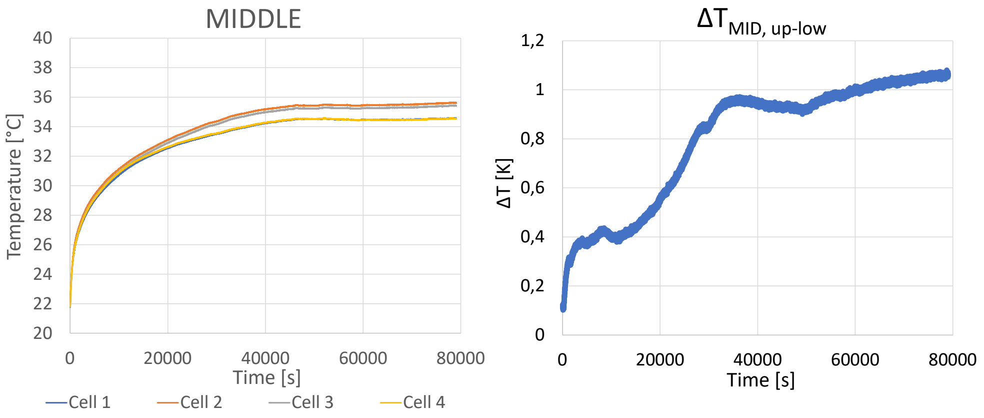

Figure 4.78. *Copper-foam-loaded PCM, Test 2.3: temperature trends recorded in the middle of all the cells (left) and ΔT trend between in the middle of the upper and the lower cells (right).*

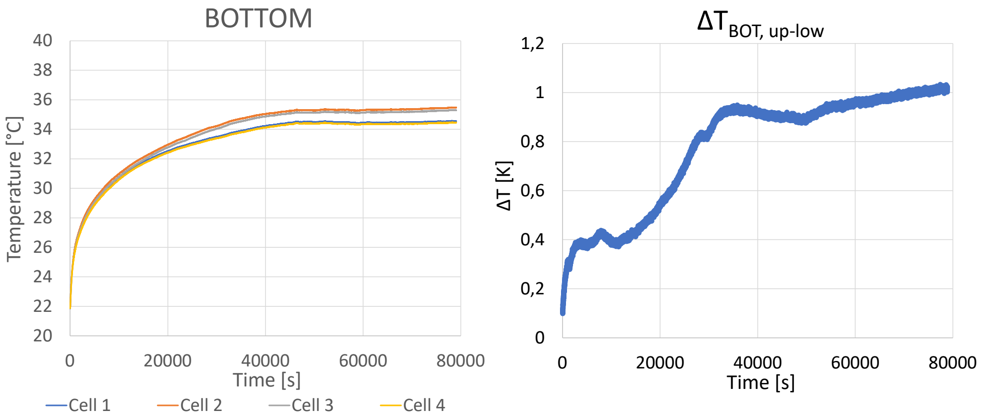

Figure 4.79. *Copper-foam-loaded PCM, Test 2.3: temperature trends recorded on the bottom of all the cells (left) and ΔT trend between the bottom of the upper and the lower cells (right).*

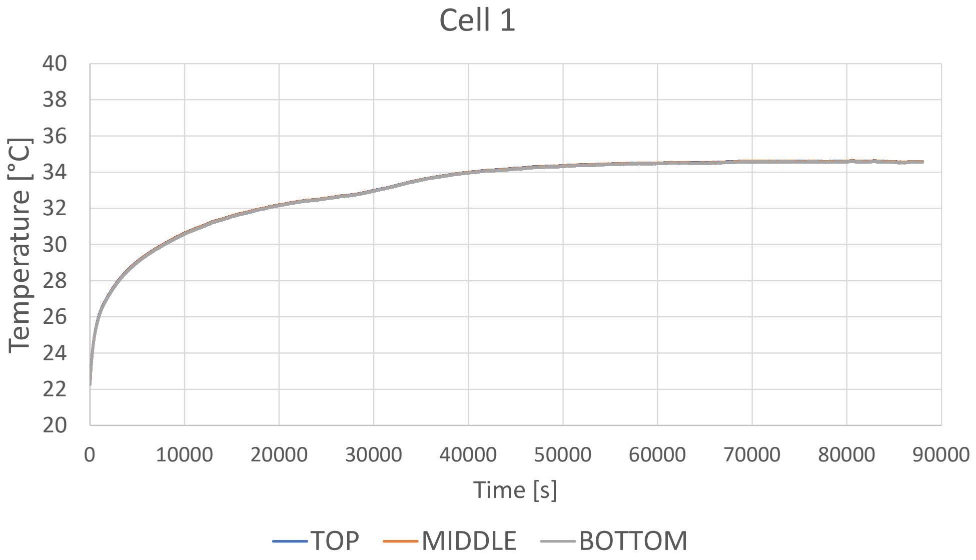

Figure 4.80. *Copper-foam-loaded PCM, Test 2.4: temperature trends recorded by* TC_{TOP}*,* TC_{MID} *and* TC_{BOT} *along Cell 1.*

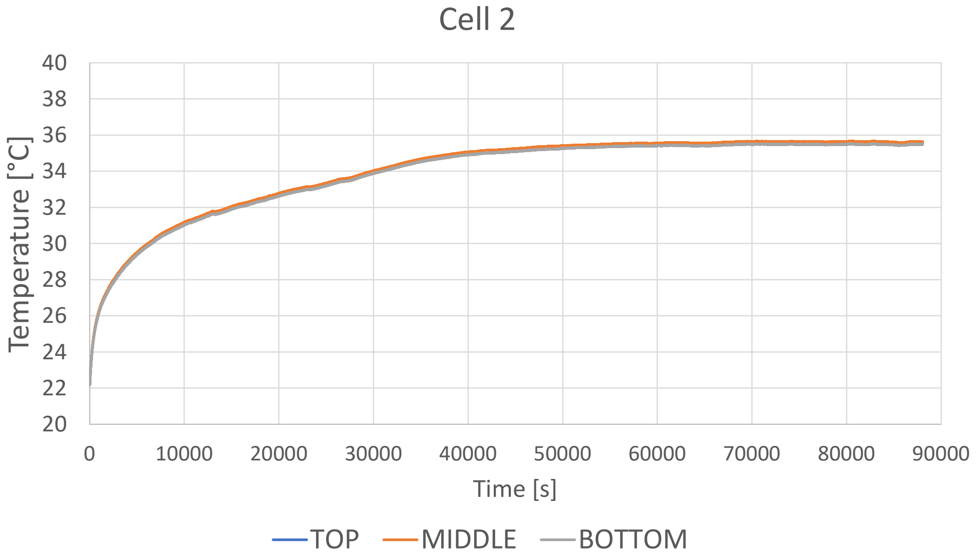

Figure 4.81. *Copper-foam-loaded PCM, Test 2.4: temperature trends recorded by* TC_{TOP}*,* TC_{MID} *and* TC_{BOT} *along Cell 2.*

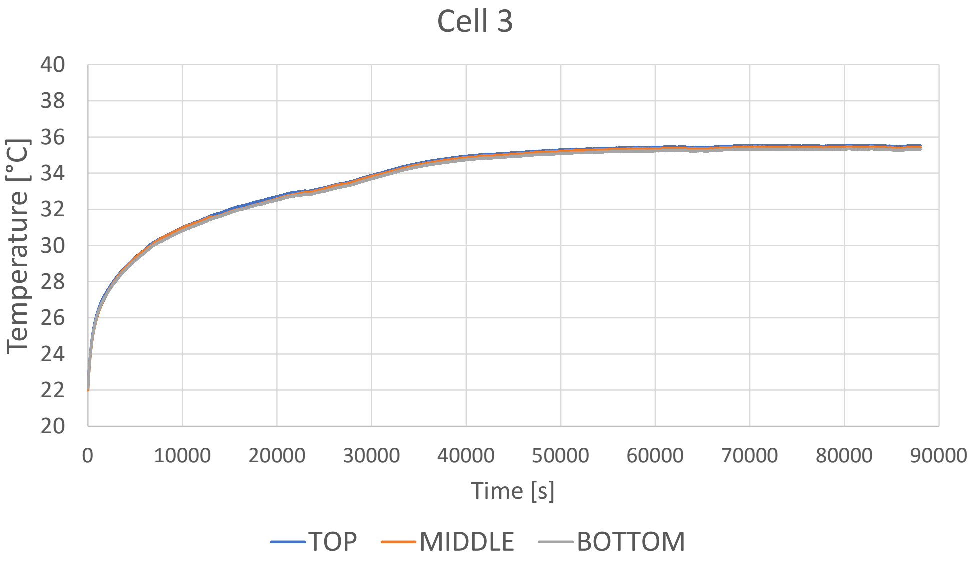

Figure 4.82. *Copper-foam-loaded PCM, Test 2.4: temperature trends recorded by* TC_{TOP}, TC_{MID} *and* TC_{BOT} *along Cell 3.*

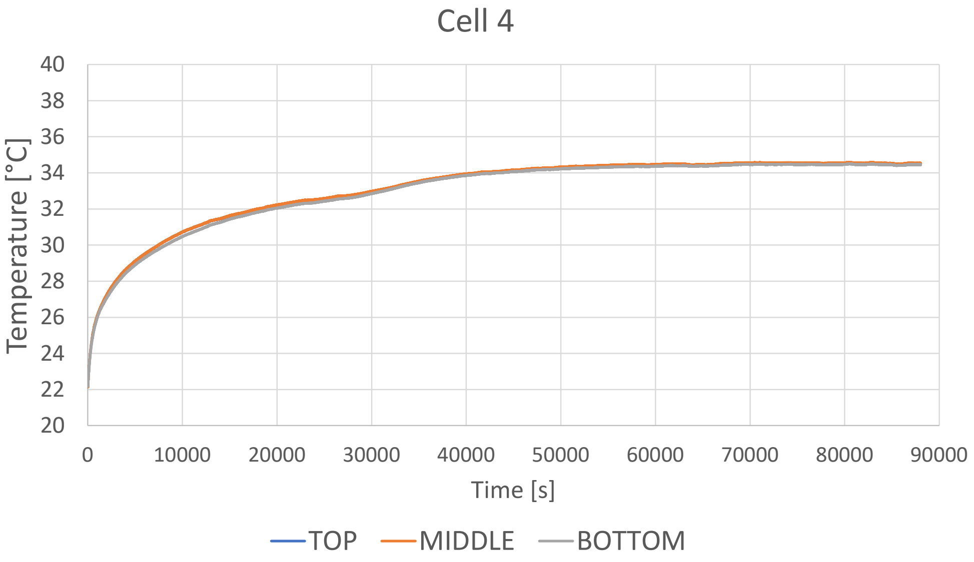

Figure 4.83. *Copper-foam-loaded PCM, Test 2.4: temperature trends recorded by* TC_{TOP}, TC_{MID} *and* TC_{BOT} *along Cell 4.*

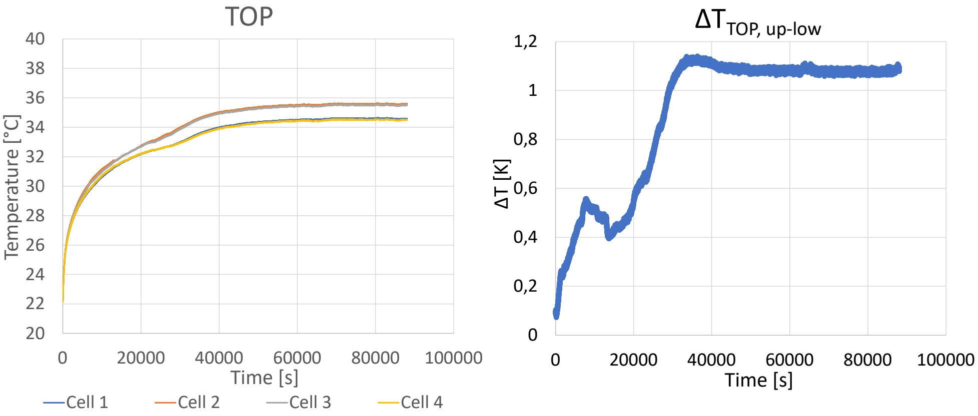

Figure 4.84. *Copper-foam-loaded PCM, Test 2.4: temperature trends recorded on the top of all the cells (left) and* ΔT *trend between the top of the upper and the lower cells (right).*

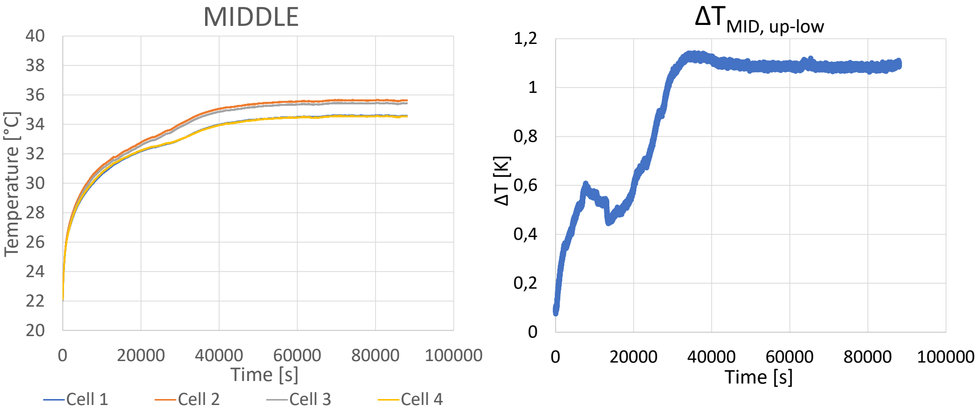

Figure 4.85. *Copper-foam-loaded PCM, Test 2.4: temperature trends recorded in the middle of all the cells (left) and* ΔT *trend between in the middle of the upper and the lower cells (right).*

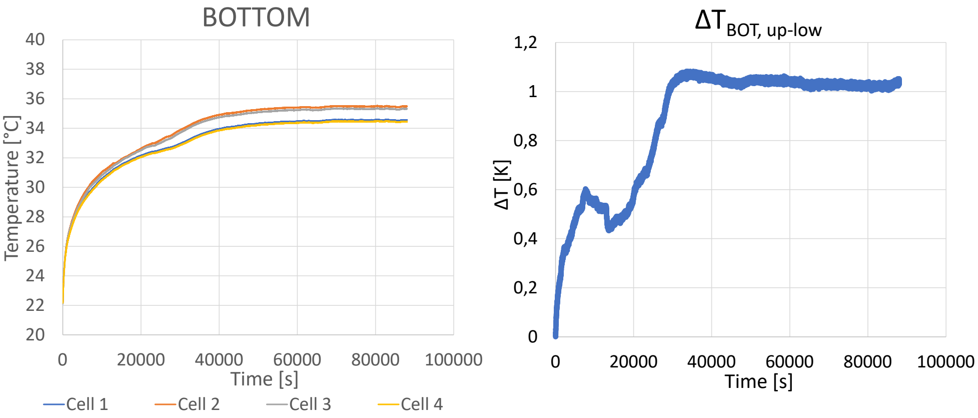

Figure 4.86. *Copper-foam-loaded PCM, Test 2.4: temperature trends recorded on the bottom of all the cells (left) and* ΔT *trend between the bottom of the upper and the lower cells (right).*

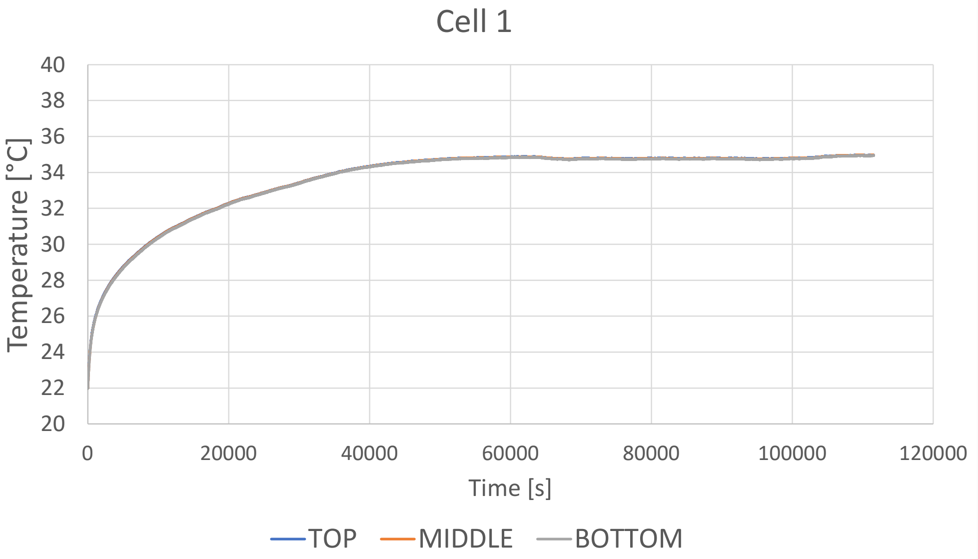

Figure 4.87. *Copper-foam-loaded PCM, Test 2.5: temperature trends recorded by* TC_{TOP}, TC_{MID} *and* TC_{BOT} *along Cell 1.*

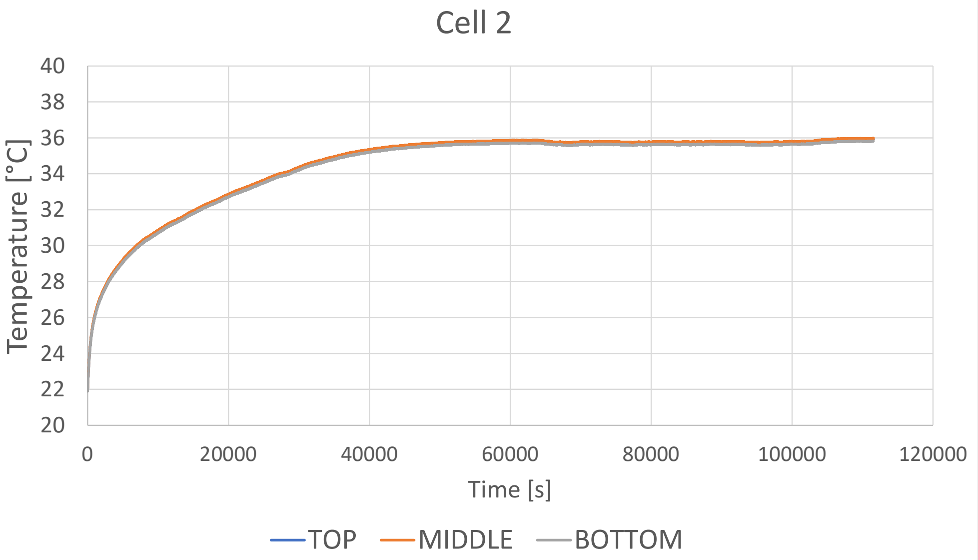

Figure 4.88. *Copper-foam-loaded PCM, Test 2.5: temperature trends recorded by* TC_{TOP}, TC_{MID} *and* TC_{BOT} *along Cell 2.*

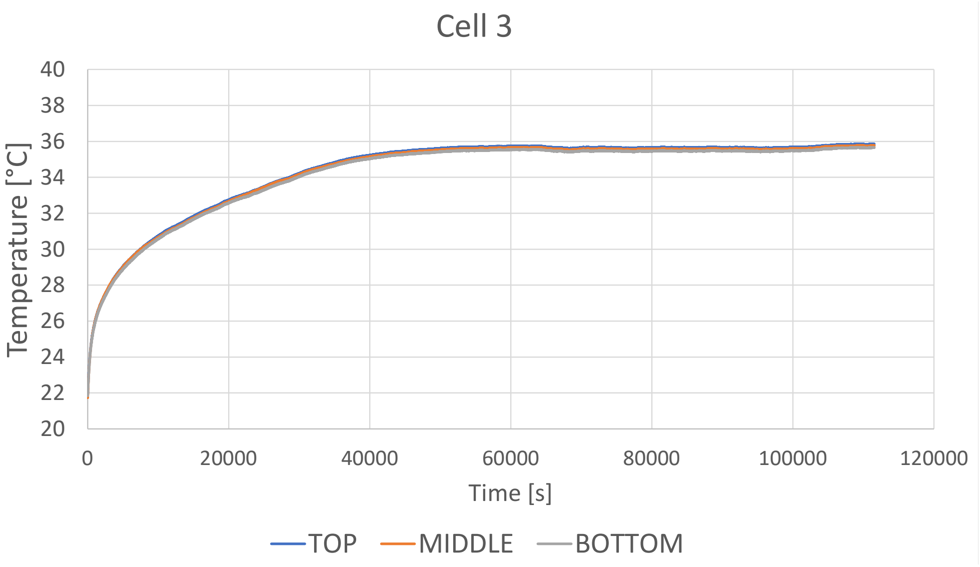

Figure 4.89. *Copper-foam-loaded PCM, Test 2.5: temperature trends recorded by* TC_{TOP}, TC_{MID} *and* TC_{BOT} *along Cell 3.*

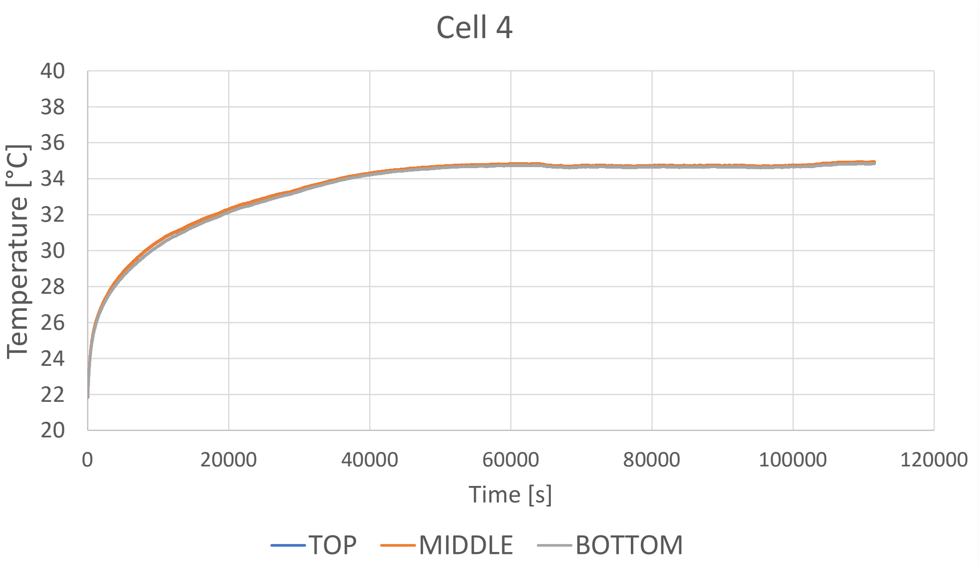

Figure 4.90. *Copper-foam-loaded PCM, Test 2.5: temperature trends recorded by* TC_{TOP}, TC_{MID} *and* TC_{BOT} *along Cell 4.*

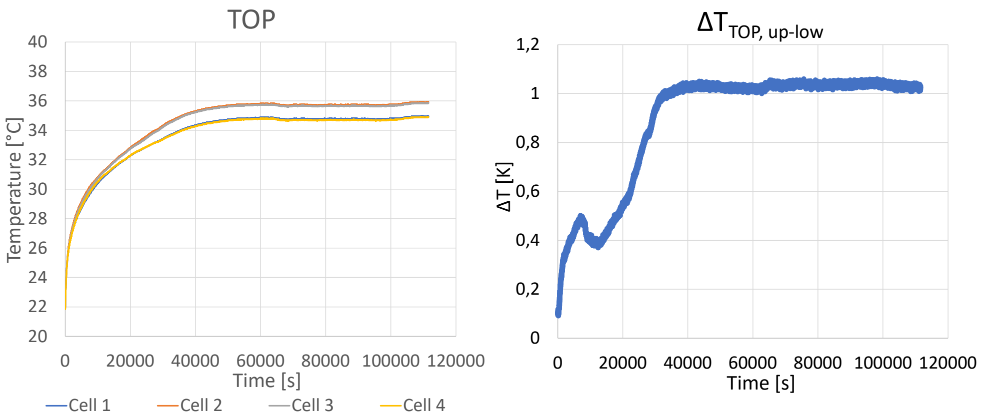

Figure 4.91. *Copper-foam-loaded PCM, Test 2.5: temperature trends recorded on the top of all the cells (left) and* ΔT *trend between the top of the upper and the lower cells (right).*

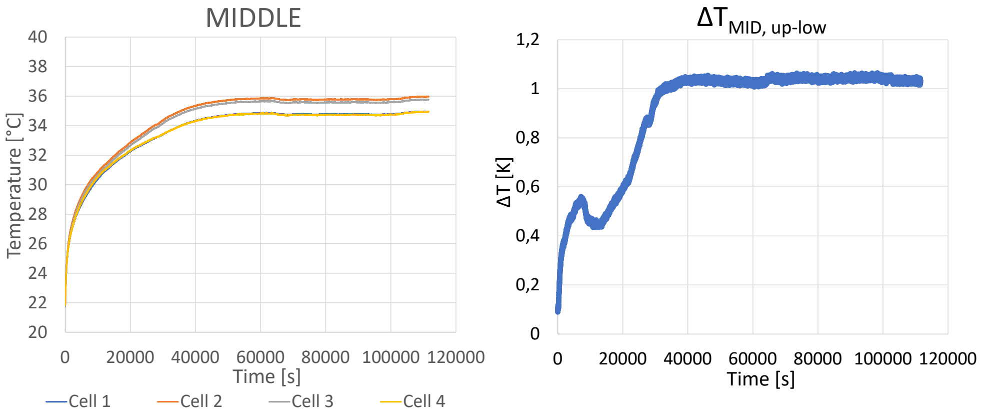

Figure 4.92. *Copper-foam-loaded PCM, Test 2.5: temperature trends recorded in the middle of all the cells (left) and* ΔT *trend between in the middle of the upper and the lower cells (right).*

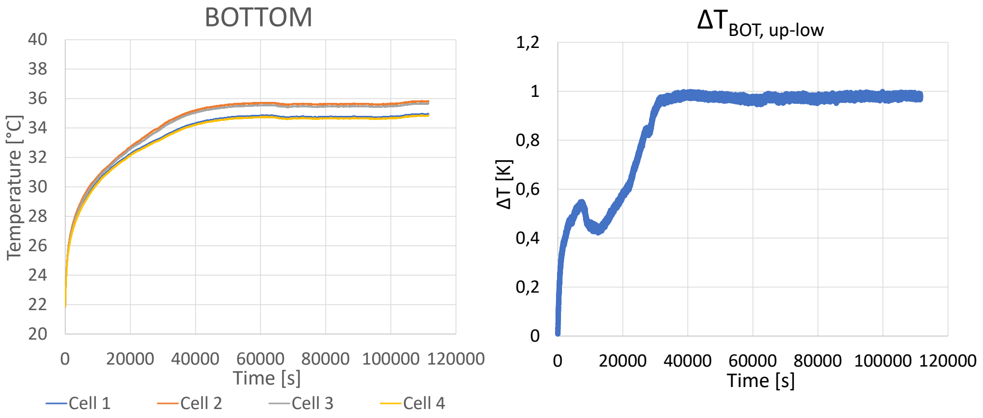

Figure 4.93. *Copper-foam-loaded PCM, Test 2.5: temperature trends recorded on the bottom of all the cells (left) and* ΔT *trend between the bottom of the upper and the lower cells (right).*

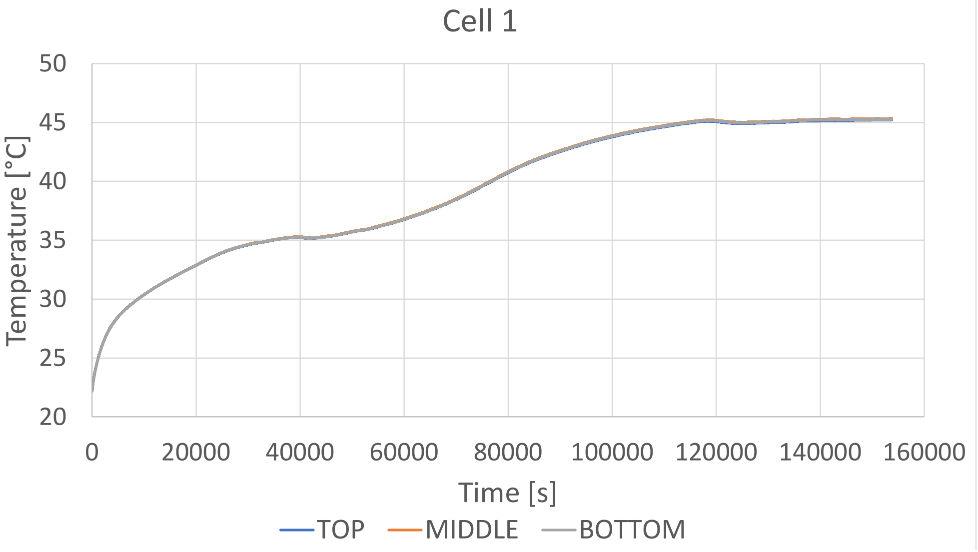

Figure 4.94. *Insulated system, pure PCM, Test 3.2: temperature trends recorded by* TC_{TOP}*,* TC_{MID} *and* TC_{BOT} *along Cell 1.*

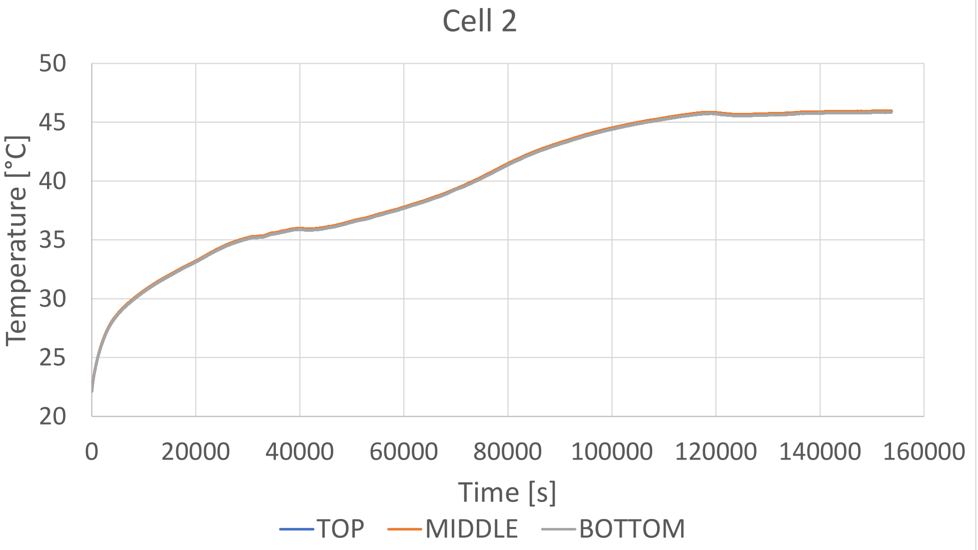

Figure 4.95. *Insulated system, pure PCM, Test 3.2: temperature trends recorded by* TC_{TOP}*,* TC_{MID} *and* TC_{BOT} *along Cell 2.*

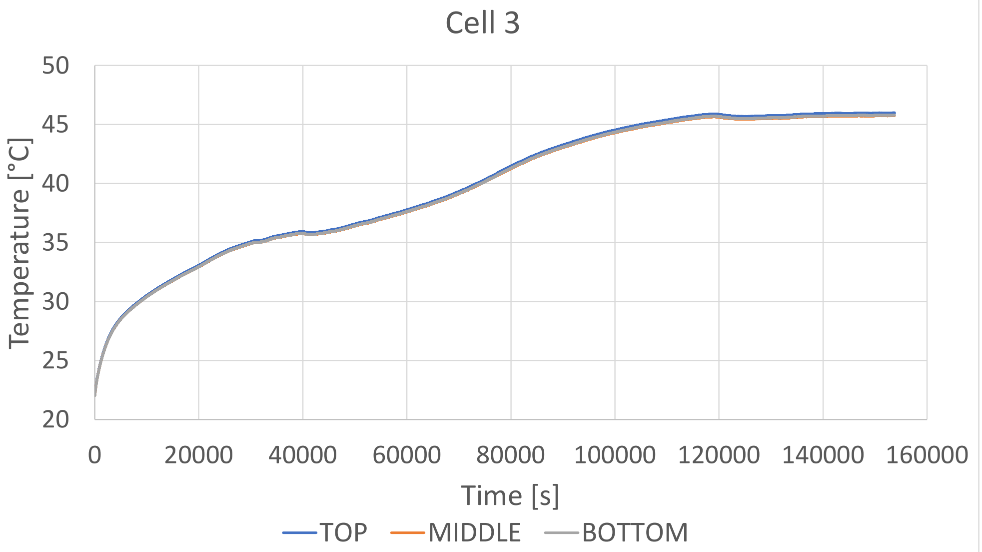

Figure 4.96. *Insulated system, pure PCM, Test 3.2: temperature trends recorded by* TC_{TOP}, TC_{MID} *and* TC_{BOT} *along Cell 3.*

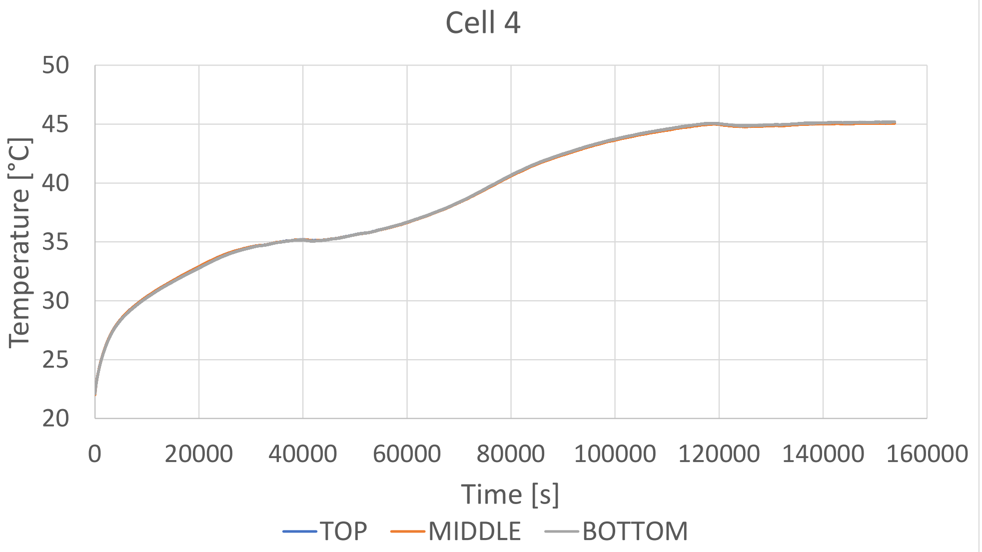

Figure 4.97. *Insulated system, pure PCM, Test 3.2: temperature trends recorded by* TC_{TOP}, TC_{MID} *and* TC_{BOT} *along Cell 4.*

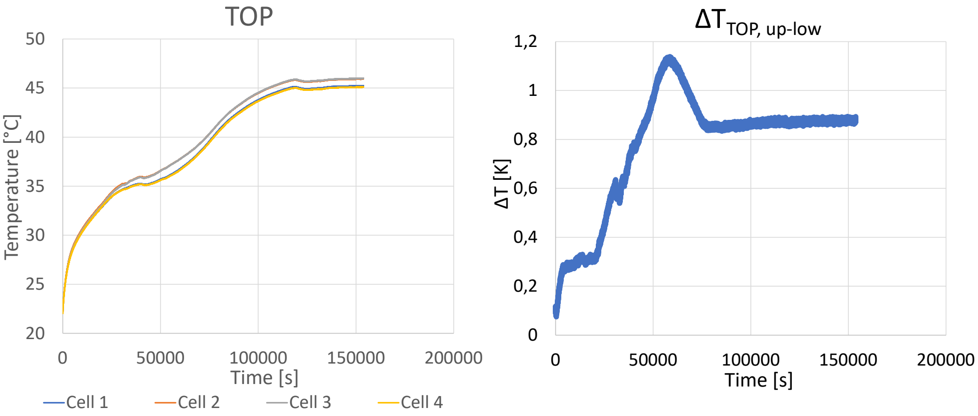

Figure 4.98. *Insulated system, pure PCM, Test 3.2: temperature trends recorded on the top of all the cells (left) and* ΔT *trend between the top of the upper and the lower cells (right).*

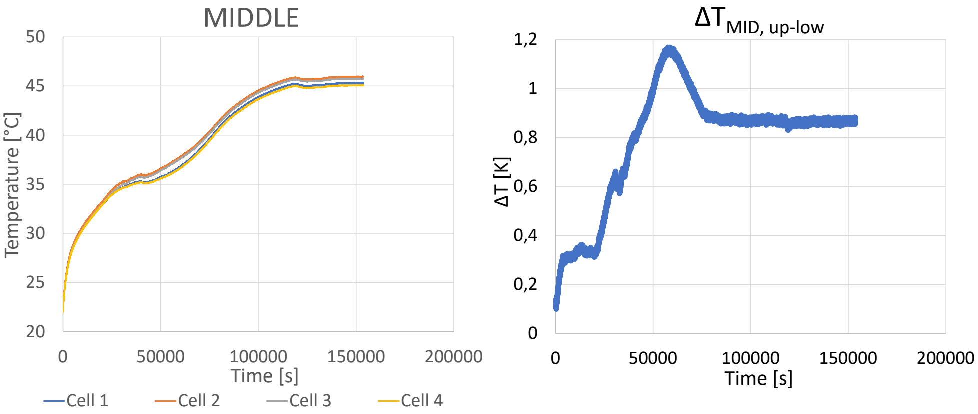

Figure 4.99. *Insulated system, pure PCM, Test 3.2: temperature trends recorded in the middle of all the cells (left) and* ΔT *trend between the middle of the upper and the lower cells (right).*

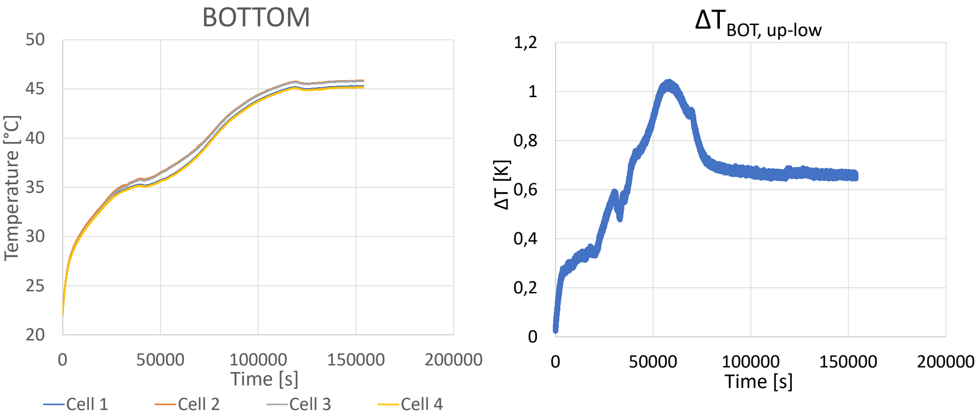

Figure 4.100. *Insulated system, pure PCM, Test 3.2: temperature trends recorded on the bottom of all the cells (left) and* ΔT *trend between the bottom of the upper and the lower cells (right).*

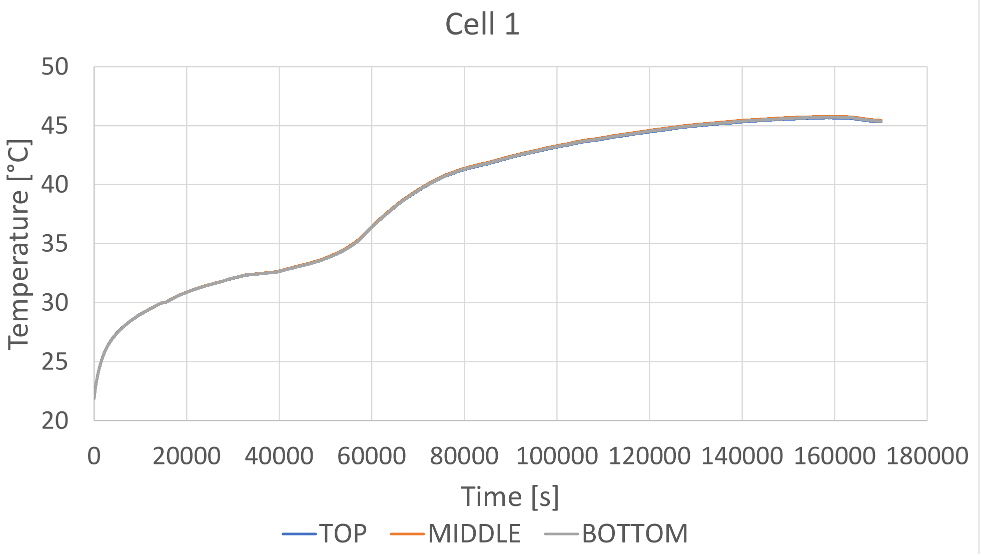

Figure 4.101. *Insulated system, pure PCM, Test 3.3: temperature trends recorded by* TC_{TOP}, TC_{MID} *and* TC_{BOT} *along Cell 1.*

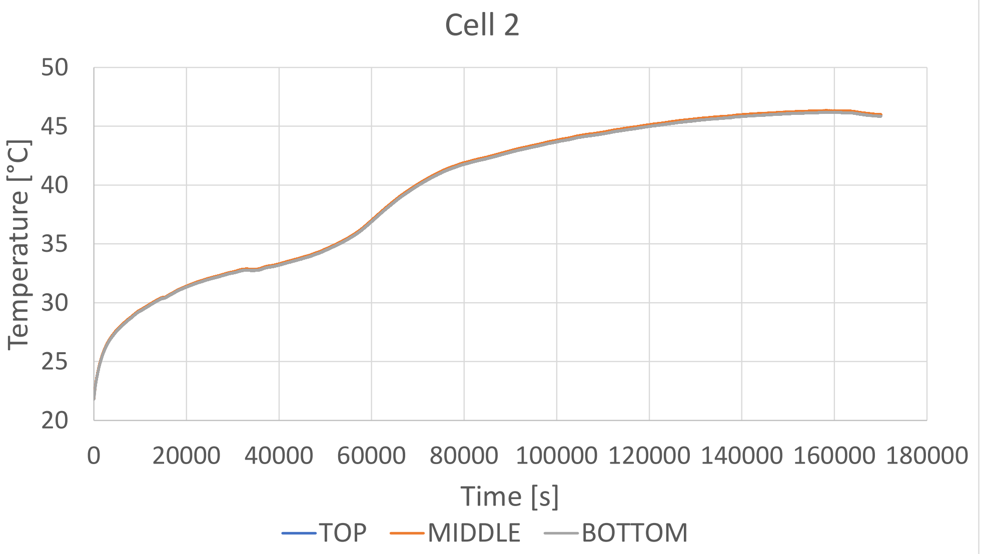

Figure 4.102. *Insulated system, pure PCM, Test 3.3: temperature trends recorded by* TC_{TOP}, TC_{MID} *and* TC_{BOT} *along Cell 2.*

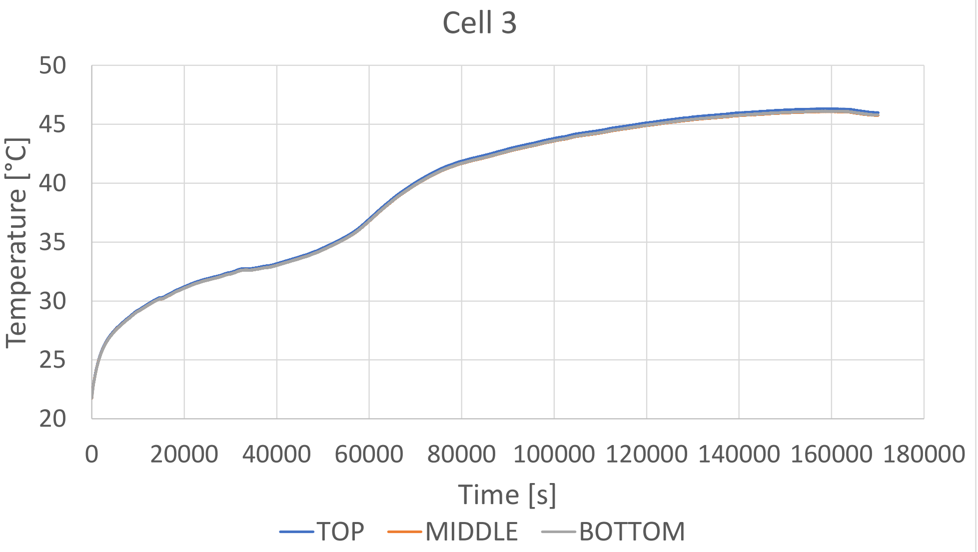

Figure 4.103. *Insulated system, pure PCM, Test 3.3: temperature trends recorded by* TC_{TOP}*,* TC_{MID} *and* TC_{BOT} *along Cell 3.*

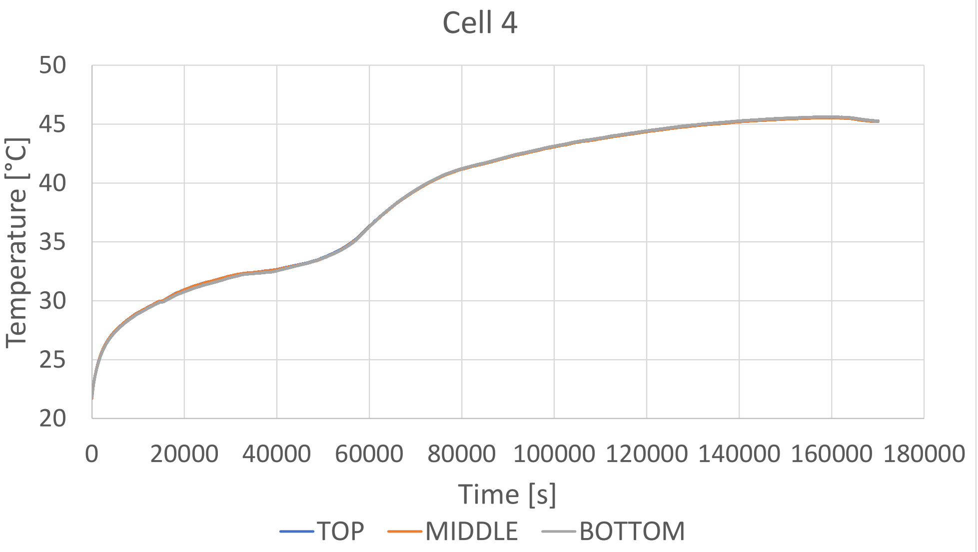

Figure 4.104. *Insulated system, pure PCM, Test 3.3: temperature trends recorded by* TC_{TOP}*,* TC_{MID} *and* TC_{BOT} *along Cell 4.*

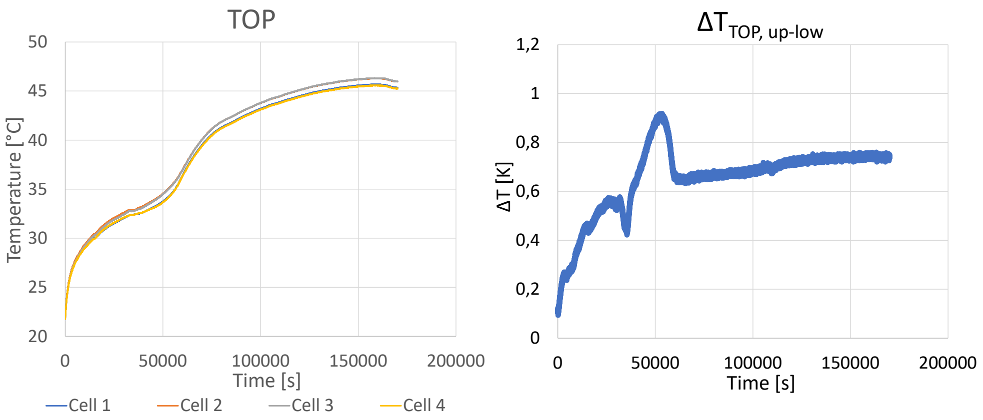

Figure 4.105. *Insulated system, pure PCM, Test 3.3: temperature trends recorded on the top of all the cells (left) and* ΔT *trend between the top of the upper and the lower cells (right).*

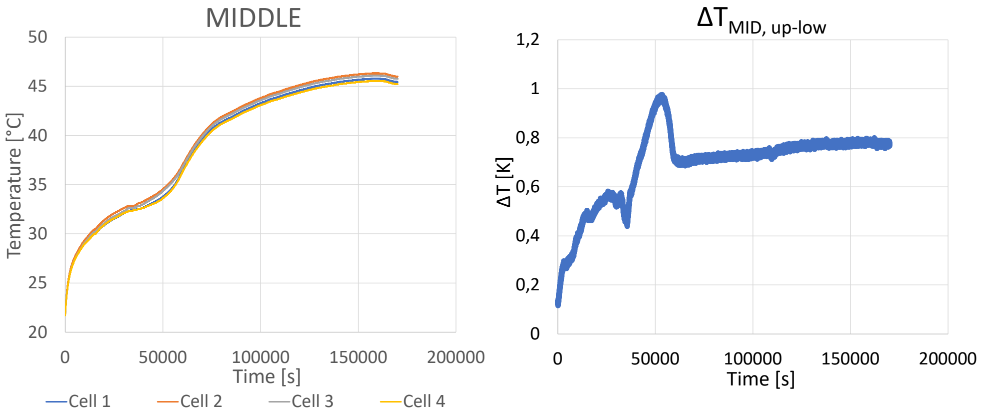

Figure 4.106. *Insulated system, pure PCM, Test 3.3: temperature trends recorded in the middle of all the cells (left) and* ΔT *trend between the middle of the upper and the lower cells (right).*

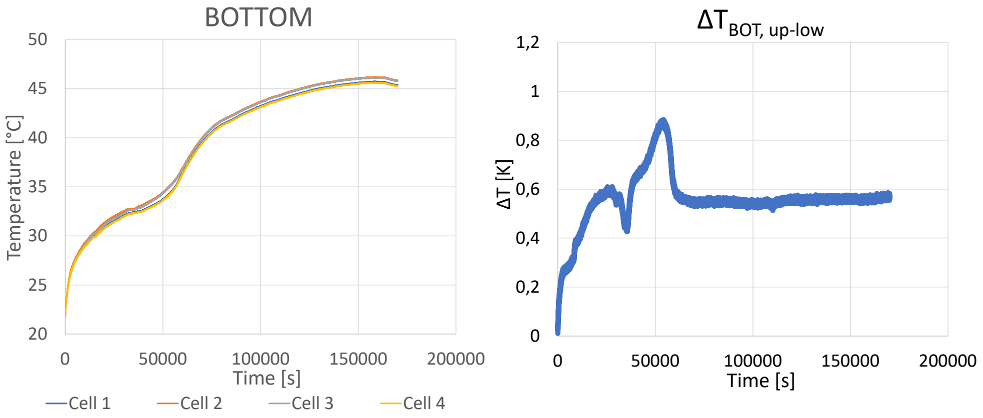

Figure 4.107. *Insulated system, pure PCM, Test 3.3: temperature trends recorded on the bottom of all the cells (left) and* ΔT *trend between the bottom of the upper and the lower cells (right).*

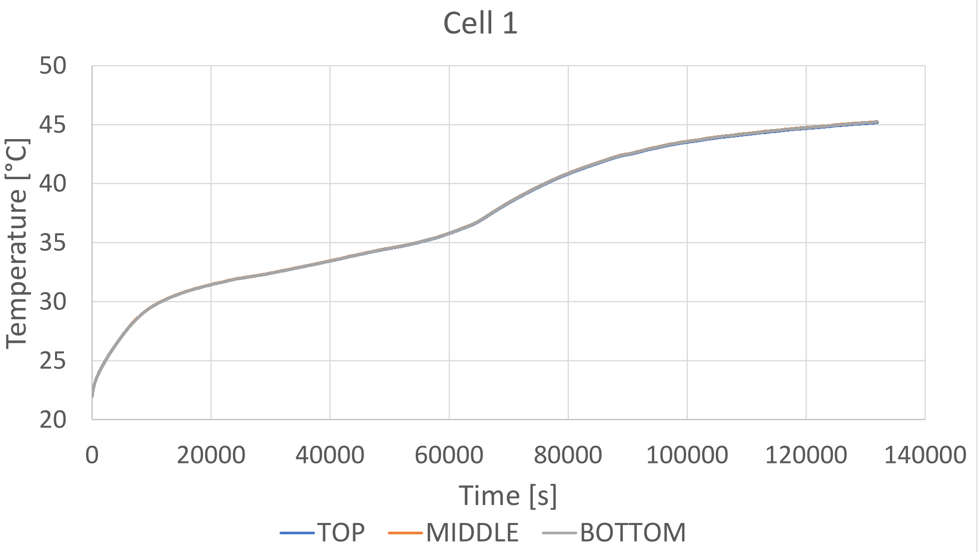

Figure 4.108. *Insulated system, copper-foam-loaded PCM, Test 4.2: temperature trends recorded by* TC_{TOP}, TC_{MID} *and* TC_{BOT} *along Cell 1.*

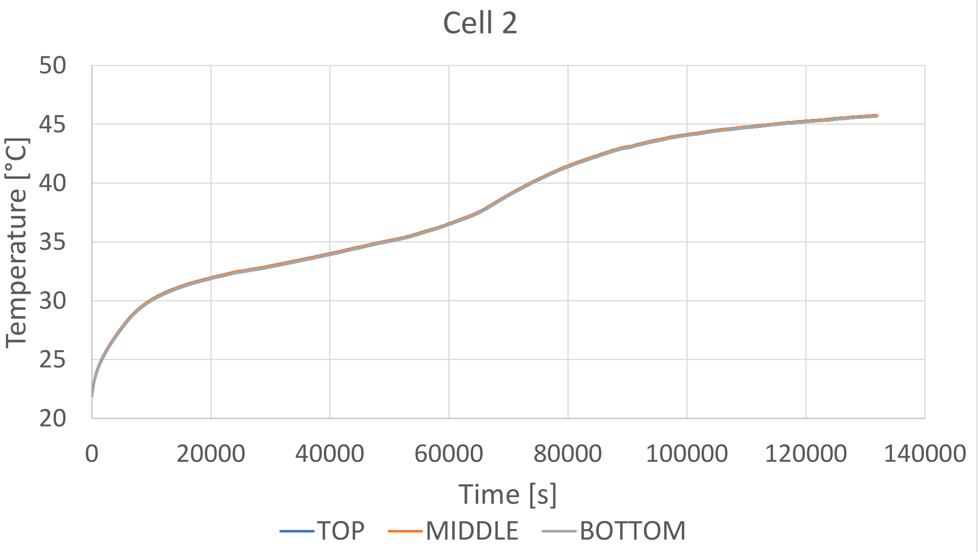

Figure 4.109. *Insulated system, copper-foam-loaded PCM, Test 4.2: temperature trends recorded by* TC_{TOP}, TC_{MID} *and* TC_{BOT} *along Cell 2.*

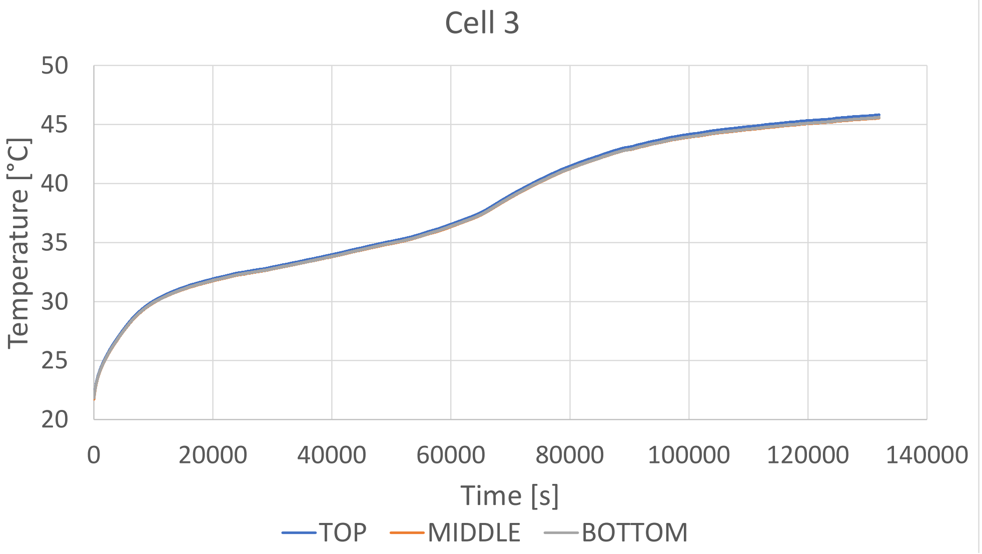

Figure 4.110. *Insulated system, copper-foam-loaded PCM, Test 4.2: temperature trends recorded by* TC_{TOP}*,* TC_{MID} *and* TC_{BOT} *along Cell 3.*

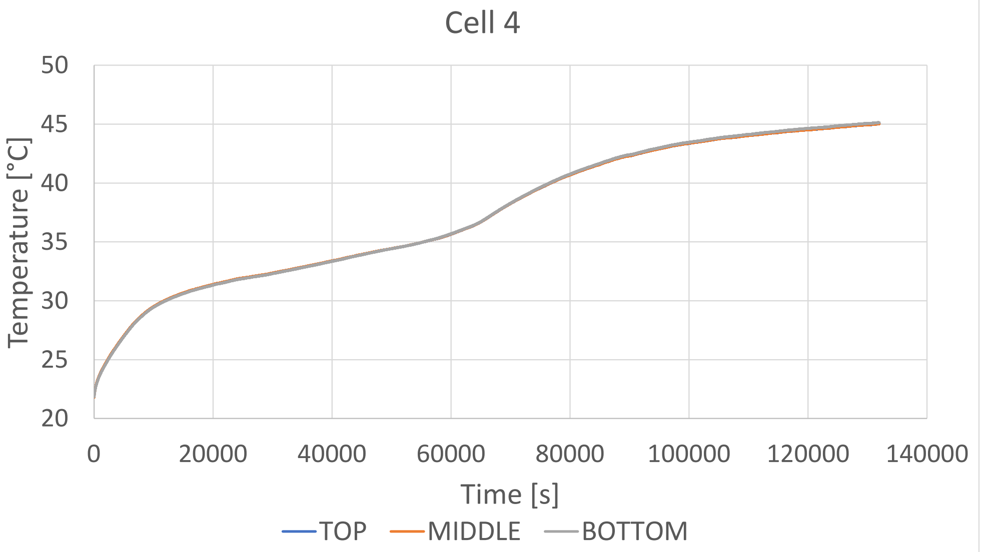

Figure 4.111. *Insulated system, copper-foam-loaded PCM, Test 4.2: temperature trends recorded by* TC_{TOP}*,* TC_{MID} *and* TC_{BOT} *along Cell 4.*

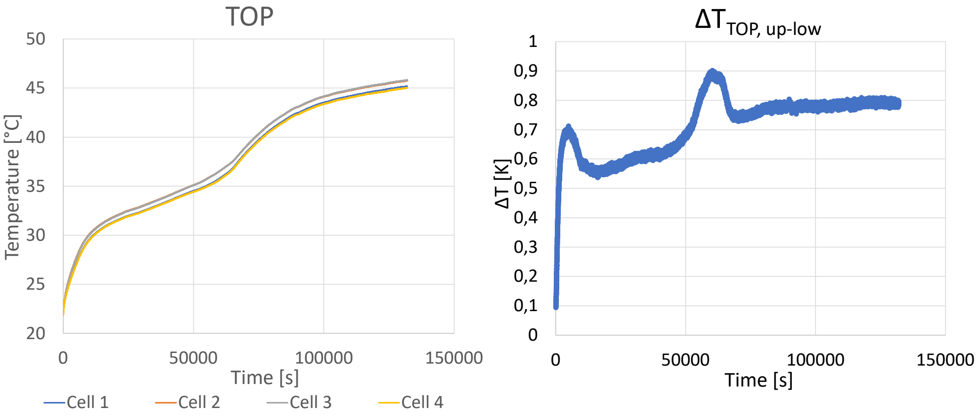

Figure 4.112. *Insulated system, copper-foam-loaded PCM, Test 4.2: temperature trends recorded on the top of all the cells (left) and* ΔT *trend between the top of the upper and the lower cells (right).*

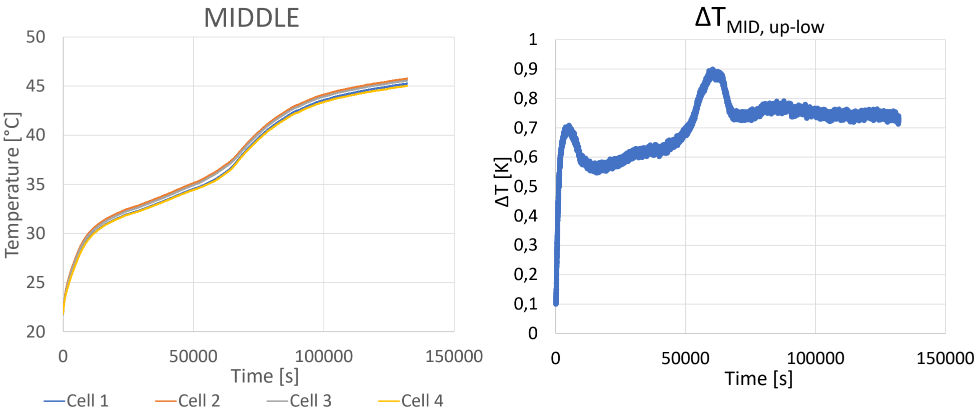

Figure 4.113. *Insulated system, copper-foam-loaded PCM, Test 4.2: temperature trends recorded in the middle of all the cells (left) and* ΔT *trend between the middle of the upper and the lower cells (right).*

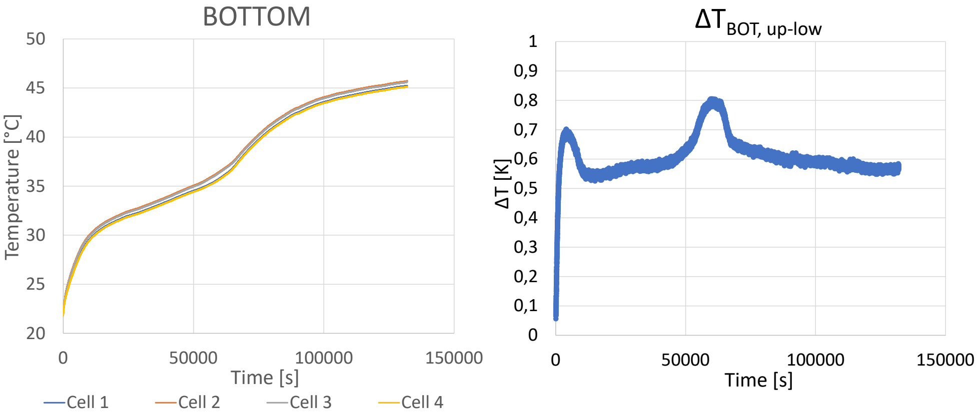

Figure 4.114. *Insulated system, copper-foam-loaded PCM, Test 4.2: temperature trends recorded on the bottom of all the cells (left) and* ΔT *trend between the bottom of the upper and the lower cells (right).*

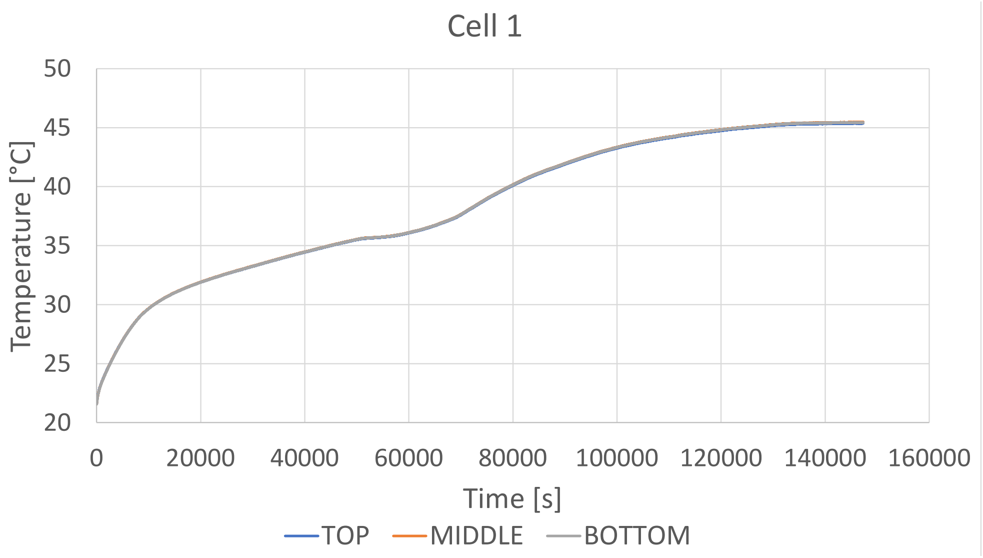

Figure 4.115. *Insulated system, copper-foam-loaded PCM, Test 4.3: temperature trends recorded by* TC_{TOP}*,* TC_{MID} *and* TC_{BOT} *along Cell 1.*

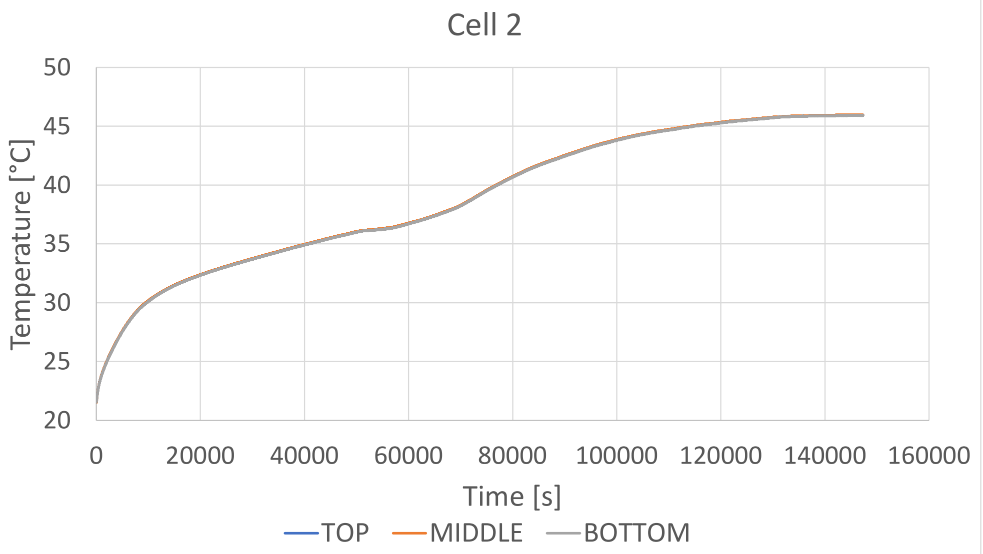

Figure 4.116. *Insulated system, copper-foam-loaded PCM, Test 4.3: temperature trends recorded by* TC_{TOP}*,* TC_{MID} *and* TC_{BOT} *along Cell 2.*

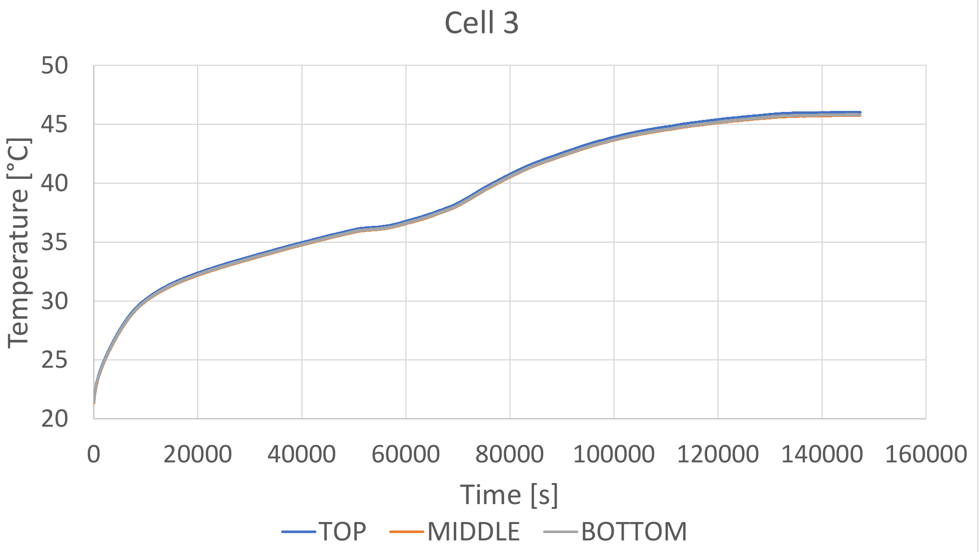

Figure 4.117. *Insulated system, copper-foam-loaded PCM, Test 4.3: temperature trends recorded by* TC_{TOP}*,* TC_{MID} *and* TC_{BOT} *along Cell 3.*

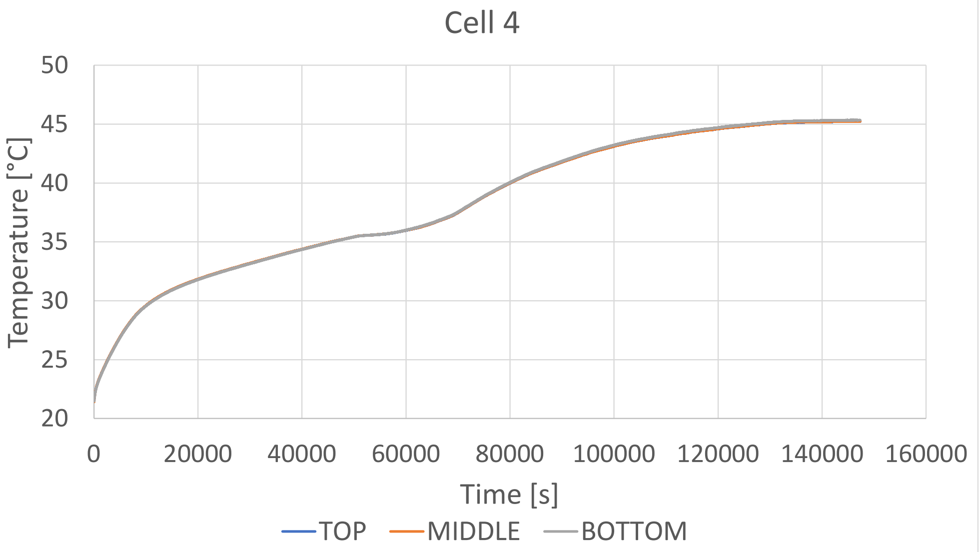

Figure 4.118. *Insulated system, copper-foam-loaded PCM, Test 4.3: temperature trends recorded by* TC_{TOP}*,* TC_{MID} *and* TC_{BOT} *along Cell 4.*

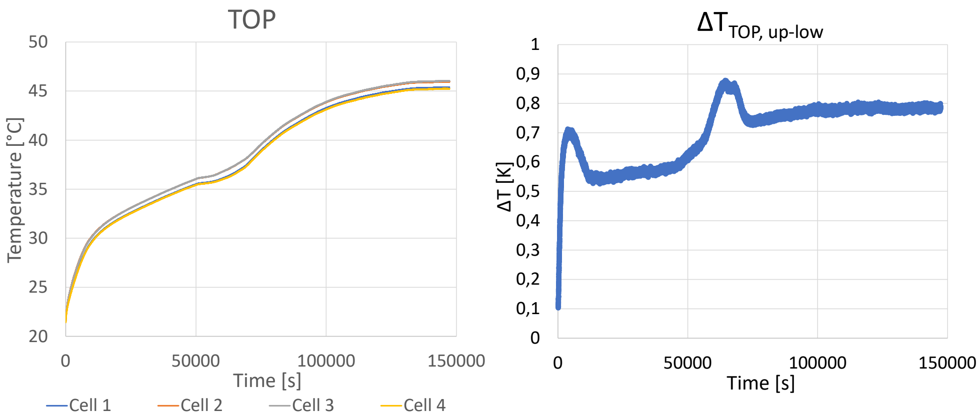

Figure 4.119. *Insulated system, copper-foam-loaded PCM, Test 4.3: temperature trends recorded on the top of all the cells (left) and* ΔT *trend between the top of the upper and the lower cells (right).*

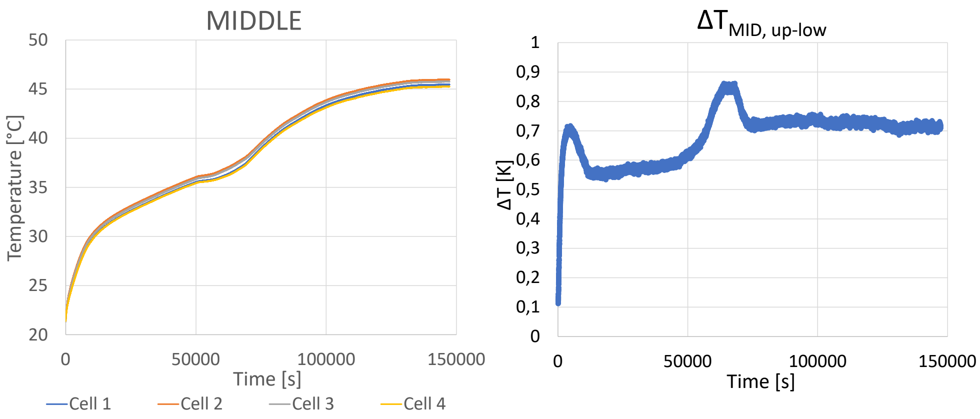

Figure 4.120. *Insulated system, copper-foam-loaded PCM, Test 4.3: temperature trends recorded in the middle of all the cells (left) and* ΔT *trend between the middle of the upper and the lower cells (right).*

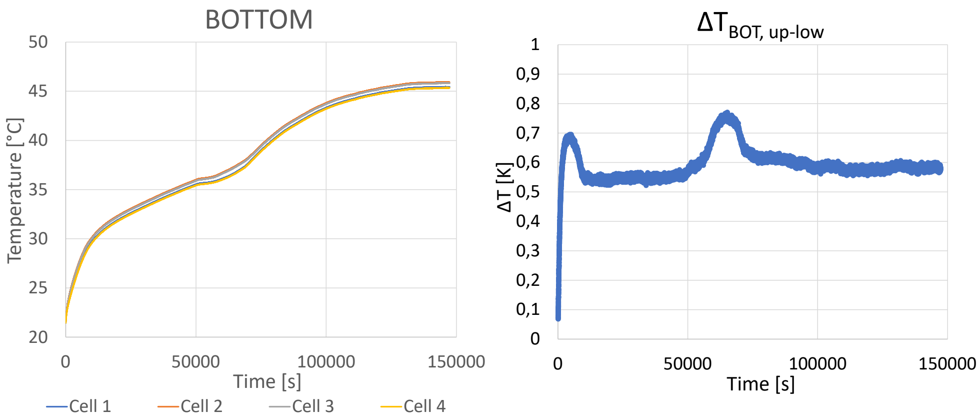

Figure 4.121. *Insulated system, copper-foam-loaded PCM, Test 4.3: temperature trends recorded on the bottom of all the cells (left) and* ΔT *trend between the bottom of the upper and the lower cells (right).*

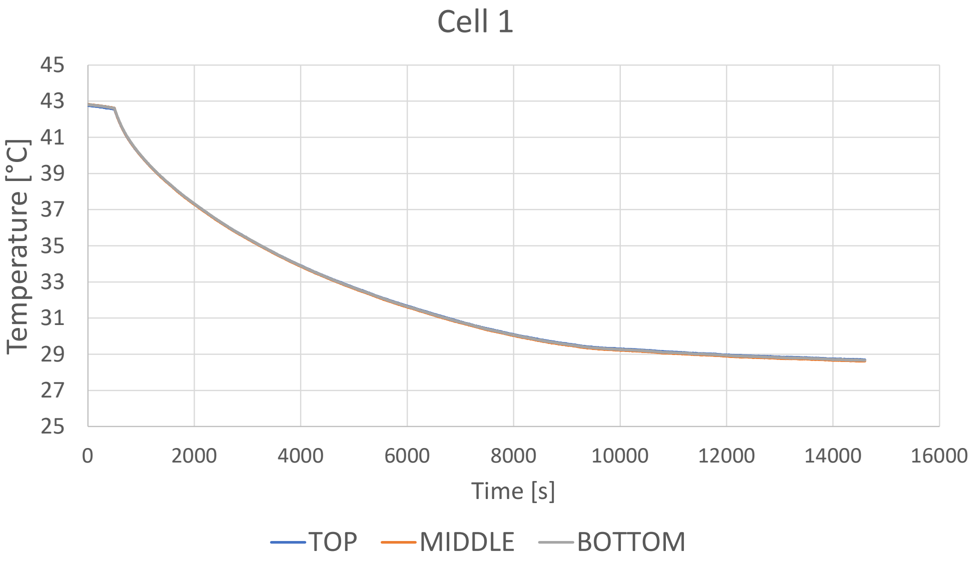

Figure 4.122. *Insulated system, pure PCM and water cooling, Test 5.2: temperature trends recorded by* TC_{TOP}, TC_{MID} *and* TC_{BOT} *along Cell 1.*

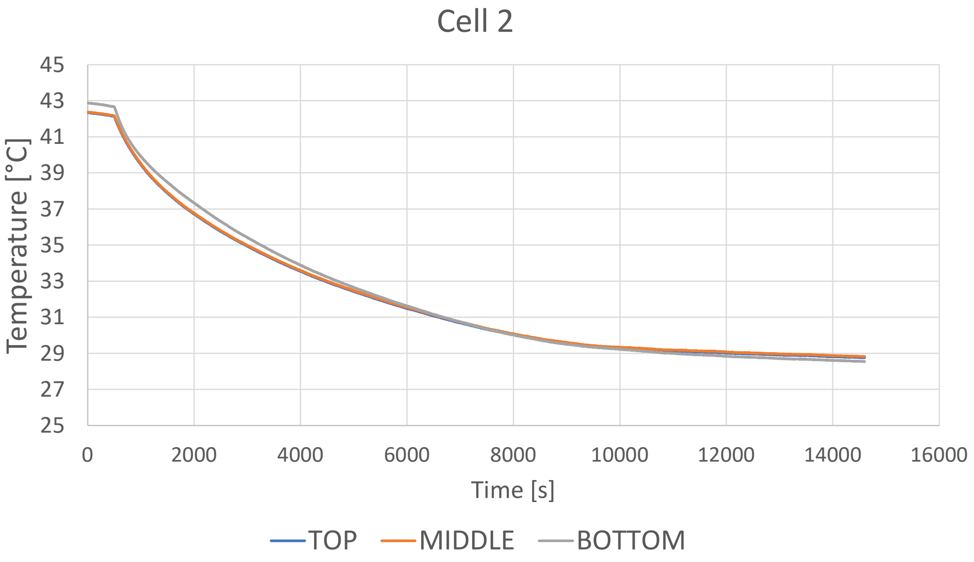

Figure 4.123. *Insulated system, pure PCM and water cooling, Test 5.2: temperature trends recorded by* TC_{TOP}, TC_{MID} *and* TC_{BOT} *along Cell 2.*

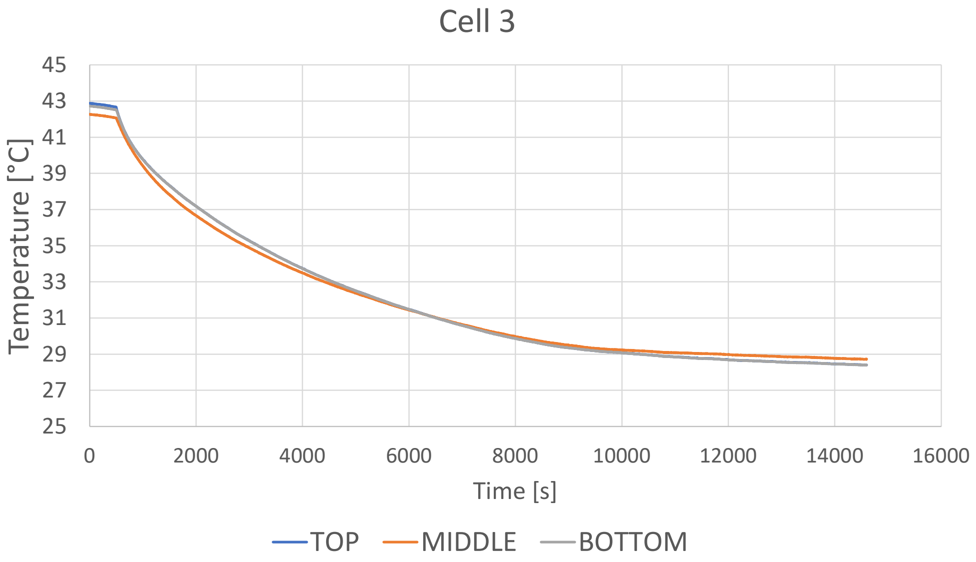

Figure 4.124. *Insulated system, pure PCM and water cooling, Test 5.2: temperature trends recorded by* TC_{TOP}, TC_{MID} *and* TC_{BOT} *along Cell 3.*

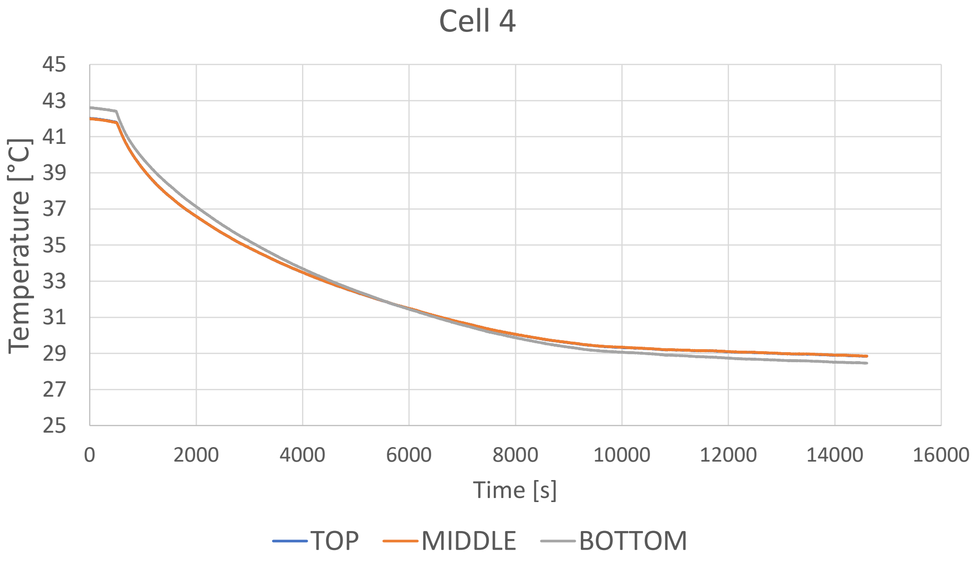

Figure 4.125. *Insulated system, pure PCM and water cooling, Test 5.2: temperature trends recorded by* TC_{TOP}, TC_{MID} *and* TC_{BOT} *along Cell 4.*

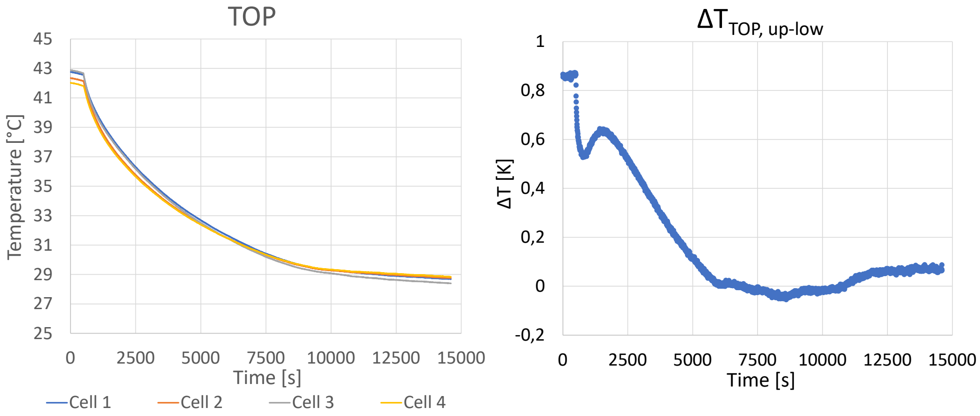

Figure 4.126. *Insulated system, pure PCM and water cooling, Test 5.2: temperature trends recorded on the top of all the cells (left) and* ΔT *trend between the top of the upper and the lower cells (right).*

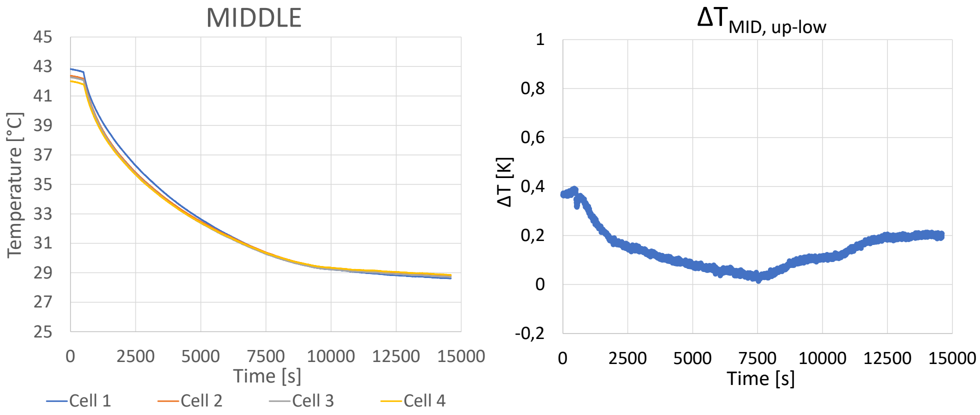

Figure 4.127. *Insulated system, pure PCM and water cooling, Test 5.2: temperature trends recorded in the middle of all the cells (left) and* ΔT *trend between the middle of the upper and the lower cells (right).*

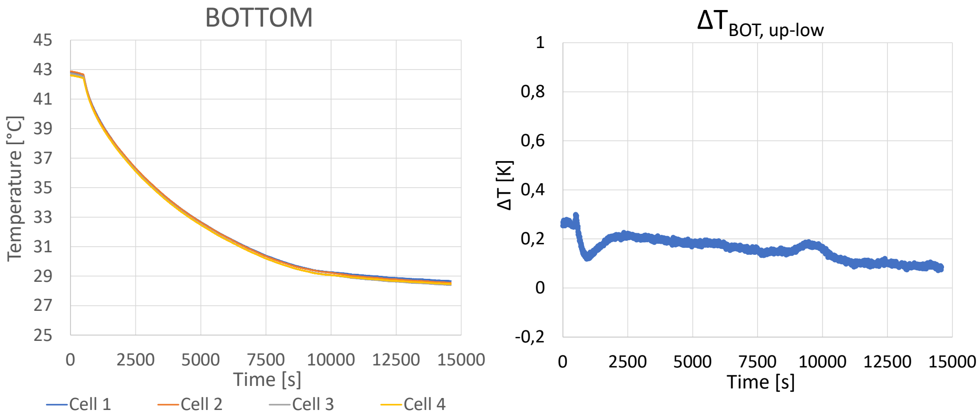

Figure 4.128. *Insulated system, pure PCM and water cooling, Test 5.2: temperature trends recorded on the bottom of all the cells (left) and* ΔT *trend between the bottom of the upper and the lower cells (right).*

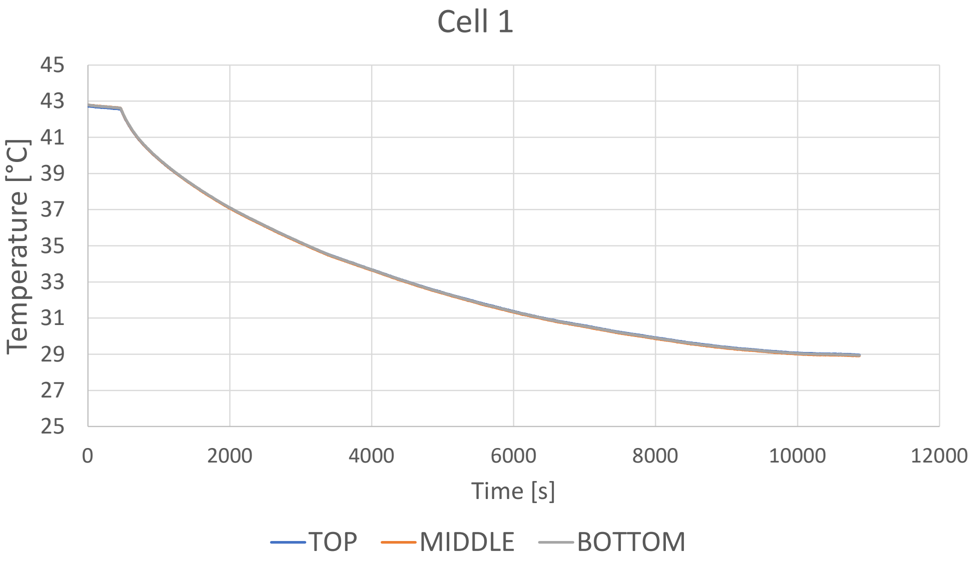

Figure 4.129. *Insulated system, pure PCM and water cooling, Test 5.3: temperature trends recorded by* TC_{TOP}*,* TC_{MID} *and* TC_{BOT} *along Cell 1.*

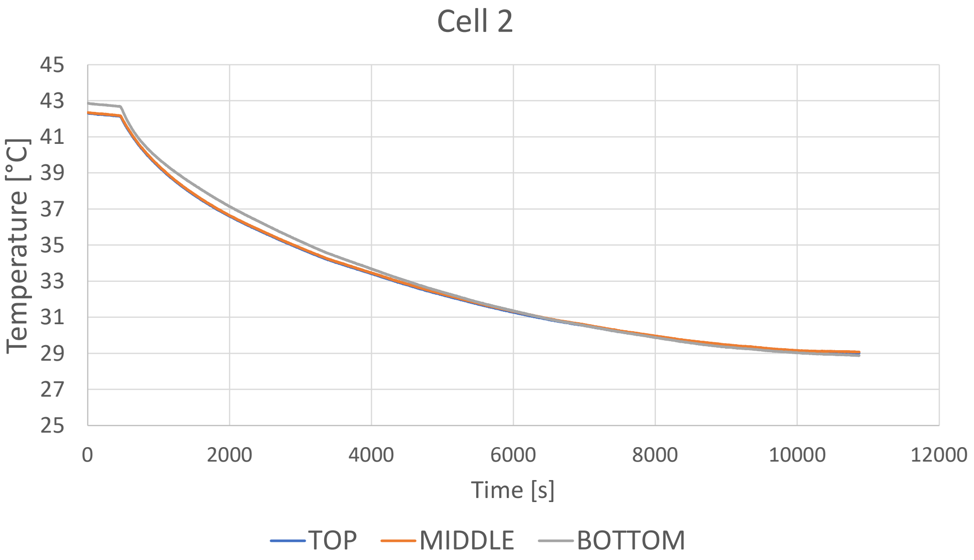

Figure 4.130. *Insulated system, pure PCM and water cooling, Test 5.3: temperature trends recorded by* TC_{TOP}*,* TC_{MID} *and* TC_{BOT} *along Cell 2.*

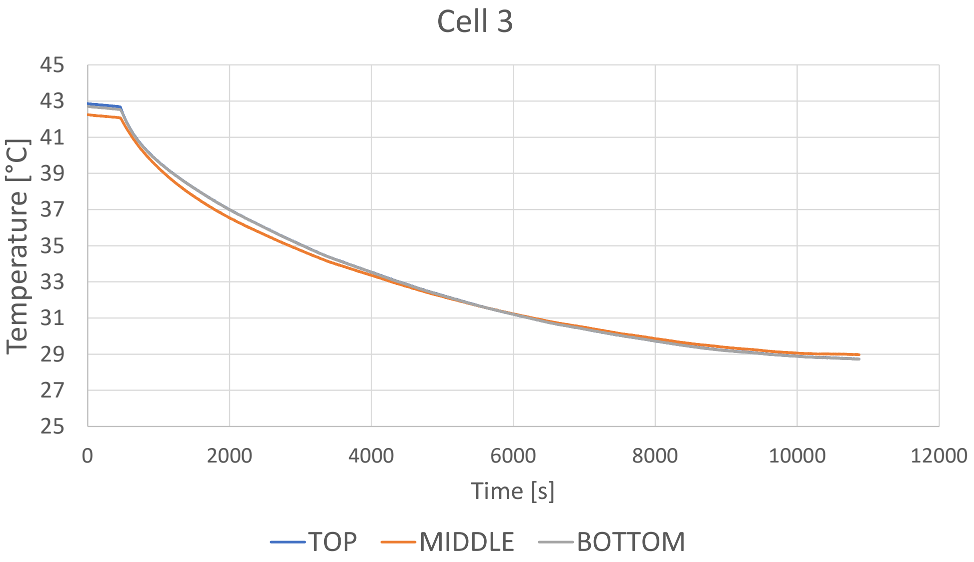

Figure 4.131. *Insulated system, pure PCM and water cooling, Test 5.3: temperature trends recorded by* TC_{TOP}, TC_{MID} *and* TC_{BOT} *along Cell 3.*

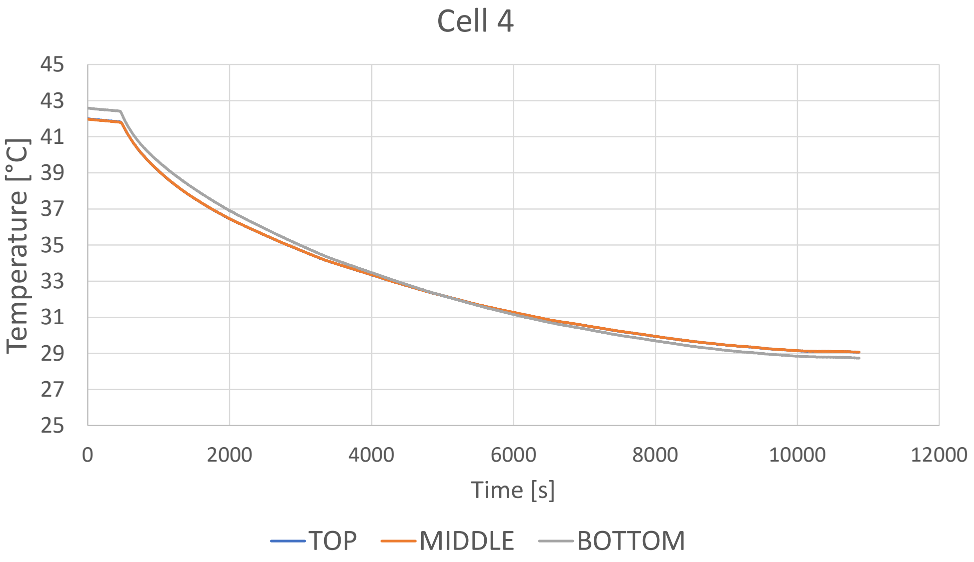

Figure 4.132. *Insulated system, pure PCM and water cooling, Test 5.3: temperature trends recorded by* TC_{TOP}, TC_{MID} *and* TC_{BOT} *along Cell 4.*

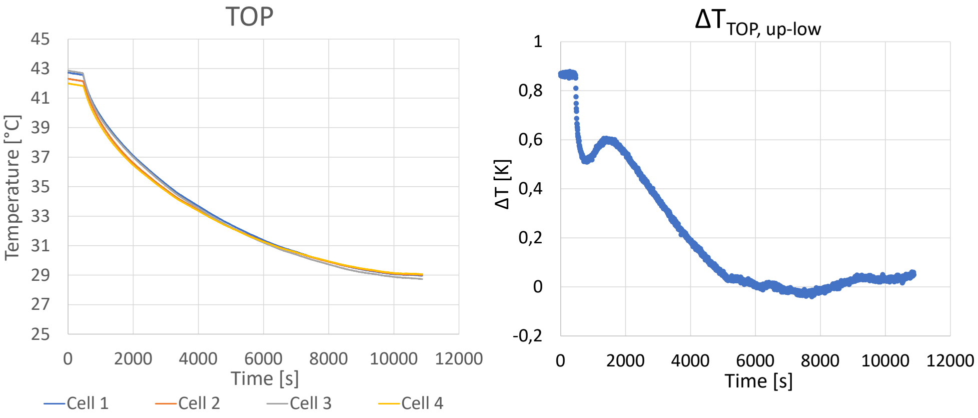

Figure 4.133. *Insulated system, pure PCM and water cooling, Test 5.3: temperature trends recorded on the top of all the cells (left) and ΔT trend between the top of the upper and the lower cells (right).*

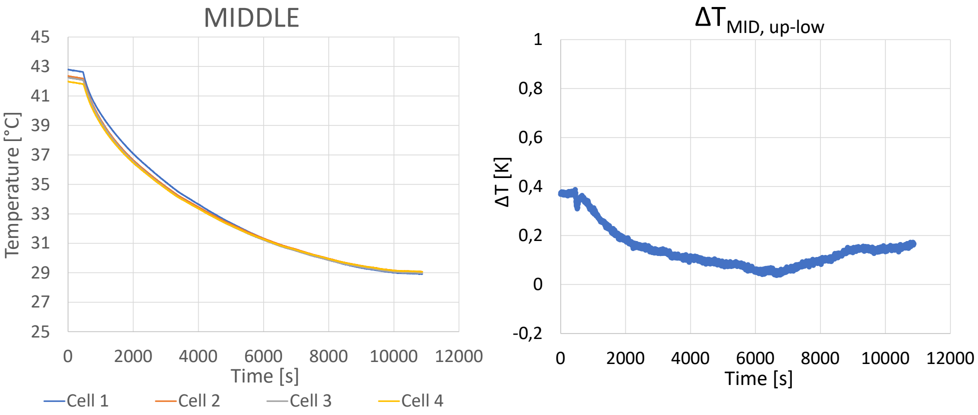

Figure 4.134. *Insulated system, pure PCM and water cooling, Test 5.3: temperature trends recorded in the middle of all the cells (left) and ΔT trend between the middle of the upper and the lower cells (right).*

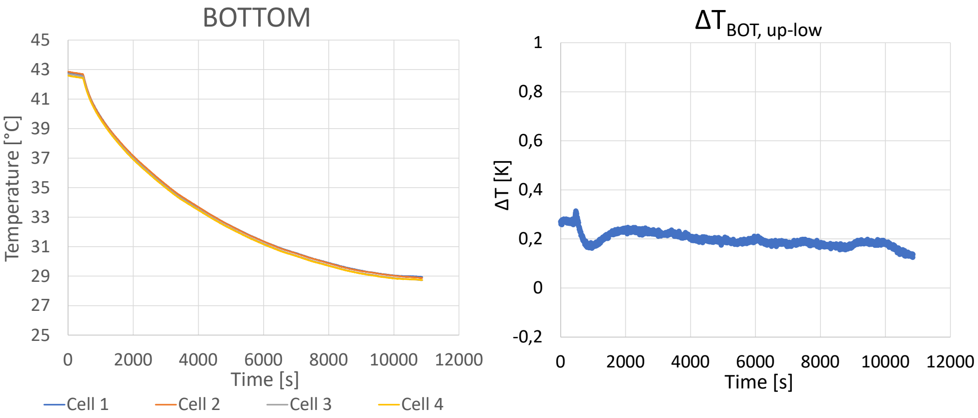

Figure 4.135. *Insulated system, pure PCM and water cooling, Test 5.3: temperature trends recorded on the bottom of all the cells (left) and ΔT trend between the bottom of the upper and the lower cells (right).*

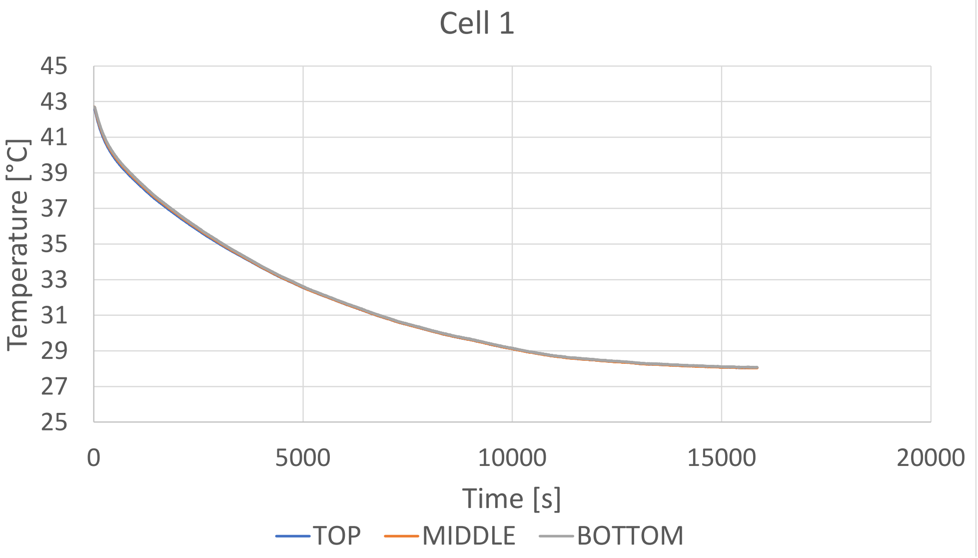

Figure 4.136. *Insulated system, copper-foam-loaded PCM and water cooling, Test 6.2: temperature trends recorded by* TC_{TOP}, TC_{MID} *and* TC_{BOT} *along Cell 1.*

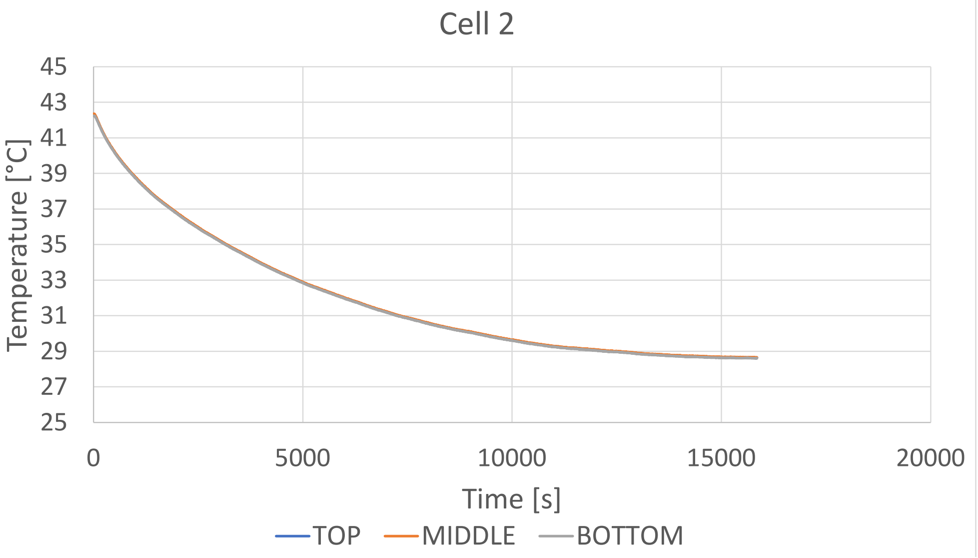

Figure 4.137. *Insulated system, copper-foam-loaded PCM and water cooling, Test 6.2: temperature trends recorded by* TC_{TOP}, TC_{MID} *and* TC_{BOT} *along Cell 2.*

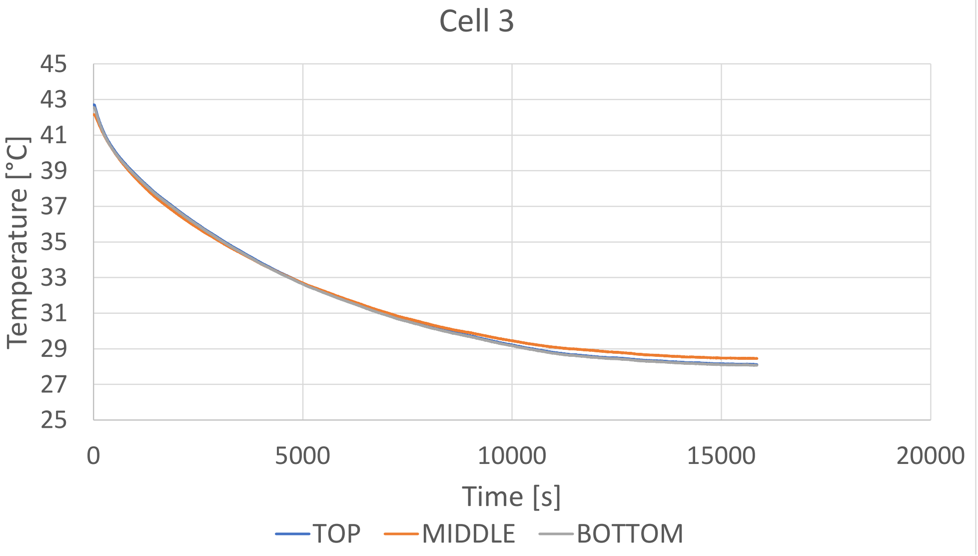

Figure 4.138. *Insulated system, copper-foam-loaded PCM and water cooling, Test 6.2: temperature trends recorded by* TC_{TOP}, TC_{MID} *and* TC_{BOT} *along Cell 3.*

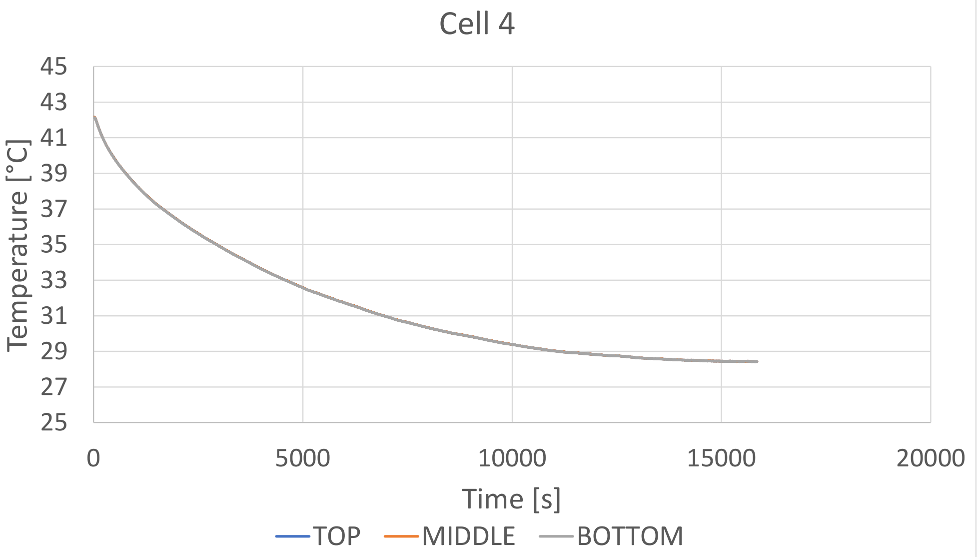

Figure 4.139. *Insulated system, copper-foam-loaded PCM and water cooling, Test 6.2: temperature trends recorded by* TC_{TOP}, TC_{MID} *and* TC_{BOT} *along Cell 4.*

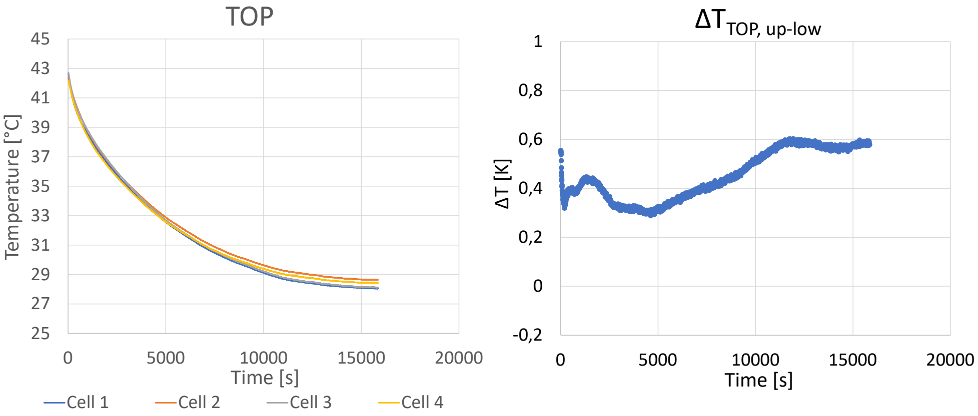

Figure 4.140. *Insulated system, copper-foam-loaded PCM and water cooling, Test 6.2: temperature trends recorded on the top of all the cells (left) and* ΔT *trend between the top of the upper and the lower cells (right).*

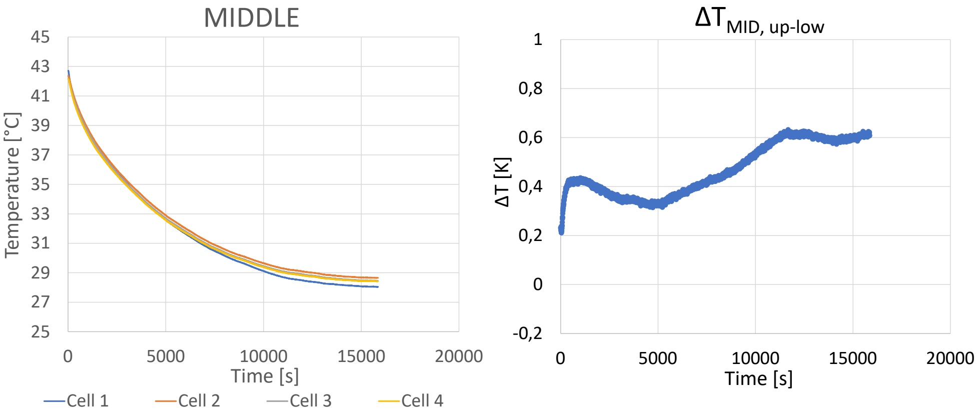

Figure 4.141. *Insulated system, copper-foam-loaded PCM and water cooling, Test 6.2: temperature trends recorded in the middle of all the cells (left) and* ΔT *trend between the middle of the upper and the lower cells (right).*

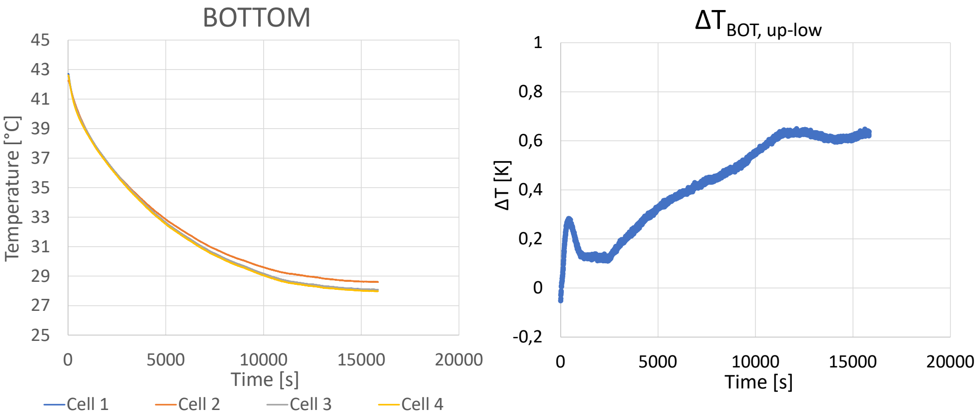

Figure 4.142. *Insulated system, copper-foam-loaded PCM and water cooling, Test 6.2: temperature trends recorded on the bottom of all the cells (left) and* ΔT *trend between the bottom of the upper and the lower cells (right).*

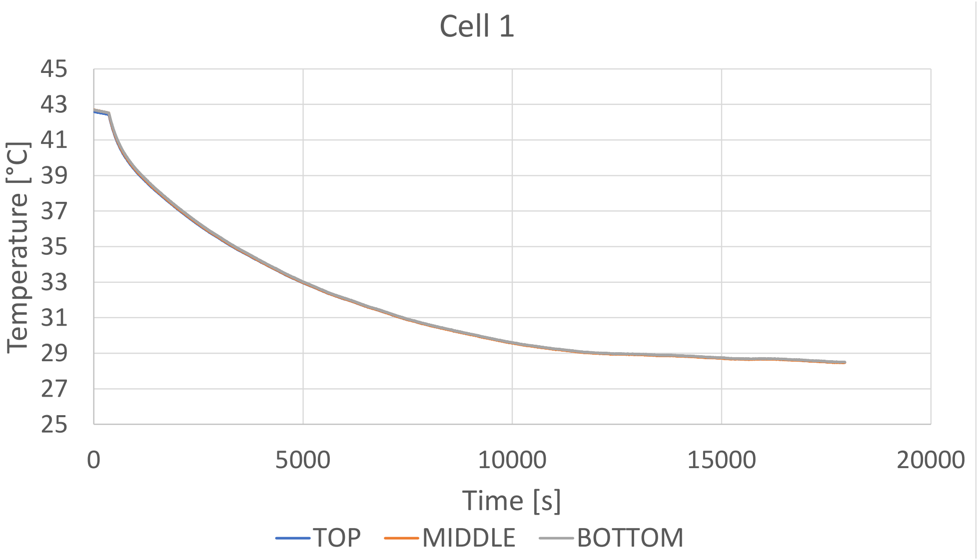

Figure 4.143. *Insulated system, copper-foam-loaded PCM and water cooling, Test 6.3: temperature trends recorded by* TC_{TOP}, TC_{MID} *and* TC_{BOT} *along Cell 1.*

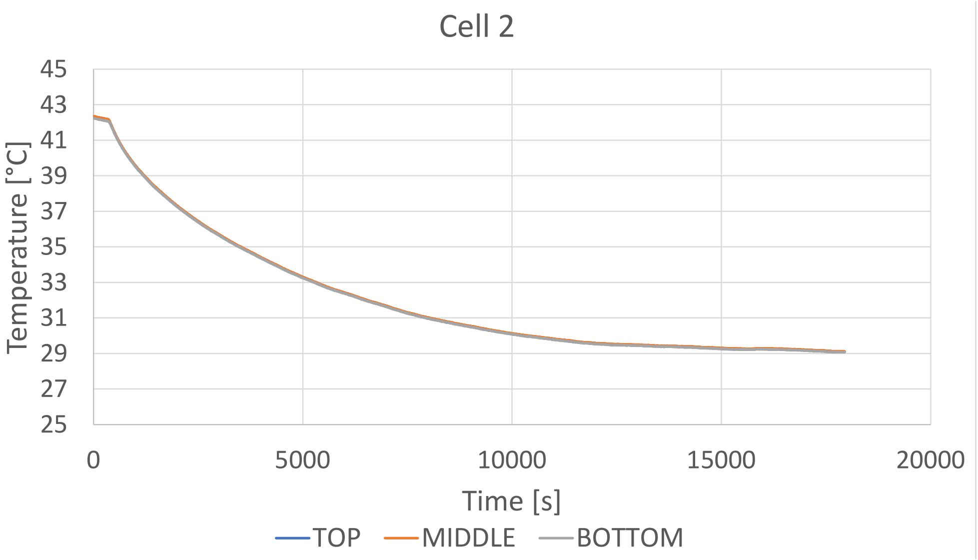

Figure 4.144. *Insulated system, copper-foam-loaded PCM and water cooling, Test 6.3: temperature trends recorded by* TC_{TOP}, TC_{MID} *and* TC_{BOT} *along Cell 2.*

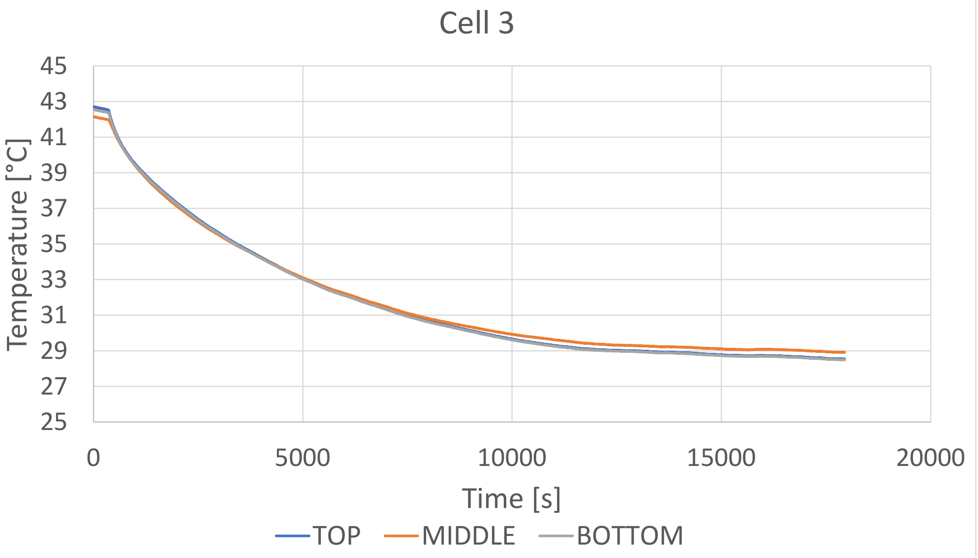

Figure 4.145. *Insulated system, copper-foam-loaded PCM and water cooling, Test 6.3: temperature trends recorded by* TC_{TOP}, TC_{MID} *and* TC_{BOT} *along Cell 3.*

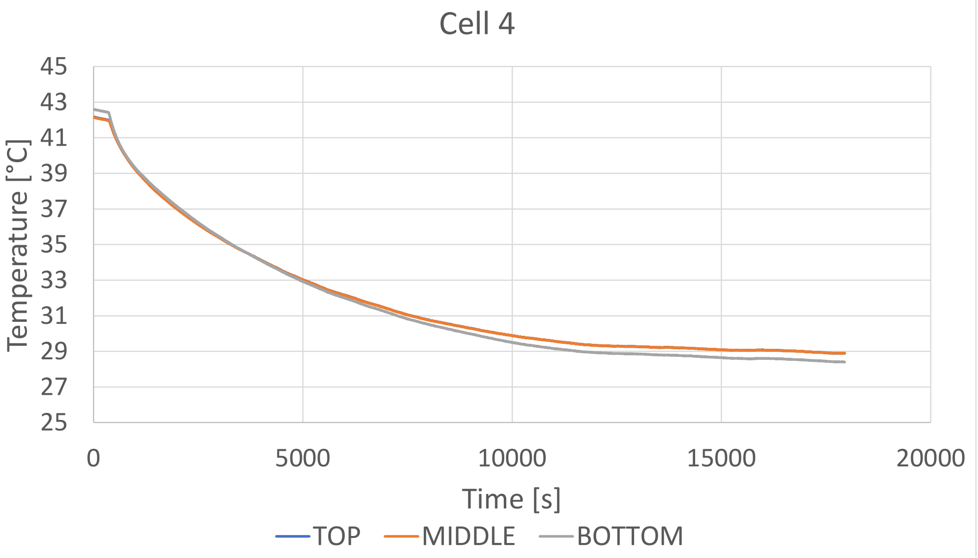

Figure 4.146. *Insulated system, copper-foam-loaded PCM and water cooling, Test 6.3: temperature trends recorded by* TC_{TOP}, TC_{MID} *and* TC_{BOT} *along Cell 4.*

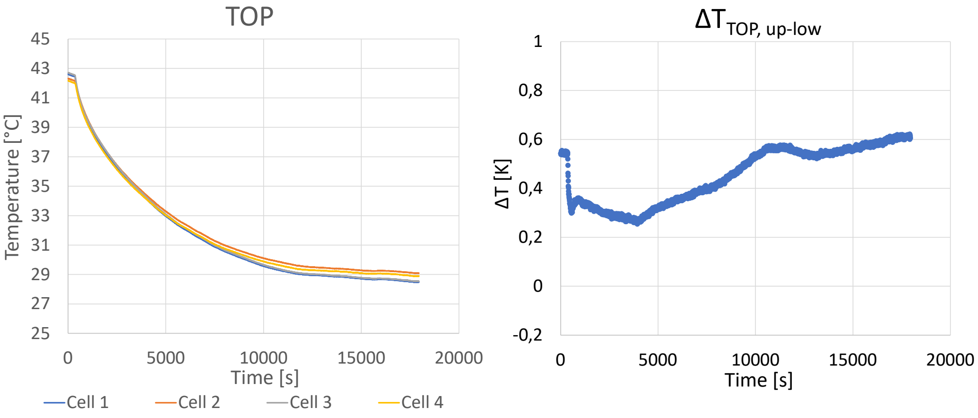

Figure 4.147. *Insulated system, copper-foam-loaded PCM and water cooling, Test 6.3: temperature trends recorded on the top of all the cells (left) and* ΔT *trend between the top of the upper and the lower cells (right).*

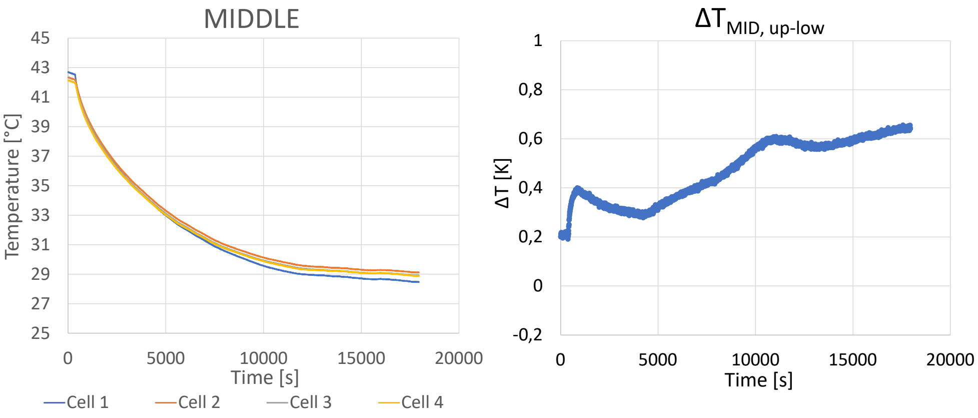

Figure 4.148. *Insulated system, copper-foam-loaded PCM and water cooling, Test 6.3: temperature trends recorded in the middle of all the cells (left) and* ΔT *trend between the middle of the upper and the lower cells (right).*

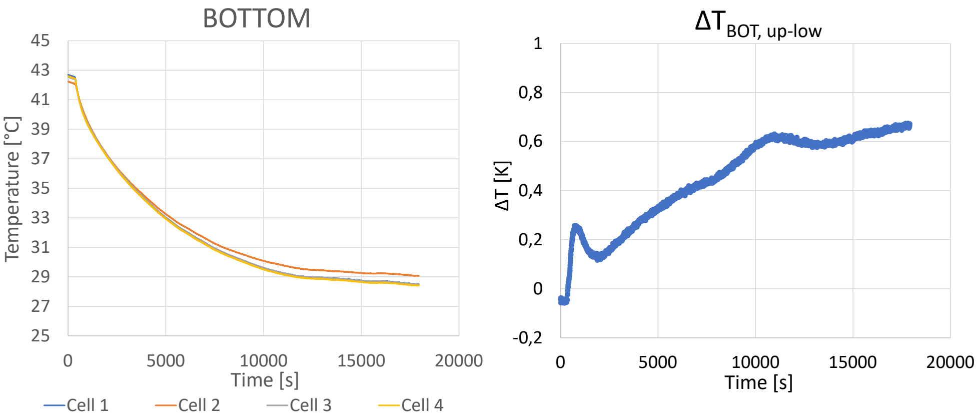

Figure 4.149. *Insulated system, copper-foam-loaded PCM and water cooling, Test 6.3: temperature trends recorded on the bottom of all the cells (left) and* ΔT *trend between the bottom of the upper and the lower cells (right).*

NOMENCLATURE

Symbols

CED	Cumulative energy demand	$[\mathrm{MJ}]$
ED	Energy demand	$[\mathrm{MJ}]$
ED_{s}	Specific energy demand	$[\mathrm{MJ}/\mathrm{kg}_{\mathrm{material}}]$
$F_{\mathrm{day,\,cargo}}$	Cargo daily fuel consumption	$[\mathrm{t}/\mathrm{d}]$
$F_{\mathrm{TOT,\,cargo}}$	Cargo total fuel consumption	$[\mathrm{t}]$
$\%FS$	Full scale uncertainty	$[\%]$
$\Delta T_{\mathrm{BOT,\,max}}$	Maximum ΔT_{BOT} between the upper and the lower cells	$[\mathrm{K}]$
ΔT_{BOT}	ΔT between the bottom of the upper and the lower cells	$[\mathrm{K}]$
ΔT_{BP}	ΔT on the bottom plane	$[\mathrm{K}]$
$\Delta T_{\mathrm{MID,\,max}}$	Maximum ΔT_{MID} between the upper and the lower cells	$[\mathrm{K}]$
ΔT_{MID}	ΔT between the middle of the upper and the lower cells	$[\mathrm{K}]$
$\Delta T_{\mathrm{TOP,\,max}}$	Maximum ΔT_{TOP} between the upper and the lower cells	$[\mathrm{K}]$
ΔT_{TOP}	ΔT between the top of the upper and the lower cells	$[\mathrm{K}]$
ΔT_{TP}	ΔT on the top plane	$[\mathrm{K}]$
$\Delta T_{\mathrm{UP\text{-}LOW}}$	ΔT between the upper and the lower cells	$[\mathrm{K}]$
$\widetilde{\Delta T}_{\mathrm{BOT,\,max}}$	Average of $\Delta T_{\mathrm{BOT,\,max}}$	$[\mathrm{K}]$
$\widetilde{\Delta T}_{\mathrm{MID,\,max}}$	Average of $\Delta T_{\mathrm{MID,\,max}}$	$[\mathrm{K}]$
$\widetilde{\Delta T}_{\mathrm{TOP,\,max}}$	Average of $\Delta T_{\mathrm{TOP,\,max}}$	$[\mathrm{K}]$
$f_{\mathrm{CO_2,\,cargo}}$	Emission factor for cargo ships	$[\mathrm{g}_{\mathrm{CO_2}}/\mathrm{kmt}]$
$f_{\mathrm{CO_2,\,truck}}$	Emission factor for trucks	$[\mathrm{kg}_{\mathrm{CO_2}}/\mathrm{L}]$
$F_{\mathrm{TOT,\,truck}}$	Truck total fuel consumption	$[\mathrm{L}]$
FS	Full scale	$[-]$
GWP_{s}	Specific global warming potential	$[\mathrm{kg}_{\mathrm{CO_2}}/\mathrm{kg}_{\mathrm{material}}]$
GWP_{TOT}	Total global warming potential	$[\mathrm{kg}_{\mathrm{CO_2}}]$
H_{d}	Fuel calorific value for diesel	$[\mathrm{MJ}/\mathrm{kg}_{\mathrm{fuel}}]$

H_{HFO}	Fuel calorific value for HFO	$[\text{MJ}/\text{kg}_{\text{fuel}}]$
k	Heat transfer coefficient	[W/K]
Pl_{cargo}	Cargo maximum payload	[kg]
Pl_{truck}	Truck maximum payload	[kg]
T_{AIR}	Air temperature	[°C]
T_{BOT}	Temperature on the bottom of the cell	[°C]
T_{BP}	Temperature on the bottom plane	[°C]
$T_{\text{dif, max}}$	Maximum temperature difference	[K]
T_{dif}	Temperature difference	[K]
T_{env}	Environmental temperature	[°C]
T_{max}	Maximum temperature	[°C]
$t_{\text{melt, pure}}$	Pure PCM melting time	[s]
T_{melt}	Melting temperature	[°C]
T_{MID}	Temperature in the middle of the cell	[°C]
T_{min}	Minimum temperature	[°C]
$T_{\text{PCM, DOWN}}$	Temperature of the PCM under the 4-cells module	[°C]
$T_{\text{PCM, UP}}$	Temperature of the PCM above the 4-cells module	[°C]
$T_{\text{ris, max}}$	Maximum temperature rising	[K]
T_{ris}	Temperature rising	[K]
T_{soft}	Softening temperature	[°C]
T_{TOP}	Temperature on the top of the cell	[°C]
T_{TP}	Temperature on the top plane	[°C]
TC_{BOT}	TC put on the bottom of the cell	$[-]$
TC_{MID}	TC put in the middle of the cell	$[-]$
$TC_{\text{PCM, DOWN}}$	TC immersed into the PCM, under the 4-cells module	$[-]$
$TC_{\text{PCM, UP}}$	TC immersed into the PCM, above the 4-cells module	$[-]$
TC_{TOP}	TC put on the top of the cell	$[-]$
U	Global heat transfer coefficient	$[\text{W}/\text{m}^2\text{K}]$
V_{case}	Case volume	$[\text{m}^3]$

Abbreviations

ABS	Acrylonitrile butadiene styrene
$ASC18$	American Solar Challenge 2018
BEV	Battery electric vehicle
BP	Battery pack
$BWSC19$	Bridgestone World Solar Challenge 2019
$CAGR$	Compound annual growth rate
DMC	Dimethyl carbonate
DOD	Degree of discharge
EC	Ethylene carbonate
ED	Energy demand
EOL	End-of-life
$ESC21$	European Solar Challenge 2021
ESS	Energy storage system
EV	Electric vehicle
FRP	Fiber reinforced plastic
GHG	Greenhouse gas
GWP	Global warming potential
HFO	Heavy fuel oil
HM	High-modulus
HP	Heat pipe
$HPCP$	Heat pipe cooling plate
HS	High-strength
$ILCD$	International Reference Life Cycle Data System
ISO	International Organization for Standardization
LCA	Life cycle assessment
LCI	Life cycle inventory
$LCIA$	Life cycle impact assessment
LCT	Life cycle thinking

LHS	Latent heat storage
LIB	Lithium-ion battery
$LTES$	Latent thermal energy storage
$LTESS$	Latent thermal energy storage system
$MTHX$	Multi-tube heat exchanger
NMC	Lithium-nickel-manganese-cobalt-oxide
PCM	Phase change material
PE	Polyethylene
PLM	Product lifecycle management
POM	Polyoxymethylene
PP	Polypropylene
PPI	Pores per inch
$PVDF$	Polyvinylidene fluoride
$RHE - HP$	Remote heat transfer heat pipe
RTD	Resistance temperature detector
RTM	Resin transfer molding
SAF	Submerged arc furnace
SHS	Sensible heat storage
SOC	State of charge
SOH	State of health
TC	Thermocouple
TEC	Thermoelectric cooling
$TESS$	Thermal energy storage system
TEU	Twenty-foot Equivalent Unit
UD	Unidirectional
$VARTM$	Vacuum-assisted resin transfer molding

BIBLIOGRAPHY

[1] SS Godara et al. "Review on history and characterization of polymer composite materials". In: *Materials Today: Proceedings* 44 (2021), pp. 2674–2677.

[2] "FORD SHOWS AUTO BUILT OF PLASTIC; Strong Material Derived From Soy Beans, Wheat, Corn is Used for Body and Fenders SAVING OF STEEL IS CITED Car Is 1,000 Pounds Lighter Than Metal Ones – 12 Years of Research Developed It". In: *The New York Times* (1941).

[3] Joris Smits. "Fiber-reinforced polymer bridge design in the Netherlands: Architectural challenges toward innovative, sustainable, and durable bridges". In: *Engineering* 2.4 (2016), pp. 518–527.

[4] Marco Regi and Francesco Sintoni. *Ritorno al futuro*. Compositi Magazine. June 2014. URL: `https://www.compositimagazine.it/ritorno-futuro/`.

[5] Seçkin Erden and Kingsley Ho. "Fiber reinforced composites". In: *Fiber Technology for Fiber-Reinforced Composites*. Elsevier, 2017, pp. 51–79.

[6] As Zh Khurshudyan. "A mesoscopic model for particle-reinforced composites". In: *Continuum Mechanics and Thermodynamics* (2019), pp. 1–15.

[7] Lin Feng Ng and Kathiravan Subramaniam. "Composite Sandwich Panels with the Metallic Facesheets". In: *Sandwich Composites*. Vol. 1. CRC Press, 2022, pp. 61–74.

[8] Wai Leong Eugene Wong and Sankaranarayanan Seetharaman. "Metal matrix composites". In: *Advances in Machining of Composite Materials*. Springer, 2021, pp. 129–158.

[9] Jibran Khaliq. "Ceramic Matrix Composites (CMCs)". In: *Advances in Machining of Composite Materials*. Springer, 2021, pp. 285–309.

[10] Patricia L Smaldone. "Lightweight composite materials for electronic enclosures". In: *Diversity into the next century* (1995), pp. 819–829.

[11] Maurizio Arena et al. "Multifunctional performance of a nano-modified fiber reinforced composite aeronautical panel". In: *Materials* 12.6 (2019), p. 869.

[12] Andreas Bardenhagen, Vishal Sethi, Heena Gudwani, et al. "Spider-silk composite material for aerospace application". In: *Acta Astronautica* (2021).

[13] Xu Dong Yang, Fan Gu, and Xin Chen. "Performance Improvement of Carbon Fiber Reinforced Epoxy Composite Sports Equipment". In: *Key Engineering Materials*. Vol. 871. Trans Tech Publ. 2021, pp. 228–233.

[14] Jovana Spasenović and Ivan Blagojević. "Composite materials in automotive industry: A review". In: *Industrija* 49.2 (2021), pp. 57–68.

[15] Django Mathijsen. "McLaren: 40 years in the lead in automotive carbon fiber". In: *Reinforced Plastics* 65.6 (2021), pp. 34–37. ISSN: 0034-3617. DOI: `https://doi.org/10.1016/S0034-3617(21)00272-1`. URL: `https://www.sciencedirect.com/science/article/pii/S0034361721002721`.

[16] Eneyw Gardie et al. “Numerical analysis of reinforced carbon fiber composite material for lightweight automotive wheel application”. In: *Materials Today: Proceedings* (2021).

[17] K.M. Hurley and P.E. George. “Carbon fiber recycling: Optimizing fiber volume fraction in recycled short-fiber laminates”. In: *International SAMPE Technical Conference* (Jan. 2011).

[18] R Napolitano et al. “Development of Sustainable Perspective of Carbon Fibers Recycling and Reusing for Construction Materials”. In: *RILEM Spring Convention and Conference*. Springer. 2020, pp. 131–142.

[19] Peter E Caltagirone et al. “Substitution of virgin carbon fiber with low-cost recycled fiber in automotive grade injection molding polyamide 66 for equivalent composite mechanical performance with improved sustainability”. In: *Composites Part B: Engineering* 221 (2021), p. 109007.

[20] Pawan Soami. *Introducing the Composite Materials Module*. COMSOL. Dec. 2018. URL: `https://www.comsol.com/blogs/introducing-the-composite-materials-module/`.

[21] MC Tanzi, S Farè, and G Candiani. “Organization structure, and properties of materials”. In: *Foundations of Biomaterials Engineering, Elsevier* (2019), pp. 3–103.

[22] Tommaso Maria Brugo. *Lecture notes: Laboratorio di Progettazione con Materiali Compositi*. Sept. 2019.

[23] Lovatt Andrew and Shercliff Hugh. *Material selection and processing*. University of Cambridge - Department of Engineering. 2002. URL: `http://www-materials.eng.cam.ac.uk/mpsite/`.

[24] Toray Advanced Composites. *Properties and Applications of Toray High Temperature Composites*. AZoM. 2014. URL: `https://www.azom.com/article.aspx?ArticleID=11255`.

[25] V Rubio, Prabhu Ramanujam, and Jon Binner. “Ultra-high temperature ceramic composite”. In: *Advances in Applied Ceramics* 117.sup1 (2018), s56–s61.

[26] Igor V Andrianov, Alexander L Kalamkarov, and Dieter Weichert. “Buckling of fibers in fiber-reinforced composites”. In: *Composites Part B: Engineering* 43.4 (2012), pp. 2058–2062.

[27] Anshuman Shrivastava. *Introduction to plastics engineering*. William Andrew, 2018.

[28] FYC Boey and SW Lye. “Effects of vacuum and pressure in an autoclave curing process for a thermosetting fibre-reinforced composite”. In: *Journal of materials processing technology* 23.2 (1990), pp. 121–131.

[29] Luigi Nele, Alessandra Caggiano, and Roberto Teti. “Autoclave cycle optimization for high performance composite parts manufacturing”. In: *Procedia CIRP* 57 (2016), pp. 241–246.

[30] *Lamborghini Sesto Elemento: La few-off più leggera*. https://www.lamborghini.com/it-en. 2019. URL: `https://www.lamborghini.com/it-en/news/lamborghini-sesto-elemento-la-few-piu-leggera`.

[31] Amanda Jacob. *Lamborghini unveils Sesto Elemento carbon fibre concept car*. Materials Today. 2010. URL: `https://www.materialstoday.com/composite-applications/news/lamborghini-unveils-sesto-elemento-carbon-fibre/`.

[32] D Dai and M Fan. "Wood fibres as reinforcements in natural fibre composites: structure, properties, processing and applications". In: *Natural Fibre Composites*. Elsevier, 2014, pp. 3–65.

[33] Vito Saldutto. *Materiali compositi: le tecniche di laminazione*. Close-up Engineering. 2021. URL: `https://vehiclecue.it/materiali-compositi-tecniche-laminazione-automotive/26901/`.

[34] Mind Composites. 2021. URL: `https://www.mindcomposites.com/`.

[35] *Multiple laminates in single 2D or 3D Ply Table*. SIEMENS. 2019. URL: `https://community.sw.siemens.com/s/article/multiple-laminates-in-single-2d-or-3d-ply-table`.

[36] David Greenfield. *Siemens to Acquire Engineering Software Provider Vistagy*. Automation World. 2011. URL: `https://www.automationworld.com/home/news/13305823/siemens-to-acquire-engineering-software-provider-vistagy`.

[37] Emiliano Ragoni. *L'auto solare emiliana che ha conquistato l'America, descritta da chi l'ha progettata*. Forbes. 2018. URL: `https://forbes.it/2018/08/06/lauto-solare-emiliana-che-ha-conquistato-lamerica-descritta-da-chi-lha-progettata/`.

[38] Morena Falcone. "Caratterizzazione sperimentale delle strutture vorticose generate in coda ad un'auto solare". MA thesis. Alma Mater Studiorum - Università di Bologna, Mar. 2018. URL: `http://amslaurea.unibo.it/15229/`.

[39] Giangiacomo Minak et al. "Structural design and manufacturing of a cruiser class solar vehicle". In: *Journal of Visual Experiments* 143.e58525 (2019).

[40] Marco Giachi and Marco Bertoldi. *EMILIA 4 LT: 3000 km senza una goccia di carburante*. CAD3D.it. 2020. URL: `https://www.cad3d.it/emilia4-lt-on-the-road-again/2164/`.

[41] Ana Pavlović et al. "On the modal behaviour of ultralight composite sandwich automotive panels". In: *Composite Structures* 248 (2020), p. 112523.

[42] Ana Pavlovic et al. "Multi-objective design optimization of the reinforced composite roof in a solar vehicle". In: *Applied Sciences* 10.8 (2020), p. 2665.

[43] Cristiano Fragassa, Ana Pavlovic, and Giangiacomo Minak. "On the structural behaviour of a CFRP safety cage in a solar powered electric vehicle". In: *Composite Structures* 252 (2020), p. 112698.

[44] Huaqiang Liu et al. "Thermal issues about Li-ion batteries and recent progress in battery thermal management systems: A review". In: *Energy Conversion and Management* 150 (2017), pp. 304–330.

[45] IEA. *Global EV Outlook 2021*. Ed. by Paris IEA. 2021. URL: `https://www.iea.org/reports/global-ev-outlook-2021`.

[46] European Commission and Directorate-General for Communication. *Make transport greener*. 2021. URL: `https://data.europa.eu/doi/10.2775/63094`.

[47] *Optemus - Optemus | Optimised and Systematic Energy Management in Electric Vehicles*. http://www.optemus.eu/. 2021.

[48] Stephen Wilke et al. "Preventing Thermal Runaway Propagation in Lithium Ion Battery Packs Using a Phase Change Composite Material: An Experimental Study". In: *Journal of Power Sources* 340 (Feb. 2017), pp. 51–59. ISSN: 0378-7753. DOI: `10.1016/j.jpowsour.2016.11.018`.

[49] Feng Leng, Cher Ming Tan, and Michael Pecht. "Effect of Temperature on the Aging Rate of Li Ion Battery Operating above Room Temperature". In: *Scientific Reports* 5.1 (Aug. 2015), p. 12967. ISSN: 2045-2322. DOI: `10.1038/srep12967`.

[50] Peammawat Chanthevee et al. "A Simplified Approach for Heat Generation Due to Entropy Change in Cylindrical LCO Battery". In: *2018 IEEE Transportation Electrification Conference and Expo, Asia-Pacific (ITEC Asia-Pacific)*. June 2018, pp. 1–5. DOI: `10.1109/ITEC-AP.2018.8433303`.

[51] Claudio Rossi and Beatrice Pulvirenti. *Lecture notes: LiBER Lithium Batteries Emilia Romagna*. 2020.

[52] Jianmin Ma et al. "The 2021 battery technology roadmap". In: *Journal of Physics D: Applied Physics* 54.18 (2021), p. 183001.

[53] *The lithium-ion battery life cycle report*. Circular Energy Storage - Research and Consulting. 2021.

[54] Kim Jaewan, Oh Jinwoo, and Lee Hoseong. "Review on battery thermal management system for electric vehicles". In: *Applied Thermal Engineering* 149 (2019), pp. 192–212.

[55] Marcy Lowe et al. "Lithium-ion Batteries for Electric Vehicles: THE U.S. VALUE CHAIN". In: *Center on Globalization, Governance & Competitiveness* (2010).

[56] Gene Berdichevsky et al. "The tesla roadster battery system". In: *Tesla Motors* 1.5 (2006), pp. 1–5.

[57] Michel Armand et al. "Lithium-ion batteries – Current state of the art and anticipated developments". In: *Journal of Power Sources* 479 (2020), p. 228708. ISSN: 0378-7753. DOI: `https://doi.org/10.1016/j.jpowsour.2020.228708`. URL: `https://www.sciencedirect.com/science/article/pii/S0378775320310120`.

[58] Jason B Quinn et al. "Energy density of cylindrical Li-ion cells: a comparison of commercial 18650 to the 21700 cells". In: *Journal of The Electrochemical Society* 165.14 (2018), A3284.

[59] Fred Lambert. *Panasonic unveils its Tesla 4680 battery cell, production to start next year*. Electrek. Oct. 2021. URL: `https://electrek.co/2021/10/25/panasonic-unveils-tesla-4680-battery-cell-production-next-year/`.

[60] S Ziemann et al. "The future of mobility and its critical raw materials". In: *Metallurgical Research & Technology* 110.1 (2013), pp. 47–54.

[61] A. Opitz et al. "Can Li-Ion batteries be the panacea for automotive applications?" In: *Renewable and Sustainable Energy Reviews* 68 (2017), pp. 685–692.

[62] Yuqi Huang et al. "Study on the thermal interaction and heat dissipation of cylindrical Lithium-Ion Battery cells". In: *Energy Procedia* 142 (2017), pp. 4029–4036.

[63] D.C. Erb et al. "Analytical methods for determining the effects of lithium-ion cell size in aligned air-cooled battery packs". In: *Journal of Energy Storage* 10 (2017), pp. 39–47.

[64] Tao Wang et al. "Thermal investigation of lithium-ion battery module with different cell arrangement structures and forced air-cooling strategies". In: *Applied Energy* 134 (2014), pp. 229–238.

[65] Zhao Lu et al. "Parametric study of forced air cooling strategy for lithium-ion battery pack with staggered arrangement". In: *Applied Thermal Engineering* 136 (2018), pp. 28–40.

[66] Christoph Bolsinger and Kai Peter Birke. "Effect of different cooling configurations on thermal gradients inside cylindrical battery cells". In: *Journal of Energy Storage* 21 (2019), pp. 222–230.

[67] Z An et al. "Modeling and analysis of thermal runaway in Li-ion cell". In: *Applied Thermal Engineering* 160 (2019), p. 113960.

[68] Alysha Liebscher and Gary Gayman. "Preventing Thermal Runaway in Electric Vehicle Batteries". In: *MachineDesign* (2018). URL: `https://www.machinedesign.com/materials/preventing-thermal-runaway-electric-vehicle-batteries`.

[69] Qian Wang et al. "A critical review of thermal management models and solutions of lithium-ion batteries for the development of pure electric vehicles". In: *Renewable and Sustainable Energy Reviews* 64 (2016), pp. 106–128.

[70] Noboru Sato. "Thermal behavior analysis of lithium-ion batteries for electric and hybrid vehicles". In: *Journal of power sources* 99.1-2 (2001), pp. 70–77.

[71] Haobing Zhou et al. "Thermal performance of cylindrical Lithium-ion battery thermal management system based on air distribution pipe". In: *International Journal of Heat and Mass Transfer* 131 (2019), pp. 984–998.

[72] Xiaosong Hu et al. "Battery warm-up methodologies at subzero temperatures for automotive applications: Recent advances and perspectives". In: *Progress in Energy and Combustion Science* 77 (2020), p. 100806.

[73] S.S. Zhang, K. Xu, and T.R. Jow. "The low temperature performance of Li-ion batteries". In: *Journal of Power Sources* 225 (2003), pp. 137–140.

[74] Bahman Shabani and Manu Biju. "Theoretical modelling methods for thermal management of batteries". In: *Energies* 8.9 (2015), pp. 10153–10177.

[75] Seyed Mazyar Hosseini Moghaddam. "Designing battery thermal management systems (BTMS) for cylindrical Lithium-ion battery modules using CFD". Thesis. 2019.

[76] Weixiong Wu et al. "A critical review of battery thermal performance and liquid based battery thermal management". In: *Energy Conversion and Management* (2019), pp. 262–281.

[77] Jiuchun Jiang et al. "A low-temperature internal heating strategy without lifetime reduction for large-size automotive lithium-ion battery pack". In: *Applied Energy* 230 (2018), pp. 257–266.

[78] X.M. Xu and R.He. "Research on the heat dissipation performance of battery pack based on forced air cooling". In: *Journal of Power Sources* 240 (2013), pp. 33–41.

[79] Xiaoming Xu et al. "Heat dissipation performance of electric vehicle cabin under natural wind cooling". In: *Advances in Mechanical Engineering* 10.10 (2018), p. 1687814018803819.

[80] Shujie Wu et al. "The state of the art on preheating lithium-ion batteries in cold weather". In: *Journal of Energy Storage* 27 (2020), p. 101059.

[81] Gang Zhao et al. "A review of air-cooling battery thermal management systems for electric and hybrid electric vehicles". In: *Journal of Power Sources* 501 (2021), p. 230001.

[82] Jinhong Xie et al. "Structural optimization of lithium-ion battery pack with forced air cooling system". In: *Applied Thermal Engineering* 126 (2017), pp. 583–593.

[83] Yuqian Fan et al. "Optimization of cooling strategies for an electric vehicle in high-temperature environment". In: *Applied Thermal Engineering* (2021), p. 117088.

[84] Dinesh Kumar Sharma and Aneesh Prabhakar. "A review on air cooled and air centric hybrid thermal management techniques for Li-ion battery packs in electric vehicles". In: *Journal of Energy Storage* 41 (2021), p. 102885.

[85] Jiaqiang E et al. "Effects of the different air cooling strategies on cooling performance of a lithium-ion battery module with baffle". In: *Applied Thermal Engineering* 144 (2018), pp. 231–241.

[86] Kai Chen et al. "Configuration optimization of battery pack in parallel air-cooled battery thermal management system using an optimization strategy". In: *Applied Thermal Engineering* 123 (2017), pp. 177–186.

[87] Sihui Hong et al. "Design of flow configuration for parallel air-cooled battery thermal management system with secondary vent". In: *international Journal of Heat and Mass Transfer* 116 (2018), pp. 1204–1212.

[88] Seham Shahid and Martin Agelin-Chaab. "Experimental and numerical studies on air cooling and temperature uniformity in a battery pack". In: *International Journal of Energy Research* 42.6 (2018), pp. 2246–2262.

[89] Tairan Yang et al. "Investigation of the thermal performance of axial-flow air cooling for the lithium-ion battery pack". In: *International Journal of Thermal Science* 108 (2016), pp. 132–144.

[90] Ali M. Sefidan, Atta Sojoudi, and Suvash C. Saha. "Nanofluid-based cooling of cylindrical lithium-ion battery packs employing forced air flow". In: *International Journal of Thermal Sciences* 177 (2017), pp. 44–58.

[91] Morena Falcone et al. “Lithium-Ion Battery Thermal Management Systems: A Survey and New CFD Results”. In: *Batteries* 7.4 (2021), p. 86.

[92] Yi Yang et al. “Heat dissipation analysis of different flow path for parallel liquid cooling battery thermal management system”. In: *International Journal of Energy Research* 44.7 (2020), pp. 5165–5176.

[93] Guofeng Chang et al. “Effects of reciprocating liquid flow battery thermal management system on thermal characteristics and uniformity of large lithium-ion battery pack”. In: *International Journal of Energy Research* 44.8 (2020), pp. 6383–6395.

[94] Jinwei Liu et al. “Thermal characteristics of power battery pack with liquid-based thermal management”. In: *Applied Thermal Engineering* 164 (2020), p. 114421.

[95] Xingwang Tang et al. “Performance analysis on liquid-cooled battery thermal management for electric vehicles based on machine learning”. In: *Journal of Power Sources* 494 (2021), p. 229727.

[96] K. Darcovich et al. “Comparison of cooling plate configurations for automotive battery pack thermal management”. In: *applied Thermal Engineering* 155 (2019), pp. 185–195.

[97] Tao Deng et al. “Novel leaf-like channels for cooling rectangular lithium ion batteries”. In: *Applied Thermal Engineering* 150 (2019), pp. 1186–1196.

[98] Nandy Putra, Bambang Ariantara, and Rangga Aji Pamungkas. “Experimental investigation on performance of lithium-ion battery thermal management system using flat plate loop heat pipe for electric vehicle application”. In: *Applied Thermal Engineering* 99 (2016), pp. 784–789.

[99] Jianqin Wang et al. “Sensitivity analysis of factors influencing a heat pipe-based thermal management system for a battery module with cylindrical cells”. In: *Applied Thermal Engineering* 151 (2019), pp. 475–485.

[100] Zhonghao Rao et al. “Experimental investigation on thermal management of electric vehicle battery with heat pipe”. In: *Energy Conversion and Management* 65 (2013), pp. 92–97.

[101] Y. Lyu et al. “Electric vehicle battery thermal management system with thermoelectric cooling”. In: *Energy Reports* 5 (2019), pp. 822–827.

[102] Pingang Zhang et al. “Melting heat transfer characteristics of a composite phase change material fabricated by paraffin and metal foam”. In: *Applied Energy* 185 (2017), pp. 1971–1983.

[103] Hongjie Wu et al. “Electro-thermal modeling and cooling optimization for 18650 battery pack”. In: *2016 IEEE Vehicle Power and Propulsion Conference (VPPC)*. IEEE. 2016, pp. 1–5.

[104] *SE250AB Thermal Gel*. Sheen Electronical Technology Co. URL: `https://www.sheenthermal.com/se250ab-thermal-gel.html`.

[105] Mike Millikin. *XING Mobility partners with Castrol to deliver advanced, immersion-cooled battery systems for EVs*. Green Car Congress. Apr. 2021. URL: `https://www.greencarcongress.com/2021/04/20210427-xing.html`.

[106] Junko Yoshida. *Xing Mobility Electrifies 1969 Chevy Camaro*. EETimes. Jan. 2019. URL: `https://www.eetimes.com/xing-mobility-electrifies-1969-chevy-camaro/`.

[107] Fredrik Larsson et al. "Characteristics of lithium-ion batteries during fire tests". In: *Journal of Power Sources* 271 (Nov. 2014). DOI: `10.1016/j.jpowsour.2014.08.027`.

[108] Lingxi Kong et al. "Li-Ion Battery Fire Hazards and Safety Strategies". In: *Energies* 11.9 (2018), p. 2191. ISSN: 1996-1073. URL: `https://www.mdpi.com/1996-1073/11/9/2191`.

[109] Qing Gao et al. "An experimental investigation of refrigerant emergency spray on cooling and oxygen suppression for overheating power battery". In: *journal of Power Sources* 415 (2019), pp. 33–43.

[110] Christos Pagkalos et al. "Evaluation of water and paraffin PCM as storage media for use in thermal energy storage applications: A numerical approach". In: *International Journal of Thermofluids* 1-2 (2020), p. 100006. ISSN: 2666-2027. DOI: `https://doi.org/10.1016/j.ijft.2019.100006`. URL: `http://www.sciencedirect.com/science/article/pii/S2666202719300060`.

[111] William R. Sutterlin. *A Phase Change Materials Comparison: Vegetable-based vs. Paraffin-based PCMs*. Web Page. 2015. URL: `https://www.chemicalonline.com/doc/a-phase-change-materials-comparison-vegetable-based-vs-paraffin-based-pcms-0001`.

[112] Hussam Jouhara et al. "Latent thermal energy storage technologies and applications: A review". In: *International Journal of Thermofluids* 5 (2020), p. 100039.

[113] Palanisamy Muthukumar and Hakeem Niyas. "Materials, Design and Development of Latent Heat Storage Systems for Medium and Large-Scale Applications: Issues and Challenges". In: (2020). DOI: `10.1016/B978-0-12-803581-8.11154-3`.

[114] A Abhat. "Low temperature latent heat thermal energy storage: heat storage materials". In: *Solar energy* 30.4 (1983), pp. 313–332.

[115] Charalambos N Elias and Vassilis N Stathopoulos. "A comprehensive review of recent advances in materials aspects of phase change materials in thermal energy storage". In: *Energy Procedia* 161 (2019), pp. 385–394.

[116] Laura Colla et al. "Nano-PCMs for enhanced energy storage and passive cooling applications". In: *Applied Thermal Engineering* 110 (2017), pp. 584–589.

[117] Yongcai Li, Shuli Liu, and Yaqin Zhang. "Experimental Study of the Heat Transfer Performance of PCMs Within Metal Finned Containers". In: Sept. 2014, pp. 669–684. ISBN: 978-3-319-07976-9. DOI: `10.1007/978-3-319-07977-6_44`.

[118] Rami Zeinelabdein, Siddig Omer, and Guohui Gan. "Critical review of latent heat storage systems for free cooling in buildingserformance studies of refrigerated van having". In: *Renewable and Sustainable Energy Reviews* 82 (2018), pp. 2843–2868.

[119] Mohamed Fadl and Philip C Eames. "An experimental investigation of the heat transfer and energy storage characteristics of a compact latent heat thermal energy storage system for domestic hot water applications". In: *Energy* 188 (2019), p. 116083.

[120] Awni H Alkhazaleh and Baljinder K Kandola. "Thermal and Flammability Properties of Paraffin/Nanoclay Composite Phase Change Materials Incorporated in Building Materials for Thermal Energy Storage". In: *International Journal of Energy and Power Engineering* 11.6 (2017), pp. 696–701.

[121] Mazyar Ahrari et al. "A review on application of phase change materials in textiles finishing". In: *International Journal of Materials and Metallurgical Engineering* 11.5 (2017), pp. 400–405.

[122] BMW Media Information. *BMW Motorrad Rider Equipment 2018*. Tech. rep. Nov. 2017, p. 23.

[123] Munesh Kumar Sharma and Dharam Buddhi. "Performance studies of refrigerated van having PCM for generating off site refrigeration effect". In: *Journal of Pure and Applied Science and Technology* 3.1 (2013), pp. 1–12.

[124] Eduard Oró et al. "Improving thermal performance of freezers using phase change materials". In: *International journal of refrigeration* 35.4 (2012), pp. 984–991.

[125] Mobin Borhani et al. "Performance Enhancement of a Thermoelectric Harvester with a PCM/Metal Foam Composite". In: *Renewable Energy* (2021).

[126] Shuang-Fei Li, Zhen-hua Liu, and Xue-Jiao Wang. "A comprehensive review on positive cold energy storage technologies and applications in air conditioning with phase change materials". In: *Applied Energy* 255 (2019), p. 113667.

[127] Rasoul Pakrouh et al. "A numerical method for PCM-based pin fin heat sinks optimization". In: *Energy Conversion and Management* 103 (2015), pp. 542–552.

[128] Qinlong Ren, Penghua Guo, and Jianjun Zhu. "Thermal management of electronic devices using pin-fin based cascade microencapsulated PCM/expanded graphite composite". In: *International Journal of Heat and Mass Transfer* 149 (2020), p. 119199.

[129] Andrew Mills and Said Al-Hallaj. "Simulation of passive thermal management system for lithium-ion battery packs". In: *Journal of power sources* 141.2 (2005), pp. 307–315.

[130] Anan Ashrabi Ananno et al. "Design and numerical analysis of a hybrid geothermal PCM flat plate solar collector dryer for developing countries". In: *Solar Energy* 196 (2020), pp. 270–286.

[131] Mehdi Eisapour et al. "Exergy and energy analysis of wavy tubes photovoltaic-thermal systems using microencapsulated PCM nano-slurry coolant fluid". In: *Applied Energy* 266 (2020), p. 114849.

[132] Joris Jaguemont et al. "Phase-change materials (PCM) for automotive applications: A review". In: *Applied Thermal Engineering* 132 (2018), pp. 308–320.

[133] Lucia Ianniciello, Pascal Henry Biwolé, and Patrick Achard. "Electric vehicles batteries thermal management systems employing phase change materials". In: *Journal of power sources* 378 (2018), pp. 383–403.

[134] Said Al-Hallaj and J. Robert Selman. "A novel thermal management system for electric vehicle batteries using phase-change material". In: *Journal of the Electrochemical Society* 147.9 (2000), p. 3231.

[135] Charles-Victor Hémery et al. "Experimental performances of a battery thermal management system using a phase change material". In: *Journal of Power Sources* 270 (2014), pp. 349–358.

[136] Mehdi Esapour et al. "Melting and solidification of PCM embedded in porous metal foam in horizontal multi-tube heat storage system". In: *Energy conversion and management* 171 (2018), pp. 398–410.

[137] Mohamed Moussa El Idi and Mustapha Karkri. "Heating and cooling conditions effects on the kinetic of phase change of PCM embedded in metal foam". In: *Case Studies in Thermal Engineering* 21 (2020), p. 100716.

[138] Pascal Henry Biwole et al. "Influence of fin size and distribution on solid-liquid phase change in a rectangular enclosure". In: *International Journal of Thermal Sciences* 124 (2018), pp. 433–446.

[139] Abduljalil Al-Abidi et al. "Numerical study of PCM solidification in a triplex tube heat exchanger with internal and external fins". In: *International Journal of Heat and Mass Transfer* 61 (2013), pp. 684–695.

[140] Chenzhen Ji et al. "Non-uniform heat transfer suppression to enhance PCM melting by angled fins". In: *Applied Thermal Engineering* 129 (2018), pp. 269–279.

[141] Müslüm Arıcı et al. "Melting of nanoparticle-enhanced paraffin wax in a rectangular enclosure with partially active walls". In: *International Journal of Heat and Mass Transfer* 104 (2017), pp. 7–17.

[142] Jogi Krishna, Pisipaty S. Kishore, and A. Brusly Solomon. "Heat pipe with nano enhanced-PCM for electronic cooling application". In: *Experimental Thermal and Fluid Science* 81 (2017), pp. 84–92.

[143] Valan Arasu and Arun S. Mujumdar. "Numerical study on melting of paraffin wax with Al2O3 in a square enclosure". In: *International Communications in Heat and Mass Transfer* 39.1 (2012), pp. 8–16.

[144] Ali A. Rabienataj Darzi, Mahmoud Jourabian, and Mousa Farhadi. "Melting and solidification of PCM enhanced by radial conductive fins and nanoparticles in cylindrical annulus". In: *Energy conversion and management* 118 (2016), pp. 253–263.

[145] Luisa F. Cabeza et al. "Heat transfer enhancement in water when used as PCM in thermal energy storage". In: *Applied thermal engineering* 22.10 (2002), pp. 1141–1151.

[146] Fereshteh Samimi et al. "Thermal management analysis of a Li-ion battery cell using phase change material loaded with carbon fibers". In: *Energy* 96 (2016), pp. 355–371.

[147] Liwu Fan and Jay M Khodadadi. "Thermal conductivity enhancement of phase change materials for thermal energy storage: a review". In: *Renewable and sustainable energy reviews* 15.1 (2011), pp. 24–46.

[148] Giulia Righetti et al. "Experimental investigation of phase change of medium/high temperature paraffin wax embedded in 3D periodic structure". In: *International Journal of Thermofluids* 5 (2020), p. 100035.

[149] Giulia Righetti et al. "Experimental study of phase change material (PCM) embedded in 3D periodic structures realized via additive manufacturing". In: *International Journal of Thermal Sciences* 153 (2020), p. 106376.

[150] Tauseef-Ur-Rehman et al. "A critical review on heat transfer augmentation of phase change materials embedded with porous materials/foams". In: *International Journal of Heat and Mass Transfer* 135 (2019), pp. 649–673.

[151] Ahmed Alhusseny et al. "Impact of using a PCM-metal foam composite on charging/discharging process of bundled-tube LHTES units". In: *International Journal of Heat and Mass Transfer* 150 (2020), p. 119320.

[152] Ali Ghahremannezhad et al. "Thermal performance analysis of phase change materials (PCMs) embedded in gradient porous metal foams". In: *Applied Thermal Engineering* 179 (2020), p. 115731.

[153] Jasim M. Mahdi and Emmanuel C. Nsofor. "Multiple-segment metal foam application in the shell-and-tube PCM thermal energy storage system". In: *Journal of Energy Storage* 20 (2018), pp. 529–541.

[154] Tauseef-Ur-Rehman and Hafiz Ali. "Experimental study on the thermal behavior of RT-35HC paraffin within copper and Iron-Nickel open cell foams: energy storage for thermal management of electronics". In: *International Journal of Heat and Mass Transfer* 146 (2020), p. 118852.

[155] Anandaroop Bhattacharya, Varaprasad V Calmidi, and Roop L. Mahajan. "Thermophysical properties of high porosity metal foams". In: *International journal of heat and mass transfer* 45.5 (2002), pp. 1017–1031.

[156] M Silvestrini et al. "Experimental thermal performance comparison of pure and metal foam-loaded PCMs". In: *Journal of Physics: Conference Series*. Vol. 2116. IOP Publishing. 2021, p. 012058.

[157] Giulia Righetti et al. "Phase change materials embedded in porous matrices for hybrid thermal energy storages: Experimental results and modeling". In: *International Journal of Refrigeration* 106 (2019), pp. 266–277.

[158] Battula Venkata Sai Dinesh and Anirban Bhattacharya. "Comparison of energy absorption characteristics of PCM-metal foam systems with different pore size distributions". In: *Journal of Energy Storage* 28 (2020), p. 101190.

[159] Rubitherm®. *Rubitherm® data sheet - RT35*. URL: `https://www.rubitherm.eu/media/products/datasheets/Techdata_-RT35_EN_06082018.PDF`.

[160] *Software and Manual that will be installed*. SRM-20. URL: `https://startup.rolanddg.com/monoFab/SRM-20/SRM-20_EN/On/sp-srm_about-apps_on_en.html`.

[161] Morena Falcone et al. “Experimental analysis of latent thermal energy storage systems based on pure and copper-foam-loaded PCMs”. In: *38th UIT International Heat Transfer Conference*. 2021, pp. 18–25.

[162] Eurobatex®. *Eurobatex® data sheet*. URL: `http://www.unionfoam.it/allegati/EUROBATEX/Scheda%20tecnica.pdf`.

[163] Claudia Naldi et al. “Numerical model calibration for composite-PCM LTES”. In: *IIR Conferences*. 2021, p. 7. URL: `http://www.aicarr.org/Documents/Convegni/2020/IIR_ABSTRACTS_LIST.pdf`.

[164] Peng Wang. “Application of Phase Change Energy Storage Materials in BTMS Based on Element Analysis”. In: *Chemical Engineering Transactions* 62 (2017), pp. 91–96.

[165] Thanh-Ha Tran et al. “Experimental investigation on the feasibility of heat pipe cooling for HEV/EV lithium-ion battery”. In: *Applied Thermal Engineering* 63.2 (2014), pp. 551–558.

[166] Hamidreza Behi et al. “Comprehensive Passive Thermal Management Systems for Electric Vehicles”. In: *Energies* 14.13 (Jan. 2021), p. 3881. DOI: `10.3390/en14133881`.

[167] Mohamed Moussa El Idi, Mustapha Karkri, and Mahamadou Abdou Tankari. “A Passive Thermal Management System of Li-ion Batteries Using PCM Composites: Experimental and Numerical Investigations”. In: *International Journal of Heat and Mass Transfer* 169 (Apr. 2021), p. 120894. ISSN: 0017-9310. DOI: `10.1016/j.ijheatmasstransfer.2020.120894`.

[168] Wenfu Situ et al. “A Thermal Management System for Rectangular LiFePO4 Battery Module Using Novel Double Copper Mesh-Enhanced Phase Change Material Plates”. In: *Energy* 141 (Dec. 2017), pp. 613–623. ISSN: 0360-5442. DOI: `10.1016/j.energy.2017.09.083`.

[169] Maan Al-Zareer, Ibrahim Dincer, and Marc A. Rosen. “A Novel Approach for Performance Improvement of Liquid to Vapor Based Battery Cooling Systems”. In: *Energy Conversion and Management* 187 (May 2019), pp. 191–204. ISSN: 0196-8904. DOI: `10.1016/j.enconman.2019.02.063`.

[170] Lip Huat Saw et al. “Novel Thermal Management System Using Mist Cooling for Lithium-Ion Battery Packs”. In: *Applied Energy* 223 (Aug. 2018), pp. 146–158. ISSN: 0306-2619. DOI: `10.1016/j.apenergy.2018.04.042`.

[171] Ziye Ling et al. “A Hybrid Thermal Management System for Lithium Ion Batteries Combining Phase Change Materials with Forced-Air Cooling”. In: *Applied Energy* 148 (June 2015), pp. 403–409. ISSN: 0306-2619. DOI: `10.1016/j.apenergy.2015.03.080`.

[172] Roberto Bubbico et al. “Analysis of Passive Temperature Control Systems Using Phase Change Materials for Application to Secondary Batteries Cooling”. In: *Journal of Thermal Science and Engineering Applications* 10.6 (Aug. 2018). ISSN: 1948-5085. DOI: `10.1115/1.4040643`.

[173] Zichen Wang et al. "Paraffin and Paraffin/Aluminum Foam Composite Phase Change Material Heat Storage Experimental Study Based on Thermal Management of Li-ion Battery". In: *Applied Thermal Engineering* 78 (Mar. 2015), pp. 428–436. ISSN: 1359-4311. DOI: `10.1016/j.applthermaleng.2015.01.009`.

[174] RS. *RS 8606909 cartridge heater - Data sheet*. URL: `https://docs.rs-online.com/ae4d/0900766b8158491f.pdf`.

[175] LOCTITE. *LOCTITE SI 100 - Data sheet*. URL: `https://www.tme.eu/Document/dabc3adb89c27fcf5674cf89fbc0b908/EN_TDS_LOCTITE_SI_100_1401.pdf`.

[176] Lena Spitthoff, Paul R. Shearing, and Odne Stokke Burheim. "Temperature, Ageing and Thermal Management of Lithium-Ion Batteries". In: *Energies* 14.5 (2021), p. 1248.

[177] January EC. "Communication from the commission to the European parliament, the council, the European economic and social committee and the committee of the regions; towards a comprehensive climate change agreement in Copenhagen". In: *Additional background information* (2009).

[178] *Economia circolare - Perché "circolare"*. Circular Economy Network. 2018. URL: `https://circulareconomynetwork.it/economia-circolare/`.

[179] EC JCR. "ILCD handbook: general guide for life cycle assessment—provisions and action steps". In: *Luxembourg: Publications Office of the European Union* (2010).

[180] Ellen MacArthur Foundation. *Towards a circular economy: Business rationale for an accelerated transition*. 2015.

[181] Magnus Schulz et al. "Circular economy considerations in choices of LCA methodology: How to handle EV battery repurposing?" In: *Procedia CIRP* 90 (2020), pp. 182–186.

[182] Stephen Ashkin. *Cradle To Grave Vs. Cradle To Cradle*. ClearLink. Jan. 2008. URL: `https://www.cleanlink.com/cp/article/Cradle-To-Grave-Vs-Cradle-To-Cradle--9277`.

[183] William McDonough and Michael Braungart. *Cradle to cradle: Remaking the way we make things*. North point press, 2002.

[184] HS Matthews, CT Hendrickson, and DH Matthews. *Life Cycle Assessment: Quantitative Approaches for Decisions That Matter*. 2018.

[185] Giorgio Cantino. *Lecture notes: OpenLCA Basic Training*. Nov. 2021.

[186] Henrikke Baumann and Anne-Marie Tillman. "The Hitch hiker's Guide to LCA: an Orientation in Life Cycle Assessment Methodology and Application". In: (2004).

[187] Ilija Sazdovski, Alba Bala, and Pere Fullana-i-Palmer. "Linking LCA literature with circular economy value creation: A review on beverage packaging". In: *Science of The Total Environment* (2021), p. 145322.

[188] Kemal Aganovic et al. "Pilot scale thermal and alternative pasteurization of tomato and watermelon juice: An energy comparison and life cycle assessment". In: *Journal of cleaner production* 141 (2017), pp. 514–525.

[189] Karin Andersson, Thomas Ohlsson, and Pär Olsson. "Screening life cycle assessment (LCA) of tomato ketchup: a case study". In: *Journal of cleaner production* 6.3-4 (1998), pp. 277–288.

[190] David Amienyo, Cecil Camilleri, and Adisa Azapagic. "Environmental impacts of consumption of Australian red wine in the UK". In: *Journal of Cleaner Production* 72 (2014), pp. 110–119.

[191] David Amienyo and Adisa Azapagic. "Life cycle environmental impacts and costs of beer production and consumption in the UK". In: *The International Journal of Life Cycle Assessment* 21.4 (2016), pp. 492–509.

[192] AE Scheepens, JG Vogtländer, and JC Brezet. "Two life cycle assessment (LCA) based methods to analyse and design complex (regional) circular economy systems. Case: Making water tourism more sustainable". In: *Journal of Cleaner Production* 114 (2016), pp. 257–268.

[193] Teresa Linhares and Maria Teresa Pessoa de Amorim. "LCA of textile dyeing with Acacia Dealbata tree bark: a case study research". In: *Procedia engineering* 200 (2017), pp. 365–369.

[194] Francesco Del Pero, Massimo Delogu, and Marco Pierini. "The effect of lightweighting in automotive LCA perspective: Estimation of mass-induced fuel consumption reduction for gasoline turbocharged vehicles". In: *Journal of Cleaner Production* 154 (2017), pp. 566–577.

[195] Thaís dos Santos Pegoretti et al. "Use of recycled natural fibres in industrial products: A comparative LCA case study on acoustic components in the Brazilian automotive sector". In: *Resources, Conservation and Recycling* 84 (2014), pp. 1–14. ISSN: 0921-3449. DOI: `https://doi.org/10.1016/j.resconrec.2013.12.010`. URL: `https://www.sciencedirect.com/science/article/pii/S0921344913002760`.

[196] Faiza Arshad et al. "Life Cycle Assessment of Lithium-ion Batteries: A Critical Review". In: *Resources, Conservation and Recycling* 180 (2022), p. 106164. ISSN: 0921-3449. DOI: `https://doi.org/10.1016/j.resconrec.2022.106164`. URL: `https://www.sciencedirect.com/science/article/pii/S092134492200012X`.

[197] Florian Degen and Marius Schütte. "Life cycle assessment of the energy consumption and GHG emissions of state-of-the-art automotive battery cell production". In: *Journal of Cleaner Production* 330 (2022), p. 129798.

[198] Marco Raugei and Patricia Winfield. "Prospective LCA of the production and EoL recycling of a novel type of Li-ion battery for electric vehicles". In: *Journal of Cleaner Production* 213 (2019), pp. 926–932.

[199] *LiBER – Lithium Battery for Emilia Romagna*. LiBER. 2020. URL: `https://liberproject.eu/en/home-eng/`.

[200] Hans Eric Melin. *Analysis of the climate impact of lithium-ion batteries and how to measure it*. Circular Energy Storage. July 2019. URL: `https://www.google.com/url?sa=t&rct=j&q=&esrc=s&source=web&cd=&ved=2ahUKEwiLweWSxNH1AhWRQ_EDHbhJDisQFnoECAQQAQ&url=https%5C%3A%5C%2F%5C%2Fwww.transportenvironment.org%5C%2Fwp-content%5C%2Fuploads%5C%2F2021%5C%2F07%5C%2F2019_11_Analysis_CO2_footprint_lithium-ion_batteries.pdf&usg=AOvVaw24S_-KOy3jWRVcR_2cmp5f`.

[201] *Guidelines for Measuring and Managing CO_2 Emission from Freight Transport Operations*. ECTA - European Chemical Transport Association. 2011. URL: `https://www.ecta.com/`.

[202] The Editors of Encyclopaedia Britannica. *Paul-Louis-Toussaint Héroult*. Britannica. URL: `https://www.britannica.com/technology/Hall-Heroult-process`.

[203] P Kapranos et al. "Advanced casting methodologies: Inert environment vacuum casting and solidification, die casting, compocasting, and roll casting". In: (2014).

[204] *Eco-profiles for determining environmental impacts of plastics*. Plastics Europe. URL: `https://plasticseurope.org/sustainability/circularity/life-cycle-thinking/eco-profiles-set/`.

[205] *Flammability UL94 - Preliminary Screening of Plastics for Fire Performance*. Omnexus - The material selection platform. URL: `https://omnexus.specialchem.com/polymer-properties/properties/flammability-ul94`.

[206] Kabata, Skorek, and Rajagopalan. "Calculation of the direct energy consumption in heat treatment processes". In: *Proceedings of Canadian Conference on Electrical and Computer Engineering*. 1994, 89–92 vol.1. DOI: `10.1109/CCECE.1994.405654`.

[207] The Aluminum Association. *The Environmental Footprint of Semi-Finished Aluminum Products in North America*. Dec. 2013.

[208] *ecoinvent Database*. ei - ecoinvent. URL: `https://ecoinvent.org/the-ecoinvent-database/`.

[209] Sabyasachi Das, Chao Liang, and Jennifer B Dunn. "Life Cycle Assessment of Polymers and Their Recycling". In: *Circular Economy of Polymers: Topics in Recycling Technologies*. ACS Publications, 2021, pp. 143–170.

[210] Niklas von der Assen et al. "Life-Cycle Assessment Principles for the Integrated Product and Process Design of Polymers from CO2". In: *Computer Aided Chemical Engineering*. Vol. 37. Elsevier, 2015, pp. 1235–1240.

[211] *Molicel® safety data sheet*. Dec. 2019. URL: `http://www.molicel.com/wp-content/uploads/00058ar-Molicel-SDS-Y2020.pdf`.

[212] *NMC Battery Material (LiNiMnCoO2)*. TARGAY. URL: `https://www.targray.com/li-ion-battery/cathode-materials/nmc`.

[213] *Batteries - Finding solutions for a longer life*. Ashland. 2022. URL: `https://www.ashland.com/industries/energy/batteries`.

[214] Linda Ager-Wick Ellingsen et al. "Life cycle assessment of a lithium-ion battery vehicle pack". In: *Journal of Industrial Ecology* 18.1 (2014), pp. 113–124.

[215] *Life cycle inventory data*. CMP - Center for environmental assessment of product and material systems. URL: `http://cpmdatabase.cpm.chalmers.se/`.

[216] Nelson Bunyui Manjong et al. "Life Cycle Modelling of Extraction and Processing of Battery Minerals—A Parametric Approach". In: *Batteries* 7.3 (2021), p. 57.

[217] *Natural resources - Brines*. SQM - Solution for human progress. 2018. URL: `https://www.sqm.com/en/acerca-de-sqm/recursos-naturales/nuestros-recursos/`.

[218] Hanjiro Ambrose and Alissa Kendall. "Understanding the future of lithium: Part 2, temporally and spatially resolved life-cycle assessment modeling". In: *Journal of Industrial Ecology* 24.1 (2020), pp. 90–100.

[219] Anna Stamp, Daniel J Lang, and Patrick A Wäger. "Environmental impacts of a transition toward e-mobility: the present and future role of lithium carbonate production". In: *Journal of Cleaner Production* 23.1 (2012), pp. 104–112.

[220] Songyan Jiang et al. "Environmental impacts of lithium production showing the importance of primary data of upstream process in life-cycle assessment". In: *Journal of environmental management* 262 (2020), p. 110253.

[221] J. Dunn et al. *Material and Energy Flows in the Production of Cathode and Anode Materials for Lithium Ion Batteries*. Argonne National Laboratory. Oct. 2014. URL: `https://greet.es.anl.gov/publication-anode-cathode-liion`.

[222] *Life Cycle Assessment (LCA) of Cobalt and Cobalt Compounds*. Cobalt Institute. 2015. URL: `https://www.cobaltinstitute.org/sustainability/life-cycle-assessment/`.

[223] Rosa Adriana Domínguez Vega. "Exergy cost assessment in global mining". PhD thesis. Universidad de Zaragoza, 2014.

[224] *Nickel energizing batteries*. Nickel Institute. 2021. URL: `https://nickelinstitute.org/media/8d926a9b562cbb4/2021-review-ni_energizing-batteries-v3.pdf`.

[225] *Nickel metal life cycle data*. Nickel Institute. 2020. URL: `https://nickelinstitute.org/media/4809/lca-nickel-metal-final.pdf`.

[226] Qiang Dai et al. "Life cycle analysis of lithium-ion batteries for automotive applications". In: *Batteries* 5.2 (2019), p. 48.

[227] *High-performance Cu Foil Rolls for LiB Manufacturing*. TARGAY. URL: `https://www.targray.com/li-ion-battery/foils/copper`.

[228] *Electrolytic Copper Foil*. Evoqua Water Technologies. 2022. URL: `https://www.evoqua.com/en/brands/magneto-special-anodes/Metal-Plating/Electrolytic-Copper-Foil/#:~:text=Copper%5C%20Foil%5C%20Production%5C%20Process&text=Generally%5C%2C%5C%20all%5C%20foil%5C%20manufacturers%5C%20dissolve,aqueous%5C%20solution%5C%20of%5C%20copper%5C%20sulfate`.

[229] *Copper Environmental Profile*. International Copper Alliance. 2022. URL: `https://copperalliance.org/sustainable-copper/about-copper/copper-environmental-profile/`.

[230] TE Norgate and WJ Rankin. "Life cycle assessment of copper and nickel production". In: (2000).

[231] *NMC Powder for Battery Manufacturers*. TARGAY. URL: `https://www.targray.com/li-ion-battery/cathode-materials/nmc`.

[232] *What do we know about next-generation NMC 811 cathode?* Research Interfaces. Feb. 2018. URL: `https://researchinterfaces.com/know-next-generation-nmc-811-cathode/`.

[233] Shabbir Ahmed et al. "Cost and energy demand of producing nickel manganese cobalt cathode material for lithium ion batteries". In: *Journal of Power Sources* 342 (2017), pp. 733–740.

[234] Shigeki Nakanishi et al. "Effect of surface treatment for aluminum foils on discharge properties of lithium-ion battery". In: *Transactions of Nonferrous Metals Society of China* 24.7 (2014), pp. 2314–2319.

[235] Naresh Susarla and Shabbir Ahmed. "Estimating Cost and Energy Demand in Producing Lithium Hexafluorophosphate for Li-Ion Battery Electrolyte". In: *Industrial & Engineering Chemistry Research* 58.9 (2019), pp. 3754–3766.

[236] Jennifer B Dunn et al. *Material and energy flows in the materials production, assembly, and end-of-life stages of the automotive lithium-ion battery life cycle*. Tech. rep. Argonne National Lab.(ANL), Argonne, IL (United States), 2014.

[237] The Editors of Encyclopaedia Britannica. *Mineral resources, noncarboniferous*. Britannica. URL: `https://www.britannica.com/place/Chile/Mineral-resources-noncarboniferous`.

[238] *Chile set to revive its dormant cobalt sector*. Resource World. 2019. URL: `https://resourceworld.com/chile-set-to-revive-its-dormant-cobalt-sector/`.

[239] Rupankar Majumder. *Chile's export of aluminium foil during 2018-20 marks a sharp rise with a minimal drop*. AICircle. May 2021. URL: `https://www.alcircle.com/news/chiles-export-of-aluminium-foil-during-2018-20-marks-a-sharp-rise-with-a-minimal-drop-65168`.

[240] Alfredo Cruzat Ossa. "Genesis of manganese deposits in northern Chile". In: *Economic Geology* 65.6 (1970), pp. 681–689.

[241] *Silicon-Chemistry Carbon Balance - An assessment gas emissions and reductions*. CES - Silicones Europe. URL: `https://www.siliconescarbonbalance.eu/#`.

[242] M Takla et al. "Energy and exergy analysis of the silicon production process". In: *Energy* 58 (2013), pp. 138–146.

[243] *The world's leading, high performance, open source Life Cycle Assessment software*. openLCA. URL: `https://www.openlca.org/`.

[244] Vincenzo Senatore et al. "Innovative membrane photobioreactor for sustainable CO2 capture and utilization". In: *Chemosphere* 273 (2021), p. 129682.

[245] Mirco Magnini. “Lab. Thesis”. MA thesis. University of Bologna, Jan. 2007.

[246] Reza Langari Alan S. Morris. “Chapter 5 - Calibration of Measuring Sensors and Instruments”. In: (2016), pp. 131–143.